frontiers | Research Topics

Carbon dynamics in freshwater, coastal and oceanic ecosystems in response to the SDG goals

Edited by
Jeng-Wei Tsai and Keisuke Nakayama

Published in
Frontiers in Marine Science

ISSN 1664-8714
ISBN 978-2-8325-2726-9
DOI 10.3389/978-2-8325-2726-9

About Frontiers

Frontiers is more than just an open access publisher of scholarly articles: it is a pioneering approach to the world of academia, radically improving the way scholarly research is managed. The grand vision of Frontiers is a world where all people have an equal opportunity to seek, share and generate knowledge. Frontiers provides immediate and permanent online open access to all its publications, but this alone is not enough to realize our grand goals.

Frontiers journal series

The Frontiers journal series is a multi-tier and interdisciplinary set of open-access, online journals, promising a paradigm shift from the current review, selection and dissemination processes in academic publishing. All Frontiers journals are driven by researchers for researchers; therefore, they constitute a service to the scholarly community. At the same time, the *Frontiers journal series* operates on a revolutionary invention, the tiered publishing system, initially addressing specific communities of scholars, and gradually climbing up to broader public understanding, thus serving the interests of the lay society, too.

Dedication to quality

Each Frontiers article is a landmark of the highest quality, thanks to genuinely collaborative interactions between authors and review editors, who include some of the world's best academicians. Research must be certified by peers before entering a stream of knowledge that may eventually reach the public - and shape society; therefore, Frontiers only applies the most rigorous and unbiased reviews. Frontiers revolutionizes research publishing by freely delivering the most outstanding research, evaluated with no bias from both the academic and social point of view. By applying the most advanced information technologies, Frontiers is catapulting scholarly publishing into a new generation.

What are Frontiers Research Topics?

Frontiers Research Topics are very popular trademarks of the *Frontiers journals series*: they are collections of at least ten articles, all centered on a particular subject. With their unique mix of varied contributions from Original Research to Review Articles, Frontiers Research Topics unify the most influential researchers, the latest key findings and historical advances in a hot research area.

Find out more on how to host your own Frontiers Research Topic or contribute to one as an author by contacting the Frontiers editorial office: frontiersin.org/about/contact

Carbon dynamics in freshwater, coastal and oceanic ecosystems in response to the SDG goals

Topic editors

Jeng-Wei Tsai — National Pingtung University of Science and Technology, Taiwan

Keisuke Nakayama — Kobe University, Japan

Citation

Tsai, J.-W., Nakayama, K., eds. (2023). *Carbon dynamics in freshwater, coastal and oceanic ecosystems in response to the SDG goals*. Lausanne: Frontiers Media SA. doi: 10.3389/978-2-8325-2726-9

Table of contents

frontiers | Frontiers in Marine Science

TYPE Editorial
PUBLISHED 01 June 2023
DOI 10.3389/fmars.2023.1212305

OPEN ACCESS

EDITED AND REVIEWED BY
Eric 'Pieter Achterberg,
Helmholtz Association of German Research Centres (HZ), Germany

*CORRESPONDENCE
Jeng-Wei Tsai
tsaijw@mail.npust.edu.tw
Keisuke Nakayama
nakayama@phoenix.kobe-u.ac.jp

RECEIVED 26 April 2023
ACCEPTED 23 May 2023
PUBLISHED 01 June 2023

CITATION
Tsai J-W and Nakayama K (2023) Editorial: Carbon dynamics in freshwater, coastal and oceanic ecosystems in response to the SDG goals.
Front. Mar. Sci. 10:1212305.
doi: 10.3389/fmars.2023.1212305

Editorial: Carbon dynamics in freshwater, coastal and oceanic ecosystems in response to the SDG goals

Jeng-Wei Tsai[1]* and Keisuke Nakayama[2]*

[1]Graduate Institute of Bioresources, National Pingtung University of Science and Technology, Pingtung, Taiwan, [2]Graduate School of Engineering, Kobe University, Kobe, Japan

KEYWORDS

dissolved organic matters (DOM), blue carbon, climate change, natural solution, hydrological modeling

Editorial on the Research Topic

Carbon dynamics in freshwater, coastal and oceanic ecosystems in response to the SDG goals

Introduction

Ocean and coastal areas are buffers against global warming by absorbing 23% CO2 from the atmosphere (Sabine et al., 2004; DeVries et al., 2017). Significantly, coastal and oceanic vegetated ecosystems (such as wetlands, corals, mangroves, seagrass meadows, and kelps), so-called "blue carbon ecosystems" (B.C.E.), have been paid attention to absorb and sequester carbon dioxide from the atmosphere (Nellemann et al., 2009). Recently, freshwater carbon ecosystems, such as lakes, ponds and reservoirs, have also been revealed to contribute to atmospheric carbon sequestration. However, variations in climate patterns, biodiversity spectrums, and anthropogenic activities (e.g., non-sustainable resource extraction, land-based pollution and habitat degradation) across the ecosystems could alter the fragile balance of B.C.E. as carbon sinks or sources (Malhi et al., 2020; Abbass et al., 2022). Also, higher spatiotemporal carbon flux variation was observed in coastal and estuary ecosystems due to intensive anthropogenic activities, natural biological processes, and fluctuating terrestrial loads (Asmala et al., 2016, Asmala et al., 2020). Consequently, understanding the factors and processes that drive the spatiotemporal variations in Dissolved Organic Matter (D.O.M.) quantity and quality under changing environmental conditions would benefit the sustainable use of natural resources in freshwater, coastal and oceanic ecosystems. To contribute to the S.D.G. Goals in Climate Action (Goal 13) and Life Below Water (Goal 14), this Research Topic focuses on carbon dynamics, e.g., GHG emission/storage (blue carbon), as well as environmental stresses such as acidification, fishery resource and pollution (e.g., eutrophication, dead zone and metal pollution) in freshwater, coastal and oceanic ecosystems. Eleven research articles were collected on this Research Topic, as summarized below.

Shallow coastal waters have attracted due to their strong carbon sequestration capacity. Macroalgae culture is considered a natural-based solution for marine carbon sequestration.

Research Topics revealed that carbon sequestration by kelp culture is applicable; 5% of DOC released by *S. japonica* was transformed to refractory DOC, and an estimated 1–2% of the net primary production of cultured kelp was sequestrated as refractory DOC. Also, tidal flats are expected to have the same carbon sequential potential as shallow coastal areas. However, the complicated temporal and spatial variation of carbon dioxide (CO_2) makes it difficult to accurately estimate the air-water CO_2 fluxes (fCO_2). For example, the size of an Submerged Aquatic Vegetation (S.A.V.) patch significantly affects flows and carbon sequestration. In contrast to small-scale phenomena, the higher fCO_2 values in the cyclonic and non-eddy regions were revealed due to the upwelling, increasing the surface fCO_2. Additionally, physical processes (such as the residence time and water depth) drive CO_2 and O_2 temporal and spatial patterns; otherwise, biological processes (benthic algae biomass and respiration) may also affect variability within lakes, ponds and reservoirs.

From the water quality perspective, nutrient pollution threatens the seagrass community and may adversely affect their carbon sequestration potential, diminishing the carbon sequestration potential of seagrass ecosystems. Higher nutrient loading elevated labile organic carbon content (e.g., free amino acids and soluble sugars). Contrary, refractory organic carbon compositions of seagrass tissues (i.e., cellulose-associated organic matter) decreased with increasing nutrient loading. Also, an urbanized enclosed bay has environmental problems, such as hypoxia, which degrades carbon dioxide absorption from the atmosphere to the water surface.

As a necessity of new research, the importance of "blue carbon" (marine carbon) in the global quest to achieve carbon neutrality has been well understood. However, freshwater carbon has yet to be considered as a climate change mitigation approach, although freshwater areas (5.0 million km^2) are more extensive than coastal areas (1.8 million km^2) and are expected to have more significant potential for carbon sequestration. Therefore, we need more investigations on both not only marine carbon but also freshwater carbon. The results of this study provide new and deeper insights into coastal carbon dynamics to propose climate change mitigation in future climate and to achieve the S.D.G.s.

Author contributions

J-WT and KN structured this Research Topic. All guest editors have edited and reviewed the editorial articles, and approved the submitted version.

Funding

This study was supported by National Science and Technology Council, Taiwan, R.O.C. (MOST 111-2313-B-039 -001 -MY3) for J-WT. Also, This study was supported by Japan Society for the Promotion of Science, Japan (18KK0119, 22H01601, 22H05726) for KN.

Conflict of interest

The authors declare that the research was conducted in the absence of any commercial or financial relationships that could be construed as a potential conflict of interest.

Publisher's note

References

Abbass, K., Qasim, M. Z., Song, H., Murshed, M., Mahmood, H., and Younis, I. (2022). A review of the global climate change impacts, adaptation, and sustainable mitigation measures. *Environ. Sci. Pollut. Res.* 29, 42539–42559. doi: 10.1007/s11356-022-19718-6

Asmala, E., Kaartokallio, H., Carstensen, J., and Thomas, D. N. (2016). Variation in riverine inputs affect dissolved organic matter characteristics throughout the estuarine gradient. *Front. Mar. Sci.* 2. doi: 10.3389/fmars.2015.00125

Asmala, E., Osburn, C. L., Paerl, R. W., and Paerl, H. W. (2020). Elevated organic carbon pulses persist in estuarine environment after major storm events. *Limnology Oceanography Lett.* 6, 43–50. doi: 10.1002/lol2.10169

DeVries, T., Holzer, M., and Primeau, F. (2017). Recent increase in oceanic carbon uptake driven by weaker upper-ocean overturning. *Nature* 542, 215–218. doi: 10.1038/nature21068

Malhi, Y., Janet, F., Nathalie, S., Martin, S., Monica, G. T., Christopher, B. F., et al. (2020). Climate change and ecosystems: threats, opportunities and solutions. *Philos. Trans. R. Soc. B.* 375:20190104. doi: 10.1098/rstb.2019.0104

Nellemann, C., Corcoran, E., Duarte, C. M., Valdes, L., De Young, C., Fonseca, L., et al. (2009). *Blue carbon. a rapid response assessment* (GRID-Arendal, Birkeland Trykkeri AS, Birkeland: United Nations Environmental Programme).

Sabine, C. L., Feely, R. A., Gruber, N., Key, R. M., Lee, K., Bullister, J. L., et al. (2004). The oceanic sink for anthropogenic CO_2. *Science* 305, 367–371. doi: 10.1126/science.1097403

frontiers | Frontiers in Marine Science

TYPE Original Research
PUBLISHED 11 August 2022
DOI 10.3389/fmars.2022.970678

OPEN ACCESS

EDITED BY
Keisuke Nakayama,
Kobe University, Japan

REVIEWED BY
Andreey Andreev,
V.I. Il'ichev Pacific Oceanological Institute (RAS), Russia
Akira TAI,
Kyushu University, Japan

*CORRESPONDENCE
Dongseon Kim
dkim@kiost.ac.kr

SPECIALTY SECTION
This article was submitted to Marine Biogeochemistry, a section of the journal Frontiers in Marine Science

RECEIVED 16 June 2022
ACCEPTED 25 July 2022
PUBLISHED 11 August 2022

CITATION
Kim D, Lee S-E, Cho S, Kang D-J, Park G-H and Kang SK (2022) Mesoscale eddy effects on sea-air CO_2 fluxes in the northern Philippine Sea. *Front. Mar. Sci.* 9:970678. doi: 10.3389/fmars.2022.970678

Mesoscale eddy effects on sea-air CO_2 fluxes in the northern Philippine Sea

Dongseon Kim*, Seon-Eun Lee, Sosul Cho, Dong-Jin Kang, Geun-Ha Park and Sok Kuh Kang

Marine Environment and Climate Research Division, Korea Institute of Ocean Science & Technology, Busan, South Korea

To determine the effects of mesoscale eddies on sea-air CO_2 flux, we investigated the surface fugacity of CO_2 (surface fCO_2) distribution in the northern Philippine Sea, where mesoscale eddies are common. Surface fCO_2 showed large spatial variations, such that values were high in the non-eddy and cyclonic eddy regions, while they were low within the anticyclonic eddy. The maximum fCO_2 was observed in the non-eddy region; higher fCO_2 values were observed in the area surrounding the cyclonic eddy than at the center of the cyclonic eddy. Within the cyclonic eddy, the contribution of dissolved inorganic carbon (DIC) enrichment because of upwelling was considerably offset by cooling. In the non-eddy region, the contribution of DIC enrichment from upwelling was rarely offset by cooling; thus, the maximum fCO_2 was observed in the non-eddy region. Surface fCO_2 showed a robust correlation with sea surface temperature (SST) within the cyclonic and anticyclonic eddies, but it did not display any correlation in the non-eddy region. Temperature was a major factor that controlled surface fCO_2 in the anticyclonic eddy, but this effect was absent in the cyclonic eddy. Temperature-normalized fCO_2 exhibited a clear negative relationship with SST in the cyclonic eddy and the non-eddy region, indicating that surface fCO_2 was considerably affected by the upwelling of high-fCO_2 deep water in both regions. Sea-air CO_2 fluxes ranged from 0.011 to 9.92 mmol m^{-2} day^{-1} and all values were positive, indicating that the entire study area acted as a CO_2 source during the research period. The estimated mean sea-air CO_2 fluxes in the cyclonic eddy, anticyclonic eddy, and non-eddy region were 1.10 $\pm$ 0.75, 0.64 $\pm$ 0.66, and 1.42 $\pm$ 1.12 mmol m^{-2} day^{-1}, respectively. The sea-air CO_2 fluxes considerably varied according to eddy type; they were almost twofold higher in the cyclonic eddy than in the anticyclonic eddy. In the cyclonic eddy and non-eddy regions, upwelling caused surface fCO_2 to increase, thereby increasing sea-air CO_2 flux.

KEYWORDS

cyclonic eddy, anticyclonic eddy, sea-air CO_2 flux, surface fCO_2, philippine sea

Introduction

The Philippine Sea is a marginal sea bounded by the Philippines and Taiwan to the west, the Ryukyu Island arc to the north, and the Izu–Mariana Ridge to the east (Ramp et al., 2017). This sea is oceanographically bounded by the North Equatorial Current to the south, Kuroshio Current to the west, and Ryukyu Current to the north (Yaremchuk and Qu, 2004; Andres et al., 2008; Ramp et al., 2017). The Subtropical Counter Current (STCC) flows eastward in the Philippine Sea; it is present at shallow depths (~100 m) around 17–27°N latitude and 130–180°E longitude (Chang and Oey, 2014). The STCC region contains cyclonic and anticyclonic eddies with diameters of ~300 km that propagate westward at approximately 8–10 km day^{-1} (Chelton et al., 2011). These STCC eddies have large impacts on ocean circulation in the western North Pacific Ocean (Zhang et al., 2001; Miyazawa et al., 2008; Sheu et al., 2010).

In the open ocean, mesoscale eddies have considerable impacts on surface fugacity of CO_2 (fCO_2) and sea-air CO_2 flux (Mahadevan et al., 2004; Gonzalez-Davila et al., 2006; Chen et al., 2007; Song et al., 2016; Moreau et al., 2017; Orselli et al., 2019). In cyclonic eddies, the uplift of subsurface waters may initially increase surface fCO_2, but this increase is largely offset by the lower temperature and biological productivity of the uplifted waters (Mahadevan et al., 2004); they have suggested that the vertical transport of dissolved inorganic carbon (DIC), temperature, and nitrate, as well as their contributions to surface fCO_2, mainly depend on their vertical gradients below the mixed layer. In the subtropical North Pacific Ocean, a negative relationship between sea surface temperature (SST) and surface fCO_2 is observed in a cold cyclonic eddy; the magnitude of the CO_2 sink decreases by 17% with the passage of a mesoscale cyclonic eddy (Chen et al., 2007). In the subtropical North Atlantic Ocean, surface fCO_2 is 15 μatm lower inside the cyclonic eddy than in surrounding waters (Gonzalez-Davila et al., 2006). In the South Atlantic Ocean, anticyclonic eddies serve as CO_2 sinks relative to the surrounding waters (Orselli et al., 2019). In the Southern Ocean, eddy effects on sea-air CO_2 fluxes are rather complex; compared with cyclonic eddies, anticyclonic eddies take up more CO_2 during summer (this relationship is reversed in winter), and anticyclonic eddies exhibit more outgassing than do cyclonic eddies (Song et al., 2016). In the open ocean, therefore, the impacts of mesoscale eddies on sea-air CO_2 fluxes are not simple; the overall sign and magnitude depend on a complex balance of physical and biological processes.

Several researchers have reported that surface fCO_2 is nearly equilibrated with atmospheric CO_2 in the Philippine Sea; therefore, the sea-air CO_2 flux is near zero (Inoue et al., 1995; Ishii et al., 2001; Takahashi et al., 2009; Ishii et al., 2014; Yasunaka et al., 2019). No zonal survey of surface fCO_2 has been conducted in the STCC region of the Philippine Sea where both cyclonic and anticyclonic eddies are abundant. These mesoscale eddies can affect the zonal distribution of surface fCO_2 and sea-air CO_2 flux in the Philippine Sea. In this study, we conducted a zonal survey of surface fCO_2 in the northern Philippine Sea where cyclonic and anticyclonic eddies frequently occur. We identified the major factors that control surface fCO_2 in the northern Philippine Sea. In addition, we explored how surface fCO_2 was affected by changes in SST, sea surface salinity (SSS), DIC, and total alkalinity (TA). Finally, we characterized the sea-air CO_2 flux in cyclonic eddy, anticyclonic eddy, and non-eddy regions to elucidate the effects of mesoscale eddies on sea-air CO_2 flux in the northern Philippine Sea.

Materials and methods

This study was conducted on the R/V ISABU in the northern Philippine Sea from September 14th to 23rd, 2017 (Figure 1). Underway samples were collected using the flow-through system onboard R/V ISABU. Surface fCO_2 was obtained from a commercial underway pCO_2 system (Model 8050, General Oceanics Inc., FL, USA) equipped on the vessel; the system consisted of a non-dispersive infrared analyzer (Li-7000, LI-COR Inc., NE, USA) connected through an 8-port switching valve to three types of gases (standard gases, ambient air, and air equilibrated with flowing seawater). The analyzer was calibrated at 14-h intervals using three standard gases with different CO_2 concentrations (202, 350, and 447 ppm in dry air) after it had been zeroed and spanned using ultra-high-purity standard N_2 gas (zero-CO_2 gas) and 447-ppm CO_2 standard gas, respectively. The system was operated on the following cycle: 3 standard gases, 10 measurements of ambient air, 40 measurements of air equilibrated with seawater, and 3 repeats of all previous measurements except the standard gases. CO_2 measurement was conducted in mole fraction in dry air (xCO_2) mode at 4-min intervals, then converted into fCO_2 through correction for non-ideality and water vapor fraction based on the method established by Pierrot et al. (2009). Because atmospheric and seawater CO_2 measurements were not conducted concurrently, the atmospheric CO_2 value associated with each seawater measurement was linearly interpolated from the two nearest atmospheric measurement sets. Underway SST and SSS data were obtained alongside CO_2 measurements using a digital thermometer (SBE-38, Sea-Bird Scientific, WA, USA) and a thermosalinograph (SBE-45, Sea-Bird Scientific), respectively, installed near the seawater intake of the vessel.

Vertical profiles of temperature and salinity were measured with a calibrated conductivity–temperature–depth/pressure recorder (SBE-911; Sea-Bird Electronics Inc., WA, USA) at 29 stations (Figure 1). Seawater samples were collected for the measurement of DIC, TA, nitrate+nitrite (hereafter referred to as nitrate), and chlorophyll-*a* using a rosette sampler with 10-L

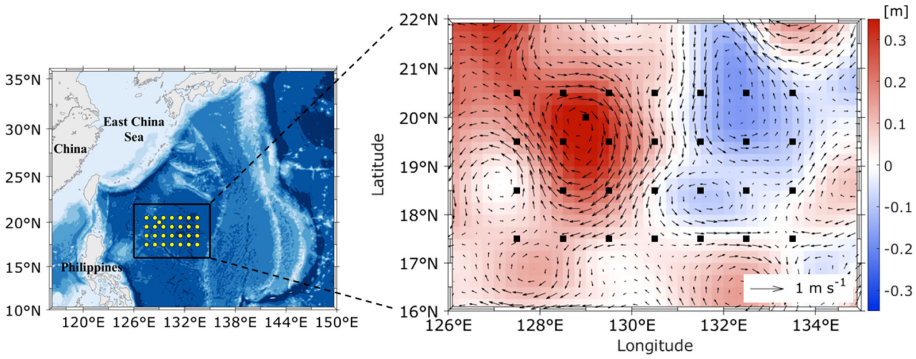

FIGURE 1
Map of the study area and locations of sampling stations overlaid on mean sea surface height anomaly and geostrophic velocity in the northern Philippine Sea from September 14th to 23rd, 2017. Red color indicates an anticyclonic eddy, and blue color indicates a cyclonic eddy.

Niskin bottles mounted on the conductivity–temperature–depth/pressure assembly. DIC concentrations were determined using the VINDTA 3D system (Marianda, Kiel, Germany) coupled to a CO_2 coulometric titrator (Model 5011: UIC, Inc., Joliet, IL, USA). TA concentrations were determined with a potentiometric titration system (AS-ALK2, Apollo SciTech LLC, DE, USA). The measurement uncertainty of DIC and TA was evaluated on a daily basis using certified reference materials provided by the Scripps Institution of Oceanography (University of California, San Diego, CA, USA). The precisions of DIC and TA were ± 2 μmol kg^{-1} and ± 3 μmol kg^{-1}, respectively. Nitrate concentrations were measured using a four-channel continuous auto-analyzer (QuAAtro 39, Seal Analytical Inc., Germany). Reference materials for nitrate in seawater provided by "KANSO Technos" (Lot. No. "BV") were measured alongside standards in each batch. The analytical error for nitrate was ± 0.14 μmol kg^{-1}. Water samples for chlorophyll-*a* analysis were filtered through GF/F filters (47 mm, Whatman). Chlorophyll-*a* concentrations were determined using extracted filtrate mixed with 90% acetone for 24 h shipboard with a fluorometer (Trilogy; Turner Designs, USA) that had been previously calibrated against pure chlorophyll-*a* (Sigma, USA).

Temperature-normalized surface fCO_2 values were calculated by normalizing surface fCO_2 based on temperature to examine the effects of SST on the distribution of surface fCO_2, as suggested by Takahashi et al. (1993), using the following equation:

$$\text{Temperature} - \text{normalized surface} \quad fCO_2 = \text{surface}\, fCO_2 \exp[0.0423(SST_{aver} - SST_{meas})] \quad (1)$$

where 0.0423 is the thermodynamic coefficient (Takahashi et al., 1993), SST_{aver} is the average of all underway SST measurements within the study area (30.1°C), and SST_{meas} is the observed value for each CO_2 measurement.

Sea-air CO_2 flux was calculated using the following equations:

$$\text{Sea} - \text{air}\, CO_2 \text{flux} = kK_0(\text{surface}\, fCO_2 - \text{atmospheric}\, fCO_2) \quad (3)$$

$$k = 0.251\, U_{10}^2 (Sc/660)^{-0.5} \quad (4)$$

where k and K_0 are the gas transfer velocity and the solubility coefficient of CO_2 in seawater, respectively (Weiss, 1974). For the coefficient k, we used the constant value (0.251) from the formulation of Wanninkhof (2014). U_{10} and Sc indicate wind speed collected at 10 m altitude and the Schmidt number, respectively. Wind speed data were obtained from an automatic weather station installed on R/V ISABU during underway CO_2 measurement.

Daily mean satellite altimeter gridded sea level anomaly data with 0.25° × 0.25° spatial resolution were used to examine the appearance and movement of eddies; they were obtained from a data product estimated through the optimal interpolation method, which merged available measurements from multiple altimeter missions. These data are available online from the Copernicus Marine Service (https://marine.copernicus.eu).

Results

In the study area, two eddies (cyclonic and anticyclonic) were identified on the basis of sea surface height anomaly (SSHA) during the research period (Figure 1). SSHA is negative for a cyclonic eddy, whereas it is positive for an anticyclonic eddy. The cyclonic eddy propagated westward at a rate of 8 km day^{-1}, while the anticyclonic eddy propagated

southwestward at a rate of 6 km day^{-1} during the research period. The widths of the anticyclonic and cyclonic eddies had ranges of 400–440 km and 120–160 km, respectively, during the research period (Figure 1). The anticyclonic eddy was stronger than the cyclonic eddy. Surface waters in the cyclonic eddy were typically colder and more saline, while they were warmer and fresher in the anticyclonic eddy (Figures 2A, B). Surface fCO_2 ranged from 384.2 to 406.7 µatm, with a mean of 393.2 µatm; atmospheric fCO_2 varied from 379.2 to 383.1 µatm, with a mean of 381.2 µatm. Lower surface fCO_2 was observed in the anticyclonic eddy containing fresher and warmer waters (Figure 2C). The cyclonic eddy, with saltier and colder waters, showed moderate surface fCO_2 (395–400 µatm). Higher surface fCO_2 (> 400 µatm) was found in the area surrounding the cyclonic eddy (Figure 2C). Surface DIC concentrations ranged from 1902 to 1963 µmol kg^{-1}, with higher values in the cyclonic eddy and lower values in the anticyclonic eddy (Figure 2D). Surface TA displayed a distribution pattern similar to DIC, with a concentration range of 2237–2288 µmol kg^{-1} (Figure 2E).

The vertical distributions of temperature, salinity, seawater density, DIC, TA, nitrate, and chlorophyll-*a* were plotted along the 19.5°N transect, where both cyclonic and anticyclonic eddies were observed (Figure 3). The upper layer from the surface to 200 m was warmer and less salty in the anticyclonic eddy than in the cyclonic eddy (Figures 3A, B). The uplifted structure of the cyclonic eddy was clearly observed from the vertical distributions of temperature, salinity, and seawater density, whereas a downwelled structure was observed in the anticyclonic eddy. DIC concentrations generally showed low values (< 1940 µmol kg^{-1}) within the upper 50 m of the anticyclonic eddy; these low values were associated with low salinity in this layer (Figure 3D). The DIC concentration was approximately 40 µmol kg^{-1} higher at 50 m of water depth in the cyclonic eddy than at the same depth in the anticyclonic eddy. DIC exhibited a distinct downwelling pattern within the 300 m water depth of the anticyclonic eddy. TA displayed a vertical distribution similar to DIC, with a downwelling pattern within the upper 300 m of water in the anticyclonic eddy (Figure 3F). Nitrate was completely depleted

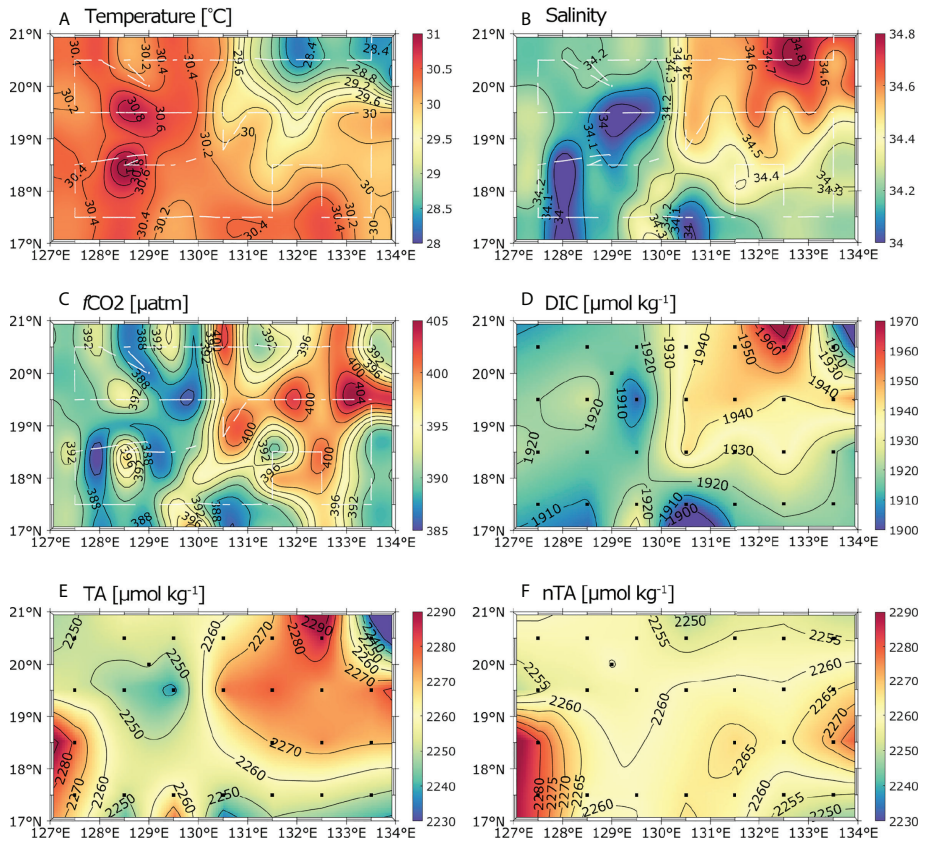

FIGURE 2
Surface distributions of temperature **(A)**, salinity **(B)**, fCO2 **(C)**, DIC **(D)**, TA **(E)**, and salinity-normalized TA (nTA, F) in the study area. Underway and discrete measurements are shown in white lines **(A–C)** and black dots **(D, E)**, respectively.

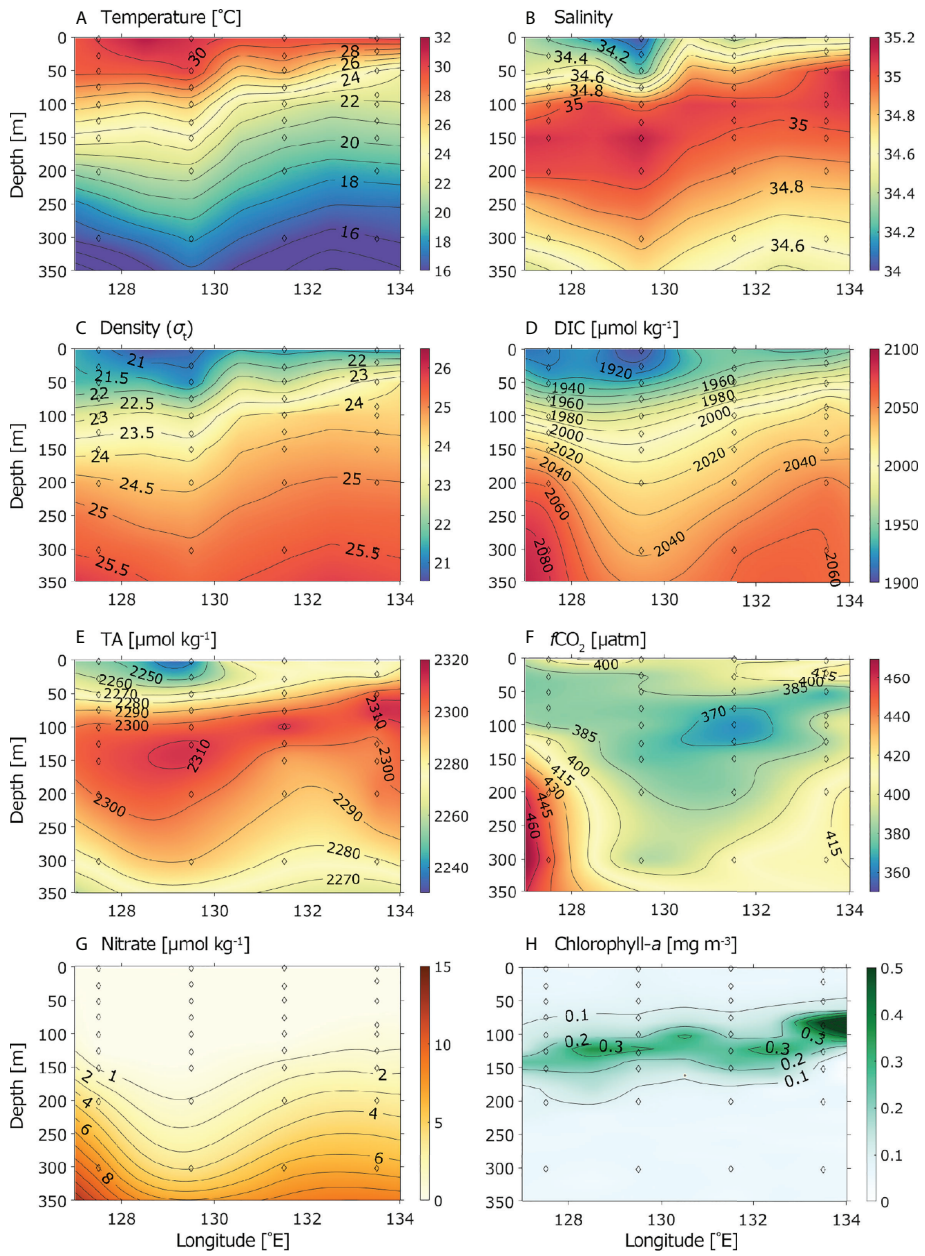

FIGURE 3
Vertical distributions of temperature **(A)**, salinity **(B)**, seawater density **(C)**, DIC **(D)**, TA **(E)**, fCO2 **(F)**, nitrate **(G)**, and chlorophyll-a **(H)** along the 19.5°N transect. Open diamonds indicate sampling depths.

within the upper 100 m of the water column in the study area, with extremely low concentrations (< 1.0 μmol kg^{-1}, Figure 3G). Nitrate showed a downwelling pattern below 150 m in depth within the anticyclonic eddy. Chlorophyll-*a* concentrations were rather low (< 0.1 mg m^{-3}) and uniform within the upper 80 m of water (Figure 3H). A subsurface chlorophyll maximum was observed at the depth of 130 m in the anticyclonic eddy and at 100 m in the cyclonic eddy.

Discussion

Major factors controlling the surface fCO_2 distribution

In the open ocean, surface fCO_2 generally exhibits a significant correlation with SST (Stephens et al., 1995; Bates et al., 1998; Nelson et al., 2001; Takahashi et al., 2002; Olsen

et al., 2004; Chen et al., 2007; Parard et al., 2016). However, in the study area, surface fCO_2 was not strongly correlated with SST; there was considerable variation in the data (Figure 4A). We divided the study area into three regions on the basis of SSHA: cyclonic eddy (SSHA ≤ −0.1 m), anticyclonic eddy (SSHA ≥ 0.1 m), and non-eddy (−0.1 m < SSHA < 0.1 m). Surface fCO_2 exhibited a significant correlation ($r = 0.75$, $p < 0.001$) with SST within the cyclonic eddy (Figure 4B) and a relatively strong correlation ($r = 0.61$, $p < 0.001$) within the anticyclonic eddy; it did not exhibit a correlation in the non-eddy region (Figure 4B). These results substantially differ from findings in the subtropical northeastern Pacific, where surface fCO_2 showed a positive linear relationship with SST outside of a cyclonic eddy and a negative relationship with SST within the cyclonic eddy (Chen et al., 2007). This discrepancy was presumably related to different vertical gradients of temperature and DIC below the mixed layer in these two areas; such gradients drive the vertical transport of temperature and DIC (Mahadevan et al., 2004).

Surface fCO_2 was positively linearly correlated with SST within the anticyclonic eddy, such that its values were positioned along two lines (Figure 5). These two lines were separated by approximately 5 µatm of surface fCO_2 at a given SST. The slopes ($\partial \ln fCO_2/\partial T$) of those two lines were identical (0.0358), which was similar to the isochemical trend (0.0423) identified by Takahashi et al. (1993); the findings suggested that temperature was a major factor controlling surface fCO_2 within the anticyclonic eddy. The two lines were separated according to latitude; the upper line was located along the 20.5°N transect, while the lower line was located at the 18.5 and 19.5°N transects. SSS did not considerably differ between the two transects, but surface DIC concentrations were slightly higher along the 20.5°N transect than along the 18.5 and 19.5°N transects (Figure 2D); thus, fCO_2 of the upper line was 5 µatm higher at a given SST, compared with fCO_2 of the lower line.

Surface fCO_2 was also positively correlated with SST within the cyclonic eddy (Figure 4B), with a slope ($\partial \ln fCO_2/\partial T$) of 0.0128, which was much lower than the isochemical trend (0.0423); this finding suggested that temperature was not a major factor controlling surface fCO_2 within the cyclonic eddy. In the plot of temperature-normalized fCO_2 at 30.1°C vs. SST, a negative relationship was clearly present within the cyclonic eddy (Figure 6A). This negative relationship within the cyclonic eddy may be attributed to the upwelling of high-fCO_2 deep water. The highest temperature-normalized fCO_2 value (428.4 µatm) was observed at the minimum temperature (28.2°C), which was found at the center of the cyclonic eddy. The temperature-normalized fCO_2 value increased by 30.4 µatm from a mean value of 398.0 µatm in the non-eddy region to the maximum value of 428.4 µatm within the cyclonic eddy because of the upwelling of cold high-fCO_2 deep water. When this cold high-fCO_2 deep water reached the surface and flowed away from the eddy center, it mixed with warm low-fCO_2 surface water; thus, temperature-normalized fCO_2 decreased with increasing SST. In addition, temperature-normalized fCO_2 decreased because of CO_2 efflux and biological uptake (Takahashi et al., 2002; Chen et al., 2007). The cyclonic eddy showed positive ΔfCO_2 values (surface fCO_2 – atmospheric fCO_2), with a range of 5.2–24 µatm (Figure 7A); this finding indicated that CO_2 was outgassed in the study area in September 2017. Thus, the temperature-normalized fCO_2 might be reduced because of CO_2 efflux. Biological uptake is an important driver of decreased surface fCO_2 in the ocean. The upwelling of nitrate-enriched deep water may enhance biological production because nitrate is completely depleted in the surface water (Figure 3G) and DIC is consumed during biological uptake fueled by upwelled nitrate, which causes surface fCO_2 to decrease. In the study area, nitrate concentrations were extremely low (< 1.0 µmol kg^{-1}) within the upper 100 m of the water column and showed no uplifted structure (Figure 3G). In addition,

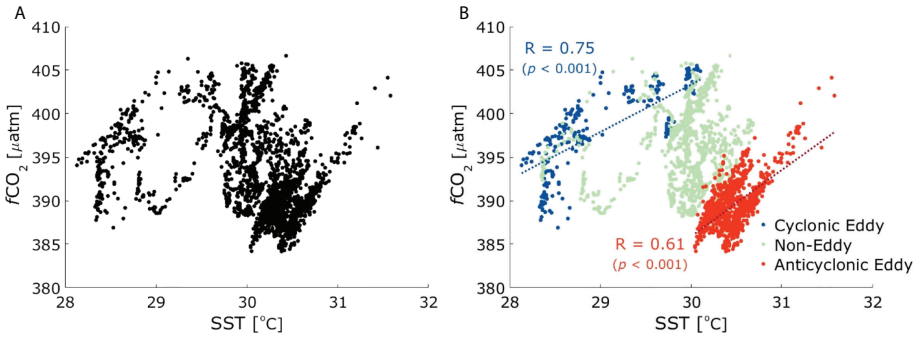

FIGURE 4
Plots of fCO_2 vs. SST in the study region **(A)** and three subregions **(B)**; cyclonic eddy, anticyclonic eddy, and non-eddy. Blue dots indicate a cyclonic eddy, green dots are non-eddy region, and red dots are an anticyclonic eddy. Dotted lines indicate linear regressions in the cyclonic and anticyclonic eddies.

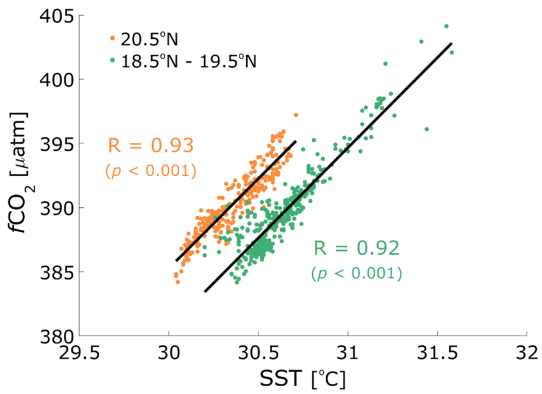

FIGURE 5
Plots of fCO_2 vs. SST in the anticyclonic eddy. Solid lines indicate linear regressions at 20.5°N and 18.5°N-19.5°N transects.

chlorophyll-*a* concentrations were rather low (< 0.1 mg m^{-3}) and uniform within the upper 80 m of the water column (Figure 3H). Thus, biological uptake may not considerably influence the temperature-normalized fCO_2 decrease in the study area.

In the non-eddy region, temperature-normalized fCO_2 also showed a negative relationship with SST (Figure 6B). This negative relationship indicated that the non-eddy region was affected by the upwelling of high-fCO_2 deep water. Higher temperature-normalized fCO_2 values were found in the area surrounding the cyclonic eddy. Chen et al. (2007) observed that temperature-normalized pCO_2 values were nearly independent of the temperature outside the cyclonic eddy in the subtropical northeastern Pacific Ocean; they suggested that temperature was a major factor controlling surface pCO_2 in that region. Thus, surface pCO_2 behavior in the subtropical northeastern Pacific Ocean markedly differed from surface pCO_2 behavior in our study area (the northern Philippine Sea), where temperature was not a major factor controlling surface fCO_2 outside of the cyclonic eddy. In our study, we found that the upwelling of high-fCO_2 deep water considerably influenced surface fCO_2 in the area surrounding the cyclonic eddy. The cyclonic eddy propagated westward at a rate of 8 km day^{-1}. The area surrounding the cyclonic eddy may be affected by the upwelling of high-fCO_2 deep water; this possibility was corroborated by the observation of elevated temperature-normalized fCO_2 values only in the area surrounding the cyclonic eddy. In the the anticyclonic eddy, most temperature-normalized fCO_2 values were present within the narrow SST range of 30–31°C, and a weak negative relationship with SST was observed (Figure 6C).

Spatial variations of surface fCO_2

Surface fCO_2 showed high spatial variability, such that values were high in the non-eddy region and anticyclonic

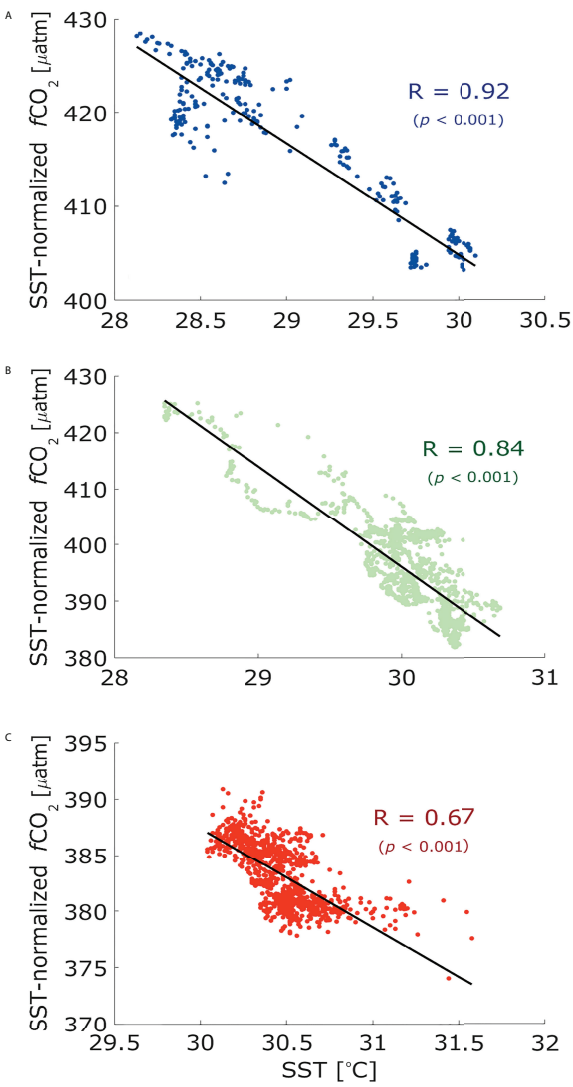

FIGURE 6
Plots of temperature-normalized fCO2 vs. SST in the cyclonic eddy **(A)**, non-eddy region **(B)**, and anticyclonic eddy **(C)**. Solid lines indicate linear regressions.

eddy, while they were low within the cyclonic eddy (Figure 2C). The maximum fCO_2 was observed in the non-eddy region, which was located at the center of the study area (Figure 2C). Indeed, elevated surface fCO_2 was observed in the area surrounding the cyclonic eddy, but it was absent from the center of the cyclonic eddy (Figure 2C). The upwelled water enriched in DIC had a high fCO_2 value, but its impact was offset by the low temperature of the upwelled water. To determine the effect of upwelling on surface fCO_2 in the cyclonic eddy and non-eddy regions, we explored the effects of changes in SST, SSS, DIC, and TA on surface fCO_2 by using the following equation (Takahashi et al., 1993; Sarmiento and Gruber, 2006);

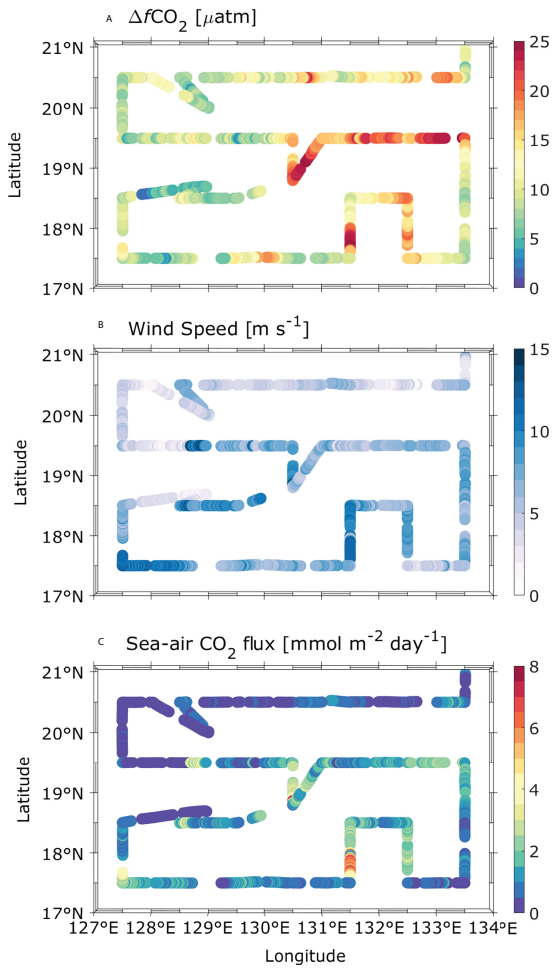

FIGURE 7
Spatial distributions of ΔfCO_2**(A)**, wind speed **(B)**, and sea-air CO_2 fluxes **(C)** in the northern Philippine Sea from September 14th to 23rd, 2017.

$$\frac{\delta pCO2}{pCO2} \approx \frac{1}{pCO2}\frac{\delta pCO2}{\delta SST}\delta SST + \frac{1}{pCO2}\frac{\delta pCO2}{\delta SSS}\delta SSS + \frac{1}{pCO2}\frac{\delta pCO2}{\delta DIC}\delta DIC + \frac{1}{pCO2}\frac{\delta pCO2}{\delta TA}\delta TA \quad \approx \beta\delta SST + \alpha\frac{\delta SSS}{SSS} + \gamma_{DIC}\frac{\delta DIC}{DIC} + \gamma_{TA}\frac{\delta TA}{TA}$$

The equation used by authors (p. 7) is valid only along the water pathway (Lagrangian approach). The presented equation takes into account the changes in the seawater pCO2 due to evaporation/precipitation, warming/cooling, and photosynthesis/organic matter degradation. But it does not take into account the changes in the seawater pCO2 due to mixing (horizontal and vertical) with the water masses of different origin and different initial (pre-formed) values of pCO2 (T, S, TA, DIC). It's necessarily to add some contents on cyclone and anticyclone water origin.

Anaswer: The changes in the seawater pCO_2 due to mixing (horizontal and vertical) with the water masses make the changes in the DIC concentrations, and thereby, we can calculate the pCO_2 changes due to mixing from the DIC changes by using the Revelle factor. Thus, this equation takes into account the changes in the seawater pCO_2 due to mixing (horizontal and vertical) with the water masses.

where β is approximately $0.0423°C^{-1}$, α is 1.0, γ_{DIC} is 9.5, and γ_{TA} is −8.9 (Sarmiento and Gruber, 2006). Assuming that upwelling was not active in the anticyclonic eddy, that eddy would be served as a reference point for the comparison of δfCO_2 values between the cyclonic eddy and non-eddy regions. Thus, the observed δfCO_2 values in the cyclonic eddy were fCO_2 differences between the cyclonic eddy and the anticyclonic eddy (Table 1). The observed δfCO_2 values in the non-eddy region were fCO_2 differences between the non-eddy region and anticyclonic eddy (Table 2). The observed δfCO_2 values closely aligned with the δfCO_2 values calculated from δSST, δSSS, δDIC, and δTA in both the cyclonic eddy and non-eddy regions (Tables 1, 2). The differences between the observed δfCO_2 and calculated δfCO_2 values were < 10% (Tables 1, 2).

Mean surface fCO_2 values were 12.2 μatm higher in the cyclonic eddy than in the anticyclonic eddy (Table 1). δfCO_2 increased by 65.6 μatm because of DIC enrichment driven by upwelling in the cyclonic eddy, while it decreased by 37.2 μatm because of the TA increase (Table 1). Thus, the δfCO_2 value increased by 28.4 μatm because of the combined effects of DIC and TA enrichment with upwelling in the cyclonic eddy. SST contributed a δfCO_2 decrease of 19.9 μatm, while SSS contributed a δfCO_2 increase of 4.4 μatm (Table 1).

Mean surface fCO_2 values were 4.8 μatm higher in the non-eddy region than in the anticyclonic eddy (Table 2). δfCO_2 increased by 22.7 μatm because of the DIC increase, while it decreased by 12.4 μatm because of the TA increase (Table 2). Thus, the δfCO_2 value increased by 10.3 μatm overall because of DIC and TA increases in the non-eddy region. SST contributed a δfCO_2 decrease of 6.7 μatm, while SSS contributed a δfCO_2 increase of 1.3 μatm (Table 2).

The maximum δfCO_2 value observed in the cyclonic eddy was 16.8 μatm (Table 1). The DIC and TA enrichment by upwelling contributed the δfCO_2 increase of 41.7 μatm, while SST and SSS contributed the δfCO_2 decrease of 24.4 μatm

TABLE 1 Observed δfCO_2, δSST, δSSS, δDIC, and δTA in the cyclonic eddy, maximum and minimum fCO_2 sites. Calculated δfCO_2 values from δSST, δSSS, δDIC, and δTA are shown in brackets.

	δfCO_2	δSST	δSSS	δDIC	δTA
Mean values in the cyclonic eddy	12.2 (12.8)	-1.19 (-19.9)	0.41 (4.4)	33.8 (65.6)	24.0 (-37.2)
Values at the maximum fCO_2 site	16.8 (17.3)	-1.84 (-30.7)	0.59 (6.3)	48.6 (94.3)	33.9 (-52.6)
Values at the minimum fCO_2 site	9.3 (9.7)	-0.64 (-10.7)	0.29 (3.1)	23.7 (46.0)	18.5 (-28.7)

Observed δfCO_2 values in the cyclonic eddy are fCO_2 differences between the cyclonic eddy and the anticyclonic eddy.

TABLE 2 Observed δfCO_2, δSST, δSSS, δDIC, and δTA in the non-eddy region, maximum and minimum fCO_2 sites. Calculated δfCO_2 from δSST, δSSS, δDIC, and δTA are shown in brackets.

	δfCO_2	δSST	δSSS	δDIC	δTA
Mean values in the non-eddy region	4.8 (4.9)	-0.40 (-6.7)	0.12 (1.3)	11.7 (22.7)	8.0 (-12.4)
Values at the maximum fCO_2 site	25.8 (26.9)	-0.25 (-4.2)	0.36 (3.9)	28.5 (55.3)	18.1 (-28.1)
Values at the minimum fCO_2 site	-17.1 (-19.3)	-0.47 (-7.9)	0.08 (0.9)	7.0 (13.6)	16.7 (-25.9)

Observed δfCO_2 values in the non-eddy region are fCO_2 differences between the non-eddy region and anticyclonic eddy.

(Table 1). In contrast, the maximum δfCO_2 value observed in the non-eddy region was 25.8 µatm (Table 2). The DIC and TA enrichment contributed the δfCO_2 increase of 27.2 µatm, while SST and SSS contributed the δfCO_2 decrease of 0.3 µatm (Table 2). In the cyclonic eddy, the contribution of DIC enrichment by upwelling was largely balanced by cooling. In the non-eddy region, however, the contribution of DIC enrichment by upwelling was rarely balanced by cooling; this was the main reason for maximum fCO_2 observation in the non-eddy region. DIC enrichment in the non-eddy region was presumably associated with the upwelling because it was observed in the area surrounding the cyclonic eddy.

Variations of sea-air CO_2 fluxes

ΔfCO_2 (surface fCO_2 – atmospheric fCO_2) varied from 5.2 to 25.7 µatm; it had consistently positive values. ΔfCO_2 exhibited high spatial variability, such that values were high within the anticyclonic eddy and low within the cyclonic eddy (Figure 7A). Wind speed obtained from the R/V ISABU automatic weather station had a range of 0.6–15.8 m s^{-1} and exhibited high spatial variability, such that values were elevated in the non-eddy region (Figure 7B). Sea-air CO_2 fluxes were calculated from ΔfCO_2 and wind speed. In the study area, sea-air CO_2 fluxes ranged from 0.011 to 9.92 mmol m^{-2} day^{-1} and all values were positive, indicating that the entire study area acted as a CO_2 source during the research period (Figure 7C). The estimated mean sea-air CO_2 fluxes in the cyclonic eddy, anticyclonic eddy, and non-eddy region were 1.10 ± 0.75, 0.64 ± 0.66, and 1.42 ± 1.12 mmol m^{-2} day^{-1}, respectively. The sea-air CO_2 fluxes considerably varied according to eddy type; they were almost twofold higher in the cyclonic eddy than in the anticyclonic eddy. In the cyclonic eddy and non-eddy regions, upwelling caused surface fCO_2 to increase, thereby increasing sea-air CO_2 flux. However, the CO_2 flux was slightly greater in the non-eddy region than in the cyclonic eddy. The mean ΔfCO_2 was higher in the cyclonic eddy than in the non-eddy region, but CO_2 flux was higher in the non-eddy region because of the high wind speed (Figure 7). In addition, maximum ΔfCO_2 was observed in the non-eddy region because the DIC enrichment caused by upwelling was rarely offset by cooling in this region.

The study area was located in the northern Philippine Sea, where surface fCO_2 was nearly equilibrated with atmospheric CO_2, and the sea-air CO_2 flux was therefore rather small (< 0.6 mmol m^{-2} day^{-1}; Takahashi et al., 2002; Takahashi et al., 2009; Ishii et al., 2014; Yasunaka et al., 2019). In this study, CO_2 flux in the anticyclonic eddy was similar to previously reported results. However, CO_2 fluxes in the cyclonic eddy and non-eddy region were approximately twofold greater than in previous studies. The cyclonic eddy caused the CO_2 flux to increase because of the upwelling of high-fCO_2 deep water. In the non-eddy region, high CO_2 fluxes were observed in the area surrounding the cyclonic eddy, indicating that the non-eddy region was affected by the upwelling of high-fCO_2 deep water. In the study area, a cyclonic eddy with a width of 120–160 km propagated westward at a rate of 8 km day^{-1}. After the cyclonic eddy had passed, the waters surrounding the cyclonic eddy had high DIC concentrations, which caused surface fCO_2 to increase during the warming of cold upwelled water. Indeed, the waters surrounding the cyclonic eddy showed higher CO_2 fluxes compared with the area around the anticyclonic eddy (Figure 7C).

Conclusions

This study examined how mesoscale eddies affect surface fCO_2 and sea-air CO_2 flux in the northern Philippine Sea. Surface fCO_2 showed high spatial variability, such that values were high in the non-eddy region and cyclonic eddy, while they were low within the anticyclonic eddy. Temperature was a major factor controlling surface fCO_2 in the anticyclonic eddy, but such an effect was not observed in the cyclonic eddy. Surface fCO_2 was influenced by the upwelling of high-fCO_2 deep water in the non-eddy region and cyclonic eddy. In the northern Philippine Sea, surface fCO_2 was strongly positively correlated with SST within cyclonic and anticyclonic eddies, while it showed no correlation in the non-eddy region. In the subtropical northeastern Pacific, in contrast, surface fCO_2 showed a positive linear relationship with SST outside of a cyclonic eddy and a negative relationship with SST within the cyclonic eddy (Chen et al., 2007). This discrepancy was presumably related to different vertical gradients of temperature and DIC below the mixed layer in these two areas; such gradients drive the vertical transport of temperature and DIC. Therefore, the effects of mesoscale eddies on surface fCO_2 were highly variable in the open ocean. To overcome this problem, more intensive surveys must be conducted across broad areas of the open ocean.

In the northern Philippine Sea, a cyclonic eddy caused surface fCO_2 to increase because of the upwelling of high-fCO_2 deep water, thereby increasing local sea-air CO_2 flux, which was nearly twofold greater than the flux within an

anticyclonic eddy. However, surface fCO_2 and sea-air CO_2 flux were not strongly affected by the anticyclonic eddy. Numerous researchers have attempted to estimate surface fCO_2 and sea-air CO_2 flux in the open ocean using the general surface fCO_2 and SST relationship (Olsen et al., 2004; Park and Wanninkhof, 2012). However, in open-ocean areas where multiple eddies are present, sea-air CO_2 flux estimated in this manner might be considerably underestimated within cyclonic eddies and the surrounding areas because cyclonic eddies increase CO_2 flux due to the upwelling of high-fCO_2 deep water. Therefore, estimation of sea-air CO_2 flux using the general surface fCO_2 and SST relationship should be avoided in the open ocean where cyclonic eddies occur.

Data availability statement

The datasets presented in this study can be found in online repositories. The names of the repository/repositories and accession number(s) can be found below: https://doi.org/10.22711/idr/941.

Author contributions

DK, S-EL, and SC were responsible for data analysis and writing the manuscript. G-HP contributed with discussions and data analysis. D-JK and SSK performed a field survey and analyzed the data set. All authors contributed to the article and approved the submitted version.

Funding

This work was supported by the project PEA0012 of the Korea Institute of Ocean Science and Technology, and in part by the project entitled 'Study on Northwestern Pacific Warming and Genesis and Rapid Intensification of Typhoon', funded by the Ministry of Oceans and Fisheries (20220566)

Conflict of interest

The authors declare that the research was conducted in the absence of any commercial or financial relationships that could be construed as a potential conflict of interest.

Publisher's note

All claims expressed in this article are solely those of the authors and do not necessarily represent those of their affiliated organizations, or those of the publisher, the editors and the reviewers. Any product that may be evaluated in this article, or claim that may be made by its manufacturer, is not guaranteed or endorsed by the publisher.

References

Andres, M., Park, J. H., Winibush, M., Zhu, X. H., Chang, K. I., and Ichikawa, H. (2008). Study of the Kuroshio/Ryukyu current system based on satellite-altimeter and *in situ* measurements. *J. Oceanogr* 64 (6), 937–950. doi: 10.1007/s10872-008-0077-2

Bates, N. R., Takahashi, T., Chipman, D. W., and Knap, A. H. (1998). Variability of pCO_2 on diel to seasonal timescales in the Sargasso Sea near Bermuda. *J. Geophys Res-Ocean* 103 (C8), 15567–15585. doi: 10.1029/98jc00247

Chang, Y. L., and Oey, L. Y. (2014). Instability of the north pacific subtropical countercurrent. *J. Phys. Oceanogr* 44 (3), 818–833. doi: 10.1175/jpo-d-13-0162.1

Chelton, D. B., Schlax, M. G., and Samelson, R. M. (2011). Global observations of nonlinear mesoscale eddies. *Prog. Oceanogr* 91 (2), 167–216. doi: 10.1016/j.pocean.2011.01.002

Chen, F. Z., Cai, W. J., Benitez-Nelson, C., and Wang, Y. C. (2007). Sea Surface pCO_2-SST relationships across a cold-core cyclonic eddy: Implications for understanding regional variability and air-sea gas exchange. *Geophys Res. Lett.* 34 (10). doi: 10.1029/2006gl028058

Gonzalez-Davila, M., Santana-Casiano, J. M., de Armas, D., Escanez, J., and Suarez-Tangil, M. (2006). The influence of island generated eddies on the carbon dioxide system, south of the canary islands. *Mar. Chem.* 99 (1-4), 177–190. doi: 10.1016/j.marchem.2005.11.004

Inoue, H. Y., Matsueda, H., Ishii, M., Fushimi, K., Hirota, M., Asanuma, I., et al. (1995). Long-term trend of the partial pressure of carbon dioxide (pCO_2) in surface waters of the western north pacific 1984-1993. *Tell Ser. B-Chem Phys. Meteorol* 47 (4), 391–413. doi: 10.1034/j.1600-0889.47.issue4.2.x

Ishii, M., Feely, R. A., Rodgers, K. B., Park, G. H., Wanninkhof, R., Sasano, D., et al. (2014). Air-sea CO_2 flux in the pacific ocean for the period 1990-2009. *Biogeosciences* 11 (3), 709–734. doi: 10.5194/bg-11-709-2014

Ishii, M., Inoue, H. Y., Matsueda, H., Saito, S., Fushimi, K., Nemoto, K., et al. (2001). Seasonal variation in total inorganic carbon and its controlling processes in surface waters of the western north pacific subtropical gyre. *Mar. Chem.* 75 (1-2), 17–32. doi: 10.1016/s0304-4203(01)00023-8

Mahadevan, A., Levy, M., and Memery, L. (2004). Mesoscale variability of sea surface pCO_2: What does it respond to? *Global Biogeochem Cycle* 18 (1). doi: 10.1029/2003gb002102

Miyazawa, Y., Kagimoto, T., Guo, X. Y., and Sakuma, H. (2008). The kuroshio large meander formation in 2004 analyzed by an eddy-resolving ocean forecast system. *J. Geophys Res-Ocean* 113 (C10). doi: 10.1029/2007jc004226

Moreau, S., Della Penna, A., Llort, J., Patel, R., Langlais, C., Boyd, P. W., et al. (2017). Eddy-induced carbon transport across the Antarctic circumpolar current. *Global Biogeochem Cycle* 31 (9), 1368–1386. doi: 10.1002/2017gb005669

Nelson, N. B., Bates, N. R., Siegel, D. A., and Michaels, A. F. (2001). Spatial variability of the CO_2 sink in the Sargasso Sea. *Deep-Sea Res. Part Ii-Top Stud. Oceanogr* 48 (8-9), 1801–1821. doi: 10.1016/s0967-0645(00)00162-4

Olsen, A., Trinanes, J. A., and Wanninkhof, R. (2004). Sea-Air flux of CO_2 in the Caribbean Sea estimated using *in situ* and remote sensing data. *Remote Sens. Environ.* 89 (3), 309–325. doi: 10.1016/j.rse.2003.10.011

Orselli, I. B. M., Kerr, R., de Azevedo, J. L. L., Galdino, F., Araujo, M., and Garcia, C. A. E. (2019). The sea-air CO_2 net fluxes in the south Atlantic ocean and the role played by agulhas eddies. *Prog. Oceanogr* 170, 40–52. doi: 10.1016/j.pocean.2018.10.006

Parard, G., Charantonis, A. A., and Rutgersson, A. (2016). Using satellite data to estimate partial pressure of CO_2 in the Baltic Sea. *J. Geophys Res-Biogeosci* 121 (3), 1002–1015. doi: 10.1002/2015jg003064

Park, G. H., and Wanninkhof, R. (2012). A large increase of the CO_2 sink in the western tropical north Atlantic from 2002 to 2009. *J. Geophys Res-Ocean* 117. doi: 10.1029/2011jc007803

Pierrot, D., Neill, C., Sullivan, K., Castle, R., Wanninkhof, R., Luger, H., et al. (2009). Recommendations for autonomous underway pCO_2 measuring systems and data-reduction routines. *Deep-Sea Res. Part Ii-Top Stud. Oceanogr* 56 (8-10), 512–522. doi: 10.1016/j.dsr2.2008.12.005

Ramp, S. R., Colosi, J. A., Worcester, P. F., Bahr, F. L., Heaney, K. D., Mercer, J. A., et al. (2017). Eddy properties in the subtropical countercurrent, Western Philippine Sea. *Deep-Sea Res. Part I-Oceanogr Res. Pap* 125, 11–25. doi: 10.1016/j.dsr.2017.03.010

Sarmiento, J. L., and Gruber, N. (2006). *Ocean biogeochemical dynamics* (New Jersey: Princeton University Press).

Sheu, W. J., Wu, C. R., and Oey, L. Y. (2010). Blocking and Westward passage of eddies in the Luzon strait. *Deep-Sea Res. Part Ii-Top Stud. Oceanogr* 57 (19-20), 1783–1791. doi: 10.1016/j.dsr2.2010.04.004

Song, H., Marshall, J., Munro, D. R., Dutkiewicz, S., Sweeney, C., McGillicuddy, D. J., et al. (2016). Mesoscale modulation of air-sea CO_2 flux in drake passage. *J. Geophys Res-Ocean* 121 (9), 6635–6649. doi: 10.1002/2016jc011714

Stephens, M. P., Samuels, G., Olson, D. B., and Fine, R. A. (1995). Sea-Air flux of CO_2 in the north pacific using shipboard and satellite data. *J. Geophys Res-Ocean* 100 (C7), 13571–13583. doi: 10.1029/95jc00901

Takahashi, T., Olafsson, J., Goddard, J. G., Chipman, D. W., and Sutherland, S. C. (1993). Seasonal variation of CO_2 and nutrients in the high-latitude surface oceans: A comparative study. *Global Biogeochem Cycle* 7 (4), 843–878. doi: 10.1029/93gb02263

Takahashi, T., Sutherland, S. C., Sweeney, C., Poisson, A., Metzl, N., Tilbrook, B., et al. (2002). Global sea-air CO2 flux based on climatological surface ocean pCO_2, and seasonal biological and temperature effects. *Deep-Sea Res. Part Ii-Top Stud. Oceanogr* 49 (9-10), 1601–1622. doi: 10.1016/s0967-0645(02)00003-6

Takahashi, T., Sutherland, S. C., Wanninkhof, R., Sweeney, C., Feely, R. A., Chipman, D. W., et al. (2009). Climatological mean and decadal change in surface ocean pCO_2, and net sea-air CO2 flux over the global oceans. *Deep-Sea Res. Part Ii-Top Stud. Oceanogr* 56 (8-10), 554–577. doi: 10.1016/j.dsr2.2008.12.009

Wanninkhof, R. (2014). Relationship between wind speed and gas exchange over the ocean revisited. *Limnol Oceanogr: Methods* 12, 351–362. doi: 10.4319/lom.2014.12.351

Weiss, R. F. (1974). Carbon dioxide in water and seawater: the solubility of a non-ideal gas. *Mar. Chem.* 2 (3), 203–215. doi: 10.1016/0304-4203(74)90015-2

Yaremchuk, M., and Qu, T. D. (2004). Seasonal variability of the large-scale currents near the coast of the Philippines. *J. Phys. Oceanogr* 34 (4), 844–855. doi: 10.1175/1520-0485(2004)034<0844:Svotlc>2.0.Co;2

Yasunaka, S., Kouketsu, S., Strutton, P. G., Sutton, A. J., Murata, A., Nakaoka, S., et al. (2019). Spatio-temporal variability of surface water pCO_2 and nutrients in the tropical pacific from 1981 to 2015. *Deep-Sea Res. Part Ii-Top Stud. Oceanogr* 169. doi: 10.1016/j.dsr2.2019.104680

Zhang, D. X., Lee, T. N., Johns, W. E., Liu, C. T., and Zantopp, R. (2001). The kuroshio east of Taiwan: Modes of variability and relationship to interior ocean mesoscale eddies. *J. Phys. Oceanogr* 31 (4), 1054–1074. doi: 10.1175/1520-0485(2001)031<1054:Tkeotm>2.0.Co;2

frontiers | Frontiers in Marine Science

TYPE Original Research
PUBLISHED 22 August 2022
DOI 10.3389/fmars.2022.986415

OPEN ACCESS

EDITED BY
Jeng-Wei Tsai,
China Medical University, Taiwan

REVIEWED BY
Kenta Watanabe,
Port and Airport Research Institute (PARI), Japan
Amrit Kumar Mishra,
The University of Hong Kong, Hong Kong SAR, China

*CORRESPONDENCE
Xiaoping Huang
xphuang@scsio.ac.cn
Songlin Liu
liusonglin@scsio.ac.cn

SPECIALTY SECTION
This article was submitted to Marine Biogeochemistry, a section of the journal Frontiers in Marine Science

RECEIVED 05 July 2022
ACCEPTED 02 August 2022
PUBLISHED 22 August 2022

CITATION
Luo H, Liu S, Ren Y, Jiang Z, Wu Y, Zhang X, Li J and Huang X (2022) Eutrophication decreases *Halophila beccarii* plant organic carbon contribution to sequestration potential. *Front. Mar. Sci.* 9:986415. doi: 10.3389/fmars.2022.986415

Eutrophication decreases *Halophila beccarii* plant organic carbon contribution to sequestration potential

Hongxue Luo[1,2,3,4,5,6], Songlin Liu[1,2,3,5,6*], Yuzheng Ren[1,2,3,4,5,6], Zhijian Jiang[1,2,3,4,5,6], Yunchao Wu[1,2,3,5,6], Xia Zhang[1,2,3,5,6], Jinlong Li[1,2,3,4,5,6] and Xiaoping Huang[1,2,3,4,5,6*]

[1]Key Laboratory of Tropical Marine Bio-Resources and Ecology, South China Sea Institute of Oceanology, Chinese Academy of Sciences, Guangzhou, China, [2]Sanya Institute of Ocean Eco-Environmental Engineering, Sanya, China, [3]Southern Marine Science and Engineering Guangdong Laboratory (Guangzhou), Guangzhou, China, [4]University of Chinese Academy of Sciences, Beijing, China, [5]Innovation Academy of South China Sea Ecology and Environmental Engineering, Chinese Academy of Sciences, Guangzhou, China, [6]Guangdong Provincial Key Laboratory of Applied Marine Biology, South China Sea Institute of Oceanology, Chinese Academy of Sciences, Guangzhou, China

Seagrass ecosystems rank among the most effective blue carbon sinks in climate change mitigation and greenhouse gas removal. Nutrient pollution has emerged as a leading threat to seagrass decline and has diminished the carbon sequestration potential in recent decades. Changes in the nutrient regime can also impact the organic carbon compositions (labile and refractory organic carbon compositions) of seagrass tissues, with important implications for determining the quantity and quality of carbon sequestration. However, there is still little information about the impact of nutrient loading on seagrass plant refractory organic carbon composition (ROC), which hinders our ability to reveal the driving mechanisms of anthropogenic factors that decrease seagrass organic carbon sequestration capability. Here, a multidisciplinary approach was employed to investigate the organic carbon variations of *Halophila beccarii* at five seagrass meadows with contrasting nutrient loading levels. The results showed that *H. beccarii* plant nitrogen (N) content ranged from 2.21% to 5.65%, which well reflected the external nutrient loading levels. High nutrient loading elevated labile organic carbon content, like free amino acids and soluble sugars. Nevertheless, ROC content (cellulose-associated organic matter) decreased with increasing nutrient loading, which presented a significant negative linear correlation with plant N content. These results provide evidence that eutrophic conditions enhance *H. beccarii* plant quality (high N and labile organic carbon) and consequently decrease plant ROC sequestration potential. This suggests that reducing nitrogen input to seagrass meadows would aid in increasing seagrass carbon storage.

KEYWORDS

***Halophila beccarii*, nutrient loading, organic carbon, labile, recalcitrant**

Introduction

Seagrass ecosystems are one of the coastal blue carbon ecosystems and have great potential to mitigate global climate change (Macreadie et al., 2019). Although only occupying<0.2% of the global ocean surface, seagrass ecosystems contribute ~10% of marine organic carbon sequestration (Duarte et al., 2013). Seagrass contributes to more than half of all organic carbon storage (Kennedy et al., 2010), and in some seagrass meadows, it even accounts for 90% (Reef et al., 2017), which is mostly due to the abundance of refractory chemical compositions of organic matter (>50%) in seagrass plants (Trevathan-Tackett et al., 2017). Refractory carbon like lignocellulose is selectively preserved in sediments to avoid decomposition (Klap et al., 2000), while polysaccharides are continuously reduced during the diagenetic process through complex biochemical reactions (Kaal et al., 2019). Therefore, seagrass plant organic carbon compositions, particularly their refractory compositions, are the foundation of the high accumulation and preservation potential of organic carbon in seagrass ecosystems (Kaal et al., 2019).

Organic carbon in seagrass plants can be generally divided into labile organic carbon (LOC) compositions and refractory organic carbon (ROC) compositions (Kaal et al., 2016). Amino acids, non-structural carbohydrate compounds (NSC, such as, soluble sugar, and starch), and hemicellulose are the main components of seagrass LOC, while ROC is always represented as cellulose and lignin (Zieman et al., 1984; Peduzzi and Herndl, 1991; Vichkovitten and Holmer, 2004; Trevathan-Tackett et al., 2017; Cragg et al., 2020). Many common chemical methods are used for measuring the contents of plant organic carbon compounds. For example, the phenol–sulfuric acid colorimetric method was used to determine soluble sugar and starch contents (Dubois, 1956), and the vanillin/HCl method, near-infrared reflectance spectroscopy, and filter-bag technique were applied for measuring the contents of tannin, fiber, and lignin, respectively (Lawler et al., 2006; Torbatinejad et al., 2007; Siegalwillott et al., 2010). Thermogravimetric analysis (TGA) is a quantitative technique that uses the increase or decrease in the mass of substances with temperature to characterize physical and chemical changes and has been widely used for plant chemical composition analysis recently (Dimitrakopoulos, 2001). TGA provides a lower material mass (10 mg) and the ability to provide accurate and rapid component characterization (Dimitrakopoulos, 2001). The organic carbon composition of marine macroalgae and vascular plants was assessed by TGA. For example, previous reports have suggested that the lignocellulose content of seagrass rhizomes is 50%–60% of dry weight (Trevathan-Tackett et al., 2017), and marine macroalgae do contain refractory compounds including xylans and sulfated polysaccharides (Trevathan-Tackett et al., 2016).

Coastal nutrient loading is a leading threat to seagrass meadow decline (Jiang et al., 2020), which is mainly due to algal overgrowth and reduction of light availability, as well as ammonium toxicity (Burkholder et al., 2007). Meanwhile, nutrient loading can affect the carbon metabolism in seagrass plants (Touchette and Burkholder, 2000), and consequently change the organic carbon composition of seagrass plants (Pazzaglia et al., 2020; Helber et al., 2021a). Nutrient addition can always increase the content of amino acids in seagrass tissues (Udy and Dennison, 1997; Invers et al., 2004), while the response of sucrose content in seagrass to nutritional loading shows variation. For example, nitrogen and phosphorus enrichment were found to increase sucrose contents in *Enhalus acoroides* leaf (Artika et al., 2020), but sucrose contents of *Halophila stipulacea* and *Posidonia oceanica* leaf were observed unchanged and decreased after nitrogen and phosphorus additions, respectively (Pazzaglia et al., 2020; Helber et al., 2021b). Previous studies reported that nutrient loading could change the LOC content of seagrass plants (Brun et al., 2002; Touchette and Burkholder, 2007; Jiménez-Ramos et al., 2017; Artika et al., 2020; Hernán et al., 2021). However, there is still little information on seagrass ROC changes in response to nutrient loading.

Halophila beccarii is a small monoecious seagrass mainly distributed throughout the tropical Indo-Pacific region (Udagedara and Dahanayaka, 2020). The blue carbon stock of *H. beccarii* meadows ranged from 2.655 Mg C/ha to 12 Mg C/ha (Jiang et al., 2017; Kaladharan et al., 2021). The organic carbon concentration in the sediment within the *H. beccarii* seagrass meadow is 110%–134% greater than nearby bare sediment (Kaladharan et al., 2021), possibly due to abundant *H. beccarii* plant organic carbon inputs into *in situ* sediment (Premarathne et al., 2021). *H. beccarii* is widely distributed in tropical and subtropical regions of China, which are at a risk of further nutrient loading pressure due to intense human activities (urban runoffs, fishing, dredging) (Jiang et al., 2017; Jiang et al., 2020). This trend could accelerate the loss of seagrass ecosystems and a reduction in carbon contribution. In this study, we investigated *H. beccarii* LOC and ROC compositions in five different nutrient-loaded seagrass meadows in the Guangdong and Hainan provinces, Southern China. We hypothesized that nutrient loading would increase the LOC content but decrease the ROC of *H. beccarii*. The goal of this study was to further determine the relationship between eutrophication and carbon storage capacity of *H. beccarii* and, with this result, help resource managers maximize the organic carbon sequestration potential in seagrass ecosystems.

Materials and methods

Sample collection

During October 2021, we collected the *H. beccarii* plants from five seagrass meadows: Yifengxi (YFX, 23.54N, 116.92E), Hailing Island (HL, 21.68N, 111.91E), Liusha Bay (LS, 20.39N, 109.98E), Tangjia Bay (TJ, 22.33N, 113.59E), and Qiaotou (QT, 19.948N, 110.093 E) (Figure 1). Three 25 cm × 25 cm quadrats (distance between quadrats is >5 m) were randomly thrown into each seagrass meadow, and *H. beccarii* plants were dug out

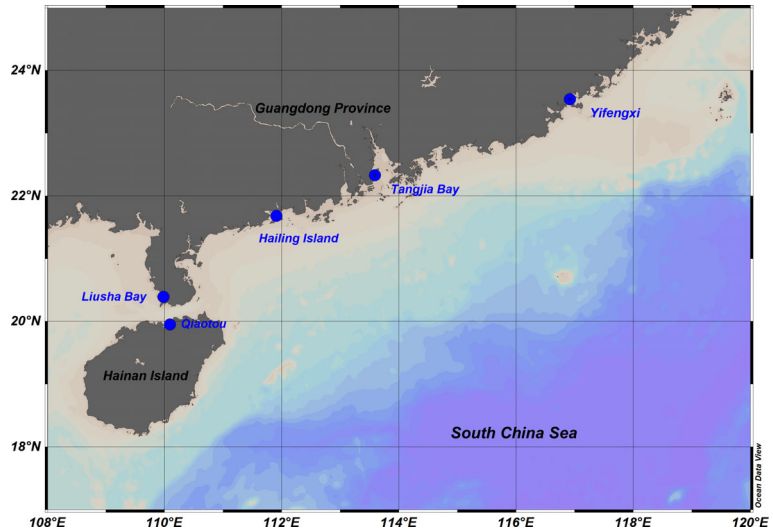

FIGURE 1
Sampling sites along the coast of Guangdong province and Hainan Island.

together with underground roots in the quadrats to ensure the integrity of the plants. After being rinsed with seawater, they were put into polyethylene sealing bags. Meanwhile, seawater around each quadrat was collected and quickly filtered onto the GF/F filter. The seagrass plants and filtered seawater samples were stored at −20 °C until they were back in the laboratory.

Measurements

The SEAL AutoAnalyzer 3 High Resolution (Seal Analytical, BRAN+LUEBBE, Germany) was used to analyze dissolved inorganic nitrogen (DIN = nitrate + nitrite + ammonium) and dissolved inorganic phosphate (DIP) in filtered seawater. The Seal AA3 HR is a completely automated analysis system for colorimetric analysis of dissolved nutrients in environmental samples (Zhang et al., 2019).

The whole body of seagrass plants was first dried at 60 °C in an oven to constant weight, and then the dry sample was fully ground to a homogenized state by a grinding instrument (mortar grinder ST-B220, SKTEM, China). Powdered samples were analyzed in duplicate for carbon and nitrogen content using a CHN analyzer (Vario EL, Elemental Analyser System GmbH, Germany). Elemental content was calculated on a dry weight basis (mass of element/dry weight of sample ∗ 100%), while elemental ratios were calculated on a mole: mole basis. All isotopic analyses were measured using a standard isotope ratio mass spectrometer (Thermo Scientific MAT 253) procedures. All isotopic data were expressed in the conventional delta notation (‰): $\delta^{13}C_{sample}$ or $\delta^{15}N_{sample} = (R_{sample}/R_{reference} - 1) \times 1{,}000$ where R = $^{13}C/^{12}C$ or $^{15}N/^{14}N$. Soluble sugars (sucrose, glucose, and fructose) from ground samples were measured by the anthrone colorimetric method (Jan and Roel, 1993). Free amino acid was measured using the Ninhydrin colorimetric method with an absorbance of 570 nm (Lee et al., 2003).

The remaining dry samples of the whole body of the seagrass were subsequently analyzed by thermogravimetric analysis (TGA, TG209F1, 0.1 µg balance sensitivity, Netzsch, Germany). About 10 mg of the ground sample was placed in a platinum cup and heated under N_2(*gas flow* = 100 *ml* min^{-1}) with a heating ramp rate of 10°C min^{-1}, ranging from 28 to 600°C (Liu et al., 2020). The rate-of-change derivative (% mass loss $°C^{-1}$) can be used to describe the thermal intervals (TI) and consequently indicates distinct temperatures of organic matter (OM) loss. The TI_1 (labile; soluble carbohydrates, hemicellulose) ranged from 180°C to 300°C. TI_2 (cellulose-associated recalcitrant organic matter) extended from 300°C to 400°C, then from 400°C to 600°C was determined as TI_3 (lignin-associated recalcitrant organic matter and insoluble polysaccharide residues). The range of mass loss ($TI_{1\text{-}3}$) was recalculated as a portion of total organic matter (OM) from 180°C to 600°C. The proportions of TI_1, TI_2, and TI_3 in total OM are represented as TI_1/OM, TI_2/OM, and TI_3/OM.

Data analysis

One-way analysis of variance (ANOVA) was used to determine if there were any statistically significant changes in environmental nutrients, elemental content, soluble sugars, amino acids, TI_1, TI_2, TI_3, and OM of *H. beccarii* among the

five seagrass meadows. A Tukey *post hoc* test was applied to identify the significantly different components of the above parameters. The effect, with $p<0.05$, was considered statistically significant. Before this test, the homogeneity of variance was tested with Levene's test. Data were log-transformed to achieve the homogeneity of variance where the heterogeneity of variance was found. TI_1, TI_2, TI_3, TI_1/OM, TI_2/OM, and TI_3/OM are converted into arcsine square roots before ANOVA. The relationships among seawater nutrients and seagrass nitrogen content with organic carbon compositions were examined by the Pearson's correlation coefficient, respectively. The above-mentioned statistical analyses were performed using Excel 2010, SPSS 22.0, and R 4.1.3, respectively.

Results

Environmental variables

DIN and DIP of seawater ranged from 14.89–162.94 μmol/L to 0.18–7.79 μmol/L, respectively, with significant differences among the five seagrass meadows (Table 1, DIN: F = 15.050, $p<0.001$; DIP: F = 5.541, p = 0.013).NO_2^- , NO_3^-, and NH_4^+ accounted for 1.67%–5.09%, 31.79%–75.11%, and 22.55%–63.12% of DIN, respectively. There were significant differences in all the above-mentioned environmental variables among the five seagrass meadows (Table 1). The DIN of YFX was 4-fold higher than that of LS, and the DIN contents of HL, TJ, and QT did not differ significantly (F = 0.202, p = 0.823).

Carbon, nitrogen content, stable isotope analysis ($\delta^{13}C$ and $\delta^{15}N$), amino acid and carbohydrate

Biochemical parameters of *H. beccarii* were observed to be significantly different among the sampling sites, with the exception of carbon content (Table 2). We recorded a broad range of nitrogen content values and C/N ratios of *H. beccarii*. The nitrogen content and C/N ratios for *H. beccarii* ranged from 2.21% to 5.65% and from 7.24 to 15.57, respectively (Table 2). The highest and lowest nitrogen content and C/N ratio values were both observed in YFX and QT, respectively (Table 2). However, the carbon content of plants in the five seagrass meadows tended to be similar (Table 2; F = 1.964, p = 0.176).

The $\delta^{13}C$ signature of *H. beccarii* in the five seagrass meadows ranged from −20.764‰ to −14.802‰, with HL and LS as the most depleted and richest values, respectively (Table 2). Additionally, there was a significantly higher $\delta^{15}N$ value in *H. beccarii* of YFX than in other seagrass meadows (Table 2). The soluble sugar content of YFX was triple-fold higher than that of LS (Figure 2A), while the amino acid content of *H. beccarii* at YFX was higher than that at other sites (Figure 2B).

TGA analysis

TGA showed that the decomposition resulted in an obvious loss of organic matter for *H. beccarii* in five seagrass meadows (Figure 3). All samples manifested similar Z-shaped TG curves and the rate of change indicated that most of the differences among the areas occurred during losses between 100 °C–180 °C and 200 °C–400 °C (Figure 3). Figure 4 shows the specific mass loss of organic matter for *H. beccarii*. Although the total OM content of *H. beccarii* in HL was ~10% higher than that in LS, no significant differences were observed in the OM content of *H. beccarii* among the different seagrass meadows (Figure 4D; F = 1.518, p = 0.269). Overall, TI_1 generally decreased as the nutrient level decreased (Figure 4A), while the opposite trend was observed in TI_2 (Figure 4B). Furthermore, there was no significant difference in the TI_3 content among the five seagrass meadows (Figure 4C; F = 1.064, p = 0.423). According to the proportion of different TIs in OM, the proportion of TI_1/OM and TI_2/OM differed significantly among the five seagrass meadows (TI_1/OM: F = 47.336, $p<0.001$; TI_2/OM: F = 38.749, $p<0.001$) (Figure 5). Similar to the TI_3, the TI_3/OM was homogeneous among the three seagrass meadows (F = 3.106, p = 0.066) (Figure 5).

TABLE 1 Seawater nutrients parameters in HI, LS, TJ, YFX, and QT (Mean ± SE). The different capital letters indicate significant differences among the five seagrass meadows. Identical superscripts indicate non-significantly different means.

Area	YFX	HL	LS	TJ	QT
NO_2^-	5.75 ± 1.28^{B}	2.04 ± 0.41^{A}	1.31 ± 0.25^{A}	1.02 ± 0.18^{A}	2.03 ± 0.46^{A}
NO_3^-	40.39 ± 5.71^{B}	20.60 ± 1.90^{AB}	13.04 ± 2.30^{AB}	34.07 ± 6.70^{AB}	35.18 ± 6.51^{A}
NH_4^+	75.41 ± 13.82^{C}	38.44 ± 2.17^{BC}	13.85 ± 1.71^{A}	20.09 ± 3.22^{AB}	19.43 ± 4.23^{A}
DIN (μmol/L)	121.55 ± 20.79^{C}	61.08 ± 2.04^{B}	28.20 ± 4.20^{A}	55.19 ± 9.99^{B}	56.64 ± 5.99^{B}
DIP (μmol/L)	4.88 ± 1.46^{B}	2.18 ± 0.28^{B}	1.58 ± 0.14^{B}	0.50 ± 0.24^{A}	1.85 ± 0.33^{B}

DIN, dissolved inorganic nitrogen, DIN = NO_2^- + NO_3^- + NH_4^+.

TABLE 2 Carbon, Nitrogen Content, Stable Isotope Analysis ($\delta^{13}C$ and $\delta^{15}N$) of seagrass tissue in five meadows (Mean ± SE).

Area	YFX	HL	LS	TJ	QT
C (%)	34.20 ± 0.45^{A}	36.45 ± 0.56^{A}	28.87 ± 4.09^{A}	33.49 ± 0.38^{A}	32.58 ± 1.44^{A}
N (%)	5.46 ± 0.10^{C}	3.78 ± 0.03^{B}	3.03 ± 0.46^{AB}	2.78 ± 0.09^{AB}	2.50 ± 0.10^{A}
C: N	7.31 ± 0.07^{A}	11.24 ± 0.17^{B}	11.18 ± 0.32^{B}	14.10 ± 0.47^{C}	15.23 ± 0.22^{C}
$\delta^{13}C$ (‰)	-18.28 ± 0.19^{AB}	-20.06 ± 0.35^{A}	-15.09 ± 0.07^{C}	-15.80 ± 0.65^{BC}	-17.62 ± 0.01^{AB}
$\delta^{15}N$(‰)	12.41 ± 0.06^{C}	6.80 ± 1.00^{AB}	6.21 ± 0.86^{AB}	6.99 ± 0.24^{B}	4.07 ± 0.03^{A}

Relationship between nutrient content and environmental nutrient level of *H. beccarii*

The heatmap based on Pearson's correlation analysis revealed that the amino acids, soluble sugars, TI_1, and TI_1/OM of *H. beccarii* had significantly positive correlations with N content (Figure 6A). In contrast, TI_2/OM showed a significantly negative correlation with N content (Figure 6A). TI_2 was negatively correlated with N content, but not significantly (Figure 6A). Furthermore, there was no positive or negative correlation between TI_3 or TI_3/OM and N content (Figure 6A). Additionally, amino acids, soluble sugars of *H. beccarii* had significantly positive correlations with seawater NH_4^+ while TI_2/OM had a significantly negative correlation with seawater NH_4^+ (Figure 6B).

Discussion

The seawater nutrients in our study seagrass meadows (DIN: 14.89–162.94 μmol/L, DIP: 0.18–7.79 μmol/L) were higher than those in other seagrass meadows in Florida Bay (Median DIN = 3.56 μmol/L, Median TP = 0.31 μmol/L) (Fourqurean et al., 2003), Alfaques Bay, Mediterranean (NH_4^+ <10 μmol/L, DIP: 0.1–0.5 μmol/L) (Pérez and Romero, 1994), Cau Hai lagoon, Vietnam (DIN: 77.45 μg/L) (Dang et al., 2020), and Akrotiri Bay, Cyprus, Red Sea (DIN: 0.03–0.65 μmol/L) (Alexandre et al., 2014), which suggested that the *H. beccarii* seagrass meadows distributed along the southern China coastal areas were exposed to a higher nutrient loading pressure. The DIN and DIP concentrations among five seagrass meadows indicated distinct nutrient loading pressure that *H. beccarii* suffered. TJ had the lowest concentration of DIP, which can be attributed to its open water conditions and intense hydrodynamic exchange. External inorganic nutrients (nitrogen and phosphorus) can be absorbed by seagrass leaves and roots, with absorption kinetics that depend on external inorganic nutrient concentrations (Brun et al., 2002). The nutrient content of seagrass plants has been widely used as a good indicator for seagrass health monitoring and can well reflect the external nutrient loading (Yang et al., 2018). Plants from low nutrient environments have significantly lower N-content and higher C:N ratios than those from high-nutrient environments (Lee and Dunton, 1999). In this study, the N content of *H. beccarii* plants had significantly positive relationships with, NH_4^+ and DIN, but not with NO_2^-

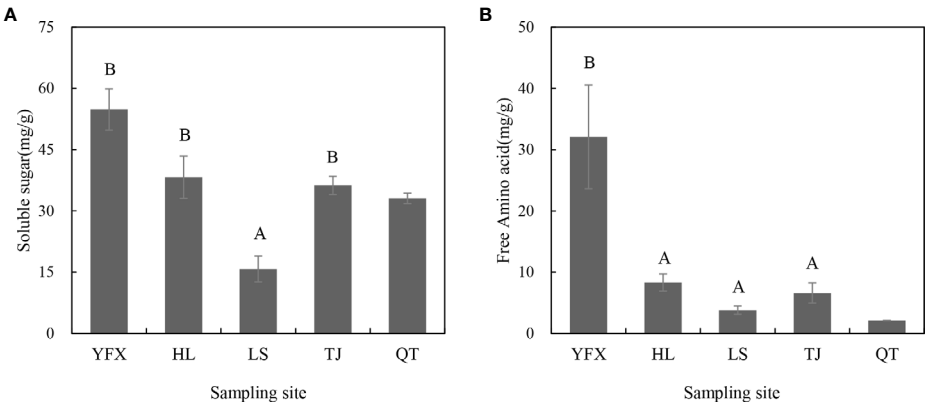

FIGURE 2
Souble sugars (A) and free amino acid (B) content of seagrass plant in five areas. Different letters above bars indicate significant differences (p<0.05) among regions. Values represent mean ± S.E. Due to the lack of sample size of QT, variables just have one or two values.

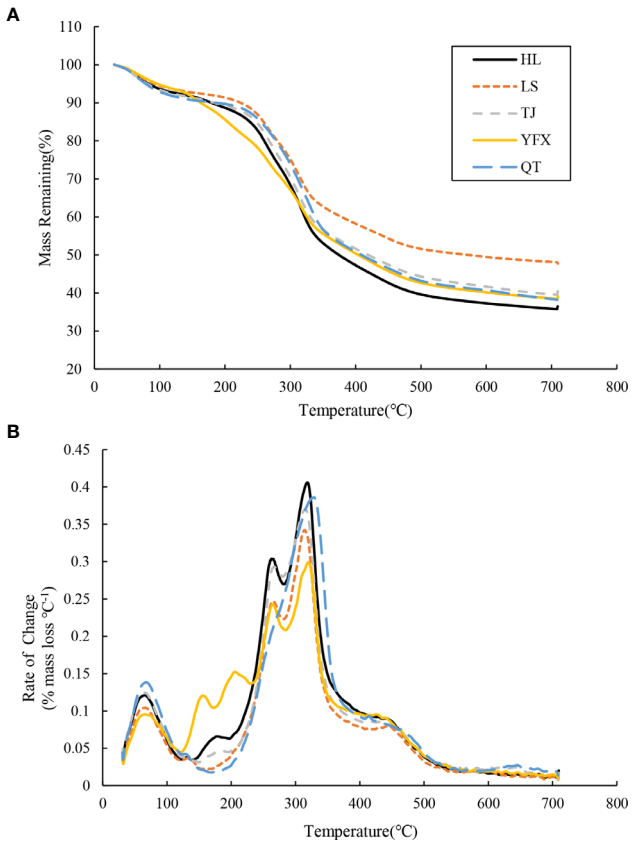

FIGURE 3
Thermograms for the seagrass among five seagrass meadows, **(A)** % mass remaining with increasing temperature and **(B)** derivate rate-of-change (% mass loss per °C) with increasing pyrolysis temperature.

(Supplementary Figure 1). Although both NO_3^- and NH_4^+ can be absorbed by *H. beccarii*, NO_2^- content is generally low in the water column and NH_4^+ uptake by seagrass is a more energy-saving process than NO_3^- (Turpin, 2010). In the study area, it can be assumed that NH_4^+ represents a substantial source of nitrogen for *H. beccarii*. However, *H. beccarii* plant nitrogen content in LS was much higher than that in TJ and QT, although LS has the lowest external nutrient load. This should be ascribed to macroalgae bloom (*Ulva lactuca*) at LS during our sampling period (Supplementary Figure 2), resulting in a decrease in nutrient levels in the water column due to macroalgae absorption. Additionally, variation in $\delta^{15}N$ can be used as an indicator of eutrophication as well (Cole et al., 2004). More enriched *H. beccarii* $\delta^{15}N$ in LS than in QT suggested that there were more human wastewater inputs (Helber et al., 2021b). Therefore, *H. beccarii* plant nitrogen content well reflected the external nutrient loading.

Carbon and nitrogen metabolism are interconnected. An alteration in one process is likely to set off cascading responses affecting other biochemical mechanisms. Variations in external nutrient loading may cause the change of carbohydrate storage reserves in seagrass through nitrogen metabolism. TI_1 represented the total content of soluble carbohydrates (soluble sugar and starch), amino acids, and hemicellulose. NH_4^+ does not accumulate in healthy seagrass leaves due to its toxicity in chloroplasts, so energy-dependent rapid assimilation into amino acids is catalyzed by the glutamine synthetase/glutamate synthase pathway (Touchette and Burkholder, 2000), which should be responsible for the higher amino acid content in *H. beccarii* at high nutrient loading seagrass meadows (Invers et al., 2004). In our study, a significant positive correlation was found between amino acid content and N content, seawater NH_4^+, NO_2^-, and DIN. Soluble sugar is the main component of non-structural carbohydrate (TNC) (Vichkovitten et al., 2007), acting as a carbon reserve for ammonium assimilation *via* the tricarboxylic acid cycle (Brun et al., 2008). Under nutrient enrichment, the internal carbohydrate concentrations decreased significantly, which was mainly due to the nitrogen assimilation process (Brun et al., 2008) and the lack of an ammonium uptake feedback mechanism (Burkholder et al., 1992). In contrast to previous studies (Campbell et al., 2012; Helber et al., 2021b), soluble sugar content was higher at the high nutrient seagrass meadow in this study. This might be due to keeping a high

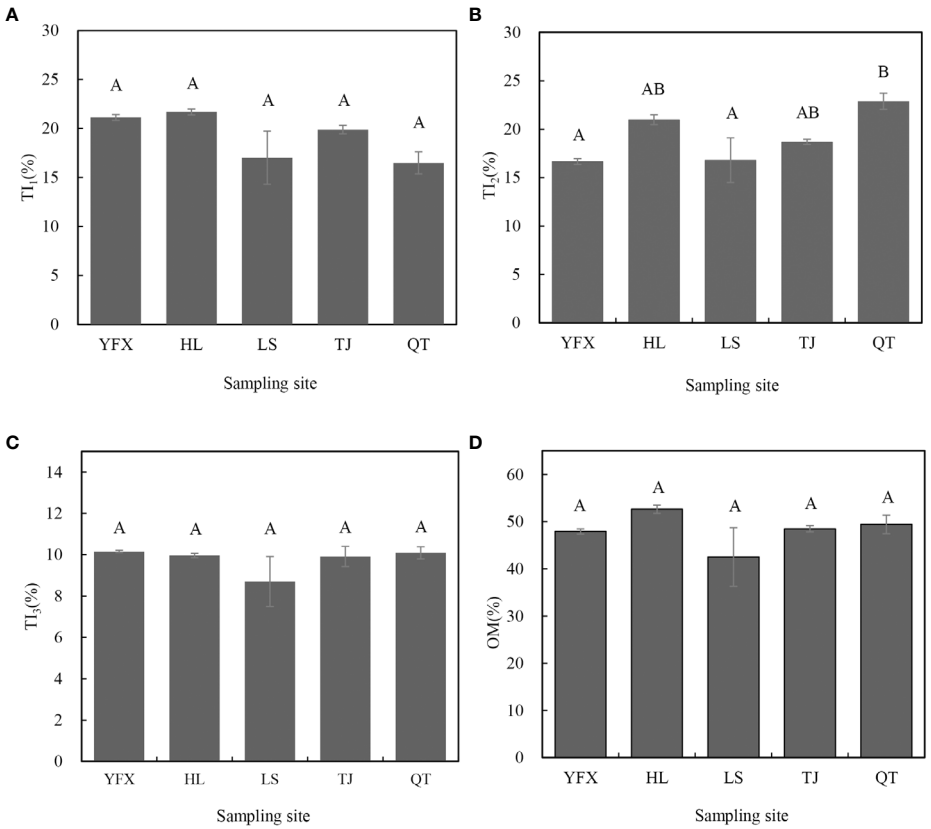

FIGURE 4
TI_1 **(A)**, TI_2 **(B)**, TI_3 **(C)**, and OM **(D)** as percent of total mass (Mean ± S.E.). TIs represent distinct organic matter components percent in total mass from TGA (TI_1: labile, amino acid, carbohydrates, hemicellulose, 180–300°C; TI_2: cellulose-associated recalcitrant organic matter, 300–400°C; and TI_3: refractory, lignin-associated recalcitrant organic matter and residues, 400–600°C).

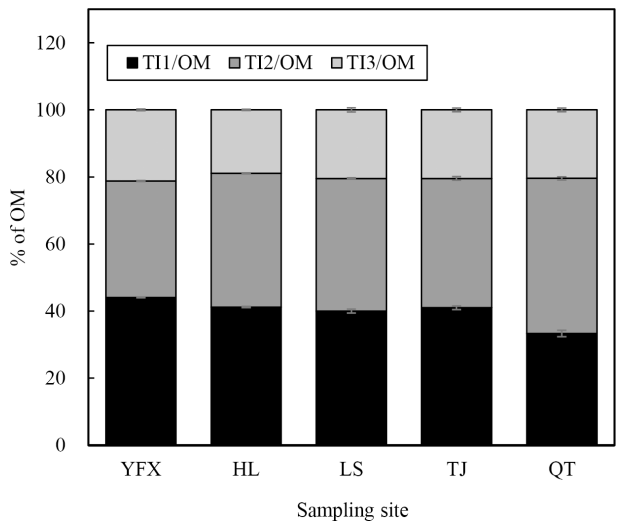

FIGURE 5
Thermal intervals (TIs) in total organic matter (OM) across all location was represented as TIs/OM. TIs represent distinct organic matter components from TGA. Values represent mean ± S.E.

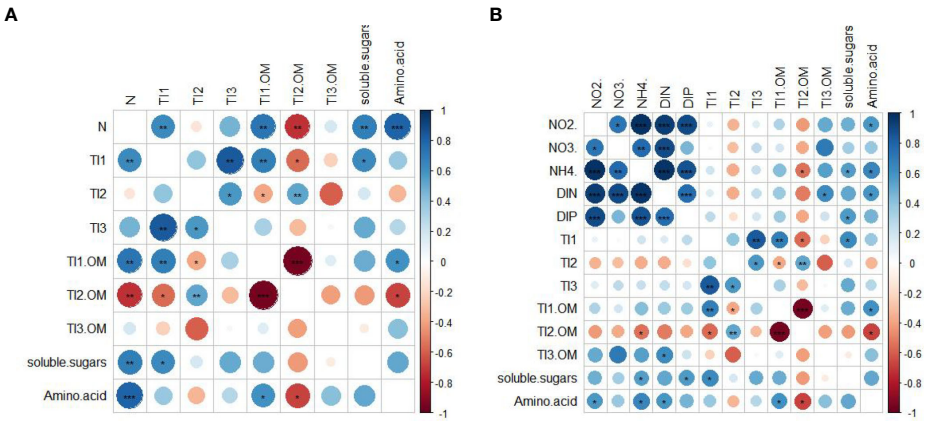

FIGURE 6
Relationship between nitrogen content and thermal organic matter of seagrass (A). Relationship between seawater nutrient concentrations and thermal organic matter of seagrass (B). Blue represents a positive correlation between variables and red represents a negative correlation (*$p<0.05$, **$p<0.01$, ***$p<0.001$).

energy metabolism to cope with high nutrient loading conditions (Brun et al., 2002). Ammonium enrichment improved photosynthetic efficiency, allowing the tissues to meet the increased carbon demands caused by ammonium assimilation into organic nitrogen compounds (Brun et al., 2002). Additionally, *H. beccarii* soluble sugar at LS was observed to have the lowest content, which might be due to light deficiency during the macroalgae bloom period. Seagrass photosynthetic rate declines and mobilizes carbohydrate reserves to maintain metabolic processes under low light conditions (Ralph et al., 2007), resulting in a significant decrease in the soluble sugar content (Burke et al., 1996; Schmidt et al., 2012). Hemicellulose is a structural carbohydrate that plays a vital role in the strength of plant cell walls (Xu et al., 2020). Hemicellulose accounts for the major part of TI_1, so the hemicellulose content should follow the same trend as TI_1. Therefore, nutrient loading increased the quantity of labile components like amino acid and soluble sugar contents in the living *H. beccarii* plant. On the other hand, appropriate nutrient loading can promote seagrass production through changes in maximum rate of photosynthesis and increased chlorophyll concentrations as well (Agawin et al., 1996; Lee and Dunton, 1999), thus allowing for greater seagrass carbon fixation (Lee and Dunton, 1999). Nevertheless, only the seagrass plant organic carbon compositions were measured in this study, and the seagrass production in response to eutrophication should be conducted in future research.

Cellulose strands form microfibrils that act as a framework for other wall components such as hemicelluloses, proteins, and lignin (Ogden et al., 2018). The overall cellulose content of vascular plants varies substantially depending on the thermogravimetric interval, ranging from 24% to 50% (Trevathan-Tackett et al., 2016), with seagrass having a cellulose content of 33%–46% (Trevathan-Tackett et al., 2017). In this study, the mass loss of TI_2 decreased as N content increased, and TI_2/OM was negatively correlated with N content and seawater NH_4^+ indicating that cellulose depletion under high nutrient loading conditions occur. In terrestrial ecosystems, high N leads to a reduction of cellulose in angiosperms, which is due to decreased expression of genes involved in cellulose production in response to elevated nitrogen levels (Zhang et al., 2017). Under high nutrient loading conditions, seagrass diverts carbon and energy produced by photosynthesis toward nitrogen uptake and assimilation, which consequently leads to less carbon and energy being allocated to the production of cellulose (Shan et al., 2018). This explains the difference in cellulose content of *H. beccarii* at different nitrogen content gradients. Furthermore, even though our study discovered no significant correlation between nitrogen and TI_3 content, it does not suggest that nutrient loading had no impact on lignin biosynthesis in *H. beccarii*. Lignin is a refractory biomacromolecule composed of three phenylropanoid units: p-hydroxyphenyl (H), guaiacyl (G), and syringyl (S) (Mottiar et al., 2016), with determining the refractory degree of lignin (Bonawitz et al., 2014). The study of terrestrial ecosystems showed that nutrient loading significantly influenced the composition of these three monomers (Pitre et al., 2007). As a matter of future research, we recommend elucidating the effects of nutrient loading on the unit compositions of lignin in seagrass tissues, with important implications for seagrass blue carbon potential. Additionally, we did not distinguish the differences in organic carbon compositions between tissues by only using the whole body of *H. beccarii*. According to previous studies, the ratios of aboveground (leaf) to belowground biomass (rhizome and root) of *H. beccarii* were similar in different sites of Southern China (ranging from 0.71 to 1) (Jiang et al., 2020). We assumed that the samples collected in different sites had similar ratios of aboveground to belowground biomass.

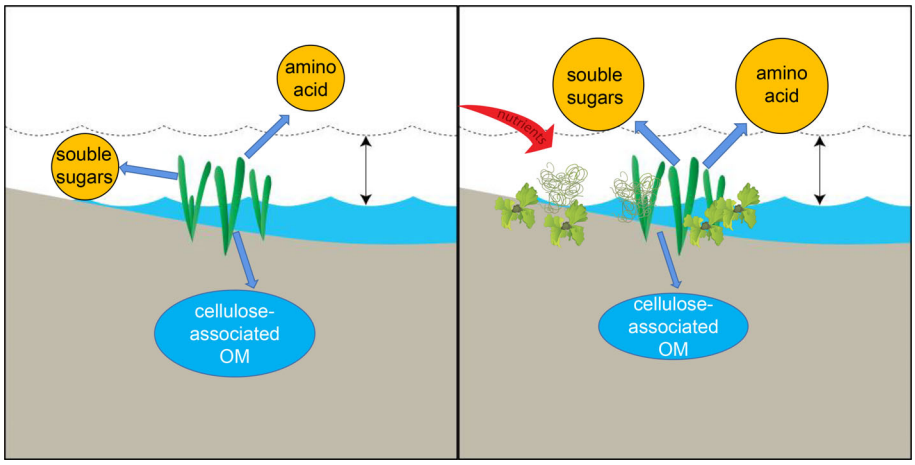

FIGURE 7
Impact of eutrophication on seagrass meadow. The dashed wave line and blue wave line represents high tide and low tide, respectively.

Our study revealed that eutrophication could increase the content of labile organic carbon but reduce the refractory components by 4.19%–6.23% (Figure 7). It is necessary to point out that the effects of nutrient load on seagrass production and biomass were complex. Moderate nutrient loads may enhance the total production of seagrass (Connell et al., 2017). Extreme nutrient loads would hamper the production and biomass of seagrass (increased shading by epiphytic algae) (Schmidt et al., 2012). However, we did not measure the parameters of *H. beccarii* production or the biomass in this study, which limited us to estimating the trade-off of the plant carbon stock. In the future research, field investigation and laboratory simulation should be conducted to study the effects of eutrophication on *H. beccarii* primary production and organic carbon compositions. It has been widely reported that eutrophication has been identified as a leading threat to seagrass worldwide (Burkholder et al., 2007). Our study demonstrated that eutrophication would decrease the seagrass plant refractory carbon contribution to carbon sequestration. Therefore, better management of fish farming, shoreline rehabilitation, and sewage discharge and restoration measurements are required to regulate anthropogenic nutrient inputs and maintain their natural carbon sinks.

Conclusion

Interactions among seagrass organic carbon compositions and eutrophication were discussed in our study. Our results supported our initial hypothesis: eutrophication improves the content of labile organic carbon such as soluble sugars and amino acids while decreasing refractory organic carbon through the carbon allocation of *H. beccarii*. However, *H. beccarii* in southern China is threatened by accelerating eutrophication, which might weaken the contribution of seagrass plants to refractory carbon stock. One important subject is to determine nutrient thresholds for a maximum of seagrass carbon stock. In addition, the carbon and nitrogen cycles of seagrass, as well as the mechanisms by which labile and refractory carbon respond to eutrophication, need to be investigated further.

Data availability statement

The original contributions presented in the study are included in the article/Supplementary Material. Further inquiries can be directed to the corresponding authors.

Author contributions

HL: Conceptualization, methodology, and writing—original draft. SL: Validation, methodology, writing—review and editing, and data curation. YR: Investigation, validation, and software. ZJ: Project administration and investigation. YW: Formal analysis and software. XZ: Resources and data curation. JL: Formal analysis. XH: Supervision, writing—review and editing, and funding acquisition. All authors contributed to the article and approved the submitted version.

Funding

This work was supported by the National Natural Science Foundation of China (U1901221, 42176155), the Key Special

Project for Introduced Talents Team of Southern Marine Science and Engineering Guangdong Laboratory (Guangzhou) (GML2019ZD0405), Hainan Province Science and Technology Special Fund (ZDYF2020180, ZDYF2021SHFZ254), the Innovation Academy of South China Sea Ecology and Environmental Engineering, Chinese Academy of Sciences (ISEE2021PY06 and ISEE2021ZD03), and the Science and Technology Planning Project of Guangdong Province, China (2020B1212060058).

Conflict of interest

The authors declare that the research was conducted in the absence of any commercial or financial relationships that could be construed as a potential conflict of interest.

Publisher's note

Supplementary material

The Supplementary Material for this article can be found online at: https://www.frontiersin.org/articles/10.3389/fmars.2022.986415/full#supplementary-material

References

Agawin, N. S. R., Duarte, C. M., and Fortes, M. D. (1996). Nutrient limitation of Philippine seagrasses (Cape bolinao, NW philippines): *In situ* experimental evidence. *Mar. Ecol. Prog. Ser.* 138 (1-3), 233–243. doi: 10.3354/meps138233

Alexandre, A., Georgiou, D., and Rui, S. (2014). Inorganic nitrogen acquisition by the tropical seagrass halophila stipulacea. *Mar. Ecology.* 35, 387–394. doi: 10.1111/maec.12128

Artika, S. R., Ambo-Rappe, R., Teichberg, M., Moreira-Saporiti, A., and Viana, I. G. (2020). Morphological and physiological responses of enhalus acoroides seedlings under varying temperature and nutrient treatment. *Front. Mar. Science.* 7. doi: 10.3389/fmars.2020.00325

Bonawitz, N. D., Kim, J. I., Tobimatsu, Y., Ciesielski, P. N., Anderson, N. A., Ximenes, E., et al. (2014). Disruption of mediator rescues the stunted growth of a lignin-deficient arabidopsis mutant. *Nature* 509, 376–380. doi: 10.1038/nature13084

Brun, F. G., Hernández, I., Vergara, J. J., Peralta, G., and Pérez-Lloréns, J. (2002). Assessing the toxicity of ammonium pulses to the survival and growth of zostera noltii. *Mar. Ecol. Progress.* 225, 177–118. doi: 10.3354/meps225177

Brun, F., Olive, I., Malta, E. J., Vergara, J., and Pérez-Lloréns, J. (2008). Increased vulnerability of zostera noltii to stress caused by low light and elevated ammonium levels under phosphate deficiency. *Mar. Ecol. Prog. Series.* 365, 67–75. doi: 10.3354/meps07512

Burke, M. K., Dennison, W. C., and Moore, K. A. (1996). Non-structural carbohydrate reserves of eelgrass zostera marina. *Mar. Ecol. Prog. Series.* 137, 195–201. doi: 10.3354/meps137195

Burkholder, J., Mason, K., and Glasgow, H. (1992). Water-column nitrate enrichment promotes decline of eelgrass zostera manna: evidence from seasonal mesocosm experiments. *Mar. Ecol. Prog. Series.* 81, 163–178. doi: 10.3354/meps081163

Burkholder, J., Tomasko, D. A., and Touchette, B. W. (2007). Seagrasses and eutrophication. *J. Exp. Mar. Biol. Ecology.* 350, 46–72. doi: 10.1016/j.jembe.2007.06.024

Campbell, J. E., Yarbro, L. A., and Fourqurean, J. W. (2012). Negative relationships between the nutrient and carbohydrate content of the seagrass thalassia testudinum. *Aquat. Botany.* 99, 56–60. doi: 10.1016/j.aquabot.2012.02.002

Cole, M. L., Valiela, I., Kroeger, K. D., Tomasky, G. L., Cebrian, J., Wigand, C., et al. (2004). Assessment of a delta15N isotopic method to indicate anthropogenic eutrophication in aquatic ecosystems. *J. Environ. Quality.* 33, 124–132. doi: 10.2134/jeq2004.012

Connell, S. D., Fernandes, M., Burnell, O. W., Doubleday, Z. A., Griffin, K. J., Irving, A. D., et al. (2017). Testing for thresholds of ecosystem collapse in seagrass meadows. *Conserv. Biol.* 31 (5), 1196–1201. doi: 10.1111/cobi.12951

Cragg, S. M., Friess, D. A., Gillis, L. G., Trevathan-Tackett, S. M., Terrett, O. M., Watts, J. E., et al. (2020). Vascular plants are globally significant contributors to marine carbon fluxes and sinks. *Annu. Rev. Mar. science.* 12, 469–497. doi: 10.1146/annurev-marine-010318-095333

Dang, T., Hoang, N. T., Lieu, P. K., Harada, H., and Venterink, H. O. (2020). Interspecific variation in foliar nutrients and isotopes of submerged macrophytes in the cau hai lagoon, the typical brackish lagoon in vientam. *Botanica Pacifica.* 9, 61–72. doi: 10.17581/bp.2020.09207

Dimitrakopoulos, A. P. (2001). Thermogravimetric analysis of Mediterranean plant species. *J. Analytical Appl. Pyrolysis.* 60, 123–130. doi: 10.1016/S0165-2370(00)00164-9

Duarte, C. M., Losada, I. J., Hendriks, I. E., Mazarrasa, I., and Marbà, N. (2013). The role of coastal plant communities for climate change mitigation and adaptation. *Nat. Climate Change.* 3, 961–968. doi: 10.1038/NCLIMATE1970

Dubois, M. (1956). Colorimetric method for determination of sugars and related substances. *Analytical Chem.* 28, 350–356. doi: 10.1021/ac60111a017

Fourqurean, J. W., Boyer, J. N., Durako, M. J., Hefty, L. N., and Peterson, B. J. (2003). Forecasting responses of seagrass distributions to changing water quality using monitoring data. *Ecol. Applications.* 13, 474–489. doi: 10.1890/1051-0761(2003)013[0474:Frosdt]2.0.Co;2

Helber, S. B., Procaccini, G., Belshe, E. F., Santillan-Sarmiento, A., Cardini, U., Broehl, S., et al. (2021a). Unusually warm summer temperatures exacerbate population and plant level response of posidonia oceanica to anthropogenic nutrient stress. *Front. Plant Science.* 12. doi: 10.3389/fpls.2021.662682

Helber, S. B., Winters, G., Stuhr, M., Belshe, E., Bröhl, S., Schmid, M., et al. (2021b). Nutrient history affects the response and resilience of the tropical seagrass halophila stipulacea to further enrichment in its native habitat. *Front. Plant science.* 12. doi: 10.3389/fpls.2021.678341

Hernán, G., Ortega, M. J., Henderson, J., Alós, J., Boyer, K., Cimon, S., et al. (2021). Latitudinal variation in plant defence against herbivory in a marine foundation species does not follow a linear pattern: The importance of resource availability. *Global Ecol. Biogeography.* 30, 220–234. doi: 10.1111/geb.13217

Invers, O., Kraemer, G. P., Pérez, M., and Romero, J. (2004). Effects of nitrogen addition on nitrogen metabolism and carbon reserves in the temperate seagrass posidonia oceanica. *J. Exp. Mar. Biol. Ecology.* 303, 97–114. doi: 10.1016/j.jembe.2003.11.005

Jan, B., and Roel, M. (1993). An improved colorimetric method to quantify sugar content of plant tissue. *J. Exp. Botany.* 44, 1627–1629. doi: 10.1093/jxb/44.10.1627

Jiang, Z., Cui, L., Liu, S., Zhao, C., Wu, Y., Chen, Q., et al. (2020). Historical changes in seagrass beds in a rapidly urbanizing area of guangdong province: Implications for conservation and management. *Global Ecol. Conserv.* 22, e01035. doi: 10.1016/j.gecco.2020

Jiang, Z., Liu, S., Zhang, J., Zhao, C., Wu, Y., Yu, S., et al. (2017). Newly discovered seagrass beds and their potential for blue carbon in the coastal seas of hainan island, south China Sea. *Mar. pollut. Bulletin.* 125, 513–521. doi: 10.1016/j.marpolbul.2017.07.066

Jiménez-Ramos, R., Egea, L. G., Ortega, M. J., Hernández, I., Vergara, J. J., and Brun, F. G. (2017). Global and local disturbances interact to modify seagrass palatability. *PloS One* 12, e0183256. doi: 10.1371/journal.pone.0183256

Kaal, J., Serrano, O., Cortizas, A. M., Baldock, J. A., and Lavery, P. S. (2019). Millennial-scale changes in the molecular composition of posidonia australis seagrass deposits: Implications for blue carbon sequestration. *Organic Geochemistry.* 137, 103898. doi: 10.1016/j.orggeochem.2019.07.007

Kaal, J., Serrano, O., Nierop, K. G., Schellekens, J., Cortizas, A. M., and Mateo, M.-Á. (2016). Molecular composition of plant parts and sediment organic matter in a Mediterranean seagrass (Posidonia oceanica) mat. *Aquat. Botany.* 133, 50–61. doi: 10.1016/j.aquabot.2016.05.009

Kaladharan, P., Lavanya, R., and Akshara, C. (2021). Capture and storage of carbon in seagrass beds of a vulnerable species halophila beccarii (Asch.) at the kadalundi estuary, kerala, India. *J. Mar. Biol. Assoc. India* 63 (2), 126–129. doi: 10.6024/jmbai.2021.63.2.2284-19

Kennedy, H., Beggins, J., Duarte, C. M., Fourqurean, J. W., Holmer, M., Marbà, N., et al. (2010). Seagrass sediments as a global carbon sink: Isotopic constraints. *Global Biogeochemical Cycles.* 24, GB4026. doi: 10.1029/2010GB003848

Klap, A. V., Hemminga, M. A., and Boon, J. J. (2000). Retention of lignin in seagrasses: angiosperms that returned to the sea. *Mar. Ecol. Prog. Series.* 194, 1–11. doi: 10.3354/meps194001

Lawler, I. R., Aragones, L., Berding, N., Marsh, H., and Foley, W. (2006). Near-infrared reflectance spectroscopy is a rapid, cost-effective predictor of seagrass nutrients. *J. Chem. Ecology.* 32, 1353–1365. doi: 10.1007/s10886-006-9088-x

Lee, K. S., and Dunton, K. H. (1999). Influence of sediment nitrogen-availability on carbon and nitrogen dynamics in the seagrass thalassia testudinum. *Mar. Biol.* 134, 217–226. doi: 10.1007/s002270050540

Lee, S. W., Lim, J. M., Bhoo, S. H., Paik, Y. S., and Hahn, T. R. (2003). Colorimetric determination of amino acids using genipin from gardenia jasminoides. *Analytica Chimica Acta* 480, 267–274. doi: 10.1016/S0003-2670(03)00023-0

Liu, S., Trevathan-Tackett, S. M., Ewers Lewis, C. J., Huang, X., and Macreadie, P. I. (2020). Macroalgal blooms trigger the breakdown of seagrass blue carbon. *Environ. Sci. Technol.* 54, 14750–14760. doi: 10.1021/acs.est.0c03720

Macreadie, P. I., Anton, A., Raven, J. A., Beaumont, N., and Duarte, C. M. (2019). The future of blue carbon science. *Nat. Commun.* 10, 3998. doi: 10.1038/s41467-019-11693-w

Mottiar, Y., Vanholme, R., Boerjan, W., Ralph, J., and Mansfield, S. D. (2016). Designer lignins: harnessing the plasticity of lignification. *Curr. Opin. Biotechnol.* 37, 190–200. doi: 10.1016/j.copbio.2015.10.009

Ogden, M., Hoefgen, R., Roessner, U., Persson, S., and Khan, G. A. (2018). Feeding the walls: How does nutrient availability regulate CellWall composition? *Int. J. Mol. Sci.* 19, 2691. doi: 10.3390/ijms19092691

Pazzaglia, J., Santillán-Sarmiento, A., Helber, S. B., Ruocco, M., and Procaccini, G. (2020). Does warming enhance the effects of eutrophication in the seagrass posidonia oceanica? *Front. Mar. Science.* 7. doi: 10.3389/fmars.2020.564805

Peduzzi, P., and Herndl, G. J. (1991). Decomposition and significance of seagrass leaf litter(Cymodocea nodosa) for the microbial food web in coastal waters(Gulf of Trieste, northern Adriatic Sea). *Mar. Ecol. Prog. series. Oldendorf.* 71, 163–174. doi: 10.3354/meps071163

Pérez, M., and Romero, J. (1994). Growth dynamics, production, and nutrient status of the seagrass cymodocea nodosa in a Mediterranean semi-estuarine environment. *Mar. Ecology.* 15, 51–64. doi: 10.1111/j.1439-0485.1994.tb00041.x

Pitre, F. E., Pollet, B., Lafarguette, F., Cooke, J. E. K., MacKay, J. J., and Lapierre, C. (2007). Effects of increased nitrogen supply on the lignification of poplar wood. *J. Agric. Food Chem.* 55, 10306–10314. doi: 10.1021/jf071611e

Premarathne, C., Jiang, Z., He, J., Fang, Y., and Huang, X. (2021). Low light availability reduces the subsurface sediment carbon content in halophila beccarii from the south China Sea. *Front. Plant Science.* 12. doi: 10.3389/fpls.2021.664060

Ralph, P. J., Durako, M. J., Enríquez, S., Collier, C. J., and Doblin, M. A. (2007). Impact of light limitation on seagrasses. *J. Exp. Mar. Biol. Ecology.* 350, 176–193. doi: 10.1016/j.jembe.2007.06.017

Reef, R., Atwood, T. B., Samper-Villarreal, J., Adame, M. F., Sampayo, E. M., and Lovelock, C. E. (2017). Using eDNA to determine the source of organic carbon in seagrass meadows. *Limnology Oceanography.* 62, 1254–1265. doi: 10.1002/lno.10499

Schmidt, A. L., Wysmyk, J. K. C., Craig, S. E., and Lotze, H. K. (2012). Regional-scale effects of eutrophication on ecosystem structure and services of seagrass beds. *Limnology Oceanography* 57, 1389–1402. doi: 10.4319/lo.2012.57.5.1389

Shan, L., Song, C., Zhang, X., and Ren, J. (2018). Effects of long-term nitrogen and phosphorus addition on plant defence compounds in a freshwater wetland. *Ecol. Indicators.* 94, 1–6. doi: 10.1016/j.ecolind.2018.06.017

Siegalwillott, J. L., Harr, K., Hayek, L., Scott, K. C., Gerlach, T., Sirois, P., et al. (2010). Proximate nutrient analyses of four species of submerged aquatic vegetation consumed by Florida manatee (Trichechus manatus latirostris) compared to romaine lettuce (Lactuca sativa var. longifolia). *J. Zoo Wildlife Med.* 41, 594–602. doi: 10.1638/2009-0118.1

Torbatinejad, N. M., Annison, G., Rutherfurd-Markwick, K., and Sabine, J. R. (2007). Structural constituents of the seagrass posidonia australis. *J. Agric. Food Chem.* 55, 4021–4026. doi: 10.1021/jf063061a

Touchette, B. W., and Burkholder, J. M. (2000). Review of nitrogen and phosphorus metabolism in seagrasses. *J. Exp. Mar. Biol. Ecology.* 250, 133–167. doi: 10.1016/S0022-0981(00)00195-7

Touchette, B. W., and Burkholder, J. M. (2007). Carbon and nitrogen metabolism in the seagrass, zostera marina l.: Environmental control of enzymes involved in carbon allocation and nitrogen assimilation. *J. Exp. Mar. Biol. Ecology.* 350, 216–233. doi: 10.1016/j.jembe.2007.05.034

Trevathan-Tackett, S. M., Kelleway, J., Macreadie, P. I., Beardall, J., Ralph, P., and Bellgrove, A. (2016). Comparison of marine macrophytes for their contributions to blue carbon sequestration. *Ecology* 96, 3043–3057. doi: 10.1890/15-0149.1

Trevathan-Tackett, S. M., Macreadie, P. I., Sanderman, J., Baldock, J., Howes, J. M., and Ralph, P. J. (2017). A global assessment of the chemical recalcitrance of seagrass tissues: Implications for long-term carbon sequestration. *Front. Plant Science.* 8. doi: 10.3389/fpls.2017.00925

Turpin, D. H. (2010). Effects of inorganic n availability on algal photosynthesis and carbon metabolism. *J. Phycology.* 27, 14–20. doi: 10.1111/j.0022-3646.1991.00014.x

Udagedara, S., and Dahanayaka, D. D. G. L. (2020). Current status and checklist of seagrass in Sri Lanka. *Int. J. Aquat. Biology-IJAB.* 8, 317–326. doi: 10.22034/ijab.v8i5.619

Udy, J. W., and Dennison, W. C. (1997). Growth and physiological responses of three seagrass species to elevated sediment nutrients in moreton bay, Australia. *J. Exp. Mar. Biol. Ecology.* 217, 253–277. doi: 10.1016/S0022-0981(97)00060-9

Vichkovitten, T., and Holmer, M. (2004). Contribution of plant carbohydrates to sedimentary carbon mineralization. *Organic geochemistry* 35, 1053–1066. doi: 10.1016/j.orggeochem.2004.04.007

Vichkovitten, T., Holmer, M., and Frederiksen, M. S. (2007). Spatial and temporal changes in non-structural carbohydrate reserves in eelgrass (Zostera marina l.) in Danish coastal waters. *Botanica Marina* 50 (2), 75–87. doi: 10.1515/bot.2007.009

Xu, L., Zhou, J., Ni, J., Li, Y., Long, Y., and Huang, R. (2020). Investigating the pyrolysis kinetics of pinus sylvestris using thermogravimetric analysis. *Bioresources* 15, 5577–5592. doi: 10.15376/biores.15.3.5577-5592

Yang, X., Zhang, P., Li, W., Hu, C., Zhang, X., and He, P. (2018). Evaluation of four seagrass species as early warning indicators for nitrogen overloading: Implications for eutrophic evaluation and ecosystem management. *Sci. Total Environment.* 635, 1132–1143. doi: 10.1016/j.scitotenv.2018.04.227

Zhang, P. Y., Grutters, B. M. C., van Leeuwen, C. H. A., Xu, J., Petruzzella, A., van den Berg, R. F., et al. (2019). Effects of rising temperature on the growth, stoichiometry, and palatability of aquatic plants. *Front. Plant Sci.* 9. doi: 10.3389/fpls.2018.01947

Zhang, W., Wu, L., Ding, Y., Yao, X., Wu, X., Weng, F., et al. (2017). Nitrogen fertilizer application affects lodging resistance by altering secondary cell wall synthesis in japonica rice (Oryza sativa). *J. Plant Res.* 130, 859–871. doi: 10.1007/s10265-017-0943-3

Zieman, J., Macko, S., and Mills, A. (1984). Role of seagrasses and mangroves in estuarine food webs: temporal and spatial changes in stable isotope composition and amino acid content during decomposition. *Bull. Mar. Science.* 35, 380–392. doi: 10.1515/botm.1984.27.12.571

frontiers | Frontiers in Marine Science

TYPE Original Research
PUBLISHED 27 September 2022
DOI 10.3389/fmars.2022.985548

OPEN ACCESS

EDITED BY
Jeng-Wei Tsai,
China Medical University, Taiwan

REVIEWED BY
Zhanhui Qi,
Key Laboratory of South China Sea Fishery Resources Exploitation and Utilization (CAFS), China
Zengjie Jiang,
Yellow Sea Fisheries Research Institute (CAFS), China

*CORRESPONDENCE
Yuanqing Ma
mayuanqing@shandong.cn

†These authors have contributed equally to this work and share first authorship

SPECIALTY SECTION
This article was submitted to Marine Biogeochemistry, a section of the journal Frontiers in Marine Science

RECEIVED 04 July 2022
ACCEPTED 12 September 2022
PUBLISHED 27 September 2022

CITATION
Zhang M, Qin H, Wang Z, Li B and Ma Y (2022) The interaction between DOC released by cultured kelp (*Saccharina japonica*) and the bacterial community reveals the potential for increasing marine carbon sequestration by macroalgae culture. *Front. Mar. Sci.* 9:985548. doi: 10.3389/fmars.2022.985548

The interaction between DOC released by cultured kelp (*Saccharina japonica*) and the bacterial community reveals the potential for increasing marine carbon sequestration by macroalgae culture

Mingliang Zhang[1†], Huawei Qin[1†], Zhidong Wang[2], Bin Li[1] and Yuanqing Ma[1*]

[1]Marine Carbon Sink Research Center, Shandong Marine Resource and Environment Research Institute, Yantai, China, [2]College of Fisheries and Life Science, Shanghai Ocean University, Shanghai, China

Macroalgae culture as a marine carbon sequestration strategy has been recently proposed. To understand the potential for carbon sequestration by macroalgae culture, we studied the interaction of dissolved organic carbon (DOC) released by *Saccharina japonica*, an important cultured kelp species in China, and the bacterial community. We found that *S. japonica* effectively released DOC containing both labile and refractory components, and the DOC released by *S. japonica* into the water decreased average molecular weight ($Mass_{wa}$) by 18 Da, meaning it was rich in low molecular weight matter. Degradation of labile DOC components occurred during the initial 2 months of the experiment. The $Mass_{wa}$ and molecular diversity of the DOC was increased in turn by bacterial degradation, and the variation in the DOC composition resulted in the succession of the bacterial community. During labile DOC degradation, anaerobic Gammaproteobacteria, Bacteroidia and Campylobacteria were the dominant microbial classes in the water, and aerobic Iodidimonadaceae became the dominant family during the final stage of the experiment. Finally, 5% of the DOC was transformed into refractory DOC. Although the sinking biomass was not involved in the study, the produced refractory DOC through the interaction between releasing DOC and bacterial degradation indicates a potential of carbon sequestration by macroalgae culture.

KEYWORDS

macroalgae culture, carbon sequestration, bacterial community, refractory dissolved organic carbon, *Saccharina japonica*

Highlights

- The DOC released by *S. japonica* contained both labile and refractory components.
- Anaerobic and sulfidic bacteria dominated degradation of labile components in the DOC.
- 5% DOC released by *S. japonica* was transformed to refractory DOC.
- Degradation increased the $Mass_{wa}$ and molecular diversity of the DOC.

1 Introduction

The ocean accounts for 71% of Earth's area and is the largest active carbon pool in the world, with 20 and 50 times the carbon stored in either the terrestrial or atmosphere carbon pool, respectively (Post et al., 1990). The ocean also significantly buffers against global warming, by absorbing 23% CO_2 released by human activities through industrial activities (Sabine et al., 2004; DeVries et al., 2017). Removing atmospheric CO_2 by increasing ocean carbon sequestration is an effective strategy for mitigating global climate change. The most important ocean carbon sequestration strategy is the 'blue carbon' project. By protecting and restoring the blue carbon ecosystem (i.e., mangroves, salt marshes, and seagrass beds) particulate organic carbon can be sequestered in the sediments (NASEM, 2019). Although macroalgae is the most productive marine macrophyte, it has been excluded from the 'blue carbon' strategic framework initially, mainly because most macroalgae grow on rocks, precluding the burial of organic carbon in sediment (Hill et al., 2015; Dorte and Carlos, 2016). Different to forest in land, organic carbon in macroalgae biomass can be degradation in short time-scale also limited the carbon sequestration of macroalgae. However, macroalgae can indirectly sequester large amounts of carbon in seawater in the form of dissolved organic carbon (DOC) through bacterial degradation of biomass and the extracellular exudate from macroalgae (Chen et al., 2020; Watanabe et al., 2020). A portion of this final product of this bacterial degradation is refractory to further biodegradation. According to the microbial carbon pump theoretical framework, the products of bacterial degradation comprise a refractory dissolved organic carbon (RDOC) pool in the ocean carbon cycle, which can sequester carbon for 5000–6000 years (Jiao et al., 2010; Ortega et al., 2019). Therefore, the indirect production of RDOC by macroalgae provides a positive buffering effect against global warming. For the reason above, macroalgae was proposed as the fourth species of blue carbon in recent years (IPCC, 2020).

Releasing DOC is a basic physiological function for macroalgae. To protect their tissues, more than 20% of the net primary production of macroalgae is released in the form of DOC (Abdullah and Fredriksen, 2004; Wada et al., 2007; Reed et al., 2015; Gao et al., 2021). A large amount of biomass exists in the coastal ocean, and macroalgae DOC is an important component of the coastal DOC pool (Reed et al., 2015; Mahmood et al., 2017; Ortega et al., 2019). For example, in Oura Bay, Japan, 20%–34% of the coastal DOC originates from the *Ecklonia cava* Kjellman release (Wada and Hama, 2013). Macroalgae DOC provides an important metabolic substrate for bacteria along the coast, and some of the RDOC produced by bacteria indirectly originates from the macroalgae. Around the world, macroalgae indirectly sequester roughly 0.12 Pg C/yr in the form of RDOC, which is 12% of the global annual blue carbon sequestration (Krause-Jensen and Duarte, 2016; NASEM, 2019). The indirect production of RDOC by macroalgae should not be ignored in the global carbon cycle.

Macroalgae culture is a rapid developing industry, producing 34.7 million t/y (FAO, 2021). Besides providing seafood and raw material for industry, macroalgae culture is one of the most effective carbon dioxide removal approaches developed in recent years (NASEM, 2021). The production of macroalgae in China accounts for 58.2% of the global supply (FAO, 2021). Among the species cultured in China, the kelp *Saccharina japonica* is the most important. Many studies have been conducted on the interaction between natural macroalgae DOC and the bacterial community, but none have focused on cultured macroalgae DOC (Wada et al., 2008; Zhang and Wang, 2017; Chen et al., 2020). Bacterial communities are sensitive to environmental variation. Physical, chemical, and biological factors can all disturb the interaction between macroalgae DOC and bacteria in seawater, and these uncontrollable factors make *in situ* studies difficult. Nearly all DOC degradation experiments have been performed under laboratory conditions, even though degradation processes in the laboratory can be different from those in the ocean (Wada et al., 2008; Chen et al., 2020; Watanabe et al., 2020; Gao et al., 2021). In this study, the interaction and dynamics of DOC release by the cultured kelp *S. japonica* and the bacterial community succession is studied in the laboratory.

2 Material and methods

2.1 Sample collection and pretreatment

S. japonica were collected in November 2021 from Chudao (122° 35′ E, 37° 09′ N), Sangou Bay, the most productive kelp bay in northern China. Kelp with intact leaves (each with length 1.2–1.5 m and fresh weight 20–40 g) were picked from culture

ropes. Surface water was collected from 1 m below sea level. All samples were transported into laboratory in 4 h. Seawater was immediately filtered through a 0.7 μm-pore Whatman glass fiber filter to eliminate phytoplankton and particulate matter. Kelp leaves were washed five times with filtered seawater to remove particulate matter and any fouling organisms attached to the kelp (Zhang and Wang, 2017).

2.2 Experimental process

To gather the DOC released by *S. japonica*, 800 g fresh kelp biomass was placed into a 100 L glass container. To simulate the actual kelp culture, the biomass density in the collecting process was consistent with the culture density in natural water. After 48 h, when the color of water turned yellowish brown, 30 L water was transferred into degradation containers as the treatment group for the 120 d degradation experiment. Simultaneously, 30 L filtered seawater without enrichment of DOC released by *S. japonica* was established as the control group. Both groups had three replicates. All degradation containers were covered loosely to avoid contact with the atmosphere. The experiment was kept in dark conditions at room temperature (20–26°C) to reduce the impact of photodegradation and possible growth of picophytoplankton, which may have passed through the filtering process and added DOC to the experiment. During the 120 d degradation process, water samples were collected at different time points for analysis of the concentration and composition of DOC and for determination of dynamic variations in abundance and community structure of planktonic bacteria.

Samples for measuring the concentration of DOC, fluorescent dissolved organic matter (FDOM), bacterial abundance, and community structure were collected on days 0, 2, 4, 8, 16, 24, 30, 45, 60, 75, 90, and 120. Samples for DOC molecular composition were collected on days 0, 60, and 120. Samples (50 mL and 500 mL) were collected from each replicate into brown glass bottles for the analysis of DOC concentration and molecular composition, respectively. The concentration samples were also used for the analysis of FDOM. Meanwhile, 4.5 mL samples with added 5% glutaraldehyde (final concentration) were collected for the analysis of bacterial abundance. All water samples were filtered through 0.22 μm-pore polycarbonate membranes before analysis. Lastly, 500 mL water samples were filtered, and the filters were collected for the analysis of the bacterial community structure. The glass containers in all experiments were acid-washed, rinsed with Milli-Q water, and combusted at 450°C for 8 h.

2.3 Sample analysis

2.3.1 Concentrations of DOC

Concentrations of DOC were measured by the high-temperature catalytic oxidation method using a TOC-VCPH analyzer (Shimadzu, Kyoto, Japan). Potassium hydrogen diphosphate and high-carbon deep sea water produced by Hansell's laboratory were used as DOC standards. Milli-Q water was used as a blank and was analyzed every ten samples.

2.3.2 Bacterial abundance

Bacterial abundance samples were stained with SYBR Gold Nucleic Acid Gel Stain then measured with a FACSAria flow cytometer (BD Biosciences, Franklin Lakes, NJ, USA). Bacterial abundance was enumerated with Cellquest software.

2.3.3 Components of FDOM

Components of FDOM were analyzed with an excitation-emission matrix (EEM) using parallel factor (PARAFAC) analysis. EEM was measured with a fluorescence spectrophotometer (Hitachi F-4500, Tokyo, Japan) with scanning speed 1200 nm/min at 950 V. In the scanning process, the excitation (Ex) wavelength ranged from 200 to 500 nm with 5 nm increments, and the emission (Em) wavelength ranged from 250 to 550 nm with 5 nm increments. The raster for both Ex and Em was 5 nm. PARAFAC analysis of the FDOM components was performed with the drEEM toolbox (http://dreem.openfluor.org/) and MATLAB (MathWorks, Natick, MA, USA).

2.3.4 Molecular composition of DOC

The molecular composition of DOC was analyzed by Fourier transform–ion cyclotron resonance–mass spectrometry (FT-ICR-MS) using a Bruker ultra-high definition FT-ICR mass spectrometer Solarix XR 7.0T (Bruker Daltonics, Bremen, Germany) at China National Analytical Center, Guangzhou. Before the analysis, DOC was solid-phase extracted and eluted using a previously described method (Dittmar et al., 2008). Data analysis and chemical formula assignment were performed with the TRFu algorithm based on the formula criteria of $5 \le C \le 50$, $1 \le O$, $N \le 4$, $S \le 2$, $P \le 2$, $0 < O/C \le 1.2$, and $0.3 \le H/C \le 2.5$, within 1.0 ppm (Fu et al., 2020). Once formula assignment for all peaks was accomplished, parameters such as modified aromaticity index (AImod) and double-bond equivalents (DBE) were calculated for each formula. AImod and DBE were calculated according to equations (1) and (2) (Koch and Dittmar, 2006):

$$AImod = (1 + C - 0.5O - S - 0.5H - 0.5N - 0.5P)/(C - 0.5O - S - N - P) \quad (1)$$

$$DBE = 1 + C - O - S - 0.5N - 0.5P - 0.5H \quad (2)$$

where C, H, O, N, S, and P are the numbers of carbon, hydrogen, oxygen, nitrogen, sulfur, and phosphorus atoms in a molecular formula, respectively. All formulas were divided into six groups according to the values of AImod and H/C. The group with AImod > 0.66 represented polycyclic aromatic compounds. The group with $0.66 \ge$ AImod > 0.50 represented highly aromatics compounds. The group with AImod ≤ 0.50 and H/C < 1.5 represented highly unsaturated compounds. The group with AImod ≤ 0.5, 2.0 > H/C ≥ 1.5 and without nitrogen atoms in their molecular formula represented unsaturated aliphatic compounds

(N = 0). The group with AImod ≤ 0.5, 2.0 > H/C ≥ 1.5, and with nitrogen atoms in their molecular formula represented nitrogenous unsaturated aliphatic compounds (N > 0). Lastly, the group with AImod ≤ 0.5 and H/C ≥ 2.0 represented saturated fatty and sulfonic acids. To compare the overall characteristics of the samples, the weight average of the molecular weight ($Mass_{wa}$), weight average of oxygen to carbon ratios (O/C_{wa}), weight average of hydrogen to carbon ratios (H/C_{wa}), weight average of double-bond equivalents (DBE_{wa}), weight average of carbon to nitrogen ratios (C/N_{wa}), and weight average of carbon to sulfur ratios (C/S_{wa}) were calculated using a method previously described (Koch et al., 2014).

2.3.5 Bacterial community structure analysis

Three parallel samples at each sampling time point were combined before DNA extraction as per Zhao et al. (2019). Bacterial genomic DNA was extracted using the HiPure Water DNA Kit (D3145-02, MGBio, China). The DNA concentration was verified with a NanoDrop 2000 (Thermo-Fisher, United States) and 1% agarose gel electrophoresis. The 16S rRNA gene was amplified with primers targeting the V3–V4 hypervariable regions: 343F-5′-TACGGRAGGCAGCAG-3′ and 798R-5′-AGGGTATCTAATCCT-3′. Library sequencing and data processing were conducted by OE Biotech Co., Ltd. (Shanghai, China). The raw sequencing data were pre-processed by Cutadapt (version 3.4) to remove the primer sequence (Martin, 2011). The abundance of the amplicon sequence variants (ASV) was obtained by de-noising with Dada 2 (Version 1.8) (Callahan et al., 2016). All representative reads were annotated and BLAST searched against the Silva database (version 138) using QIIME 2 (version 2020.11) (Bolyen et al., 2019)

2.4 Statistical analysis

Statistical significance of differences in the DOC concentration and bacterial abundance were analyzed by one-way analysis of variance (ANOVA). The difference of bacterial communities in ASV's level was measured by analysis of similarity (ANOSIM). To test the bacterial community succession in the experiment, β-diversity was analyzed using Bray-Curtis distances based on the relative abundance matrices of the ASVs. Hierarchical cluster analysis (HCA) and nonmetric multidimensional scaling (NMDS) were calculated based on the Bray-Curtis distances.

3 Results

3.1 Variations in DOC concentration and bacterial abundance during the 120-day degradation experiment

The dynamic variations in DOC concentration and bacterial abundance had different characteristics during the 120-day degradation process. The DOC concentration reached a peak of 65.29 ± 9.58 mg C/L at the start of experiment (day 0) and decreased sharply to 10.36 ± 0.57 mg C/L on day 24 (Figure 1). Over the following 46 d, the DOC concentration declined slowly, reaching 9.46 ± 0.46 mg C/L on day 60. During the last 2 months of the experiment, the DOC concentration remained relatively stable. Based on the variation in the DOC concentration, the entire degradation process was divided into three stages: DOC rapid decline (RD) stage (day 0–24), DOC slow decline (SD) stage (day 24–60), and DOC relatively stable (RS) stage (day 60–120). At the end of the experiment, the DOC concentration in the treatment group was significantly higher than in the control ($p < 0.05$), and the DOC concentration in the control did not significantly change during the experiment. Similar to the changes in DOC concentration, the bacterial abundance was initially the highest on day 0 at 1.96 ± 0.07 $\times 10^8$ cells/mL, remained stable on day 1, then smoothly decreased to 2.03 ± 1.2 $\times 10^7$ cells/mL by day 60. During the next 2 months, bacterial abundance remained relatively stable, similar to the trend in the DOC concentration. Also similar to the variation of DOC in the control, the bacterial abundance in the control did not change significantly during the experiment. The final bacterial abundance in the treatment group was significantly higher ($p < 0.05$) than in the control.

3.2 Variation in DOC components during the 120-day degradation experiment

PARAFAC analysis of FDOM and FT-ICR-MS results were used to track the variation in DOC composition during the study. Four FDOM components (i.e., C1–C4) were identified during the 120-day degradation, with Ex|Em wavelengths of 250 (310)|400 nm, 260|465 nm, 280|340 nm, and 355|420 nm respectively (Figure S1). According to the Ex|Em wavelengths, C1 and C2 represent humic-like fluorescent components originating from autochthonous production (Gao and Guéguen, 2018; Kulkarni et al., 2018). C3 represents an autochthonous protein-like component (Bittar et al., 2015), and C4 represents humic-like fluorescent components originating from microbial degradation (Amaral et al., 2021). All components had different dynamic variations in fluorescence intensity during the 120-day degradation process (Figure 2). The fluorescence intensity of both C1 and C2 decreased slightly until the end of the experiment. Different from the other humic-like fluorescence components, the fluorescence intensity of C4 increased slowly over the entire degradation process. The fluorescence intensity of C3 declined sharply during the initial 24 days then changed little until the end of experiment. In contrast, the fluorescence intensity of all components in the control group did not change significantly during the experiment.

FT-ICR-MS analysis revealed the variation in DOC composition at the molecular level during the 120-day degradation. Throughout the experiment, a total of 11376 different molecular formulas (MFs) covering a mass range of 109–999 Da (including ^{13}C isotopologs) were identified. Based on the elemental compositions, MFs were classified into five groups, i.e., CHO-, CHON-, CHOS-, CHONS-, and CHOSP-, which represented 95% of the MFs identified in the experiment (Table 1). The MFs changed significantly during the initial 2 months of treatment. In the day 0 treatment (T0) sample, the total number of MFs in the DOC was 32% higher than in the day 0 control (C0) sample. Meanwhile, the number of MFs in the CHON-, CHOS-, CHONS-, and CHOSP- groups were 17%, 75%, 347%, and 58% higher, respectively, in T0 than C0. The relative abundance of unsaturated fatty and sulfonic acids, unsaturated aliphatic compounds (N > 0), and unsaturated aliphatic compounds (N = 0) were 2.4%, 5%, and 15% higher, respectively, in T0 than in C0 (Figure 3). After 60 days degradation, the MFs in the treatment group (T60) increased by 15% compared with T0, and the number of MFs in the CHO-, CHON-, and CHOSP- groups increased by 10%, 28%, and 116%, respectively, between T0 and T60. In contrast, the relative abundance of unsaturated fatty and sulfonic acids, unsaturated aliphatic compounds (N > 0), and unsaturated aliphatic compounds (N = 0) decreased by 3.5%, 4.5%, and 18%, respectively, between T0 and T60. During the last 2 months of the experiment, the MFs and molecular composition changed little in the treatment. In contrast, the variation in the MFs and molecular composition in the control samples was negligible during the entire experiment.

The average chemical characteristics for the treatment samples also changed significantly during the degradation process (Table 2). The $Mass_{wa}$ at T0 was 18 Da lower than in C0 because of the DOC released by *S. japonica*. DBE_{wa} and $Almod_{wa}$ were 13% and 15% lower, respectively, in T0 than in C0. In contrast, N/C_{wa} and S/C_{wa} were 75% and 142% higher, respectively, in T0 than in C0. After 60 days degradation, $Mass_{wa}$ in T60 increased by 26 Da compared with T0, and O/C_{wa}, $DBE_{wa,}$ and $Almod_{wa}$ increased by 20%, 22%, and 28%, respectively, between T0 and T60. However, H/C_{wa} and N/C_{wa} decreased by 15% and 18%, respectively, between T0 and T60. There was very little variation in the average chemical characteristics between T60 and T120, except for an increase in $Mass_{wa}$ of 10 Da. During the entire degradation process, the changes in average chemical characteristics in the control group were relatively small.

3.3 Variation in the bacterial community during the 120-day degradation experiment

During the experiment, 2228 ASVs were identified. The raw data of ASVs were uploaded into national center for biotechnology information (NCBI) sequence read archive (SRA) database (accession number: PRJNA855139). Only 16% were present in both the treatment and control (Figure S2). The bacterial community in the treatment group was significantly different from the control based on the ANOSIM analysis of ASVs (Table S1). Based on the ASVs, 28 phylum, 56 classes, 147

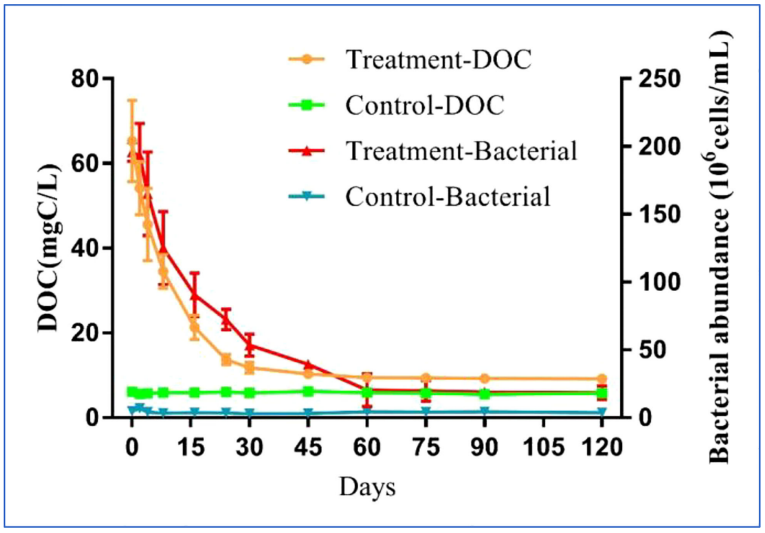

FIGURE 1
Variations of DOC concentration and bacterial abundance in the 120-day degradation of DOC released by *Saccharina japonica* and that in natural seawater.

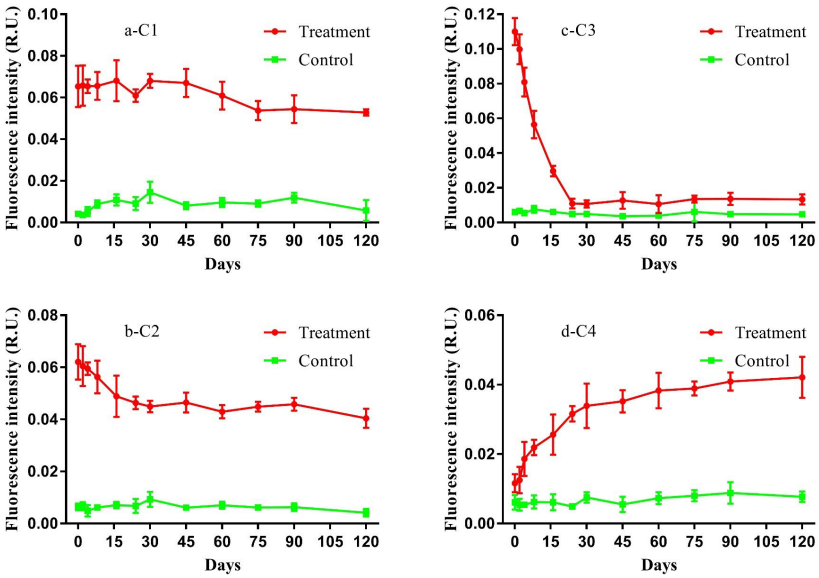

FIGURE 2
Variations of components (i.e., C1, C2, C3, and C4) of fluorescent dissolved organic matter (FDOM) in the 120-day degradation of DOC released by *Saccharina japonica* and that in natural seawater.

orders, 241 families, and 419 genera were identified. HCA and NMDS analysis showed significant bacterial community succession during the 120-day degradation. In the treatment group, the bacterial community was divided into three clusters: T-I (T0, T2, T4, and T8), T-II (T16, T24, T30, and T45), and T-III (T60, T75, T90, and T120) (Figure 4; Figure S4). In the control group, the bacterial community was divided into two clusters: C-I (C0, C2 and C4) and C-II (C8, C16, C24, C30, C45, C60, C75, C90, and C120). In adddition, T-I and C-I, T-III, and C-II clustered together. The analysis of AONSIM also revealled the bacterial community succession in treatment and control (Table S1). The dominant classes in cluster T-I were Gammaproteobacteria, Bacteroidia, and Campylobacteria, with relative abundances of each one nearly 30% (Figure 5). Alphaproteobacteria, Gammaproteobacteria, and Bacteroidia were the dominant groups in cluster T-II. The relative abundance of Gammaproteobacteria and Bacteroidia were the same in clusters T-I and cluster T-II. In contrast, the relative abundance of Alphaproteobacteria was 20% higher in cluster T-II than in T-I. Cluster T-III had only two dominant classes: Alphaproteobacteria and Gammaproteobacteria, and the relative abundance of Alphaproteobacteria was nearly 70%. In the control group, Gammaproteobacteria and Alphaproteobacteria were the dominant classes in C-I and C-II respectively, each with a relative abundance of nearly 70%.

4 Discussion

Macroalgae culture has been recently proposed as a marine negative emission technique (NASEM, 2021). However, there are no marine carbon sequestration projects using macroalgae culture in operation, mainly because the carbon sequestration ability of macroalgae is controversial (Hill et al., 2015). This study may increase the understanding of carbon sequestration through the release of DOC by macroalgae culture.

After 48 h DOC collection (day 0), the DOC concentration in the treatment group was nearly ten times that of the control, indicating that DOC is effectively released by *S. japonica*. Bacterial abundance peaked at the same time, indicating that DOC released by *S. japonica* is strongly favored by bacteria (Wada et al., 2008; Gao et al., 2021). Nearly 90% of the DOC was degraded during the DOC RD stage, and the rest of the decomposition occurred during the DOC SD stage. Bacterial abundance decreased by an order of magnitude in the DOC RD and SD stages, and then remained stable during the DOC RS stage (Figure 1). The variation in the DOC concentration and bacterial abundance indicated that most of the DOC released by *S. japonica* was decomposed during the initial 2 months of the experiment, similar to observations of previous studies (Wada et al., 2008; Watanabe et al., 2020; Gao et al., 2021; Manikandan et al., 2021). However, the DOC released by phytoplankton can

10.3389/fmars.2022.985548

TABLE 1 The numbers of molecular formulas (MFs) contained in the DOC at different sampling time points during the 120-day degradation.

	T0	T60	T120	C0	C60	C120
total	7536	8650	8579	5710	5703	5851
CHO	2330	2573	2724	2752	2678	2653
CHON	2157	2756	2864	1842	1831	1966
CHOS	1149	1119	989	655	643	596
CHONS	1054	674	566	236	177	273
CHOSP	436	940	893	276	275	231

T0, T60 and T120 represent the samples collected in treatment group on the 0, 60th and 120th day; and C0, C60 and C120 represent the samples collected in control group on the 0, 60th and 120th day.

be decomposed within days to weeks (Hama et al., 2004). This indirectly indicates that not only labile DOC components, but also some refractory DOC components are released by kelp (Wada et al., 2008). Comparing the variation in the DOC concentration between treatment and control, 5% of the DOC released by *S. japonica* was estimated to have remained as RDOC. Considering 20% or more net primary production is released as DOC by kelp (Wada et al., 2007; Gao et al., 2021), we propose that carbon sequestration by macroalgae culture through the interaction between DOC release and bacterial degradation is not negligible.

The variation in the DOC composition revealed the details of the transformation of DOC released by *S. japonica* to RDOC. Generally, protein-like components are considered an indicator of labile composition in DOC (Yang et al., 2015) and humic-like components are considered a potential tracer of RDOC (Lønborg

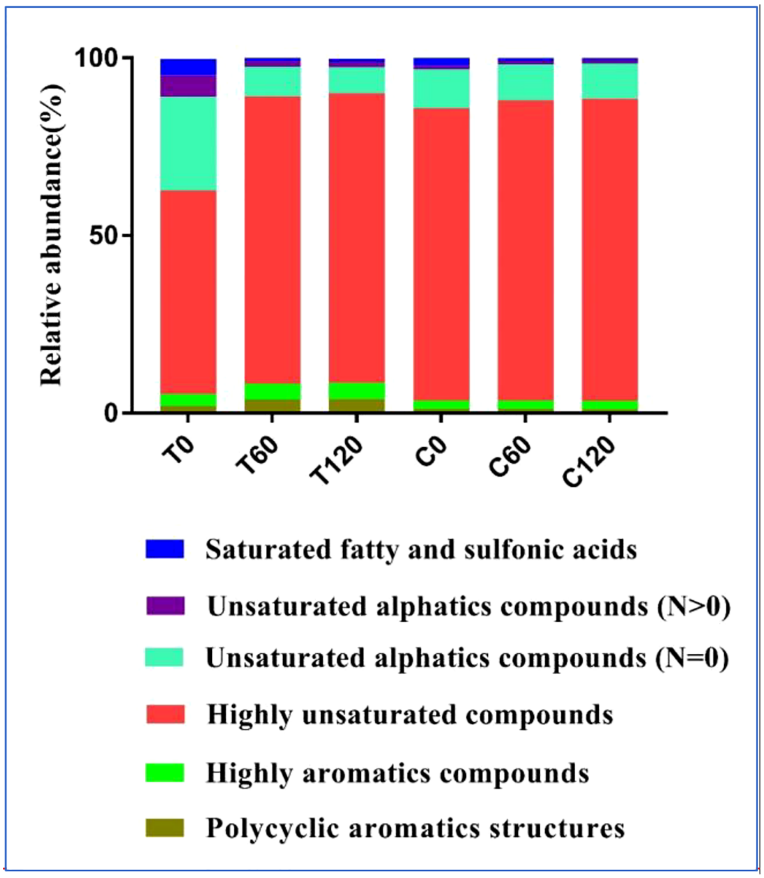

FIGURE 3
The relative abundance of DOC components identified with threshold criteria of the modified aromaticity index (Almod) values and H/C ratios in the 120-day degradation of DOC released by *Saccharina japonica* and that in natural seawater.

TABLE 2 The average chemical characteristics at different sampling points in 120-day degradation.

	T0	T60	T120	C0	C60	C120
$Mass_{wa}$	402.08	428.37	438.52	420.1	413.7	417.56
O/C_{wa}	0.422	0.505	0.495	0.44	0.438	0.439
H/C_{wa}	1.380	1.201	1.221	1.299	1.288	1.286
DBE_{wa}	7.311	8.952	8.965	8.276	8.238	8.352
N/C_{wa}	0.028	0.023	0.022	0.016	0.016	0.016
S/C_{wa}	0.017	0.017	0.016	0.007	0.005	0.005
$Almod_{wa}$	0.201	0.259	0.253	0.232	0.238	0.237

T0, T60 and T120 represent the samples collected in treatment group on the 0, 60th and 120th day; and C0, C60 and C120 represent the samples collected in control group on the 0, 60th and 120th day.

et al., 2013; Chen et al., 2020). Fluorescence analysis revealed that the labile components (C3) were rapidly exhausted during the DOC RD stage. Interestingly, humic-like components (C1 and C2) were slowly degraded during the entire experiment and did not significantly change the DOC concentration during the last 2 months of the experiment (DOC RS stage). This might represent a small percentage of the refractory components in the DOC released by *S. japonica*. Meanwhile, the RDOC component (C4) was produced gradually during the degradation process (Figure 2) (Chen et al., 2020). FT-ICR-MS analysis also revealed that both labile and refractory components were present in the DOC released by *S. japonica*. Generally, the degree of recalcitrance to biodegradation is in the order of polycyclic aromatic compounds > highly aromatics compounds > highly unsaturated compounds > unsaturated aliphatic compounds (N = 0) > unsaturated aliphatic compounds (N > 0) > saturated fatty and sulfonic acids (Schmidt et al., 2011; Cai et al., 2019). By comparing the molecular composition of T0 and C0, we found that labile components such as saturated fatty and sulfonic acids and unsaturated aliphatic compounds (N > 0) increased in relative abundance by 2.4% and 5%, respectively. Meanwhile, refractory components, such as polycyclic aromatic compounds and highly aromatics compounds, increased in relative abundance by 0.8% and 1%, respectively. This indicates that these labile components, and a small amount of refractory components, were present in the DOC released by kelp (Figure 3) (Wada et al., 2008; Watanabe et al., 2020). The relative abundance of labile and refractory components changed little between T60 and T120, suggesting that most degradation was completed during the DOC RD and SD stages.

FT-ICR-MS analysis showed the details of the RDOC production process at the molecular level. The number of MFs was 1826 higher in T0 than in C0, suggesting that DOC released by *S. japonica* contained new organic matter that does not exist in natural water. In addition, the $Mass_{wa}$ was 18 Da lower in T0 than in C0, suggesting that the new matter was mainly low molecular weight organic matter. N/C_{wa} and S/C_{wa} were 75% and 143% higher, respectively, and CHON-, CHOS-, CHOSP-, and CHONS- were 17%, 75%, 58%, 347%, higher, respectively, in T0 than in C0 (Table 1). The variation in the molecular composition stated above indicates that the DOC released by *S. japonica* provided organic molecules containing nitrogen and sulfur (Chen et al., 2020). In nature, organic molecules containing nitrogen and sulfur mainly originate from proteins, amino acid, and polypeptides, and this may be explained by the molecular composition of C3 in FDOM. The DOC released by *S. japonica* decreased the DBE_{wa} by 18% and $Almod_{wa}$ by 13%; these factors represent the degree of unsaturation and aromaticity, respectively (Table 2). This means that DOC released by *S. japonica* increased the composition of labile DOC (Wada et al., 2008; Gao et al., 2021). During the degradation in the RD and SD stages, DBE_{wa} and $Almod_{wa}$ increased by 22% and 29%, respectively, meaning that degradation produced refractory components. Meanwhile, H/C_{wa} decreased by 15% and O/C_{wa} increased by 20%, which suggested that the degradation process is similar to the chemical reaction of oxidative dehydrogenation. In the initial 2 months of degradation, the number of MFs and $Mass_{wa}$ increased by 1442 and 26 Da, respectively, but changed little during the last 2 months of degradation. This suggests that most of the degradation occurred during the initial 2 months. In addition, degradation produced high molecular weight organic matter and increased the molecular diversity in the treatment.

Van Krevelen diagrams reveal more details of the composition variation during oxidative dehydrogenation. *S. japonica* releasing DOC produced two groups of MFs (O/C > 0.5 and H/C > 1.5), which represented the saturated (refractory component) and reducible (labile component) composition, respectively (Figure 6A) (Cai et al., 2019). As the reducible components were degraded, two more groups of saturated components were produced (O/C > 0.8 and H/C < 1.5) during the initial 2 months (Figure 6B). At the end of the experiment, the increasing peak intensities and declining peak intensities almost overlapped, indicating that degree of saturation in the DOC changed little in the last 2 months of experiment (Figure 6C). Moreover, nearly 80% of the MFs in the DOC were shared between day 60 and day 120 of treatment (Figure S3).

The chemical reaction of oxidative dehydrogenation requires a high temperature, well above 100°C. However, this same reaction

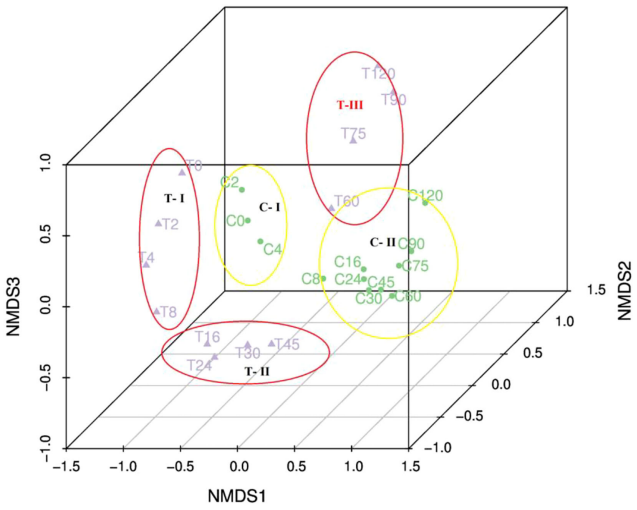

FIGURE 4
Nonmetric multidimensional scaling ordination of the bacterial communities in the 120-day degradation experiment.

can be mediated by bacteria at room temperature and in darkness. The bacterial community succession was divided into 3 groups (T-I, T-II, and T-III) during treatment, but these groups did not completely agree with the stages representing the change in DOC (RD, SD, and RS). The RD stage included all of T-I and a part of T-II. The SD stage included a part of T-II and T-III. Perhaps the bacterial community was extremely sensitive to variations in the environment, such as metabolic substrate and dissolved oxygen (DO) (Sun et al., 2012). At the start of experiment, kelp introduced abundant organic matter containing sulfur (Chen et al., 2020), and maintained 80–100 times more bacterial biomass in treatment compared with the control during the RD stage (Figure 1). The rapid consumption of DOC in the treatment group resulted in depletion of DO (Figure S5). Anaerobic and sulfur-degrading Bacteroidia and Campylobacteria became the dominant classes in T-I (Voordouw et al., 1996; Hu et al., 2016). Continuous degradation of DOC sustained the anaerobic environment in T-II, and Bacteroidia remained the dominant class in T-II. The Alphaproteobacteria class mainly comprised the Rhodobacteraceae family, which is an important sulfur-degrading family, and this class became dominant in T-II (Figure S6) (Pujalte et al., 2014). In T-III, at the completion of DOC degradation, the aerobic Iodidimonadaceae family belonging to the Alphaproteobacteria class became the dominant family (Lino et al., 2016). Generally, bacterial rapidly consume labile DOC components, resulting in an anoxic environment during treatment in T-I and T-II stages (Figure S5), and the bacterial community changes rapidly with variations in the environment (Figure 4; Figures S4, S6). RDOC is

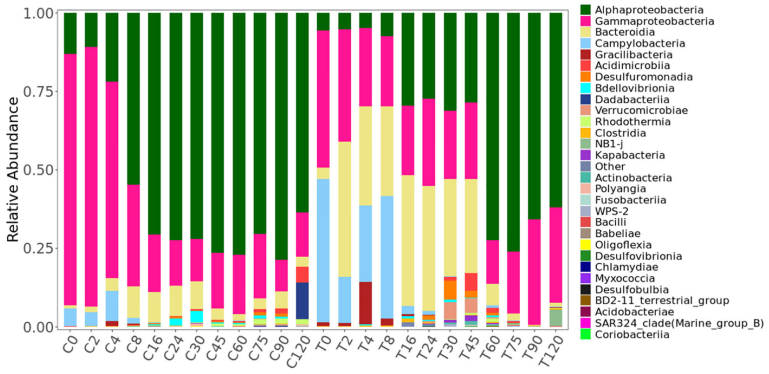

FIGURE 5
Variations in the bacterial community at the class level during the 120-day degradation of DOC released by *Saccharina japonica* and that in natural seawater.

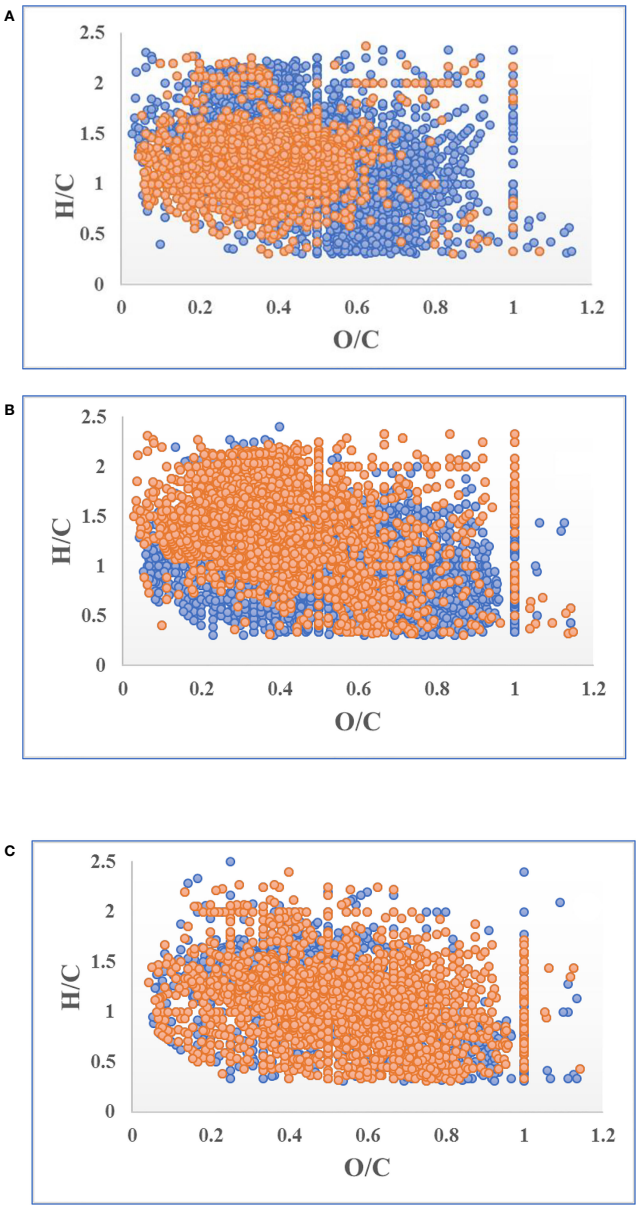

FIGURE 6
Variation in the normal peak intensity of molecular formulas (MFs) during the 120-day degradation. Blue and orange points represent increased and decreased peak intensities respectively. **(A)** Variation of MF peak intensity in T0 compared to C0; **(B)** variation of MF peak intensity in T60 compared to T0; **(C)** variation of MF peak intensity in T120 compared to T60.

the final product of degradation that then remains in the water (Figures 2, 3).

In this experiment, DO was an important factor for the succession of the bacterial community because of the limited air exchange. In contrast, DO may be ample in natural waters as wind and waves increase air exchange. Although the environmental conditions are great different, a reaction similar to oxidative dehydrogenation driven by bacteria was observed in the ocean (Medeiros et al., 2015). In the deep sea, which is the final reservoir for DOC degraded by bacteria, DOC had higher O/C_{wa} and lower H/C_{wa} than that in the surface DOC. It may indicate that RDOC producing process by interaction between DOC released by cultured kelp (*Saccharina japonica*) and the bacterial community is similar as the RDOC producing process in natural condition. This study may help to reveal the potential to increase marine carbon sequestration using macroalgae culture.

5 Conclusion

The present study shows that DOC released by *S. japonica* was rapidly degraded into RDOC by bacteria. After 2 months, LDOC components in DOC were degraded completely, and 5% of this DOC was transformed into RDOC. Although culture biomass will be harvested during the actual kelp culturing process, an estimated 1–2% of the net primary production can still be sequestrated as RDOC. This suggests that sequestrating carbon by macroalgae culture is feasible.

Data availability statement

The datasets presented in this study can be found in online repositories. The names of the repository/repositories and accession number(s) can be found below: https://www.ncbi.nlm.nih.gov/- PRJNA855139. Further inquiries can be directed to the corresponding authors.

Author contributions

MZ and HQ contributed to data curation, visualization, writing – original draft, validation. ZW and BL performed data curation and visualization. YM contributed to writing – review and editing and resource. All authors contributed to the article and approved the submitted version.

Funding

This study was supported by the National Natural Science Foundation of China (42176159) and Yantai Science and Technology Innovation and Development Planning (2020MSGY059).

Conflict of interest

The authors declare that the research was conducted in the absence of any commercial or financial relationships that could be construed as a potential conflict of interest.

Publisher's note

All claims expressed in this article are solely those of the authors and do not necessarily represent those of their affiliated organizations, or those of the publisher, the editors and the reviewers. Any product that may be evaluated in this article, or claim that may be made by its manufacturer, is not guaranteed or endorsed by the publisher.

Supplementary material

The Supplementary Material for this article can be found online at: https://www.frontiersin.org/articles/10.3389/fmars.2022.985548/full#supplementary-material

References

Abdullah, M. I., and Fredriksen, S. (2004). Production, respiration and exudation of dissolved organic matter by the kelp *Laminaria hyperborea* along the west coast of Norway. *J. Mar. Biol. Assoc. Uk* 84, 887–894. doi: 10.1017/S002531540401015Xh

Amaral, V., Ortega, T., Romera-Castillo, C., and Forja, J. (2021). Linkages between greenhouse gases (CO_2, CH_4, and N_2O) and dissolved organic matter composition in a shallow estuary. *Sci. Total Environ.* 788, 147863. doi: 10.1016/j.scitotenv.2021.147863

Bittar, T. B., Vieira, A. A., Stubbins, A., and Mopper, K. (2015). Competition between photochemical and biological degradation of dissolved organic matter from the cyanobacteria microcystis aeruginosa. *Limnol Oceanogr* 60, 1172–1194. doi: 10.1002/lno.10090

Bolyen, E., Rideout, J. R., Dillon, M. R., Bokulich, N. A., Abnet, C. C., and Al-Ghalith, G. A., et al. (2019). Reproducible, interactive, scalable and extensible microbiome data science using QIIME 2. *Nat. Biotechnol.* 37, 852–857. doi: 10.1038/s41587-019-0209-9

Cai, R., Zhou, W., He, C., Tang, K., Guo, W., Shi, Q., et al. (2019). Microbial processing of sediment-derived dissolved organic matter: implications for its subsequent biogeochemical cycling in overlying seawater. *J. Geophys Res-Biogeo* 124 (11), 3479–3490. doi: 10.1029/2019JG005212

Callahan, B. J., McMurdie, P. J., Rosen, M. J., Han, A. W., Johnson, A. J. A., and Holmes, S. P. (2016). DADA2: High-resolution sample inference from illumina amplicon data. *Nat. Methods* 13, 581–583. doi: 10.1038/nmeth.3869

Chen, J., Li, H. M., Zhang, Z. H., He, C., Shi, Q., Jiao, N., et al. (2020). DOC dynamics and bacterial community succession during long-term degradation of *Ulva prolifera* and their implications for the legacy effect of green tides on refractory DOC pool in seawater. *Water Res.* 185, 116286. doi: 10.1016/j.watres.2020.116268

DeVries, T., Holzer, M., and Primeau, F. (2017). Recent increase in oceanic carbon uptake driven by weaker upper-ocean overturning. *Nature* 542, 215–218. doi: 10.1038/nature21068

Dittmar, T., Koch, B., Hertkorn, N., and Kattner, G. (2008). A simple and efficient methodfor the solid-phase extraction of dissolved organic matter (SPE-DOM) from seawater. *Limnol. Oceanogr. Meth.* 6 (6), 230–235. doi: 10.4319/lom.2008.6.230

Dorte, K. J., and Carlos, M. D. (2016). Substantial role of macroalgae in marine carbon sequestration. *Nat. Geosci* 9, 737–742. doi: 10.1038/ngeo2790

FAO (2021). "FAO yearbook," in *Fishery and aquaculture statistics 2019/FAO annuaire*. doi: 10.4060/cb7874t

Fu, Q. L., Fujii, M., and Riedel, T. (2020). Development and comparison of formula assignment algorithms for ultrahigh-resolution mass spectra of natural organic matter. *Anal. Chim. Acta* 1125, 247–257. doi: 10.1016/j.aca.2020.05.048

Gao, Z., and Guéguen, C. (2018). Distribution of thiol, humci substances and colored dissolved organic matter during the 2015 Canadian Arctic GEOTRACES cruises. *Mar. Chem.* 203, 1–9. doi: 10.1016/j.marchem.2018.04.001

Gao, Y., Zhang, Y., Du, M., Lin, F., Jiang, W., Li, W., et al. (2021). Dissolved organic carbon from cultured kelp *Saccharina japonica*: production, bioavailability,

and bacterial degradation rates. *Aquacult Env. Interac* 13, 101–110. doi: 10.3354/aei00393

Hama, T., Yanagi, K., and Hama, J. (2004). Decrease in molecular weight of photosynthetic products of marine phytoplankton during early diagenesis. *Limnol Oceanogr* 49, 471–481. doi: 10.4319/lo.2004.49.2.0471

Hill, R., Bellgrove, A., Macreadie, P. I., Petrou, K., Beardall, J., Steven, A., et al. (2015). Can macroalgae contribute to blue carbon? an Australian perspective. *LIMNOL OCEANOGR* 60, 1689–1706. doi: 10.1002/lno.10128

Hu, X., Du, H., Ren, G., and Xu, Y. (2016). Illuminating anaerobic microbial community and cooccurrence patterns across a quality gradient in Chinese liquor fermentation pit muds. *Appl. Environ. Microb.* 82, 8. doi: 10.1128/AEM.03409-15

IPCC (2020) *Changing ocean, marine ecosystems, and dependent communities*. Available at: https://www.ipcc.ch/srocc/chapter/chapter-5/.

Jiao, N. Z., Herndl, G. J., Hansell, D. A., Benner, R., Kattner, G., Wilhelm, S. W., et al. (2010). Microbial production of recalcitrant dissolved organic matter: long term carbon storage in the global ocean. *Nat. Rev. Microbiol.* 8, 593–599. doi: 10.1038/nrmicro2386

Koch, B. P., and Dittmar, T. (2006). From mass to structure: an aromaticity index for high-resolution mass data of natural organic matter. *Rapid Commun. Mass Sp* 20 (5), 926–932. doi: 10.1002/rcm.2386

Koch, B. P., Kattner, G., Witt, M., and Passow, U. (2014). Molecular insights into the microbial formation of marine dissolved organic matter: recalcitrant or labile? *Biogeosciences* 11, 4173–4190. doi: 10.5194/bg-11-4173-2014,201

Krause-Jensen, D., and Duarte, C. M. (2016). Substantial role of macroalgae in marine carbon sequestration. *Nat. Geosci* 9, 737–742. doi: 10.1038/ngeo2790

Kulkarni, H., Mladenov, N., and Datta, S. (2018). Effects of acidification on the optical properties of dissolved organic matter from high and low arsenic groundwater and surface water. *Sci. Total Environ.* 653, 1326–1332. doi: 10.1016/j.scitotenv.2018.11.040

Lønborg, C., Middelboe, M., and Brussaard, C. P. (2013). Viral lysis of micromonas pusilla: impacts on dissolved organic matter production and composition. *Biogeochemistry* 116 (1–3), 231–240. doi: 10.1007/s10533-013-9853-1

Lino, T., Ohkuma, M., Kamagata, Y., and Amachi, S. (2016). *Iodidimonas muriae* gen. nov., sp. nov., an aerobic iodide-oxidizing bacterium isolated from brine of a natural gas and iodine recovery facility, and proposals of *Iodidimonadaceae* fam. nov., *Iodidimonadales* ord. nov., *Emcibacteraceae* fam. nov. and *Emcibacterales* ord. nov. *Int. J. Syst. Evol. Micr* 66, 12. doi: 10.1099/ijsem.0.001462

Mahmood, T., Fang, J., Jiang, Z., Ying, W., and Zhang, J. (2017). Seasonal distribution, sources and sink of dissolved organic carbon in integrated aquaculture system in coastal waters. *Aquacult Int.* 25, 71–85. doi: 10.1007/s10499-016-0014-0

Manikandan, B., Thomas, A. M., Shetye, S. S., Balamurugan, S., Mohandass, C., and Nandakumar, K. (2021). Macroalgal release of dissolved organic carbon in coral reef and its interaction with the bacteria associated with the coral *Porites lutea*. *Environ. Sci. pollut. R* 28, 66998–67010. doi: 10.1007/s11356-021-15096-7

Martin, M. (2011). Cutadapt removes adapter sequences from high-throughput sequencing reads. *EMBnet. J.* 17 (1), 10. doi: 10.14806/ej.17.1.200

Medeiros, P. M., Seidel, M., Powers, L. C., Dittmar, T., Hansell, D. A., and Miller, W. L. (2015). Dissolved organic matter composition and photochemical transformations in the northern north pacific ocean. *Geophys Res. Lett.* 42 (3), 863–870. doi: 10.1002/2014GL062663

NASEM (2019). *Negative emissions technologies and reliable sequestration: A research agenda* (Washington, DC: The National Academies Press). doi: 10.17226/25259

NASEM (2021). *A research strategy for ocean-based carbon dioxide removal and sequestration* (Washington, DC: The National Academies Press). doi: 10.17226/26278

Ortega, A., Geraldi, N. R., Alam, I., Kamau, A. A., Acinas, S. G., Logares, R., et al. (2019). Important contribution of macroalgae to oceanic carbon sequestration. *Nat. Geosci* 12 (9), 748–754. doi: 10.1038/s41561-019-0421-8

Post, W. H., Peng, T. H., Emanuel, W. R., King, A. W., Dale, V. H., and DeAngelis, D. L. (1990). The global carbon cycle. *Am. Sci.* 78(4), 310–326.

Pujalte, M. J., Lucena, T., María, A., et al. (2014). "The family rhodobacteraceae," in *The prokaryotes* (Berlin: Springer), 439–512, ISBN: . doi: 10.1007/978-3-642-30197-1_377

Reed, D. C., Carlson, C. A., Halewood, E. R., Nelson, J. C., Harrer, S. L., Rassweiler, A., et al. (2015). Patterns and controls of reef-scale production of dissolved organic carbon by giant kelp *Macrocystis pyrifera*. *limnol oceanogr* 60 (6), 1996–2008. doi: 10.1002/lno.10154

Sabine, C. L., Feely, R. A., Gruber, N., Key, R. M., Lee, K., Bullister, J. L., et al. (2004). The oceanic sink for anthropogenic CO_2. *Science* 305, 367–371. doi: 10.1126/science.1097403

Schmidt, F., Koch, B. P., Elvert, M., Schmidt, G., Witt, M., and Hinrichs, K. (2011). Diagenetic transformation of dissolved organic nitrogen compounds under contrasting sedimentary redox conditions in the black Sea. *Environ. Sci. Technol.* 45 (12), 5223–5229. doi: 10.1021/es2003414

Sun, M. Y., Dafforn, K. A., Brown, M. V., and Johnston, E. L. (2012). Bacterial communities are sensitive indicators of contaminant stress. *Mar. pollut. Bull.* 64 (5), 1029–1038. doi: 10.1016/j.marpolbul.2012.01.035

Voordouw, G., Armstrong, S. M., Reimer, M. F., Fouts, B., Telang, A. J., Shen., Y., et al. (1996). Characterization of 16S rRNA genes from oil field microbial communities indicates the presence of a variety of sulfate-reducing, fermentative, and sulfide-oxidizing bacteria. *Appl. Environ. Microb.* 62 (5), 1623–1629. doi: 10.1128/aem.62.5.1623-1629.1996

Wada, S., Aoki, M. N., Mikami, A., Komatsu, T., Tsuchiya, Y., Sato, T., et al. (2008). Bioavailability of macroalgal dissolved organic matter in seawater. *Mar. Ecol. Prog. Ser.* 370, 33–44. doi: 10.3354/meps07645

Wada, S., Aoki, M. N., Tsuchiya, Y., Sato, T., Shinagawa, H., and Hama, T. (2007). Quantitative and qualitative analyses of dissolved organic matter released from *Ecklonia cava* kjellman, in oura bay, shimoda, izu peninsula, Japan. *J. Exp. Mar. Biol. Ecol.* 349, 344–358. doi: 10.1016/j.jembe.2007.05.024

Wada, S., and Hama, T. (2013). The contribution of macroalgae to the coastal dissolved organic matter pool. *Estuar. Coast. Shelf S* 129, 77–85. doi: 10.1016/j.ecss.2013.06.007

Watanabe, K., Yoshida, G., Hori, M., Umezawa, Y., Moki, H., and Kuwae, T. (2020). Macroalgal metabolism and lateral carbon flows can create significant carbon sinks. *Biogeosciences* 17, 2425–2440. doi: 10.5194/bg-17-2425-2020

Yang, L., Chen, C. T. A., Hong, H., Chang, Y. C., and Lui, H. K. (2015). Mixing behavior and bioavailability of dissolved organic matter in two contrasting subterranean estuaries as revealed by fluorescence spectroscopy and parallel factor analysis. *Estuar. Coast. Shelf S* 166, 161–169. doi: 10.1016/j.ecss.2014.10.018

Zhang, T., and Wang, X. (2017). Release and microbial degradation of dissolved organic matter (DOM) from the macroalgae *Ulva prolifera*. *Mar. pollut. Bull.* 125 (1-2), 192–198. doi: 10.1016/j.marpolbul.2017.08.029

Zhao, Z., Gonsior, M., Schmitt-Kopplin, P., Zhan, Y., Zhang, R., Jiao, N., et al. (2019). Microbial transformation of virus-induced dissolved organic matter from picocyanobacteria: coupling of bacterial diversity and DOM chemodiversity. *ISME J.* 13 (10), 2551–2565. doi: 10.1038/s41396-019-0449-1

frontiers | Frontiers in Marine Science

TYPE Original Research
PUBLISHED 29 September 2022
DOI 10.3389/fmars.2022.989270

OPEN ACCESS

EDITED BY
Keisuke Nakayama,
Kobe University, Japan

REVIEWED BY
Shinichiro Yano,
Kyushu University, Japan
Manab Kumar Dutta,
National Centre for Earth Science Studies, India

*CORRESPONDENCE
Tatsuku Tokoro
tokoro.tatsuki@nies.go.jp

SPECIALTY SECTION
This article was submitted to Marine Biogeochemistry, a section of the journal Frontiers in Marine Science

RECEIVED 08 July 2022
ACCEPTED 05 September 2022
PUBLISHED 29 September 2022

CITATION
Tokoro T and Kuwae T (2022) Air-water CO_2 and water-sediment O_2 exchanges over a tidal flat in Tokyo Bay.
Front. Mar. Sci. 9:989270.
doi: 10.3389/fmars.2022.989270

Air-water CO_2 and water-sediment O_2 exchanges over a tidal flat in Tokyo Bay

Tatsuku Tokoro[1,2*] and Tomohiro Kuwae[2]

[1]Center for Global Environmental Research, National Institute for Environmental Studies, Tsukuba, Japan, [2]Coastal and Estuarine Environment Research Group, Port and Airport Research Institute, Yokosuka, Japan

Despite the potential for carbon storage in tidal flats, little is known about the details of relevant processes because of the complexity of intertidal physical and chemical environments and the uniqueness of the biota. We measured air-water carbon dioxide (CO_2) fluxes and water-sediment oxygen (O_2) fluxes over a tidal flat in Tokyo Bay by the eddy covariance method, which has the potential to facilitate long-term, broad-scale, continuous monitoring of carbon flows in tidal flats. The results indicated that throughout the tidal flat in Tokyo Bay, CO_2 was taken up from the atmosphere at a rate of 6.05 ± 7.14 (mean ± SD) mmol m^{-2} $hour^{-1}$, and O_2 was taken up from the water into the sediment at a rate of 0.62 ± 1.14 (mean ± SD) mmol m^{-2} $hour^{-1}$. The fact that the CO_2 uptake rate was about 18 times faster than the previously reported average uptake rate in the whole area of Tokyo Bay was attributable to physical turbulence in the water column caused by bottom friction. Statistical analysis suggested that light intensity and water temperature were the major factors responsible for variations of CO_2 and O_2 exchange, respectively. Other factors such as freshwater inputs, atmospheric stability, and wind speed also affected CO_2 and O_2 exchange. High rates of O_2 uptake from the water into the sediment surface and high rates of atmospheric CO_2 uptake into the water column occurred simultaneously (R^2 = 0.44 and 0.47 during day and night, respectively). The explanation could be that photosynthetic consumption of CO_2 and production of O_2 in the water column increased the downward CO_2 (air to water) and O_2 (water to sediment) fluxes by increasing the concentration gradients of those gases. Resuspension of sediment in the low-O_2 layer by physical disturbance would also increase the O_2 concentration gradient and the O_2 flux in the water.

KEYWORDS

CO_2 exchange, O_2 exchange, tidal flat, eddy covariance, Tokyo Bay

Introduction

Coastal marine areas are important sites of carbon storage because photosynthetic rates are high, and sedimentation and burial of carbon sequesters carbon from the atmosphere for long periods of time (Mateo et al., 1997; Mcleod et al., 2011). Quantification of carbon fluxes in coastal waters is therefore critical to identifying effective strategies for mitigating the adverse effects of anthropogenic CO_2 emissions. Recent studies have compared carbon accumulation rates and have concluded that the rates in several coastal areas are ten times larger than the rates in the open ocean (e.g., Nellemann et al., 2009). However, there is a paucity of analyses of atmospheric CO_2 exchange rates in coastal areas compared with the numerous studies of carbon accumulation rates in sediments (Frankignoulle, 1988; Kayanne et al., 1995; Borges et al., 2005; Tokoro et al., 2008; Tokoro et al., 2014). Those studies have indicated that autotrophic production in coastal ecosystems results in net CO_2 absorption from the atmosphere and counteracts the tendency of those ecosystems to emit CO_2 produced by the decomposition of organic matter from land runoff. However, precise estimation of atmospheric CO_2 exchange in coastal areas is challenging because of the complexity of the spatiotemporal variations of coastal CO_2 exchange.

Carbon accumulation rates in tidal flats (10-120 g C m^{-2} $year^{-1}$ × 0.13 million km^2, (Widdows et al., 2004; Sanders et al., 2010; Endo and Otani, 2019; Murray et al., 2019) have been estimated to be on the same order of magnitude as the rates associated with other vegetated coastal habitats like salt marshes (151 g C m^{-2} $year^{-1}$ × 0.4 million km^2, Nellemann et al., 2009). However, despite numerous measurements, little is known about the details of carbon flows in tidal flats because of the uniqueness of the biota, the complexity of the carbon flows, the intertidal conditions, and inputs of brackish water. Because tidal flats located near human population centers are easily affected by anthropogenic impacts associated with eutrophication, pollution, and land reclamation, analysis of interactions between carbon fluxes and human activities is therefore an urgent issue.

Evaluation of the interactions between atmospheric CO_2 and carbon fluxes in tidal flats is especially difficult. The mechanism of exchange is quite different between periods of sediment submergence (air–water) and exposure (air–sediment). Furthermore, the estimation of air–water CO_2 fluxes using empirical wind-driven equations, which have been used in previous studies of other coastal areas and the ocean, is likely to be inaccurate because air–water CO_2 fluxes are likely to be greatly affected by tidal-driven effects (e.g., O'connor and Dobbins, 1958; Raymond and Cole, 2001; Borges et al., 2004). Therefore, direct measurement techniques have been used to estimate atmospheric CO_2 exchange rates over tidal flats. The chamber method is a direct measurement technique that estimates CO_2 exchanges from changes of CO_2 density inside a chamber on the surface of the water or sediment. The method can be applied to both air–water and air–sediment fluxes in tidal flats (Middelburg et al., 1996; Migné et al., 2002; Spilmont et al., 2005; Klaassen and Spilmont, 2012; Sasaki et al., 2012; Otani and Endo, 2019). However, the temporal duration and spatial range of the chamber method are limited because the measurement area is usually less than 1 m^2 and the hand-operation is required for each measurement. Therefore, a comprehensive analysis of atmospheric CO_2 exchange over tidal flats is still difficult with the method. The eddy covariance (EC) method is another direct measurement method and is applicable to measurements without submerged/exposed conditions. Although the measurement area depends on several conditions like the fluctuation of wind direction, the CO_2 exchange in a scale of several hundred meters to several kilometers can be measured without any hand-operation. Although use of the EC method is costly because the equipment is expensive and the correction procedure is complex, the EC method has been used in several studies to measure CO_2 fluxes over tidal flats because the fluxes are integrated over large spatiotemporal scales (Zemmelink et al., 2009; Polsenaere et al., 2012).

Water-sediment O_2 exchange is important proxy for the analysis of inorganic and organic carbon dynamics in aquatic ecosystems because O_2 exchange usually relates to CO_2 exchange in the mole ratio of near 1:1 through photosynthetic activities, respiration and organic matter decomposition. Although the measurement of atmospheric O_2 exchange has not been reduced to practice due to the difficulty in the measurement with enough sampling rate, the EC method has been applied for the measurement of water-sediment exchange (Kuwae et al., 2006; Berg et al., 2022). The EC method for O_2 exchange has an advantage of the temporal duration and spatial range as well as for CO_2 exchange. Additionally, the EC method can measure O_2 exchange directly and avoid altering the natural conditions (e.g., flow, light and metabolism) compared with other methods using incubated cores or benthic chambers.

In this study, we used the EC method to measure atmospheric CO_2 exchange over a tidal flat in Tokyo Bay. We used other EC devices to measure exchange of O_2 between the water and sediment for comparison with the CO_2 exchange and determined whether biological activities in the water and sediment were related. Our goal was to identify the factors that regulated those fluxes. Most of the tidal flats in Tokyo Bay have disappeared because of urban development and reclamation of coastal land during the last century, and measurements in the remaining tidal flats were therefore important for the prediction of how future human activities will likely affect conditions in the bay.

Materials and methods

In situ measurements were conducted over the Banzu tidal flat in Tokyo Bay during February 2011. The Banzu tidal flat is an intertidal sand flat with an area of 7.6 km^2 and a shallow slope of 1/1000 situated on the eastern shore of Tokyo Bay, Japan (Figure 1). The sediments are fine sand flat with a median grain size of 170-190 μm (Uchiyama, 2007). The tidal range during the measurement was 0.7-1 m and about half of the area was submerged at high tide. There are no macrophytes on the tidal flat, and microphytobenthos on the sediment (2200 mg Chl-a m^{-3} and 90 mg C m^{-2}, Hosokawa, 1999) account for most of the primary production. The biomass of the secondary producers was larger than of the primary producers and was reported to be 1500 and 20,000-40,000 mg C m^{-2} in September as of bacteria and macrobenthos (mostly bivalves), respectively (Hosokawa, 1999). Although the biomass of macrobenthos in winter was reported to be one-tenth the mass of in summer, the secondary producers in the tidal flat were considered to exceed the primary producers in the biomass through the year. The large biomass of secondary producers indicates a large organic carbon fixation from plankton or detritus inflowed from the surrounding areas like Tokyo Bay. This suggested that estimation of atmospheric CO_2 exchange without direct measurements should be difficult due to large carbon input come from outside the tidal flat. Although the tidal flat consists of an estuarine delta connected to the Obitsu River (watershed area: 273.2 km^2), water exchange would be driven mainly by tidal exchange because the flow rate was far smaller than the tidal current and could not be quantified by the former observations (e.g., Uchiyama, 2007). The water of Tokyo Bay has been reported to be an atmospheric CO_2 sink because of the photosynthetic activity of phytoplankton (10-20 mg Chl-a m^{-3}) which is enhanced by sewage inputs from the surrounding urban area (Kubo et al., 2017; Tokoro et al., 2021).

The EC method for measuring atmospheric CO_2 exchange determines vertical CO_2 fluxes within the atmosphere by measurements at high frequency (10–20 Hz) of eddy movement vertically and atmospheric CO_2 density. The EC method can estimate atmospheric CO_2 exchange from measurements in air at an altitude of more than several meters and is thus applicable to measurements in the intertidal zone. The EC method also enables continuous and automatic measurements to be made over broad spatiotemporal scales. Comprehensive analysis is thus easier with the EC method than with other onsite measurement methods. We used the following equation to calculate CO_2 exchange (F; positive and negative values mean atmospheric CO_2 efflux and influx from/to water or sediment, respectively) every 30 minutes:

$$F = \overline{\rho_c{}' w'} \cdot F_1 + \mu \frac{\rho_c}{\rho_d} \overline{\rho_v' w'} \cdot F_2 + \rho_c \left(1 + \mu \frac{\rho_v}{\rho_d}\right) \frac{\overline{T_a{}' w'}}{T_a} \cdot F_2 \quad (1)$$

where F_1 and F_2 are the transfer coefficients that correct the frequency attenuation of the CO_2 exchange for the response time of the sensor, path-length averaging, sensor separation, signal processing, and the averaging time of each measurement (Massman, 2000). The first term on the right-hand side of Eq. 1 is the product of F_1 and the uncorrected CO_2 exchange calculated as the covariance of the CO_2 density ρ_c and vertical

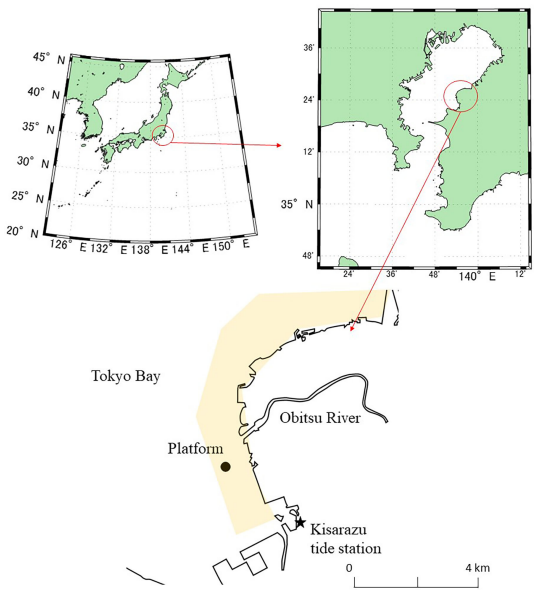

FIGURE 1
Location of the measurement site (Banzu tidal flat, Tokyo Bay, Japan). The yellow shading indicates the area of the tidal flat during low tide.

wind speed w (the bar and prime symbols indicate the mean and the deviation from the mean, respectively). The wind speed was corrected using a double rotation to make the average vertical wind speed zero during the 30-min time interval (Lee et al., 2004). The second and third terms are the product of F_2 and the Webb–Pearman–Leuning correction for the fluxes of latent heat and sensible heat, respectively (Webb et al., 1980). These terms correct for the change of air volume due to changes of moisture and temperature, respectively. The other symbols in Eq. 1 are as follows: ρ_d, dry air density; ρ_v, water vapor density; T_a, air temperature; and μ, ratio of molar weight of dry air to water vapor.

Although the EC method facilitates coastal measurements, the estimated fluxes have been associated with large uncertainties, especially for air–water CO_2 fluxes (Vesala et al., 2012; Blomquist et al., 2014; Kondo et al., 2014; Tokoro et al., 2014; Ikawa and Oechel, 2015). Several studies reported that these uncertainties were caused by the spatiotemporal heterogeneities of water temperature or turbulence conditions (Rutgersson and Smedman, 2010; Mørk et al., 2014). Although several studies have suggested methods to correct air–water CO_2 fluxes estimated by the EC method (Prytherch et al., 2010; Edson et al., 2011; Landwehr et al., 2014; Tokoro and Kuwae, 2018), we made the following simple corrections during the post-processing procedure because the measurement in this study included air–sediment CO_2 fluxes that were not covered by the above correction methods.

We used two operations to detrend measurement parameters and exclude CO_2-exchange outliers in this study. Detrending is a necessary procedure in the EC method because long-term variations that are unrelated to CO_2 eddy movement must be removed. The three main types of detrending methods involve use of mean values, linear approximation, and high-pass (recursive) filtering. The appropriate method depends on the complexity of the long-term trend. In this study, we used high-pass filtering because the temporal changes in the tidal flat were complex. High-pass filtering was carried out with an exponential moving average as follows:

$$x_i = \alpha \cdot x_{i-1} + (1 - \alpha) \cdot y_i \qquad (2)$$

where x_i and y_i are the filtered and original datum at time t_i. α is the time constant of the filtering and was set to 1.7×10^{-3} seconds in accord with McMillen (1988). We used the median absolute deviation (MAD) of the CO_2 exchange as a criterion for excluding outliers (Rousseeuw and Croux, 1993).

$$MAD = median\{|X_i - median(X)|\} \qquad (3)$$

where X_i is the original datum. A scaled MAD ($=1.4826\times MAD$) was used as an alternative to the standard deviation as an outlier criterion to avoid an outlier effect on the mean and standard deviation. This criterion was suitable for the outlier exclusion of EC data because the outlier criterion was an order of magnitude larger than the average value. In this study, a CO_2 exchange rate that deviated from the median of all the CO_2 exchange data by more than three times the scaled MAD was identified as an outlier and was excluded.

The EC method for O_2 exchange between the water and sediment was basically the same as the EC method for CO_2 exchange. The O_2 exchange was determined from the covariance of O_2 and the vertical current velocity because the change of water volume with temperature and moisture could be ignored. A sampling rate somewhat more than several Hz would be enough for O_2 and current velocity measurements because the water eddy transport at a frequency of 0.3–1.4 Hz would be the main contribution to O_2 exchange according to previous studies (Kuwae et al., 2006; Berg et al., 2022). In addition, the transfer coefficients (F_1 and F_2 in Eq. 1) could be ignored because any related parameter such as the path-length averaging distance and sensor separation are far smaller for O_2 EC devices than for CO_2 EC devices. The time lag between the O_2 and current measurement should be corrected because the time response of O_2 is slower than that of other devices like the current velocimeter. The details of the time lag correction have been described by Kuwae et al. (2006). The post-processing procedure of detrending and outlier exclusion were applied using the linear approximation and the scaled MAD, respectively, because the long-term changes of O_2 were less complicated than those of atmospheric CO_2.

CO_2 EC data were recorded every 30 minutes from 17 February 2011 at 11:30 to 24 February 2011 at 22:00. The EC measurement devices for CO_2 were installed on a platform on the tidal flat (35.401°C N, 139.893°C E) where the water depth was about 0.3–1.0 m at high tide during the measurement period (Figure 2). The platform was located near the edge of the tidal flat, and the altitude of the platform was almost zero. The duration of the exposure period was about 11–13 hours during the measurement. We used an open-path CO_2 analyzer (LI-7500; LI-COR) and a 3-D sonic anemometer (CSAT-3, Campbell) for the EC measurement of atmospheric CO_2 density and atmospheric eddy diffusion, including air temperature, respectively. The devices were placed at the top of the platform (about 5 m from the bottom). All EC data were measured at a sampling rate of 20 Hz, and the atmospheric CO_2 exchange was calculated every 30 minutes. The footprint, which is an index of measurement range of the EC measurement, depends on the measurement height, wind speed, atmospheric stability, and the roughness of the measurement site (here, 0.005 m was assumed to be the roughness of the tidal flat). Footprint estimation (Kljun et al., 2004) indicated that 90% of the CO_2 exchange measurement came from< 270 m upwind.

The EC measurements of O_2 were made only from 16:00 on 21 February to 22:30 on 24 February. The O_2 EC measurement devices were set on the platform in a direction perpendicular to the dominant direction of the tidal current to avoid artifacts during measurements (Figure 2). O_2 concentrations were measured with a Clark-type oxygen microelectrode (OX-10,

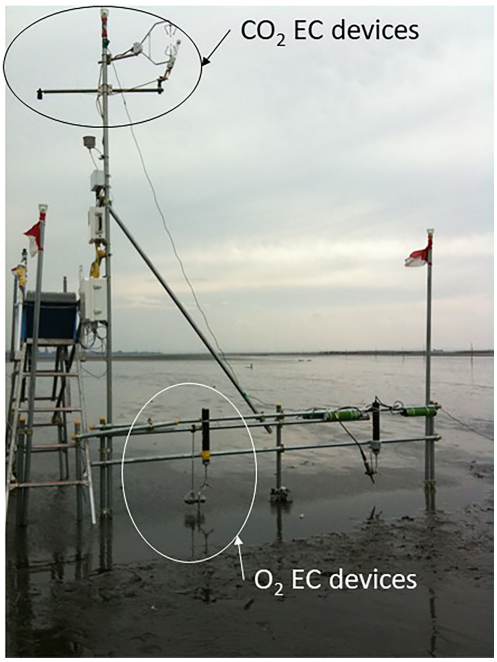

FIGURE 2
Platform for CO_2 EC and O_2 EC.

Unisense). The time for a 90% response of the microelectrode to a O_2 change was less than 0.3 s. Eddy current movements were measured with an acoustic Doppler velocimeter (ADV) (Vector, Nortek). O_2 concentrations and eddy current movements were measured at a rate of 64 Hz as a precaution in the analysis of dissipation rate near sediment (not used in this study), although about 5 Hz is enough for O_2 EC measurements. The O_2 exchange was calculated every 5 minutes, and 30-minute averages were compared to CO_2 EC data. Horizontal current velocities were also measured with the ADV. Because these devices were positioned ~5 cm above the sediment surface, the measurements were invalid when the water depth was less than 5 cm.

The details of the methods used to make the other physical measurements such as water temperature, salinity, water depth, and radiation were as follows. Water temperature and salinity were measured using a thermo-salinometer (Compact-CT, JFE-Advantech) at a sampling interval of one minute. Water depth was measured using an optical O_2 sensor (Rinko, JFE-Advantech) at sampling intervals of 10 minutes; the sensor was also used to calibrate the O_2 microelectrode. Water depths were determined from the raw O_2 sensor data and one-point calibration using the tide data at Kisarazu produced by the Japan Meteorological Agency (Figure 1). Photosynthetically active radiation (PAR) was measured with a quantum sensor (LI-190, LI-COR) installed on the top of the platform (5-m height). The sampling interval for these data was one minute. The devices, except for the PAR sensor, were installed on the platform at a height of ~5 cm above the sediment surface.

The factors that determined atmospheric CO_2 exchange rates were quantified *via* multivariate linear analysis. Because the mechanism of CO_2 exchange on tidal flats was quite different between submerged and exposed periods, the analysis was performed separately for submerged and exposed periods. Measurements made during daytime and nighttime were analyzed separately. The effects of the variables were quantified by the partial regression coefficient of the normalized predictor variables. The predictor variables were normalized by subtracting the mean and dividing by the standard deviation of each predictor variable. The partial regression coefficient was the slope of the relationship between the normalized predictor variables (water temperature, salinity, air temperature, wind speed, PAR, water depth, current speed and O_2) and the dependent variable (CO_2 exchange). Predictor variables with larger coefficients accounted for more of the variance of the dependent variable.

Results

Twenty of the CO_2 exchange data were excluded because they were outliers based on a scaled *MAD* of 6.77 mmol m^{-2} $hour^{-1}$; the remaining 338 data were used to determine atmospheric CO_2 exchange rates over the Banzu tidal flat

(Figure 3). The CO_2 exchange rate (−6.05 ± 7.14 mmol m^{-2} $hour^{-1}$, mean ± 1SD) indicates that the tidal flat was an atmospheric CO_2 sink during the measurement period. The CO_2 exchange during submerged periods (here, water depth > 0.05 m) and exposed periods were −6.51 ± 6.80 (n = 163) and −5.61 ± 7.43 mmol m^{-2} $hour^{-1}$ (n = 175), respectively. The difference between the CO_2 exchange rates was not significant (t-test, P=0.24). The CO_2 exchange rates during daytime (here, more than 10 µmol quanta m^{-2} s^{-1} PAR) and nighttime were −8.20 ± 7.35 (n = 151) and −4.31 ± 6.48 mmol m^{-2} $hour^{-1}$ (n = 187), respectively. The result indicates that the tidal flat absorbed atmospheric CO_2 through the day and the influx of atmospheric CO_2 was significantly greater during daytime than at night (t-test, P=4.2 × 10^{-7}).

After exclusion of five outliers of the O_2 exchange data based on a scaled *MAD* of 1.14 mmol m^{-2} $hour^{-1}$, the remaining 68 data were used to determine a water–sediment O_2 exchange rate of −0.62 ± 1.14 mmol m^{-2} $hour^{-1}$. The fact that the O_2 exchange rate was negative meant that the flux of O_2 was into the sediment. The water–sediment O_2 exchange rates during daytime and nighttime were −0.63 ± 1.16 (n = 26) and −0.64 ± 1.14 mmol m^{-2} $hour^{-1}$ (n = 42), respectively. The difference was not significant (t-test, P=0.97).

The averages and standard deviations of related predictor variables were as follows: water temperature, 9.33 ± 1.70°CC (n = 175); salinity, 28.92 ± 6.11 (n = 167); air temperature, 7.45 ± 2.39°CC (n = 279); wind speed, 5.34 ± 2.47 m s^{-1} (n = 279); PAR, 202 ± 326 µmol quanta m^{-2} s^{-1} (n = 358); water depth, 0.19 ± 0.27 m (n = 357); current speed, 1.08 ± 0.83 cm s^{-1} (n = 88); and dissolved O_2, 10.77 ± 0.83 mg L^{-1} (n = 174) (Figure S1). The winds blew from the northeast during most of the measurement period (February 18–23) but blew from the south on February 17 and 24.

The estimated partial regression coefficients and adjusted coefficient of determination of each analysis are shown in Table 1 (the dependent variable is CO_2 EC exchange rate), and Table 2 shows the analogous data for O_2 EC change. Because of small number of current speed and O_2 data, these variables are not used for the CO_2 EC analysis. No multi-collinearity was detected among the predictor variables; the highest correlation coefficient between the predictor variables was 0.66 (water temperature and air temperature). The analyses were significant for CO_2 and O_2 exchange except for during the night exposed period.

Discussion

Previous studies of CO_2 fluxes over tidal flats have reported both the absorption and release of atmospheric CO_2 (Middelburg et al., 1996; Migné et al., 2002; Spilmont et al., 2005; Klaassen and Spilmont, 2012; Sasaki et al., 2012; Otani and Endo, 2019). The causes of the differences in CO_2 exchange have been thought to include the conditions of vegetation and sediment as well as the season when the measurements were made. The influxes of atmospheric CO_2 measured in this study were consistent with the results of previous EC measurements in the Wadden Sea (Zemmelink et al., 2009), where the sediment

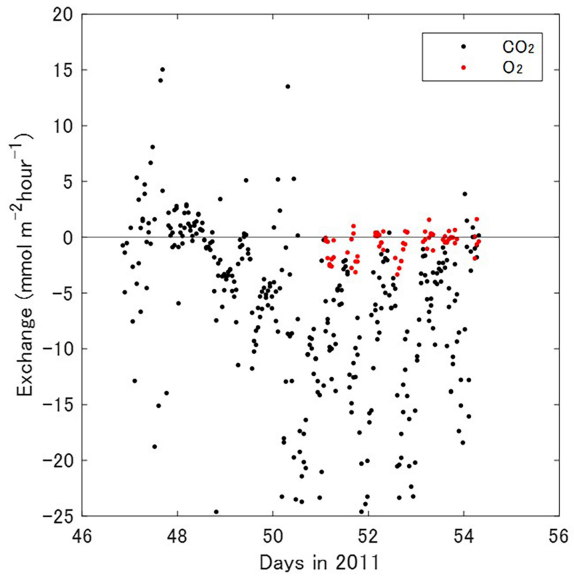

FIGURE 3
Temporal variations of atmospheric CO_2 (black) and O_2 (red) exchange rates measured by EC methods.

TABLE 1 Partial regression coefficients between the predictor variables and atmospheric CO2 exchange.

	Submergence		Exposure	
	Day	Night	Day	night
Water temp. (C^0)	**-0.036**	**-0.91**	**n.d.**	**n.d.**
Salinity (-)	**-0.57**	**-0.56**	**n.d.**	**n.d.**
Air temp. (C^0)	**0.32**	**0.72**	**-0.25**	**0.24**
Wind speed (m s^{-1})	**-0.15**	**-0.73**	**-0.42**	**0.08**
PAR (μmol m^{-2} s^{-1})	**0.58**	**n.d.**	**-0.65**	**n.d.**
Water depth (m)	**0.18**	**0.29**	**n.d.**	**n.d.**
Adjusted R^2	**0.44**	**0.54**	**0.41**	**0.04**

The adjusted coefficients of determination for each multivariate regression analysis are also shown. The shaded area indicates that the coefficient might be zero or opposite in sign or that the analysis itself is not significant. Numbers in bold font indicate the most effective parameter in each analysis.

TABLE 2 Partial regression coefficients and coefficients of determination between the predictor variables and O2 exchange rates.

	Submergence	
	Day	Night
Water temp. (C^0)	**-2.35**	**0.86**
Salinity (-)	**-0.33**	**-1.36**
Air temp. (C^0)	**0.62**	**-0.10**
Wind speed (m s^{-1})	**-1.18**	**-0.77**
PAR (μmol m^{-2} s^{-1})	**0.16**	**n.d.**
Water depth (m)	**0.22**	**-0.16**
DO (mg L^{-1})	**0.04**	**0.71**
Current velocity (cm/s)	**0.07**	**0.02**
Adjusted R^2	**0.97**	**0.51**

Details are the same as in Table 1.

and vegetation are similar to those at this study site. The sediments in the Wadden Sea consist of fine sand and silt, and the grain size is though to be the same or slightly smaller than at this study site. Both sites have communities of bacteria and microphytobenthos on the sediment surface. The CO_2 exchange during the submerged (high tide) and exposed (low tide) periods in the Wadden Sea were −10 and −11 mmol m^{-2} $hour^{-1}$, respectively, during the daytime. The corresponding fluxes during the night were −0.3 and −1.0 mmol m^{-2} $hour^{-1}$, respectively. The seawater flow from the surrounding coastal areas that generally absorbs atmospheric CO_2 is a common background of the CO_2 exchange at both sites. In addition, primary production in the water column and microbial mats on the sediment surface have been hypothesized to be the reason for atmospheric CO_2 absorption in the Wadden Sea (Zemmelink et al., 2009). Our results also indicated that the difference of atmospheric CO_2 exchange was not significant between submerged and exposed periods but was significant between daytime and nighttime. Biological activities in the water column and microbial mats might also be the main factors regulating atmospheric CO_2 exchange at our study site.

The magnitude of the rate of CO_2 uptake from the atmosphere was about 20 times larger than the magnitude of the uptake rate of 0.33 ± 0.31 mmol m^{-2} $hour^{-1}$ in Tokyo Bay reported by Tokoro et al. (2021). The previous study by Zemmelink et al. (2009) in the Wadden Sea has likewise indicated that atmospheric CO_2 absorption measured over the tidal flat was larger than that estimated in nearby European coastal zones (< 1.4 mmol m^{-2} $hour^{-1}$). A similarly large CO_2 exchange in near-shore areas has been observed in several coastal areas by direct measurements using floating chambers (Borges et al., 2004; Tokoro et al., 2008) and by the EC method (Rutgersson and Smedman, 2010; Tokoro et al., 2014; Ikawa and Oechel, 2015; and this study). These studies have indicated that large CO_2 exchange rates could be explained by physical turbulence near the water surface. Physical turbulence near the water surface in an area where the depth of the water exceeds the mixed layer depth is regulated only by wind speed, whereas physical turbulence in shallow areas is enhanced by factors like bottom friction and friction associated with macrophytes. Because of the absence of macrophytes and the turbulent conditions at the study site, we hypothesized that physical turbulence associated with bottom friction was the main reason for the enhancement of gas exchange in our study. Unfortunately, the quantification of the bottom friction effect was impossible in this study because the significant relationships of current speed and water depth to the CO_2 exchange were not confirmed from our measurements (Tables 1, 2). More

measurements of the CO_2 exchange, depth and current speed are required for the precise analysis of atmospheric CO_2 exchange over tidal flats.

The adjusted coefficient of determination indicated that about half of the variance of the CO_2 exchange could be explained by the predictor variables. The exception was the CO_2 exchange when the sediment was exposed at night. The unexplained half of the variance might have been associated with heterogeneity inside the footprint caused by differences of tidal conditions and differences of salinity due to inputs of river water. Nonlinear relationships between the predictor variables and CO_2 exchange as well as errors in EC measurements may have accounted for the rest of the unexplained variance.

The partial regression analysis for the CO_2 EC data showed that salinity and PAR were the most significant regulating factors during submerged conditions and the daytime, respectively (Table 1). The implication was that the input of freshwater and photosynthetic uptake of CO_2 in the water and on the sediment surface regulated atmospheric CO_2 exchange over the tidal flat. The salinity decreased when the water over the tidal flat was shallow. The freshwater presumably came from the Obitsu River, which discharges from the northeast onto the tidal flat (Figure 1). The fact that the prevailing winds blew from the northeast caused part of the footprint to be easily affected by discharges from the Obitsu River. Note that the sign of the PAR coefficient differed between the periods of submergence and exposure. Because atmospheric CO_2 exchange was basically negative (influx to water or sediment), the positive coefficient was inconsistent with expectations based on photosynthetic activity. High PAR might have increased the water temperature and thereby reduced the solubility of CO_2 in the water. The result could have been a decrease of atmospheric CO_2 uptake, despite an increase of photosynthetic activity in the water during the measurement period when both water temperature and PAR were low throughout the year. Because the water temperature just below the water surface could not be measured by the thermo-salinometer, such a relationship might not be apparent from the partial regression coefficient of water temperature (−0.036 and insignificant) versus the CO_2 exchange rate during the day under submerged conditions (Table 1).

The partial regression coefficients during submergence at night were negative and positive for water temperature and air temperature, respectively. The implication is that colder water and warmer air reduced the influx of atmospheric CO_2. Because an increase of temperature with height above the water surface would stabilize the atmosphere directly over the water surface, the vertical eddy transport of CO_2 might be reduced during submergence at night on the tidal flat (Cava et al., 2004). It is possible that the same reduction of vertical eddy transport of CO_2 occurred during the period of exposure, but because the temperature near the sediment surface was not measured in this study, we can neither confirm nor reject this hypothesis.

The partial regression coefficients of O_2 fluxes estimated *via* EC measurements indicated that wind speed increased O_2 absorption into the sediment during both the day and night. Physical turbulence of the water therefore had more effect on atmospheric O_2 exchange than on CO_2 exchange. However, the high coefficient of determination and partial regression coefficient of water temperature during the daytime indicated that water temperature was the dominant factor that regulated O_2 exchange between the water and sediment. The implication was that photosynthetic activity on the sediment surface during the submerged period was more affected by water temperature than by other parameters like PAR. During the night, when variations of water temperature would be smaller than during the day, the effect of water temperature would be less apparent. Freshwater input would probably have decreased O_2 absorption into the sediment because a decrease of salinity might have adversely affected photosynthesis by microphytobenthos and thereby have decreased O_2 absorption. Because the variations of water temperature were smaller at night than during the day, the effects of freshwater input might be more apparent at night than during the day.

A significant correlation between air–water CO_2 fluxes and water–sediment O_2 exchange was apparent during both the day and night (Figure 4). The implication was that high rates of O_2 absorption near the sediment surface and high rates of atmospheric CO_2 absorption into the water column over the sediment occurred simultaneously. Such a relationship seems inconsistent with the biological activity of the microphytobenthos because uptake of dissolved O_2 should be accompanied by release of CO_2 into the water column and a resultant increase of the partial pressure of CO_2 in the water, and vice versa. However, the relationship seems consistent with biological activity in the water column, wherein photosynthetic activity leads to absorption of atmospheric CO_2 and release of dissolved O_2, and vice versa. The decrease of CO_2 and increase of O_2 concentrations in the water column would cause an increase of the downward CO_2 (air to water) and O_2 (water to sediment) fluxes because the concentration gradients would increase at each boundary layer. Physical turbulence could enhance that relationship. An increase of wind speed or bottom friction could enhance both air–water CO_2 fluxes and water–sediment O_2 exchange *via* physical turbulence. Resuspension of sediment in the low-O_2 layer by physical disturbance would also increase the O_2 concentration gradient in the water. Unfortunately, the limited number of O_2 EC measurements in this study precluded further testing of this hypothesis. Additional O_2 EC data will be required for a more detailed analysis.

Summary

The mechanisms associated with the atmospheric CO_2 exchange on a tidal flat measured in this study could be summarized as follows. (1) The tidal flat in Tokyo Bay and the Wadden Sea are both sinks for atmospheric CO_2. In both cases, there are no macrophytes, and the

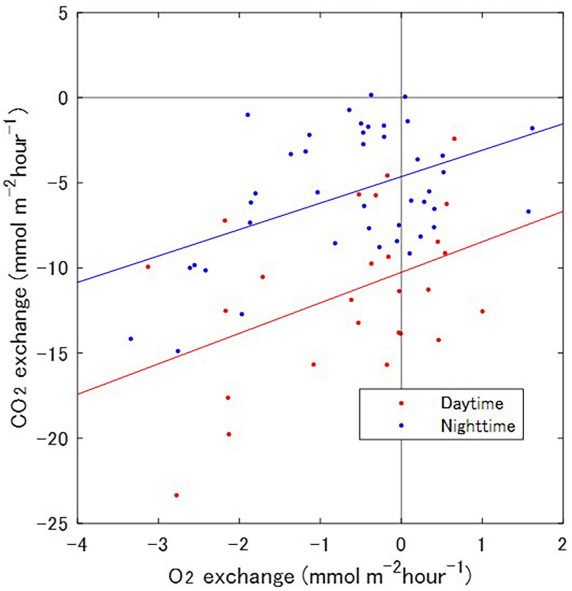

FIGURE 4
Comparison between atmospheric CO_2 and O_2 exchange rates. The red and blue dots indicate exchange rates during daytime and nighttime, respectively. The red and blue lines are the linear regressions between the two rates during the daytime (R^2 = 0.44, p = 0.03) and nighttime data (R^2 = 0.47, p = 0.002).

sediment is composed mainly of fine sand. (2) Air–water CO_2 fluxes over the tidal flat were about 20 times the fluxes in Tokyo Bay. The likely explanation is enhancement by tide-driven factors. (3) Freshwater input and PAR were important factors that regulated CO_2 exchange during submergence and the daytime, respectively. (4) A stable atmospheric layer near the water/sediment surface might have reduced atmospheric CO_2 exchange during the night. (5) O_2 exchange was affected by physical turbulence caused by wind over the water/sediment surface. O_2 absorption into the sediment would be increased by warm water and decreased by freshwater inputs during the daytime and nighttime, respectively. (6) Photosynthetic activity in water and physical turbulence increased atmospheric CO_2 absorption and the supply of O_2 to the sediment surface. This study was limited to several days in the winter, and annual measurements by EC methods are expected to provide more understanding of the carbon flow over tidal flats surrounding urbanized areas like Tokyo Bay.

Data availability statement

The original contributions presented in the study are included in the article/Supplementary Material. Further inquiries can be directed to the corresponding author.

Author contributions

Conceived and designed: TT and TK. Performed field work: TT. Analyzed the data: TT and TK. Writing led by TT.

Funding

This study was supported by a Grant-in-Aid for Scientific Research (no. 18H04156) from the Japan Society for the Promotion of Science.

Acknowledgments

We thank S. Hosokawa and E. Miyoshi for help with the field work. We also thank K. Watanabe for help with the referential work.

Conflict of interest

The authors declare that the research was conducted in the absence of any commercial or financial relationships that could be construed as a potential conflict of interest.

Publisher's note

Supplementary material

The Supplementary Material for this article can be found online at: https://www.frontiersin.org/articles/10.3389/fmars.2022.989270/full#supplementary-material

SUPPLEMENTARY FIGURE 1
Temporal variations of water temperature, salinity, air temperature, wind speed, water depth, PAR, current speed, and O_2 concentration during the measurement.

References

Berg, P., Huettel, M., Glud, R. N., Reimers, C. E., and Attard, K. M. (2022). Aquatic eddy covariance: The method and its contributions to defining oxygen and carbon fluxes in marine environments. *Annu. Rev. Mar. Sci.* 14, 431–455. doi: 10.1146/annurev-marine-042121-012329

Blomquist, B. W., Huebert, B. J., Fairall, C. W., Bariteau, L., Edson, J. B., Hare, J. E., et al. (2014). Advances in air-Sea flux measurement by eddy correlation. *Boundary-Layer Meteorol.* 152 (3), 245–276. doi: 10.1007/s10546-014-9926-2

Borges, A. V., Delille, B., and Frankignoulle, M. (2005). Budgeting sinks and sources of CO_2 in the coastal ocean: Diversity of ecosystems counts. *Geophys. Res. Lett.* 32 (14), L14601. doi: 10.1029/2005GL023053

Borges, A. V., Delille, B., Schiettecatte, L. S., Gazeau, F., Abril, G., and Frankignoulle, M. (2004). Gas transfer velocities of CO_2 in three European estuaries (Randers fjord, scheldt, and Thames). *Limnol. Oceanog.* 49 (5), 1630–1641. doi: 10.4319/lo.2004.49.5.1630

Cava, D., Giostra, U., Siqueira, M., and Katul, G. (2004). Organised motion and radiative perturbations in the nocturnal canopy sublayer above an even-aged pine forest. *Boundary-Layer Meteorol.* 112 (1), 129–157. doi: 10.1023/B:BOUN.0000020160.28184.a0

Edson, J. B., Fairall, C. W., Bariteau, L., Zappa, C. J., Cifuentes-Lorenzen, A., McGillis, W. R., et al. (2011). Direct covariance measurement of CO_2 gas transfer velocity during the 2008 southern ocean gas exchange experiment: Wind speed dependency. *J. Geophys. Research-Oceans* 116, C00f10. doi: 10.1029/2011jc007022

Endo, T., and Otani, S. (2019). "Carbon storage in tidal flats," in *Blue carbon in shallow coastal ecosystems: Carbon dynamics, policy, and implementation*. Eds. T. Kuwae and M. Hori. (Singapore: Springer Singapore), 129–151.

Frankignoulle, M. (1988). Field-measurements of air Sea CO_2 exchange. *Limnol. Oceanog.* 33 (3), 313–322. doi: 10.4319/lo.1988.33.3.0313

Hosokawa, Y. (1999). Water purification system at coastal tidal flat and possibility of its rehabilitations and construction. *Bull. Coast. Oceanog.* 36 (2), 137–144. doi: 10.32142/engankaiyo.36.2_137

Ikawa, H., and Oechel, W. C. (2015). Temporal variations in air-sea CO_2 exchange near large kelp beds near San Diego, California. *J. Geophys. Research-Oceans* 120 (1), 50–63. doi: 10.1002/2014jc010229

Kayanne, H., Suzuki, A., and Saito, H. (1995). Diurnal changes in the partial-pressure of carbon-dioxide in coral-reef water. *Science* 269 (5221), 214–216. doi: 10.1126/science.269.5221.214

Klaassen, W., and Spilmont, N. (2012). Inter-annual variability of CO_2 exchanges between an emersed tidal flat and the atmosphere. *Estuar. Coast. Shelf Sci.* 100, 18–25. doi: 10.1016/j.ecss.2011.06.002

Kljun, N., Calanca, P., Rotach, M. W., and Schmid, H. P. (2004). A simple parameterisation for flux footprint predictions. *Boundary-Layer Meteorol.* 112 (3), 503–523. doi: 10.1023/B:Boun.0000030653.71031.96

Kondo, F., Ono, K., Mano, M., Miyata, A., and Tsukamoto, O. (2014). Experimental evaluation of water vapour cross-sensitivity for accurate eddy covariance measurement of CO_2 flux using open-path CO_2/H2O gas analysers. *Tellus Ser. B-Chemical Phys. Meteorol.* 66, 23803. doi: 10.3402/tellusb.v66.23803

Kubo, A., Maeda, Y., and Kanda, J. (2017). A significant net sink for CO_2 in Tokyo bay. *Sci. Rep.* 7, 44355. doi: 10.1038/srep44355

Kuwae, T., Kamio, K., Inoue, T., Miyoshi, E., and Uchiyama, Y. (2006). Oxygen exchange flux between sediment and water in an intertidal sandflat, measured *in situ* by the eddy-correlation method. *Mar. Ecol. Prog. Ser.* 307, 59–68. doi: 10.3354/meps307059

Landwehr, S., Miller, S. D., Smith, M. J., Saltzman, E. S., and Ward, B. (2014). Analysis of the PKT correction for direct CO_2 flux measurements over the ocean. *Atmos. Chem. Phys.* 14 (7), 3361–3372. doi: 10.5194/acp-14-3361-2014

Lee, X., Massman, W. J., and Law, B. (2004). *Handbook of micrometeorology: A guide for surface flux measurement and analysis (Atmospheric and oceanographic sciences library* (Dordrecht Netherlands: Springer Netherlands).

Mørk, E. T., Sorensen, L. L., Jensen, B., and Sejr, M. K. (2014). Air-Sea gas transfer velocity in a shallow estuary. *Boundary-Layer Meteorol.* 151 (1), 119–138. doi: 10.1007/s10546-013-9869-z

Massman, W. J. (2000). A simple method for estimating frequency response corrections for eddy covariance systems. *Agric. For. Meteorol.* 104 (3), 185–198. doi: 10.1016/S0168-1923(00)00164-7

Mateo, M. A., Romero, J., Perez, M., Littler, M. M., and Littler, D. S. (1997). Dynamics of millenary organic deposits resulting from the growth of the Mediterranean seagrass *Posidonia oceanica*. *Estuar. Coast. Shelf Sci.* 44 (1), 103–110. doi: 10.1006/ecss.1996.0116

Mcleod, E., Chmura, G. L., Bouillon, S., Salm, R., Björk, M., Duarte, C. M., et al. (2011). A blueprint for blue carbon: toward an improved understanding of the role of vegetated coastal habitats in sequestering CO_2. *Front. Ecol. Environ.* 9 (10), 552–560. doi: 10.1890/110004

McMillen, R. T. (1988). An eddy-correlation technique with extended applicability to non-simple terrain. *Boundary-Layer Meteorol.* 43 (3), 231–245. doi: 10.1007/Bf00128405

Middelburg, J. J., Klaver, G., Nieuwenhuize, J., Wielemaker, A., deHaas, W., Vlug, T., et al. (1996). Organic matter mineralization in intertidal sediments along an estuarine gradient. *Mar. Ecol. Prog. Ser.* 132 (1-3), 157–168. doi: 10.3354/meps132157

Migné, A., Davoult, D., Spilmont, N., Menu, D., Boucher, G., Gattuso, J. P., et al. (2002). A closed-chamber CO_2-flux method for estimating intertidal primary production and respiration under emersed conditions. *Mar. Biol.* 140 (4), 865–869. doi: 10.1007/s00227-001-0741-1

Murray, N. J., Phinn, S. R., DeWitt, M., Ferrari, R., Johnston, R., Lyons, M. B., et al. (2019). The global distribution and trajectory of tidal flats. *Nature* 565 (7738), 222–22+. doi: 10.1038/s41586-018-0805-8

Nellemann, C., Corcoran, E., Duarte, C. M., Valdrés, L., De Young, C., Fonseca, L., et al. (2009). *Blue carbon: the role of healthy oceans in binding carbon: a rapid response assessment* (Arendal, Norway: GRID-Arendal for United Nations Environment Programme).

O'connor, D. J., and Dobbins, W. E. (1958). Mechanism of reaeration in natural streams. *Trans. Am. Soc. Civil Eng.* 123, 641–666. doi: 10.1061/TACEAT.0007609

Otani, S., and Endo, T. (2019). "CO2 flux in tidal flats and salt marshes," in *Blue carbon in shallow coastal ecosystems: Carbon dynamics, policy, and implementation*. Eds. T. Kuwae and M. Hori. (Singapore: Springer Singapore), 223–250.

Polsenaere, P., Lamaud, E., Lafon, V., Bonnefond, J. M., Bretel, P., Delille, B., et al. (2012). Spatial and temporal CO_2 exchanges measured by eddy covariance over a temperate intertidal flat and their relationships to net ecosystem production. *Biogeosciences* 9 (1), 249–268. doi: 10.5194/bg-9-249-2012

Prytherch, J., Yelland, M. J., Pascal, R. W., Moat, B. I., Skjelvan, I., and Neill, C. C. (2010). Direct measurements of the CO_2 flux over the ocean: Development of a novel method. *Geophys. Res. Lett.* 37, L03607. doi: 10.1029/2009gl041482

Raymond, P. A., and Cole, J. J. (2001). Gas exchange in rivers and estuaries: Choosing a gas transfer velocity. *Estuaries* 24 (2), 312–317. doi: 10.2307/1352954

Rousseeuw, P. J., and Croux, C. (1993). Alternatives to the median absolute deviation. *J. Am. Stat. Assoc.* 88 (424), 1273–1283. doi: 10.2307/2291267

Rutgersson, A., and Smedman, A. (2010). Enhanced air-sea CO_2 transfer due to water-side convection. *J. Mar. Syst.* 80 (1-2), 125–134. doi: 10.1016/j.jmarsys.2009.11.004

Sanders, C. J., Smoak, J. M., Naidu, A. S., Sanders, L. M., and Patchineelam, S. R. (2010). Organic carbon burial in a mangrove forest, margin and intertidal mud flat. *Estuar. Coast. Shelf Sci.* 90 (3), 168–172. doi: 10.1016/j.ecss.2010.08.013

Sasaki, A., Hagimori, Y., Yuasa, I., and Nakatsubo, T. (2012). Annual sediment respiration in estuarine sandy intertidal flats in the seto inland Sea, Japan. *Landscape Ecol. Eng.* 8 (1), 107–114. doi: 10.1007/s11355-011-0157-0

Spilmont, N., Migné, A., Lefebvre, A., Artigas, L. F., Rauch, M., and Davoult, D. (2005). Temporal variability of intertidal benthic metabolism under emersed conditions in an exposed sandy beach (Wimereux, eastern English channel, France). *J. Sea Res.* 53 (3), 161–167. doi: 10.1016/j.seares.2004.07.004

Tokoro, T., Hosokawa, S., Miyoshi, E., Tada, K., Watanabe, K., Montani, S., et al. (2014). Net uptake of atmospheric CO_2 by coastal submerged aquatic vegetation. *Global Change Biol.* 20 (6), 1873–1884. doi: 10.1111/gcb.12543

Tokoro, T., Kayanne, H., Watanabe, A., Nadaoka, K., Tamura, H., Nozaki, K., et al. (2008). High gas-transfer velocity in coastal regions with high energy-dissipation rates. *J. Geophys. Research-Oceans* 113, C11006. doi: 10.1029/2007jc004528

Tokoro, T., and Kuwae, T. (2018). Improved post-processing of eddy-covariance data to quantify atmosphere-aquatic ecosystem CO_2 exchanges. *Front. Mar. Sci.* 5. doi: 10.3389/fmars.2018.00286

Tokoro, T., Nakaoka, S., Takao, S., Kuwae, T., Kubo, A., Endo, T., et al. (2021). Contribution of biological effects to carbonate-system variations and the air-water CO_2 flux in urbanized bays in Japan. *J. Geophys. Research-Oceans* 126, e2020JC016974. doi: 10.1029/2020JC016974

Uchiyama, Y. (2007). Hydrodynamics and associated morphological variations on an estuarine intertidal sand flat. *J. Coast. Res.* 23 (4), 1015–1027. doi: 10.2112/04-0336.1

Vesala, T., Eugster, W., and Ojala, A. (2012). "Eddy covariance measurements over lakes," in *Eddy covariance: A practical guide to measurement and data analysis*. Eds. M. Aubinet, T. Vesala and D. Papale (Dordrecht: Springer Netherlands), 365–376.

Webb, E. K., Pearman, G. I., and Leuning, R. (1980). Correction of flux measurements for density effects due to heat and water-vapor transfer. *Q. J. R. Meteorol. Soc.* 106 (447), 85–100. doi: 10.1002/qj.49710644707

Widdows, J., Blauw, A., Heip, C. H. R., Herman, P. M. J., Lucas, C. H., Middelburg, J. J., et al. (2004). Role of physical and biological processes in sediment dynamics of a tidal flat in westerschelde estuary, SW Netherlands. *Mar. Ecol. Prog. Ser.* 274, 41–56. doi: 10.3354/meps274041

Zemmelink, H. J., Slagter, H. A., van Slooten, C., Snoek, J., Heusinkveld, B., Elbers, J., et al. (2009). Primary production and eddy correlation measurements of CO_2 exchange over an intertidal estuary. *Geophys. Res. Lett.* 36, L19606. doi: 10.1029/2009gl039285

frontiers | Frontiers in Marine Science

TYPE Original Research
PUBLISHED 06 October 2022
DOI 10.3389/fmars.2022.991802

OPEN ACCESS

EDITED BY
Maria Ll. Calleja,
Max Planck Institute for Chemistry, Germany

REVIEWED BY
Javier F. Bárcena,
University of Cantabria, Spain
Wei-dong Zhai,
Southern Marine Science and Engineering Guangdong Laboratory (Zhuhai), China

*CORRESPONDENCE
Shinichiro Yano
yano@civil.kyushu-u.ac.jp

SPECIALTY SECTION
This article was submitted to Marine Biogeochemistry, a section of the journal Frontiers in Marine Science

RECEIVED 12 July 2022
ACCEPTED 20 September 2022
PUBLISHED 06 October 2022

CITATION
Xiong B, Yano S, Komai K, Saito N, Komori H, Chi B, Hao L and Nakayama K (2022) Interaction between seawater carbon dioxide dynamics and stratification in shallow coastal waters: A preliminary study based on a weekly validated three-dimensional ecological model. *Front. Mar. Sci.* 9:991802. doi: 10.3389/fmars.2022.991802

Interaction between seawater carbon dioxide dynamics and stratification in shallow coastal waters: A preliminary study based on a weekly validated three-dimensional ecological model

Bing Xiong[1,2], Shinichiro Yano[3]*, Katsuaki Komai[4], Naoki Saito[5], Hiroto Komori[3], Baixin Chi[3], Lin Hao[3] and Keisuke Nakayama[6]

[1]Key Laboratory of Urban Safety Risk Monitoring and Early Warning, Tongji University, Shanghai, China, [2]Municipal Engineering Design and Research Institute, Guangzhou Municipal Group Co., Ltd., Guangzhou, China, [3]Department of Civil Engineering, Kyushu University, Fukuoka, Japan, [4]School of Earth, Energy and Environmental Engineering, Kitami Institute of Technology, Kitami, Japan, [5]Geological Survey of Japan, National Institute of Advanced Industrial Science and Technology, Tsukuba, Japan, [6]Department of Civil Engineering, Kobe University, Kobe, Japan

Shallow coastal waters (SCWs) have attracted wide attention in recent years due to their strong carbon sequestration capacity. However, the complex carbon dioxide (CO_2) dynamics in the water column makes it difficult to estimate the air–water CO_2 fluxes (F_{CO2}) accurately. We developed a numerical model of CO_2 dynamics in water based on field measurements for a typical stratified semi-enclosed shallow bay: the Yatsushiro Sea, Japan. The developed model showed an excellent ability to reproduce the stratification and CO_2 dynamics of the Yatsushiro Sea. Through numerical model simulations, we analyzed the annual CO_2 dynamics in the Yatsushiro Sea in 2018. The results show that the effect of stratification on the CO_2 dynamics in seawater varies greatly depending on the distance from the estuary and the period. In the estuarine region, stratification manifests itself throughout the year by promoting the maintenance of a high partial pressure of CO_2 (pCO_2) in surface waters, resulting in surface pCO_2 being higher than atmospheric pCO_2 for up to 40 days during the flood period (average surface pCO_2 of 539.94 μatm). In contrast, in areas farther from the estuary, stratification mainly acts to promote the maintenance of high pCO_2 in surface waters during periods of high freshwater influence. Then changes to a lower surface pCO_2 before the freshwater influence leads towards complete dissipation. Finally, we estimated the F_{CO2} of the Yatsushiro Sea in 2018, and the results showed that the Yatsushiro Sea was a sink area for atmospheric CO_2 in 2018 (–1.70 mmol/m^2/day).

KEYWORDS

carbon dioxide, shallow coastal waters, 3D numerical model, field measurement, stratification, blue carbon

1 Introduction

The ocean, which stores and sequesters large amounts of CO_2 in the form of dissolved inorganic carbon (DIC), can buffer the increase in atmospheric CO_2 concentration (McLeod et al., 2011; Le Quéré et al., 2016). Some studies have indicated that the global ocean hosts a substantial reservoir of CO_2 that is 50 times greater than that in the atmosphere and is considered an extremely significant net sink of atmospheric CO_2 (Raven and Falkowski, 1999). Meanwhile, shallow coastal waters (SCWs) comprising estuaries, shallows, intertidal flats, seagrass, salt marshes, and mangroves have recently attracted extensive scientific attention due to their valuable potential role in climate change mitigation and adaptation. Several studies have demonstrated that SCWs with vegetation such as seagrass, mangroves, and salt marshes contribute more than 50% of the total oceanic carbon storage despite making up only 0.5% of the ocean area, owing to them having the highest carbon burial rates in the ocean (average: 138–226 g C/m^2/year), about 3 to 4 orders of magnitude higher than those in open ocean sediments (0.018 g C/m^2/year) (Duarte et al., 2005; Donato et al., 2011; Fourqurean et al., 2012; Chen et al., 2013; Murdiyarso et al., 2015; Alongi et al., 2016; Kuwae et al., 2016; Nakayama et al., 2020), and being considered as established 'blue carbon' (BC) ecosystems (McKee et al., 2007; Lo Iacono et al., 2008; Nellemann, 2009; Duarte et al., 2010).

Recent studies related to the role of SCWs in climate change mitigation and adaptation are beginning to estimate the amount of atmospheric CO_2 uptake taking place through air-water CO_2 gas exchange ((1) in Figure 1) (Maher and Eyre, 2012; Bauer et al., 2013; Tokoro et al., 2014; Kubo et al., 2017). However, different from terrestrial ecosystems, submerged carbon burial ((2) in Figure 1) is not directly linked to the removal of atmospheric CO_2 due to the water column which, within complex carbon dynamics, separates the atmosphere from benthic systems. Since the level of the atmospheric pCO_2 fluctuates slightly, F_{CO2} is determined by the level of pCO_2 in surface water (Wanninkhof, 1992). However, the pCO_2 in surface water fluctuates significantly within short time scales due to the complex distribution and dynamics of DIC in the water column. Therefore, we need to understand the full suite of dynamics of pCO_2 and DIC in the water column in order to improve the accuracy of F_{CO2} estimation.

Here, we discuss the fundamental processes that critically affect the distribution and dynamics of DIC and surface pCO_2 in SCWs. Surface water DIC and pCO_2 would be reduced, since allochthonous organic carbon (C_{org}) and inorganic (C_{inorg}) ((3) in Figure 1) and DIC inputs ((4) in Figure 1) are low. Net autotrophic ecosystems (i.e., seagrasses, phytoplankton) would reduce surface DIC and pCO_2, then show a net uptake for atmospheric CO_2 through photosynthesis ((5) in Figure 1) (Maher and Eyre, 2012; Tokoro et al., 2014; Nakayama et al., 2020). Respiration will increase DIC and pCO_2 ((6) in Figure 1). The formation of calcium carbonate minerals will decrease DIC by calcification ((7) in Figure 1) and increase DIC by dissolution ((8) in Figure 1). Additionally, the reactions of the DIC cycle ((9) in Figure 1) can change the pCO_2 in surface water and therefore affect the net exchange of CO_2 with the atmosphere (Howard et al., 2017; Macreadie et al., 2017; Howard et al., 2018). According to these processes, the DIC in bottom water is generally much higher than that in surface water and will usually mix with surface water by upwelling ((10) in Figure 1). However, stratification ((11) in Figure 1) occurs seasonally in SCW regions, mainly in summer (Wakeham et al., 1987; Wiseman et al., 1997), which can hinder the upwelling of bottom water with a high DIC concentration to suppress increases in DIC and pCO_2 in the surface water. In addition, unlike the effects of stratification on bottom DIC behavior, the sinking of particle organic carbon (POC) ((12) in Figure 1) from seawater surface is not hindered by stratification (Koné et al., 2009).

Stratification controls DIC and the vertical distribution of other water properties (i.e., water temperature, salinity, nutrients, phytoplankton, and dissolved oxygen) (Sylaios et al., 2006; Boldrin et al., 2009; Howarth et al., 2011). Water temperature negatively correlates with CO_2 solubility, and DIC in seawater shows a strong dependence on salinity in several shallow coastal regions (Bakker et al., 1999; Eyre, 2000). Phytoplankton in surface water can reduce pCO_2 through photosynthesis, and nutrients enhance the growth of phytoplankton and other net autotrophic ecosystems. Moreover, stratification suppresses the upwelling of suspended particles from bottom waters; improves transparency, thereby promoting photosynthesis; and decreases the amount of pCO_2 in the surface water (Chen et al., 2008). Furthermore, despite the controversy, studies have shown that the mineralization rate is low under hypoxic conditions caused by stratification (Hartnett et al., 1998; Koho et al., 2013). These results indicated that stratification appears to be a critical environmental parameter for the distribution and dynamics of DIC and pCO_2 in SCWs, thereby strongly affecting the F_{CO2}. Moreover, many studies have reported the potential relationship between CO_2 dynamics and stratification in coastal seawater, but since these studies only measured CO_2 data in surface seawater, the interaction between CO_2 dynamics and stratification in the detailed water column is still unclear (Shim et al., 2007; Zhai and Dai, 2009; Wang and Zhai, 2021). For this purpose, fully understanding the effects of stratification on submerged carbon biogeochemical processes and air–water CO_2 exchanges in SCWs is highly significant for helping us to understand the role of SCWs in climate change mitigation.

Field measurement is generally considered one of the most effective methods for determining the biogeochemical distribution and dynamics of seawater. Recently, researchers

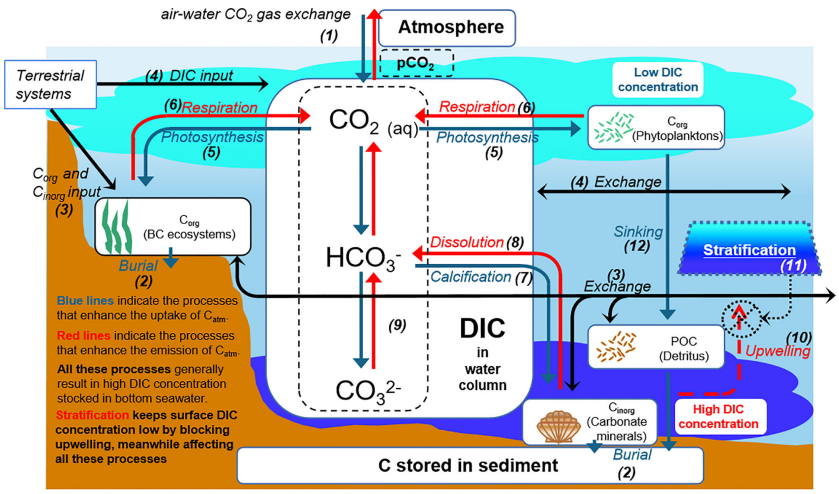

FIGURE 1
Schematic diagram of CO_2 dynamics in shallow coastal waters.

have conducted several field measurements to assess the DIC and pCO_2 dynamics in the water column of SCWs in order to estimate their contribution to atmospheric CO_2 removal (Koné et al., 2009; Chen et al., 2013; Kubo et al., 2017). However, these field measurements were conducted in surface seawater on a monthly or annual scale, but the complicated vertical distribution and dynamics of DIC and pCO_2 caused by short-term temporal events (namely, stratification) in the water column, which could be considered to affect the entire carbon absorption and storage cycle, are still unknown. Thus, field measurements conducted under several different stratification conditions are needed in order to clarify the DIC and pCO_2 vertical distribution and dynamics in SCWs. However, in the case of research on the characteristics of water quality dynamics in SCWs focusing on stratification and upwelling, the use of a tiny spatiotemporal scale is necessary, and it is hard to achieve this in field measurements. For this situation, three-dimensional (3D) numerical simulation is an effective measure that complements field measurement data and enables further analyses to be made. One study confirmed the advantages of the application of a 3D numerical model for the reproducibility of DIC and pCO_2 dynamics in the water column of SCWs (Sohma et al., 2018). Still, the model they developed was based on measurement data from surface seawater (Kubo et al., 2017), and the effects of stratification were not considered. Therefore, a 3D numerical model that can accurately describe the DIC and pCO_2 dynamics under the influence of stratification could enable us to better understand the carbon cycle in SCWs and improve the accuracy of F_{CO2} estimation.

This study has three primary objectives: (1) to examine the vertical distribution and dynamics of DIC and pCO_2 under different stratified conditions in the Yatsushiro Sea, Japan, by conducting field measurements under the three most representative stratification conditions within the hourly scale; (2) to develop a high vertical resolution hydrodynamic-ecological 3D numerical model that can accurately describe the vertical distribution and dynamics of DIC and pCO_2 under stratified conditions in the bay; (3) to analyze the CO_2 dynamics and the corresponding influence mechanism of the bay and estimate the 2018 F_{CO2} through the numerical simulation results.

2 Materials and methods

2.1 Study site and field measurements

The Yatsushiro Sea, which was selected as the target area for this study, is located in the western part of Kyushu Island, Japan (Figure 2). It is a highly enclosed inlet compared to other bays in Japan, and is characterized by a large tidal range and vast tidal flats and brackish water areas. Therefore, a unique ecosystem has developed in the bay's shallow waters, with high biodiversity and rich biological productivity. The northern part of the bay has a solid inner bay character and tidal flats, while the southern part of the bay, south of the central part, has a rapid seawater exchange and a reef-like seafloor that gradually becomes more pelagic. The southern part of the Yatsushiro Sea and the sea area around the Amakusa Islands have been selected by the Ministry of the Environment as "a sea area of high importance from the viewpoint of biodiversity." The bay is located along the coast of Kumamoto Prefecture, where the Tsushima Warm Current, a branch of the Kuroshio Current, flows. In particular, the southwestern part of the Amakusa Islands surrounding the

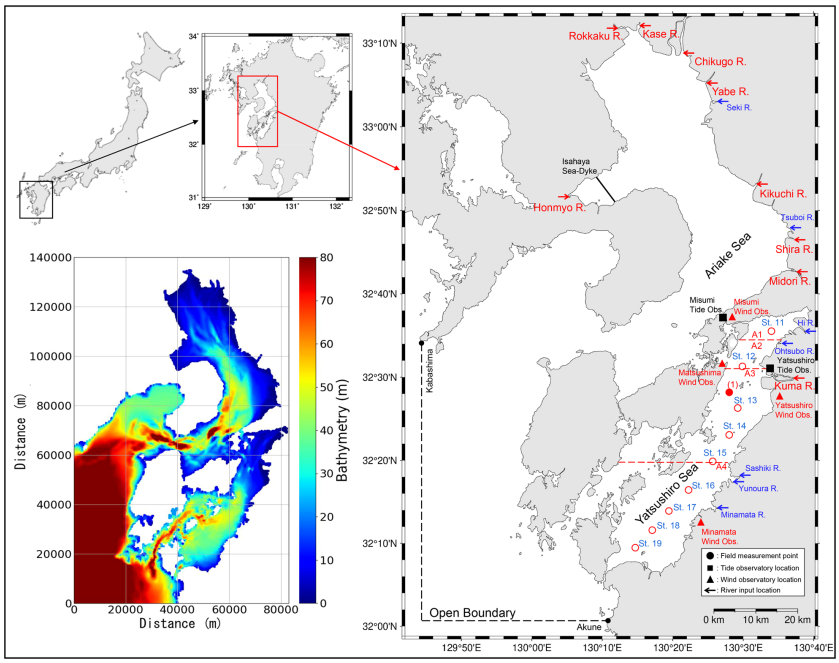

FIGURE 2
The location of the study site (right) and the domain of the numerical model (bottom left). The field measurement points are shown in the map on the right ((1) is the location of the field measurement we conducted, while St.11 to St.19 are the measurement locations of the data from MLIT), schematic diagram of the Yatsushiro Sea subdivision (A1 to A4 separated by red lines) and the location of the wind observatories (red dots).

bay is a significant habitat for reef-building corals in western Kyushu. The fifth nature conservation survey conducted by the Ministry of the Environment confirmed the existence of seagrass beds covering an area of about 1,141 ha.

The area of the bay is about 1,200 km^2. The basin area of the rivers flowing into the bay is approximately 3,000 km^2. Forty-seven rivers (one first-class river, forty-six second-class rivers) flow into the Yatsushiro Sea with a total watershed area of 3400 km^2, of which one first-class river, the Kuma River, has a catchment area that makes up about 60% of the total. The inflow of fresh water during the rainy season from June to August lowers the salinity throughout the sea area. In the inner part of the bay, the salinity decreases significantly due to the increased inflow of rivers such as the Kuma River.

The Yatsushiro Sea is considered to be a unique coastal area in terms of physical conditions such as flow, topography, and ecosystem. Since there is a lack of knowledge about blue carbon ecosystems (i.e., phytoplankton, seagrasses such as eelgrass, and corals) inhabiting the bay at the same time, new research results on air-sea CO_2 flux, pCO_2 in seawater, and related environmental factors in the bay are expected.

We conducted field measurements of the CO_2 dynamics in seawater at point (a) (32°27′30” N, 130°27′37” E, mean water depth: 20 m), which was the first attempt to investigate the seawater CO_2 dynamics in the Yatsushiro Sea. The measurement point is relatively close to the estuary of the Kuma River, where strong salt stratification is expected during flooding. The three measurement dates were all during spring tides and showed weak stratification (26 August 2018), mixed conditions (7 December 2018), and strong stratification (2 August 2019). CTD measurements and water sampling were conducted during a half-tide period (approximately 6 h) from high tide (9:00 am) to low tide (3:00 pm). CTD measurements included vertical profiles of the water temperature, salinity, and water density. Water samples were used for the analysis of DIC and TA. CTD measurements were conducted approximately every 20 min using a multi-item water quality meter (ProDSS, YSI). Water samples were collected at high tide, 1.5 h after high tide, at the full ebbing tide, 1.5 h before low tide, and at low tide, with 30 samples collected for each measurement. The samples were collected in 250 mL Duran bottles, and the DIC and TA were fixed by injecting mercury dichloride solution (250 mL). The values of DIC and TA were analyzed using a flow-through carbonate analyzer (MDO-02, made by Kimoto Electronics Co., Ltd.) and a total alkalinity titrator (ATT-15, made by Kimoto Electronics Co., Ltd., Osaka, Japan) owned by Kitami Institute of Technology. From the obtained DIC, TA, salinity, and water temperature, pCO_2 was calculated from the semi-empirical equations for carbon-based chemical equilibrium (Zeebe and Wolf-Gladrow, 2001). The equation used in this

study was the one developed in the 'seacarb' package in the R software (Lavigne and Gattuso, 2010).

The results of these three measurements were used for the calibration and validation of model values near the estuary of the Kuma River. In addition, St.11 to St.19 are the locations of the regular sites used for the environmental measurement of the water quality of the Yatsushiro Sea by the Ministry of Land, Infrastructure, Transport, and Tourism (MLIT) of Japan (Figure 2). The measurements included the vertical distribution of the water temperature, salinity, and seawater density at each site. In principle, the measurement frequency was twice a month (canceled in exceptional cases). The measurement results were used to calibrate and validate the simulation results of the CTD profiles in the whole area of the bay in this study.

2.2 Description of numerical model

Delft3D is an open-source 2D/3D numerical simulation software package that was developed by WL Delft Hydraulics (currently known as Dertares) (Lesser et al., 2004; Deltares, 2017). The software is a flexible framework for simulating water flow; water quality; waves; ecology; sediment transport in fluvial, estuarine, and coastal environments; and the interactions between the various processes.

In this study, the FLOW and WAQ modules in Delft3D (version 4.04.01) were utilized as the modeling tools. This framework has been effectively implemented to simulate ocean circulation, stratification, and water quality in various coastal waters (Niu et al., 2016; Alosairi and Alsulaiman, 2019). There have been several successful cases where the CO_2 cycle was simulated in surface water by applying the Delft3D-WAQ module (Menshutkin et al., 2014; Chen et al., 2019).

2.2.1 Hydrodynamic model Delft3D-FLOW

The mathematical principle of the hydrodynamic model Delft3D-FLOW is mainly to solve the Reynolds-Averaged Navier–Stokes (RANS) equations for incompressible fluids under shallow water assumptions using the finite difference method.

In this study, we refined the resolution of the vertical direction to further improve the accuracy of the vertical direction based on a general 3D coastal current model developed by Yano et al. (Yano et al., 2010) in order to simulate the effects of stratification more accurately. The computational domain of this model, which covers both the Ariake Sea and the Yatsushiro Sea (Figure 2).

A Cartesian coordinate system with a resolution of 10" (Δx = 250 m) was used in the horizontal direction, while a σ-coordinate system with 17 layers (2% × 10 layers, 5% × 1 layer, 10% × 3 layers, and 15% × 3 layers from the surface to the bottom, respectively) was used in the vertical direction. Horizontal eddy viscosity and eddy diffusion coefficients were evaluated using the Subgrid scale (SGS) model, and vertical eddy viscosity and eddy diffusion coefficients were evaluated using the k-ϵ turbulent model and incorporated into the tidal flatness model (dry-wet model). The calculation time frame was from 1 January 2018 to 1 January 2019, with a time step of 3 min.

The open boundary was located on the line connecting Akune, Kagoshima Prefecture, and Kabashima Strait, Nagasaki Prefecture (Figure 2). The known harmonic constants at both ends of the open boundary are estimated from measured data from 1970 and 1891 for Akune and Kabashima Suido, respectively, and the amplitudes and phase lags of major four tide components (M2, S2, K1, and O1) were adjusted according to the existing harmonic constants at both ends by Yano et al. (Yano et al., 2010). The setting of harmonic constants using in this model were shown in Table 1. A constant value of 35.15 psu was used for the salinity in the open boundary condition, with the water temperature of sea surface and seabed were using a time series obtained from the daily sea surface temperature data and data at a depth of 50 m from the Fukuoka Regional Meteorological Observatory.

In this study, freshwater inflows from eight first-class rivers (Chikugo, Yabe, Kase, Rokkaku, Kikuchi, Shira, Midori, and Kuma) and nine major second-class rivers (Kashima, Shioda, Seki, Tsuboi, Hi, Otsubo, Sashiki, Yunoura, and Minamata) were considered (Figure 2). The flow rate of the first-class rivers was the hourly flow rate at the station nearest to the estuary in the non-tidal area obtained from the hydrological water quality database of the MLIT. To account for the inflow downstream of the station, the flow rate at the station was corrected by multiplying it by a factor calculated by dividing the station's catchment area by the total area of the watershed. For second-class rivers, the calculation was based on the ratio of the catchment area to nearby first-class rivers.

The solar radiation, air temperature, humidity and wind data used in this model were a hourly time series, and were obtained from Kumamoto station and Yatsushiro station of Japan Meteorological Agency (JMA) Amedas, respectively. The wind speed was converted to equivalent sea breeze using Carruthers' land boundary wind to sea breeze conversion coefficient (Arakawa et al., 2007).

In this model, we used the region-wide average salinity and water temperature of the calculated area as of December 31, 2017, obtained from the same model calculation in the previous year, i.e., 2017, as the initial constant conditions. Model calculations for both the hydrodynamic and ecological models used a cold start from January 1, 2018, with a stabilization period of approximately 2 weeks, which did not affect the model validation results since our calibration and validation of the models started in mid-January, but had a small effect on the CO_2 flux calculations in January.

10.3389/fmars.2022.991802

TABLE 1 Harmonic constants of hydrodynamic model.

Harmonic constants					
Location components	**Akune amplitude (m)**	**Phase (°)**	**Location components**	**Kabashima amplitude (m)**	**Phase (°)**
M2	0.717	211.1	M2	0.86	219
S2	0.314	229	S2	0.36	240
K1	0.229	208.6	K1	0.25	205
O1	0.177	185.4	O1	0.19	186
P1	0.074	203.9	P1	0.083	202
N2	0.132	213.4	N2	0.147	213.4
K2	0.087	239	K2	0.098	258
SA	0.216	162.6	SA	0.216	162.6
SSA	0.044	352.3	SSA	0.044	352.3
Q1	0.042	171.9	Q1	0.042	171.9
MU2	0.031	226.1	MU2	0.031	226.1
NU2	0.027	212.6	NU2	0.027	212.6
T2	0.026	252	T2	0.026	252
2N2	0.022	208.5	2N2	0.022	208.5
L2	0.02	194.4	L2	0.02	194.4
J1	0.015	230.2	J1	0.015	230.2
MM	0.014	327	MM	0.014	327
M4	0.011	331.7	M4	0.011	331.7
MS4	0.011	35.2	MS4	0.011	35.2
OO1	0.009	246	OO1	0.009	246
M1	0.009	196.3	M1	0.009	196.3
R2	0.009	225.9	R2	0.009	225.9
LABDA2	0.008	202.2	LABDA2	0.008	202.2
RO1	0.007	186.1	RO1	0.007	186.1
PSI1	0.007	180.4	PSI1	0.007	180.4
M3	0.007	255.9	M3	0.007	255.9
MF	0.005	207.4	MF	0.005	207.4
OP2	0.005	253.3	OP2	0.005	253.3
MP1	0.004	165.3	MP1	0.004	165.3
S1	0.004	88.3	S1	0.004	88.3
SO1	0.004	302.6	SO1	0.004	302.6
2MS6	0.004	113.4	2MS6	0.004	113.4
2SM2	0.004	48.2	2SM2	0.004	48.2
MK3	0.003	234.6	MK3	0.003	234.6
FI1	0.003	198.2	FI1	0.003	198.2
MO3	0.002	163.3	MO3	0.002	163.3
M6	0.002	72.9	M6	0.002	72.9
MSF	0.002	101	MSF	0.002	101
SK3	0.002	355.2	SK3	0.002	355.2
PI1	0.001	261.4	PI1	0.001	261.4

2.2.2 Ecological model Delft3D-WAQ

Delft3D-WAQ is a module of the ecological section that is used to simulate biological processes in water bodies and sediments and various processes of solute transport and transformation. The WAQ module mainly solves the advection–diffusion–reaction equations for each computational grid by combining the results of the FLOW module (e.g., the spatial and temporal distribution of salinity, water temperature, velocity, and turbulence dispersion coefficient). Therefore, the computational domain, resolution, number of layers in the σ-coordinate system, location of the freshwater inflow, and flow velocity are the same as those in the hydrodynamic model. In

addition, all the physical conditions used for the FLOW module (e.g., the solar radiation, air temperature, humidity, wind, river inflow) were coupled into the WAQ module, and the start pattern (e.g calculation time frame and time step) were the same as the FLOW module. This ecological module offers the user a wide range of frameworks for choosing the substances and processes to be simulated, giving more flexibility in simulating physical, biochemical, and biological processes (Deltares, 2018). The structural diagram of the ecological model used in this study (Figure 3). The interaction of phytoplankton dynamics, nutrients cycling, and inorganic carbon cycling are considered in this model as the key process affecting the objective of this study (i.e., pCO_2 dynamics in the water column).

The model settings of this ecological model were chosen mainly by referring to the settings of the generic ecological model (GEM) (Blauw et al., 2008), and the detailed model setup parameters are shown in Table 2. Considering the wide coverage of this model and the complex physical and biochemical processes in the target waters, we simplified the GEM by considering only one phytoplankton species (i.e., green algae) and assuming the decomposition rate of dissolved organic matter to be that of the inorganic matter immediately after production. This simplification has been proven to be reliable in previous simulation studies for anoxic states in the Ariake Sea (Tadokoro and Yano, 2019; Hao et al., 2021). Based on the simplified model, we added the processes of DIC, TA, and pH to simulate the CO_2 dynamics in the water column.

There are three main processes that are related to phytoplankton in Delft3D-WAQ: gross primary production, respiration, and mortality. Gross primary production is the total amount of energy produced through the process of photosynthesis. By capturing the energy from sunlight, primary producers can store it in organic compounds by converting carbon dioxide and water into organic compounds (Falkowski and Raven, 2013). In this model, three factors are chosen to affect the rate of gross primary production, temperature, availability of nutrients, and light. A higher temperature increases the rate of the chemical processes taking place within the algal cells. Thus, lowering the temperature limits the growth of algal biomass (Deltares, 2018). Phytoplankton require chemical elements to function, and the most vital aspects are nitrogen and phosphorus. The limitation factor is calculated according to the Monod equation for each nutrient, where the lowest value amongst these is used. The limitation of nitrogen is chosen to be dependent on the sum of the total concentration of ammonium and nitrate. The third factor, light, is necessary in order for the process of photosynthesis to take place. The extinction of light depends on the water depth and the concentration of absorbing substances within the water, which here are determined to be algal biomass, particulate organic matter (POM), humidity input from freshwater, and background absorption. The extinction of light is calculated according to Lambert–Beer's law, where the light intensity is reduced exponentially along with the water depth in relation to the intensity at the surface. Dissolved inorganic carbon (DIC) is also regarded as a rate-limiting resource for phytoplankton, as indicated by the availability of CO_2 and bicarbonate (HCO_3) for photosynthesis (Verspagen et al., 2014). In this model, respiration is performed when the algal cell grows (increasing biomass) and to maintain the functions of the cell—i.e., the basal

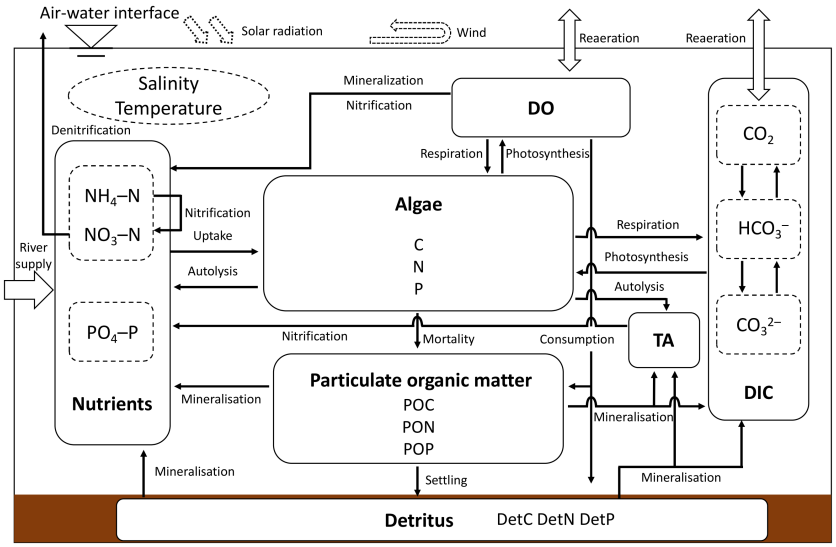

FIGURE 3
Structural diagram of the ecological model (modified from the generic ecological model developed by Blauw et al. (Blauw et al., 2008)).

TABLE 2 Process parameters of the ecological model.

Description	Symbol	Value	Unit	Reference
State Variables				
Ammonium	C_{NH4}	*	gN/m^3	
Nitrate	C_{NO3}	*	gN/m^3	
Ortho-phosphate	C_{PO4}	*	gP/m^3	
Particulate organic carbon	C_{POC}	*	gC/m^3	
Particulate organic nitrogen	C_{PON}	*	gN/m^3	
Particulate organic phosphorus	C_{POP}	*	gP/m^3	
Particulate organic carbon in sediment	$C_{s,C}$	*	gC/m^2	
Particulate organic nitrogen in sediment	$C_{s,N}$	*	gN/m^2	
Particulate organic phosphorus in sediment	$C_{s,P}$	*	gP/m^2	
Dissolved oxygen concentration	C_{DO}	*	gO_2/m^3	
Dissolved carbon dioxide concentration	C_{CO2}	*	gCO_2/m^3	
Algae biomass	C_{ALG}	*	gC/m^3	
Fluxes				
Net algae growth	B_{gro}	*	$gM/m^3/day$	
Gross primary production	B_{gpp}	*	$gM/m^3/day$	
Algae respiration	B_{rsp}	*	$gM/m^3/day$	
Algae mortality	B_{mor}	*	$gM/m^3/day$	
Decomposition of POM	B_{dec}	*	$gM/m^3/day$	
Settling flux	B_{set}	*	$gM/m^3/day$	
Autolysis of algae mortality	B_{aut}	*	$gM/m^3/day$	
Melting flux	B_{mel}	*	$gM/m^2/day$	
Nitrification	B_{nit}	*	$gM/m^3/day$	
Reaeration of O_2	$B_{rea,O2}$	*	$gO_2/m^3/day$	
Reaeration of CO_2	$B_{rea,CO2}$	*	$gCO_2/m^3/day$	
Sediment oxygen demand	B_{sod}	*	$gO_2/m^3/day$	
Limiting factors				
Nutrient limitation factor for algae growth	μ_{nut}	*	–	
Radiation limitation factor for algae growth	μ_{lt}	*	–	
Nutrient limitation factor for dec. of POM	$f_{dec,nut}$	*	–	
Oxygen limitation factor for nitrification	f_{ox}	*	–	
Parameters and constants				
Algae				
Potential maximum production rate at 20°C	α_1	1.5	day^{-1}	(D)
Potential maximum respiration rate at 20°C	α_2	0.041	day^{-1}	(Y)
Potential maximum mortality rate at 20°C	α_3	0.2	day^{-1}	(Y)
Temperature factor for primary production	β_1	1.06	–	(Y)
Temperature factor for respiration	β_2	1.07	–	(Y)
Temperature factor for mortality	β_3	1.07	–	(Y)
Half saturation constant for nitrogen for algae growth	$K_{s,N}$	0.005	gN/m^3	(G)
Half saturation constant for phosphorus for algae growth	$K_{s,P}$	0.001	gP/m^3	(G)
Light intensity at water surface	I_0	***	W/m^2	
Optimum light intensity for algae	I_{opt}	96.898	W/m^2	(Y)
Attenuation coefficient	k_{lt}	1.5	m^{-1}	(C)
Particulate organic matter				
Fraction of autolysis	α_{aut}	0.3	–	(B)

(Continued)

TABLE 2 Continued

Description	Symbol	Value	Unit	Reference
Maximum mineralization rate at 20°C of POC	$k_{decH,C}$	0.24	day^{-1}	(C)
Minimum mineralization rate at 20°C of POC	$k_{decL,C}$	0.22	day^{-1}	(C)
Maximum mineralization rate at 20°C of PON	$k_{decH,N}$	0.24	day^{-1}	(C)
Minimum mineralization rate at 20°C of PON	$k_{decL,N}$	0.08	day^{-1}	(B)
Maximum mineralization rate at 20°C of POP	$k_{decH,P}$	0.24	day^{-1}	(C)
Minimum mineralization rate at 20°C of POP	$k_{decL,P}$	0.08	day^{-1}	(B)
Temperature factor for decomposition	β_4	1.047	–	(G)
Upper limit stoichiometric constant PON	$f_{sU,N}$	0.15	gN/gC	(D)
Lower limit stoichiometric constant PON	$f_{sL,N}$	0.1	gN/gC	(D)
Upper limit stoichiometric constant POP	$f_{sU,P}$	0.015	gP/gC	(D)
Lower limit stoichiometric constant POP	$f_{sL,P}$	0.01	gP/gC	(D)
Settling velocity of POM	w_s	0.432	m/day	(Y)
Critical shear stress for POM	τ_c	0.3	N/m^2	(D)
Nutrients				
Fraction of ammonium in nitrogen uptake	f_{uptN}	*	–	
Critical ammonium concentration	C_{cNH4}	0.01	gN/m^3	(D)
N:C ratio in algae biomass	s_N	0.16	gN/gC	(D)
P:C ratio in algae biomass	s_P	0.02	gP/gC	(D)
Potential maximum elution rate at 20°C	α_5	0.03	day^{-1}	(D)
Temperature factor for elution	β_5	1.09	–	(D)
Potential maximum nitrification rate at 20°C	α_6	0.02	day^{-1}	(Y)
Temperature factor for nitrification	β_6	1.03	–	(Y)
Dissolved oxygen				
Critical concentration of DO for nitrification	$C_{cr,DO}$	1	gO_2/m^3	(D)
Optimal concentration of DO for nitrification	$C_{op,DO}$	5	gO_2/m^3	(D)
O:C ratio in POC	s_O	2.67	gO_2/gC	(D)
O:N ratio in NO_3	s_{NO}	4.571	gO_2/gN	(D)
Reaeration factor of O_2	$K_{a,O2}$	0.7	day^{-1}	(Y)
Saturation dissolved oxygen concentration	C_{DOs}	*	gO_2/m^3	
Chloride concentration	Cl	*	gCl/m^3	
Specified SOD	D_{sod0}	1.5	$gO_2/m^2/day$	(C)
Potential maximum SOD rate at 20°C	α_7	0.5	$gO_2/m^3/day$	(C)
Temperature factor for SOD	β_7	1.07	–	(C)
Critical concentration of DO for SOD	$C_{cr,sod}$	0	gO_2/m^3	(D)
Optimum concentration of DO for SOD	$C_{op,sod}$	0.5	gO_2/m^3	(C)
Dissolved inorganic carbon				
Reaeration factor of CO_2	$K_{a,CO2}$	1	day^{-1}	(C)
Saturation carbon dioxide concentration	C_{CO2s}	*	gCO_2/m^3	
Atmospheric partial pressure of CO_2	pCO_{2air}	***	µatm	
Total alkalinity		*		
Alkalinity	$Alka$	*	$gHCO_3/m^3$	(D)
pH				
Simple calculation of pH	pH_simp	*		
Minimum allowed calculated pH	pH_min	1	–	(D)
Maximum allowed calculated pH	pH_max	14	–	(D)
Physical input data				

(Continued)

TABLE 2 Continued

Description	Symbol	Value	Unit	Reference
Salinity	S	**	ppt	
Water temperature	T	**	°C	
Water depth	D	**	m	
Shear stress	τ	**	N/m^2	

* : Calculated in Delft3D-WAQ
** : Calculated in Delft3D-FLOW
*** : Observation data
(B) : Blauw, et. al. (2008)
(C) : Calibrated
(D) : Delft3D-WAQ
(G) : Gurel, et. al. (2005)
(Y) : Yamaguchi, et. al. (2018)

metabolism. The respiration rate necessary to keep the cell alive is related to the temperature. The mortality rate of algae is a function of temperature, where a higher temperature promotes a higher mortality rate. When algae die, a fraction of their biomass is directly released to the water as already dissolved inorganic matter. This process is called autolysis. However, the majority of the biomass stays intact and continues in the nutrient cycle as detritus, here referred to particulate organic matter.

This model simulates the simplified cycling of two types of nutrients: nitrogen and phosphorus. It includes three significant pools within the nutrient cycle: dissolved inorganic nutrients (NH4-N, NO3-N, and PO4-P), living organic matter (Algae), and POM. The uptake of nutrients is an equivalent result of the growth of algae. Hence, the consumed nutrient flux is proportional to the net primary production obtained using the N:C and P:C ratio in the algal biomass. Following the death of algae, the nutrients are either released back into the water body in the form of dissolved inorganic nutrients through autolysis or released back as detritus or dead organic matter. The release of nutrients by dead algae is equivalent to the N:C and P:C ratios within the algal biomass. Carbon, nitrogen, and phosphorus in the detritus are simulated as the state variables of particulate organic carbon (POC), particulate organic nitrogen (PON), and particulate organic (POP). POM comes from discharging rivers or the mortality flux of dead algae. The latter occurs through the process of mineralization, where microorganisms decompose POM into inorganic components. When algae and higher plants die, detritus is produced. Mineralization is the microbial decomposition of detritus into its fundamental inorganic components, such as carbon dioxide, ammonium, and phosphate. POM settles into the sediment during the settling process. In this case, the settling velocity is constant throughout time and unaffected by the bottom shear stress. Different forms of POM are subjected to the same settling velocity.

The main processes of inorganic carbon balance are air–water CO_2 exchange, the mineralization of organic carbon to inorganic carbon, and primary algal production. The reaeration of carbon dioxide proceeds proportionally to the difference between the saturated CO_2 concentration and the actual dissolved CO_2 concentration. The reaeration quantity per day was equivalent to the F_{CO2} diffused across the air-water interface. CO_2 in surface water tends to be saturated relative to the atmospheric CO_2 concentration. However, CO_2 production and consumption processes in the water column counteract the saturation, resulting in either a CO_2 excess or a CO_2 deficit. The saturation concentration of CO_2 in the water column is primarily a function of the atmospheric pCO_2, the water temperature, and the salinity. However, the pCO_2 in the atmosphere is assumed to be constant. In Delft3D-WAQ, the calculation of the saturation concentration is performed as a separate process, which has been implemented with two alternative formulas (Weiss, 1974; Golterman, 1982). In this study, we applied Weiss' formula. The pH, the carbonate speciation (CO_2, pCO_2, H_2CO_3, HCO_3^-, and CO_3^{2-}), and the saturation states of calcium carbonate (calcite and aragonite) in the water column and the sediment bed could be calculated from the TA and the DIC according to the carbon chemical equilibrium. Salinity and temperature from the hydrodynamic model are necessary inputs.

2.3 Model calibration and validation

In this study, the calibration and validation of the model were carried out in two steps. The first step involved calibrating and validating the hydrodynamic and ecological model parameters for the easily stratified area near the Kuma River estuary using the results of three field measurements of CO_2 dynamics in seawater at different stratification periods implemented at point (a) in Figure 2. The second step involved calibrating and validating the simulation results of the horizontal and vertical distribution of CTD for the whole area of the Yatsushiro Sea for the whole year of 2018 using CTD measurement data from the central route of the bay (the line from St.11 to St.19 in Figure 2) from the MLIT. In the first validation step, we performed a comparative validation of the water temperature, salinity, density, DIC, TA, and pCO_2, containing statistical analysis and contour plot comparison. In the second step, we calibrated and validated the water temperature, salinity, and seawater density. In addition, we

applied the concept of density stratification index (SI) proposed in (Simpson et al., 1990) for quantifying the strength of density stratification. Based on the process of calibrating and validating the SI, we improved the simulation accuracy of the hydrodynamic model for the stratification state of the whole area of the bay. The equation for calculating the SI is shown in Equation (1) (Simpson et al., 1990):

$$SI = -\frac{1}{H}\int_{-H}^{0}(\rho - \bar{\rho})g \cdot z \cdot dz \quad (1)$$

where $\rho = \rho(z)$ is the water density profile over the water column of depth H, bar is depth averaging, g is the gravitational acceleration, and z is the vertical coordinate.

To quantitatively evaluate the model performance, three performance metrics were selected: the root mean square error (RMSE), the Pearson's correlation coefficient ®, and the refined Willmott index (d_{ref}). A "good" model has a low RMSE. The Pearson's correlation coefficient r was used to evaluate the model performance. A value of 1 shows a good correlation between measurements and simulation, whereas values near 0 suggest weaker and often inconsequential correlations. The refined Willmott index d_{ref} is a modeling efficiency index that ranges from −1 to 1. A value that is closer to 1 suggests that the model is performing better. The equation for calculating the d_{ref} is shown in Equation (2) (Willmott et al., 2012). To verify the model's reproducible performance of the CTD distribution and CO_2 dynamics in seawater in the vertical direction, we also used contour plots to compare the simulation results with measurements.

$$d_{ref} = \begin{cases} 1 - \dfrac{\sum_{i=1}^{n}|m_i - o_i|}{2\cdot\sum_{i=1}^{n}|o_i - \bar{o}|}, \text{when} \\ \sum_{i=1}^{n}|m_i - o_i| \le 2\cdot\sum_{i=1}^{n}|o_i - \bar{o}| \\ \dfrac{2\cdot\sum_{i=1}^{n}|o_i - \bar{o}|}{\sum_{i=1}^{n}|m_i - o_i|} - 1, \text{when} \\ \sum_{i=1}^{n}|m_i - o_i| > 2\cdot\sum_{i=1}^{n}|o_i - \bar{o}| \end{cases} \quad (2)$$

where m_i: simulated values, o_i: measured values, $\overline{m}$: mean of simulated values, $\overline{o}$: mean of measured values, n: the number of measurement data.

2.4 Model-based simulation of CO_2 dynamics in SCWs

We applied the developed hydrodynamic-ecological model to simulate the CO_2 dynamics in the whole area of the Yatsushiro Sea for the entire year of 2018. Based on the simulation results, we analyzed the dynamics of CO_2 in the bay in horizontal and vertical directions at different periods and the corresponding influence mechanism. In addition, we also analyzed the changes in the CO_2 dynamics in seawater during the flooding period, which is the period where there are large fluctuations in stratification conditions, and the corresponding influence mechanism by comparing the vertical dynamics of the areas in the Yatsushiro Sea that are more and less influenced by freshwater inflow during the flooding period.

Finally, we used the model to estimate the F_{CO2} between seawater and the atmosphere in the Yatsushiro Sea during the full year of 2018. The F_{CO2} was calculated using the block volume method shown in Equation (2) with the pCO_2 in seawater, atmospheric pCO_2 (pCO_{2air}), the solubility K_0, and the exchange coefficient k. pCO_{2air} was set based on observation data from the JMA (at Ayari). It was indicated that the atmospheric CO_2 concentration (ppm) was numerically almost equal to the pCO_2 in the atmosphere (μatm). Therefore, the annual average measured value of 412 ppm for 2018 was converted to 412 μatm and assumed to be constant throughout the year.

$$F_{CO2} = k \cdot K_0 \cdot (pCO_2 - pCO_{2air}) \quad (3)$$

When the F_{CO2} is negative, it represents absorption from the atmosphere to seawater, while when it is positive it represents emission from seawater to the atmosphere. The solubility K_0 ($mol/m^3/atm$) was determined from the empirical equation based on the water temperature and salinity (Weiss, 1974). The exchange coefficient k was obtained from Equation (4) (Wanninkhof, 1992).

$$k = 0.39 \cdot {U_{10}}^2 \cdot \left(\frac{S_c}{660}\right)^{-0.5} \quad (4)$$

where U_{10} is the wind speed (m/s) at a height 10 m above the sea surface, S_c is the Schmidt number of CO_2, and S_c is derived from the empirical equation (Wanninkhof, 1992).

Due to the large area of the Yatsushiro Sea, it was difficult to obtain very accurate wind speed data for the calculation of F_{CO2}. Figure 2 shows the wind observation stations around the bay. In order to estimate F_{CO2} more precisely, we divided the bay into four areas (see A1 to A4 in Figure 2) near four wind observation stations by referring to the results of water quality and environmental characteristics analysis of the bay (Sonoda et al., 2013), then calculated the F_{CO2} using wind data obtained from Misumi Wind Obs., Matsushima Wind Obs., Yatsushiro Wind Obs., Minamata Wind Obs. (Figure 2) for areas A1, A2, A3, A4 separately.Also, the wind speed data was converted to equivalent sea breeze using the same method in Section 2.2.1.

In addition, U_{10} was corrected in height by a power law from the data of each observatory shown in Equation 5 (Ishizaki and Mitsuta, 1962).

$$U_{10} = U_Z \cdot \left(\frac{10}{Z}\right)^{\frac{1}{n}} \quad (5)$$

where U_Z is the wind speed (m/s) at altitude Z (m) and n is a constant determined by the surface conditions at the observation site.

3 Results and discussion

3.1 Field measurement results and model calibration and validation near the estuary

The results of the three field measurements we implemented at point (1) were used for the calibration and validation of the numerical model simulation results near the estuary of the Kuma River. The final statistical validation results are displayed in Table S1. Among these, salinity, σ_t, and water temperature were used for the verification of the hydrodynamic module. There was a strong correlation between the simulated CTD results and the measured values ($r > 0.9$). The highest correlation was found for water temperature ($r > 0.97$), but its RMSE was relatively high, probably since the measurement site was located near the estuary of the Kuma River and was thus strongly influenced by the freshwater inflow. The river temperature data input to the model was obtained from the prediction of the L–Q equation based on the temperature and flow of the previous years, which contained some errors. The RMSE of both σ_t and salinity showed low values (0.95 kg/m^3 and 0.92 psu). The d_{ref} values for each variable indicated that the model had a good performance (>0.6) for the hydrodynamic simulation of this region. In general, the model's hydrodynamic simulation performance in the Kuma River estuary was in an acceptable range overall, where the performance of the variation trend was better than the numerical fitting performance. Otherwise, since we changed the grid and increased number of layers of the hydrodynamic model developed by Yano et al., we validated the tidal level results at two sites (Misumi Tide Obs. and Yatsushiro Tide Obs. in Figure 2), which showed a good fit, as shown in Figure S2.

The biogeochemical variables (DIC, TA, and pCO_2) were chosen for the verification of the ecological model. Regarding the value of DIC, it had a Pearson correlation value of 0.94, showing a very strong correlation, while the RMSE of 33.10 µmol/kg was at a low level (1.74%) relative to the mean of the measured DIC (1899.4 µmol/kg). The simulated TA also showed a very strong correlation for the measured data ($r = 0.94$), and the ratio of RMSE to the mean of the measured values was at a very low level (2.16%). While the value of r of pCO_2 was lower (0.87) relative to the last two, but again showed a strong correlation, its RMSE value (65.56 µatm) was slightly higher (15%) relative to the ratio of the mean of the measured values, but still in an acceptable range (<30%). The reason for the large numerical errors in pCO_2 while DIC and TA had good numerical fits was that pCO_2 was calculated based on water temperature, salinity, DIC, and TA, and small errors in each of these were superimposed on the final pCO_2 calculation, resulting in large errors in pCO_2; this is a major challenge for pCO_2 simulation in water bodies. Overall, the ecological model had a relatively good performance in simulating the CO_2 dynamics in the Kuma River estuary region, as shown by the d_{ref} values (>0.6) of DIC, TA, and pCO_2.

In addition, we visualized the contour plots of the measured and simulated results separately. The variables output from the hydrodynamic model (i.e., salinity, σ_t, and water temperature) are shown in Figure S2, while the output of the variables from the ecological model (i.e., DIC, TA, and pCO_2) is shown in Figure S3.

Based on the vertical distribution of σ_t (Figure S2A), we confirmed that the field measurements were in the mixing period (7 December 2018), the weakly stratified period (26 August 2018), and the strongly stratified period (2 August 2019). In addition, the vertical distribution of salinity and water temperature show that the region also produces thermohaline stratification similar to the density stratification. As for the results of contour plots of DIC, TA, and pCO_2 (Figures S3A, C, E), the CO_2 dynamics in the water column shows a similar distribution state to that of density stratification.

The comparison of the simulated and observed values of σ_t shows that there were good fitting results for all periods (Figures S2A, B). The maximum error was only about 1 psu. And it had an excellent fitting performance for the periods in strong stratification. The bottom layer was basically consistent at 22 psu, and the error in the surface layer was about 1 psu. The other variables also showed a more excellent fit performance. However, in the simulation of pCO_2 during weak and strong stratification (Figure S3F), the state of high pCO_2 in the bottom layer under stratification was not well simulated. One of the more important reasons for this may be that the ecological module of the model did not consider the influence of zooplankton and benthic organisms, such as the process of their respiration, causing the increase in CO_2 concentration in the bottom water column not to be represented. These advanced biological processes could be added gradually in subsequent modeling. Although the simulation results of pCO_2 in the bottom layer were not satisfactory, the surface pCO_2, which mainly controls the air–water CO_2 exchange, showed a better fitting performance. Moreover, the overall CO_2 dynamic stratification state was better simulated. In summary, the simulated performance of the ecological module for CO_2 dynamics in the Kuma River estuary region was acceptable for our further analysis of the CO_2 dynamics in stratified SCWs.

3.2 Model validation of the whole Yatsushiro sea

Based on the good model fit results near the estuary of the Kuma River ((1) in Figure 2), we adjusted the hydrodynamic conditions of the hydrodynamic module to optimize the applicability of the model regarding the hydrodynamic simulation of the whole area of the Yatsushiro Sea. The

process was based on regular twice-monthly measurements of the bay central route (i.e., the line of nine measurement sites between St.11 and St.19 in Figure 2) implemented by the MLIT in 2018 to calibrate and validate the simulation results. The verified variables were salinity, σ_t, and water temperature. The validation results of the surface and bottom layers of the CTD results for each site are shown in Figure S4. As in Section 3.1, we calculated the r, RMSE, and d_{ref} values between the simulated and measured values for each site; the results are presented in Table S2.

Then, we checked the output of the contour plot, where the x-axis represents the distance between each measurement sites (St.11 to St.19 shown at the top of each figure). We selected the more representative ones among the many comparison results—that is, the results of three time points similar to the mixing period, weak stratification period, and strong stratification period in 3.1—to show. The results are shown in Figure S5.

In addition, we calculated the stratification index of field measurements and model calculations for each station separately according to Equation 1 and made a comparison plot between the simulated and measured values shown in Figure S6.

We also calculated r, RMSE, and d_{ref} for the comparison results of each station (Figure S6). The results show that the model performance for each site was within an acceptable range (Most of the r values were greater than 0.6, except for the salinity of St. 11 and St. 12). St.16, St.17, St.18, and St.19, which are farther from the Kuma River estuary and located in the southern part of the bay, showed excellent relations ($r > 0.9$). In contrast, St.13, St14, and St.15, which are located northward near the estuary of the Kuma River, performed relatively poorly. This is due to the fact that simulating areas with a large freshwater inflow, which is one of our main objectives in this study, is indeed a huge challenge. However, in general our results were still in an acceptable range ($r > 0.6$). In contrast, the fit performance of St.11 and St.12, located in the northernmost part of the bay, was poorer ($r< 0.3$), probably because the strength of the model lay in simulating the stratification phenomenon of seawater. The water depth in this region, being too small, makes it easy to produce results that exceed expectations.

3.3 Discussion of model calibration and validation

As for the calibration and validation of this model, our study was the first attempt to investigate the seawater CO_2 dynamics in the Yatsushiro Sea, which has not been studied before, and these three samples were the only actual measurements of seawater CO_2 in the Yatsushiro Sea, and our planned larger-scale field measurements were not successfully implemented due to some force majeure factors. Although we have only three carbonate measurements from one site, these three measurements are different from the conventional time scale of seawater carbonate measurements, which are often measured in days and sampled only on the surface of the seawater, but are precise measurements in the vertical direction in the water column over half a tidal period with a time interval of 1.5 hour. The three measurement periods were chosen to represent the different mixing states of the shallow seawater to a large extent, including the strongly stratified, weakly stratified and mixed periods, and to cover the seasonal factors.

Based on the validation of these three measurements, we were able to determine that the developed coupled hydrodynamic-ecological model has a relatively good performance in the Kuma River estuary area. In the subsequent analysis, we would like to extend the model to apply to the entire Yatsushiro Sea, although we were unable to calibrate and validate the CO_2 in other areas of the Yatsushiro Sea due to the constraints of the lack of measured data. For this situation, we calibrated and validated the CTD field measurements at nine stations spanning the north and south of the Yatsushiro Sea in the vertical direction throughout the year, and we also quantified the stratification intensity and validated the simulated versus measured values for the stratification intensity as well. Through such a more rigorous, model calibration validation for the biogeochemical and mixing state of the whole area of the Yatsushiro Sea, we verified that the hydrodynamic module of the coupled model can accurately describe the biogeochemical and mixing states in the Yatsushiro Sea in 2018. Moreover, due to the ecological model we developed was based on the coupled hydrodynamic model output, and the parameters of the ecological model were calibrated and validated with three representative biogeochemical and mixed-state measurements in the Yatsushiro Sea. With this model development approach, it is reasonable to assume that combining the ecological model, which can accurately describe the CO_2 dynamics in different mixing states in the Kuma River estuary, with the hydrodynamic model, which can accurately describe the biogeochemical and mixing states in the whole Yatsushiro Sea in 2018, can simulate the CO_2 dynamics in the whole Yatsushiro Sea in an acceptable range, supporting our preliminary analysis of the horizontal and vertical CO_2 dynamics of the entire bay.

However, the calibration and validation method of this model was still weak for simulating the CO_2 dynamics in a highly heterogeneous shallow coastal water. In the future work, more extensive measured data on the CO_2 dynamics of the Yatsushiro Sea with a large temporal and spatial scale are needed in order to improve the simulation performance of the model on the CO_2 dynamics of the entire bay.

3.4 Simulation and analysis of CO2 dynamics in the Yatsushiro sea

We applied the verified model to simulate the CO_2 dynamics of the Yatsushiro Sea for the whole year of 2018. The full-year

2018 Kuma River flow rate and the average density stratification index of the bay are shown in Figure 4A. We can see that the most critical driver of density stratification in the bay is the freshwater inflow from the Kuma River.

The horizontal pCO_2 distribution of the bay is shown in Figure 4B for several more typical periods—namely, the period before the massive flooding of the Kuma River in July 2018 when it was less affected by freshwater inflow (30 May 2018), the period one week after the flooding (10 July 2018), the period three weeks after the flooding (24 July 2018), and the dry winter period (1 December 2018). The x- and y-axes in this figure represent the distance, while the z-axis represents the position in the σ coordinate system in a total of 17 layers. According to the vertical resolution of the model, the 1st and 17th layers are the surface and bottom layers of the water body, respectively, while the 14th layer is the part that accounts for 45% to 55% of the total water depth, which is considered to be the middle part of the water body.

As we can see, the density stratification peaks (9 July 2018, 18:00:00, SI = 232.26) about a week after the influx of large

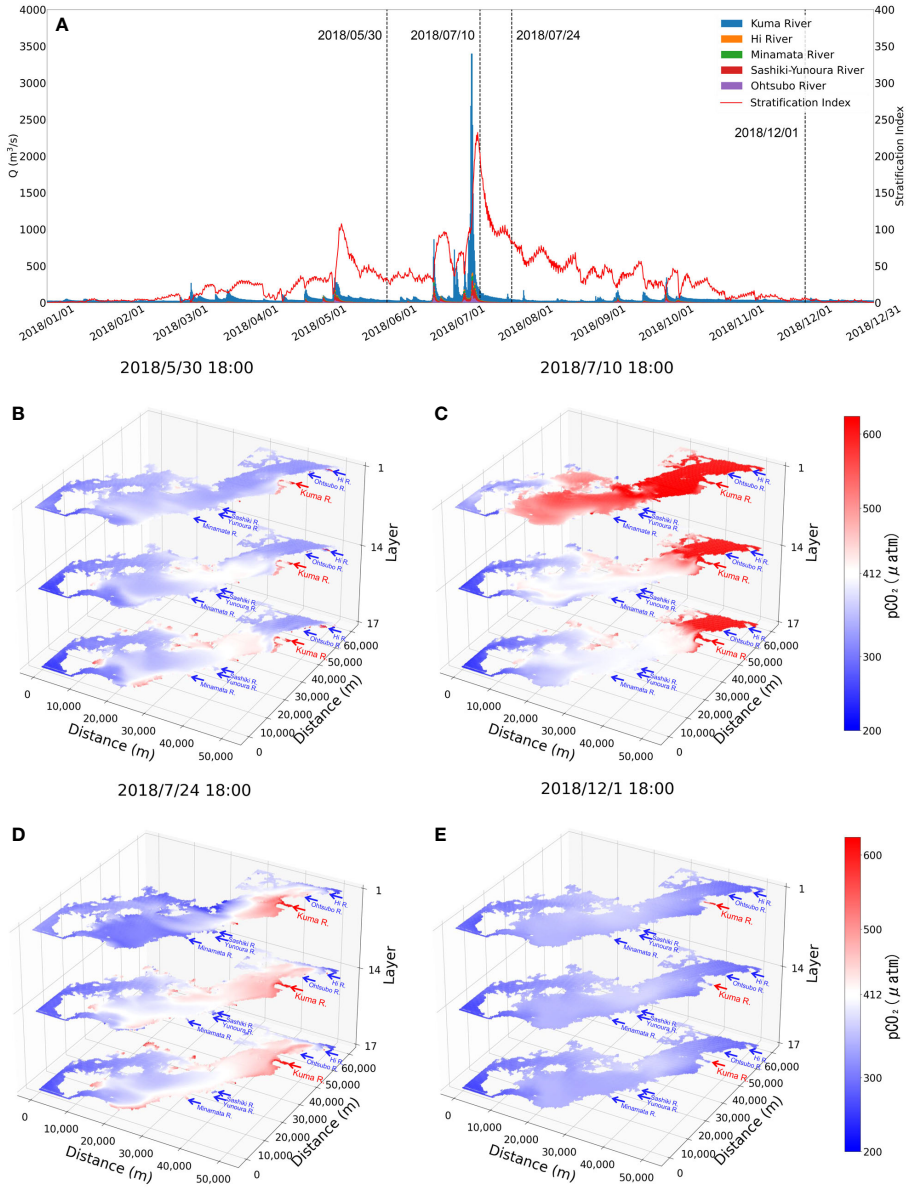

FIGURE 4
Comparison plots of the flow rate of the rivers flowing into the Yatsushiro Sea in 2018 and stratification index **(A)** and the horizontal distribution of pCO_2 for the four periods **(B–E)**.

amounts of freshwater into the bay (Figure 4C). At the same time, with the higher CO_2 concentration freshwater covering the surface of the seawater, the average pCO_2 concentration of the whole bay reaches a peak (surface pCO_{2avg} = 726.31 µatm). The bay during this period exhibits a source of atmospheric CO_2 mainly due to the freshwater inflow.

After another two weeks or so, we can see that the pCO_2 in the surface layer drops to a lower level (24 July 2018, 18:00, surface pCO_{2avg} = 357.34 µatm), with only some high pCO_2 remaining in the surface water near the estuary. In the middle and bottom layers, however, the pCO_2 is higher than that in the surface layer. The main effect of stratification at that time is to inhibit the upwelling of water with a higher level of pCO_2 in the bottom layer to the surface layer, combined with photosynthesis by phytoplankton in surface seawater, resulting in a sink of seawater for atmospheric CO_2. In addition, we found that the pCO_2 in the central part of the bay (the region between distance from 20 to 40 km of the y-axis in Figure 4) is always slightly higher than that in the southern and northern parts during the periods less affected by freshwater inflow (Figure 4B, E). The main reasons for this phenomenon are, on the one hand, that the south and the north are farther away from the Kuma River than the central part, which makes the impact of freshwater less. On the other hand, that the south is connected to the outer sea through the strait, while the north is connected to the Ariake Sea, which makes it easier for these two areas to reduce the impact of freshwater with high pCO_2 through seawater exchange.

The vertical dynamics of the two sites before and after the flooding period with time are shown in Figure 5. pCO_2 and phytoplankton biomass are examined. The two sites are St.13, near the estuary of the Kuma River (Figures 5A–C), and St.18, located in the southern part of the bay, far from the estuary (Figures 5D–F).

By the distribution of phytoplankton biomass in St.18 (Figure 5C), we found that the phytoplankton biomass in this area was much higher around two weeks after the flood than before. In contrast, St.13 had a late start of phytoplankton proliferation due to the influence of freshwater residues. We suggest that during the period after the large-scale freshwater inflow, the bay was subjected to nutrient input from terrestrial sources, leading to a large phytoplankton bloom and thus making the period exhibit a strong sink of atmospheric CO_2. This also resulted in the surface pCO_2 concentrations in most areas of the Yatsushiro Sea during this period (St.18, 24 July

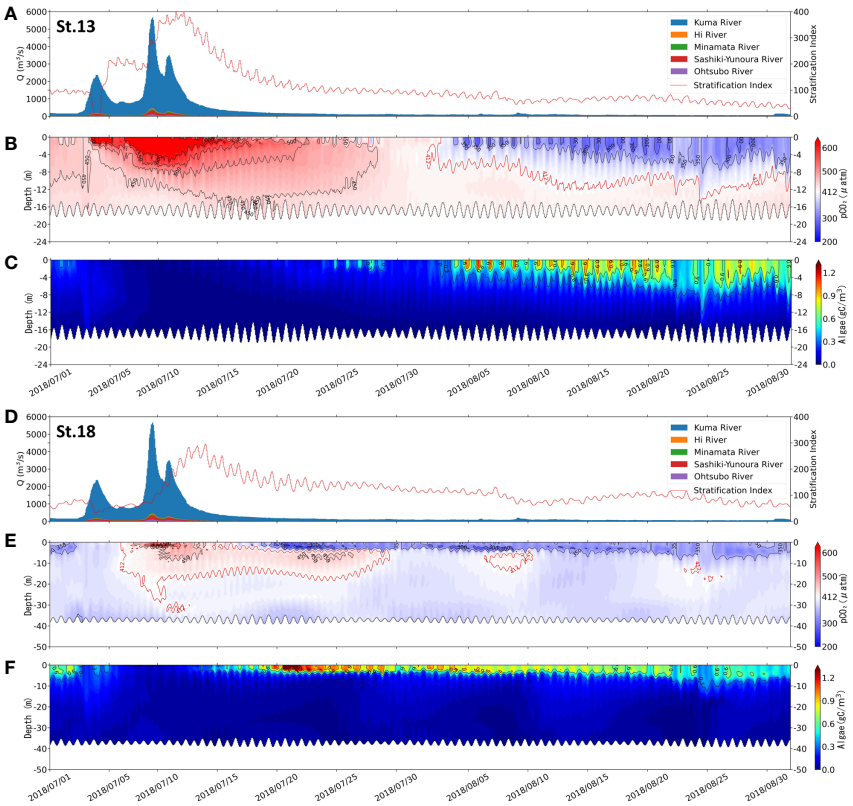

FIGURE 5
Comparison of the flow rate of the rivers flowing into the Yatsushiro Sea and stratification index **(A, D)**, pCO_2 distribution **(B, E)**, and algae biomass distribution **(C, F)** at St.13 **(A–C)** and St.18 **(D–F)** from 1 July 2018 to 1 September 2018.

2018, 18:00, surface pCO_2 = 307.83 µatm) (Figure 4D) being even lower than those before the flood (St.18, 30 May 2018 18:00, surface pCO_2 = 376.61 µatm) (Figure 4B) and during the dry period (St.18, 24 July 2018 18:00, surface pCO_2 = 352.54 µatm) (Figure 4E), except near the estuary.

At St.13, the influence of freshwater lasted for a long time, resulting in the surface pCO_2 (surface pCO_{2avg} = 539.94 µatm) being higher than the atmospheric pCO_2 (412 µatm) for about 40 days starting from June 20. However, at St.18, which is farther from the estuary, the surface layer pCO_2 decreased to a level below atmospheric pCO_2 only about 10 days after the surface layer was covered by freshwater with a high pCO_2 concentration. The surface pCO_2 concentration at this point reached the lowest value (257.82 µatm) at 17:00 on 20 July 2018, which was much lower than that of the middle layer (441.96 µatm) and the bottom layer (360.08 µatm), showing an apparent layered state.

3.5 Correlation between Surface pCO_2 and Stratification

Since stratification in the Yatsushiro Sea is mainly caused by freshwater inflow from the Kuma River, which in turn largely increases the pCO_2 concentration in the surface layer, it is difficult to evaluate the relationship between stratification and pCO_2 dynamics in isolation while ignoring the amount of pCO_2 increase caused by freshwater inflow.

The correlation plot between SI and surface pCO_2 from 1 February 2018 to 31 December 2018 is displayed in Figure 6A. As this simulation started on 1 January 2018, it took about 30 days for the simulated values to reach a more accurate value, so only the results after February 1 are analyzed here. The results show that the surface pCO_2 of St.13 had a strong positive correlation with SI over nearly one full year (r = 0.87), while St.18, which is farther away from the estuary, did not show a significant correlation (r = 0.25). We speculate that this result may be due to the strength and duration of the freshwater influence.

The value of salinity in seawater can be used as an indicator of the influence of freshwater. Figure 6B shows the trend of the surface salinity values of St.13 and St.18 in 2018. We used a salinity value of 32 psu as a cut-off, and we considered a salinity below 32 psu as being more strongly influenced by freshwater. From this figure, we know that St.13 is under a strong freshwater influence for most of the year, except for the dry winter period (mid-October to mid-January). St.18 is only about 25 days after the massive flood in July, when the salinity was below 32 psu.

We divided St.18 into a freshwater-influenced period (7/7 to 7/29), freshwater-abated period (7/29 to 10/17), and dry period (10/18 to 12/31) according to the strength of the freshwater influence in order to explore the factors affecting surface pCO_2 separately. In addition to the relationship between SI and pCO_2, we also analyzed the correlation between water temperature, DIC, and algae together, where all the values except SI were surface values. The results are displayed in Figure 7.

During the freshwater-influenced period (Figure 7A), the density stratification of St.18 was highly developed (SI > 100), with pCO_2 showing a strong positive correlation with SI (r = 0.82). During the freshwater-abated period (Figure 7B), St.18 maintained a strong stratification (SI > 80) in the first half of the period and the SI had a strong negative correlation with pCO_2 (r = −0.87). During the dry period (Figure 7C), although pCO_2 showed a strong positive correlation with SI (r = 0.84), the effect

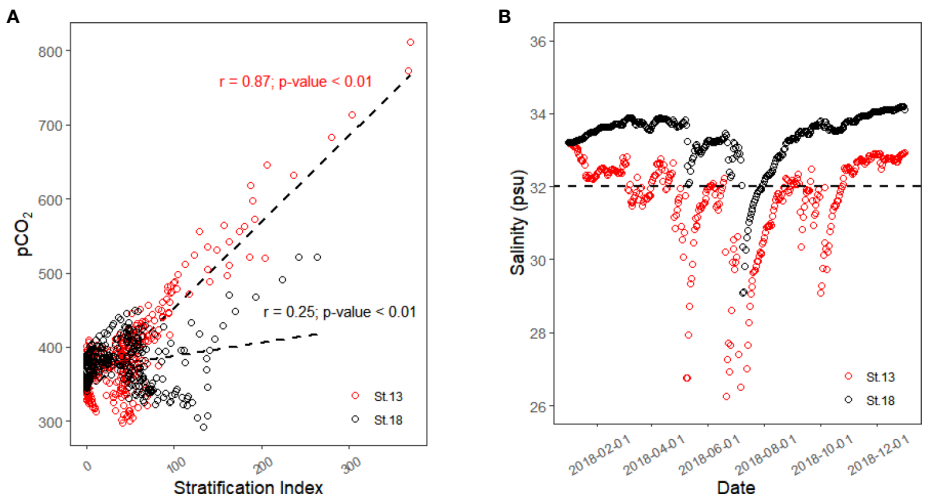

FIGURE 6
Linear correlation between surface pCO_2 and stratification index **(A)** and surface salinity of St.13 and St.18 in 2018 **(B)**.

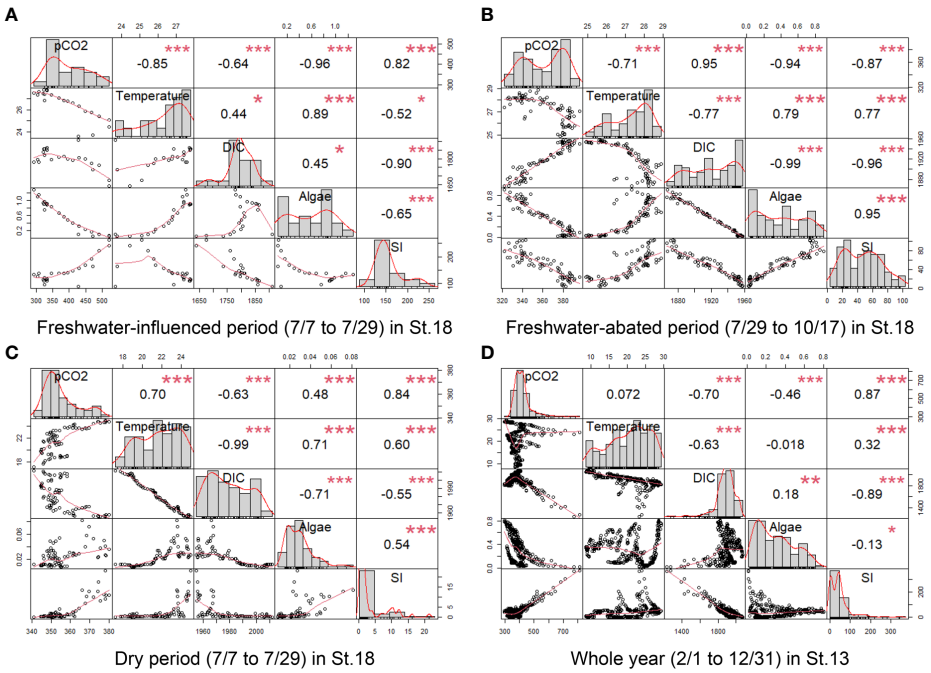

FIGURE 7
Multiple linear regression (Pearson's correlation coefficients and *p*-values) (* $p \leq 0.05$, ** $p \leq 0.01$, *** $p \leq 0.001$) at different periods of St.13 **(D)** and St.18 **(A–C)**. The items involved in the analysis were pCO_2, water temperature, salinity, DIC, TA, algae, and SI.

of SI on pCO_2 was very limited due to the very weak stratification during this period (SI< 10). In addition, regardless of the period, we found that surface DIC was negatively correlated with SI and showed a solidly negative correlation (r< −0.9) in the more stratified periods (Figures 7A, B). They had a strong negative correlation (r = −0.89) even throughout the whole year of St.13. In general, it can be concluded that in stratified waters, stratification is the main factor affecting pCO_2 in surface waters, with a positive correlation occurring during the freshwater-influenced period and a negative correlation occurring during the freshwater-abated period.

The natural fluctuation of pCO_2 in coastal water is related to biological processes such as respiration and photosynthesis (Shamberger et al., 2011; Buapet et al., 2013; Saderne et al., 2013; Edman and Anderson, 2014). In contrast, during periods of oligotrophy and low seawater temperatures, when biological activity is suppressed due to insufficient nutrient supply or low-temperature conditions, the temperature is likely to be the main factor affecting the distribution of pCO_2 in the water column (Bates et al., 1998; Borges et al., 2006). In general, phytoplankton in the surface layer reduces pCO_2 through photosynthesis—for example, from July to October when stratification is strong (Figures 7A, B), both showed very strong negative correlations (r = −0.96 and r = −0.94). However, the correlation between phytoplankton and pCO_2 was not significant for other periods, partly because of the low number of phytoplankton and partly because phytoplankton in the water column provide easily degradable organic carbon through respiration over time. The increase in temperature between July and October reduced pCO_2, which was strongly related to the influx of nutrients. Phytoplankton proliferated rapidly and had more intense biological processes under the combined effect of high nutrient levels and suitable temperatures. After October, the water temperature changed to a strong positive correlation with pCO_2 (r = 0.7).

3.6 CO2 flux of the Yatsushiro sea

From the results of the air–water CO_2 exchange fluxes by month (Figure 8), the response of F_{CO2} to stratification and freshwater inflow varies depending on the distance from the estuary of the Kuma River. The A2 area, because it is located near the estuary, always has the highest absolute value of F_{CO2}, regardless of whether it is in the absorption or emission phase. A4 area is a sink for atmospheric CO_2 at all times of the year because it is the furthest from the estuary and can easily exchange seawater with the outer ocean.

From the numerical results, the highest CO_2 release flux (19.47 mmol/m^2/day) is at A2 in July, while the highest absorption (−7.11 mmol/m^2/day) is at A2 in December. It can

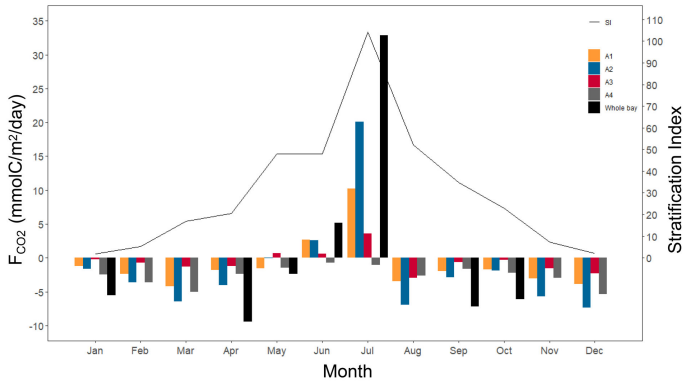

FIGURE 8
Monthly air–water CO_2 fluxes for the four areas and the whole bay (A1 to A4, Whole bay), and the stratification index of the Yatsushiro Sea.

be seen that the Yatsushiro Sea is a sink area for atmospheric CO_2 (−1.7 mmol/m^2/day) throughout the year, except for June and July, when there is a large inflow of freshwater, which is the source of atmospheric CO_2. Even in the A4 area, which is the least affected by freshwater and closest to the outer sea, its sink intensity decreases to very low in June and July (−0.73 and −1.04 mmol/m^2/day). This result shows that freshwater inflow plays a critical role in influencing the F_{CO2} of the bay. Due to the respiration of terrestrial organic carbon and the terrestrial input of freshwater CO_2, most inland waters and estuaries are substantial CO_2 contributors to the atmosphere (Borges and Abril, 2011; Chen et al., 2013; Raymond et al., 2013; Hotchkiss et al., 2015). The Yatsushiro Sea, on the other hand, experiences relatively less influence from human activities (the population of the basin is 170,000), which may result in the bay having biogeochemical processes that are more distinct from them, leading to the bay being a sink for atmospheric CO_2 throughout the year.

In this work, we only estimated the flux of air-water CO_2 exchange in the whole Yatsushiro Sea with the simplified ecological model developed this time, and did not quantify the flux of CO_2 within the water column. It is expected that, like other shallow coastal waters where blue carbon ecosystems grow, in the Yatsushiro Sea, most of the CO_2 that sinks into the seawater will be absorbed and fixed in the sediment by the biological processes of blue carbon ecosystems such as seagrass beds, corals and marine phytoplankton. In addition, the lateral carbon fluxes between the Yatsushiro Sea and the outer sea are of equal interest. Continuing field measurements of CO_2 dynamics and blue carbon ecosystems in the Yatsushiro Sea in subsequent studies, coupling the effects of higher ecosystems such as seagrass beds and coral reefs into this ecological model as well, continuing to optimize the accuracy of the model and attempting to quantify carbon fluxes within the Yatsushiro Sea taking into account stratification effects is essential to further understand the contribution of stratified shallow coastal waters with growing blue carbon ecosystems to the reduction of atmospheric CO_2.

4 Conclusions

In this study, we chose the Yatsushiro Sea, where CO_2 dynamics have never been studied before to conduct the first field measurements of CO_2 dynamics. We found that pCO_2 is stratified in the vertical direction with density stratification at the estuary of the Kuma River.

Based on the field measurement results, we considering the influence of stratification, developed a high-resolution 3D hydrodynamic-ecological numerical model that can accurately reproduce the CO_2 dynamics of the estuary area of the Kuma River, then extended the application of the ecological model by coupling it with the hydrodynamic model that can also well reproduce the CTD profiles and the mixing states of the whole Yatsushiro Sea. In terms of the hydrodynamic module, the model not only fits the estuarine measurement results very well ($d_{ref} > 0.6$) but also performs very well in the calculations for the whole domain of the bay (d_{ref} between 0.18 and 0.92). In addition, the fit of the parameter SI, which evaluates the strength of water density stratification, also has an excellent performance (d_{ref} between 0.23 and 0.76). In the ecological module, the model can basically reproduce the CO_2 dynamics in the estuary region of the Kuma River ($d_{ref} > 0.6$), and more measured CO_2 dynamics data are needed to improve the model on CO_2 dynamics of the whole bay. Also, the biological processes are still need to be improved in subsequent studies.

Using this model, we simulated the CO_2 dynamics of the bay in 2018 and preliminary analyzed the interaction between

seawater CO_2 dynamics and stratification in the bay. The results show that the CO_2 dynamics of the bay has substantial fluctuations in both the horizontal and vertical directions. Depending on the distance from the estuary and the outer sea in the horizontal direction, the surface pCO_2 varies greatly depending on the strength and duration of the freshwater influence. In the vertical direction, stratification strongly contributes to the maintenance of high pCO_2 concentrations in the surface water during the freshwater influence period. During the dissipation period of freshwater influence, stratification causes the pCO_2 concentration in the surface water to be much lower than that in the middle and bottom of the water.

Finally, we used the model to estimate the annual pattern of F_{CO2} in the bay in 2018. The results show that the Yatsushiro Sea becomes a source of atmospheric CO_2 in June and July when the freshwater inflow is high and a sink of atmospheric CO_2 at all other times. And the Yatsushiro Sea was a sink area for atmospheric CO_2 in 2018 (−1.70 mmol/m^2/day).

Data availability statement

The original contributions presented in the study are included in the article/Supplementary Material. Further inquiries can be directed to the corresponding author.

Author contributions

Conceptualization, methodology and writing—original draft preparation: BX and SY. Writing—review and check: SY, KK, and KN. Field measurements: BX, SY, NS, and HK. Numerical model development: BX, NS, BC, and LH. All authors have read and agreed to the published version of the manuscript. All authors contributed to the article and approved the submitted version.

Funding

This research was funded by JSPS KAKENHI Grant NumberJP18H01545, JP22K18832, JP22H01601 and by JST SPRING Grant Number JPMJSP2136.

Acknowledgments

This work was supported by the JSPS KAKENHI GrantNumber JP18H01545, JP22K18832 and JP22H01601, and by JST SPRING Grant NumberJPMJSP2136. The authors would like to express theirprofound thanks.

Conflict of interest

Author BX was employed by Guangzhou Municipal Group Co., Ltd.

The remaining authors declare that the research was conducted in the absence of any commercial or financial relationships that could be construed as a potential conflict of interest.

Publisher's note

Supplementary material

The Supplementary Material for this article can be found online at: https://www.frontiersin.org/articles/10.3389/fmars.2022.991802/full#supplementary-material

SUPPLEMENTARY FIGURE 1
Hydrodynamic model validation (tide level), (A) for Misumi Observatory, (B) for Yatsushiro Observatory.

SUPPLEMENTARY FIGURE 2
Comparison of contour plots of σt **(A, B)**, salinity **(C, D)**, and water temperature **(E, F)** for each mixing state at the measurement point ((1) in Figure 1) located at the estuary of the Kuma River. Measurement results (top, **(A, C, E)**) and numerical model results (bottom, **(B, D, F)**).

SUPPLEMENTARY FIGURE 3
Comparison of contour plots of DIC **(A, B)**, TA **(C, D)**, and pCO2 **(E, F)** for each mixing state at the measurement point ((1) in Figure 1) located at the estuary of the Kuma River. Measurement results (top, **(A, C, E)**) and numerical model results (bottom, **(B, D, F)**).

SUPPLEMENTARY FIGURE 4
Comparison of σt **(A)**, salinity **(B)**, and water temperature **(C)** at surface layer **(A-1, B-1, C-1)** and bottom layer **(A-2, B-2, C-2)** between the simulation and field measurement at each station (St.11 to St.19 are the results of each station respectively).

SUPPLEMENTARY FIGURE 5
Comparison of contour plots of σt **(A, B)**, salinity **(C, D)**, and water temperature **(E, F)** for each mixing state at each point located on the central line of the Yatsushiro Sea (St.11 to St19 in Figure 1). Measurement results (top, **(A, C, E)**) and numerical model results (bottom, **(B, D, F)**).

SUPPLEMENTARY FIGURE 6
Comparison of stratification index between the simulation and field measurement at each station (St.11 to St.19 are the results of each station respectively).

References

Alongi, D. M., Murdiyarso, D., Fourqurean, J. W., Kauffman, J. B., Hutahaean, A., Crooks, S., et al. (2016). Indonesia's blue carbon: a globally significant and vulnerable sink for seagrass and mangrove carbon. *Wetlands Ecol. Manage.* 24 (1), 3–13. doi: 10.1007/s11273-015-9446-y

Alosairi, Y., and Alsulaiman, N. (2019). Hydro-environmental processes governing the formation of hypoxic parcels in an inverse estuarine water body: Model validation and discussion. *Mar. pollut. Bull.* 144, 92–104. doi: 10.1016/j.marpolbul.2019.04.067

Arakawa, H., Kanda, Y., and Ishihara, T. (2007). Prediction of Sea surface wind distribution with a three dimensional wind model. *Proc. OF Coast. ENGINEERING JSCE* 54, 131–135. doi: 10.2208/proce1989.54.131

Bakker, D. C. E., de Baar, H. J. W., and de Jong, E. (1999). The dependence on temperature and salinity of dissolved inorganic carbon in East Atlantic surface waters. *Mar. Chem.* 65 (3), 263–280. doi: 10.1016/S0304-4203(99)00017-1

Bates, N. R., Takahashi, T., Chipman, D. W., and Knap, A. H. (1998). Variability of pCO2 on diel to seasonal timescales in the Sargasso Sea near Bermuda. *J. Geophys. Res.* 103(C8), 15567–15585. doi: 10.1029/98JC00247.

Bauer, J. E., Cai, W.-J., Raymond, P. A., Bianchi, T. S., Hopkinson, C. S., and Regnier, P. A. G. (2013). The changing carbon cycle of the coastal ocean. *Nature* 504 (7478), 61–70. doi: 10.1038/nature12857

Blauw, A. N., Los, H. F. J., Bokhorst, M., and Erftemeijer, P. L. A. (2008). GEM: a generic ecological model for estuaries and coastal waters. *Hydrobiologia* 618 (1), 175–175. doi: 10.1007/s10750-008-9575-x

Boldrin, A., Carniel, S., Giani, M., Marini, M., Bernardi Aubry, F., Campanelli, A., et al. (2009). Effects of bora wind on physical and biogeochemical properties of stratified waters in the northern Adriatic. *J. Geophysical Research: Oceans* 114, C08S92. doi: 10.1029/2008JC004837

Borges, A. V., and Abril, G. (2011). *5.04 - carbon dioxide and methane dynamics in estuaries*. Eds. E. Wolanski, D. McLusky and S. Coastal (Waltham: Academic Press), 119–161.

Borges, A. V., Schiettecatte, L.-S., Abril, G., Delille, B., and Gazeau, F. (2006). Carbon dioxide in European coastal waters. *Estuarine Coast. Shelf Sci.* 70, 375–387. doi: 10.1016/j.ecss.2006.05.046

Buapet, P., Gullström, M., and Björk, M. (2013). Photosynthetic activity of seagrasses and macroalgae in temperate shallow waters can alter seawater pH and total inorganic carbon content at the scale of a coastal embayment. *Mar. Freshw. Res.* 64 (11), 1040–1048. doi: 10.1071/MF12124

Chen, C. T. A., Huang, T. H., Chen, Y. C., Bai, Y., He, X., and Kang, Y. (2013). Air–sea exchanges of CO2 in the world's coastal seas. *Biogeosciences* 10 (10), 6509–6544. doi: 10.5194/bg-10-6509-2013

Chen, Z., Huang, P., and Zhang, Z. (2019). Interaction between carbon dioxide emissions and eutrophication in a drinking water reservoir: A three-dimensional ecological modeling approach. *Sci. Total Environ.* 663, 369–379. doi: 10.1016/j.scitotenv.2019.01.336

Chen, C.-T. A., Zhai, W., and Dai, M. (2008). Riverine input and air–sea CO2 exchanges near the changjiang (Yangtze river) estuary: Status quo and implication on possible future changes in metabolic status. *Continental Shelf Res.* 28 (12), 1476–1482. doi: 10.1016/j.csr.2007.10.013

Deltares (2017). *Delft3D-FLOW users' manual; simulation of multi-dimensional hydrodynamic flows and transport phenomena, including sediments. version: 3.15* (The Netherlands: Deltares, Delft).

Deltares (2018). *Delft3D functional specifications*. (The Netherlands: Deltares, Delft) 46–46.

Donato, D. C., Kauffman, J. B., Murdiyarso, D., Kurnianto, S., Stidham, M., and Kanninen, M. (2011). Mangroves among the most carbon-rich forests in the tropics. *Nat. Geosci.* 4 (5), 293–297. doi: 10.1038/ngeo1123

Duarte, C. M., Marbà, N., Gacia, E., Fourqurean, J. W., Beggins, J., Barrón, C., et al. (2010). Seagrass community metabolism: Assessing the carbon sink capacity of seagrass meadows. *Global Biogeochemical Cycles* 24, GB4032. doi: 10.1029/2010GB003793

Duarte, C. M., Middelburg, J. J., and Caraco, N. (2005). Major role of marine vegetation on the oceanic carbon cycle. *Biogeosciences* 2 (1), 1–8. doi: 10.5194/bg-2-1-2005

Edman, M. K., and Anderson, L. G. (2014). Effect on pCO2 by phytoplankton uptake of dissolved organic nutrients in the central and northern Baltic Sea, a model study. *J. Mar. Syst.* 139, 166–182. doi: 10.1016/j.jmarsys.2014.06.004

Eyre, B. D. (2000). "Regional evaluation of nutrient transformation and phytoplankton growth in nine river-dominated sub-tropical east Australian estuaries," in *Marine ecology progress series*. 205, 61–83. doi: 10.3354/meps205061

Falkowski, P. G., and Raven, J. A. (2013). *Aquatic photosynthesis: (Second Edition)*. (Princeton: Princeton University Press).

Fourqurean, J. W., Duarte, C. M., Kennedy, H., Marbà, N., Holmer, M., Mateo, M. A., et al. (2012). Seagrass ecosystems as a globally significant carbon stock. *Nat. Geosci.* 5 (7), 505–509. doi: 10.1038/ngeo1477

Golterman, H. (1982). Reviewed work: Aquatic chemistry. an introduction emphasizing chemical equilibria in natural waters. *J. Ecol.* 70 (3), 924–925. doi: 10.2307/2260132

Gurel, M., Tanik, A., Gonec, E., and Russo, R. C. (2005). *Biogeochemical Cycles*. In: J. P. Wolflin and I. E Gonenc, eds. Coastal Lagoons. s.l.: CRC Press

Hao, L., Sato, Y., Yano, S., Xiong, B., and Chi, B. (2021). Effects of Large-scale effluent of the chikugo river due to 2020 Kyushu floods on the development of hypoxia in the ariake Sea. *J. Japan Soc. Civil Engineers Ser. B2 (Coastal Engineering)* 77, I_865–I_870. doi: 10.2208/kaigan.77.2_I_865

Hartnett, H. E., Keil, R. G., Hedges, J. I., and Devol, A. H. (1998). Influence of oxygen exposure time on organic carbon preservation in continental margin sediments. *Nature* 391 (6667), 572–575. doi: 10.1038/35351

Hotchkiss, E. R., Hall, R. O.Jr., Sponseller, R. A., Butman, D., Klaminder, J., Laudon, H., et al. (2015). Sources of and processes controlling CO 2 emissions change with the size of streams and rivers. *Nat. Geosci.* 8, 696–699. doi: 10.1038/ngeo2507

Howard, J. L., Creed, J. C., Aguiar, M. V. P., and Fourqurean, J. W. (2018). CO2 released by carbonate sediment production in some coastal areas may offset the benefits of seagrass "Blue carbon" storage. *Limnology Oceanography* 63 (1), 160–172. doi: 10.1002/lno.10621

Howard, J., Sutton-Grier, A., Herr, D., Kleypas, J., Landis, E., McLeod, E., et al. (2017). Clarifying the role of coastal and marine systems in climate mitigation. *Front. Ecol. Environ.* 15 (1), 42–50. doi: 10.1002/fee.1451

Howarth, R., Chan, F., Conley, D. J., Garnier, J., Doney, S. C., Marino, R., et al. (2011). Coupled biogeochemical cycles: eutrophication and hypoxia in temperate estuaries and coastal marine ecosystems. *Front. Ecol. Environ.* 9 (1), 18–26. doi: 10.1890/100008

Ishizaki, H., and Mitsuta, Y. (1962). On the scale of peak gust and the gust factor. *Disaster Prev. Res. Inst. Annu.* 5, 135–138. Available at: https://www.dpri.kyoto-u.ac.jp/nenpo/no05/05a0/a05a0p15.pdf

Koho, K. A., Nierop, K. G. J., Moodley, L., Middelburg, J. J., Pozzato, L., Soetaert, K., et al. (2013). Microbial bioavailability regulates organic matter preservation in marine sediments. *Biogeosciences* 10 (2), 1131–1141. doi: 10.5194/bg-10-1131-2013

Koné, Y. J. M., Abril, G., Kouadio, K. N., Delille, B., and Borges, A. V. (2009). Seasonal variability of carbon dioxide in the rivers and lagoons of ivory coast (West Africa). *Estuaries Coasts* 32 (2), 246–260. doi: 10.1007/s12237-008-9121-0

Kubo, A., Maeda, Y., and Kanda, J. (2017). A significant net sink for CO2 in Tokyo bay. *Sci. Rep.* 7 (1), 44355–44355. doi: 10.1038/srep44355

Kuwae, T., Kanda, J., Kubo, A., Nakajima, F., Ogawa, H., Sohma, A., et al. (2016). Blue carbon in human-dominated estuarine and shallow coastal systems. *Ambio* 45 (3), 290–301. doi: 10.1007/s13280-015-0725-x

Lavigne, H., and Gattuso, J. (2010). *Seacarb: seawater carbonate chemistry with R. R package version 2.4.10*. Available at: http://CRAN.R-project.org/package=seacarb

Le Quéré, C., Andrew, R. M., Canadell, J. G., Sitch, S., Korsbakken, J. I., Peters, G. P., et al. (2016). Global carbon budget 2016. *Earth Syst. Sci. Data* 8 (2), 605–649. doi: 10.5194/essd-8-605-2016

Lesser, G. R., Roelvink, J. A., van Kester, J. A. T. M., and Stelling, G. S. (2004). Development and validation of a three-dimensional morphological model. *Coast. Eng.* 51, 883–915. doi: 10.1016/j.coastaleng.2004.07.014

Lo Iacono, C., Mateo, M. A., Gràcia, E., Guasch, L., Carbonell, R., Serrano, L., et al. (2008). Very high-resolution seismo-acoustic imaging of seagrass meadows (Mediterranean sea): Implications for carbon sink estimates. *Geophysical Res. Lett.* 35 (18), L18601. doi: 10.1029/2008GL034773

Macreadie, P. I., Serrano, O., Maher, D. T., Duarte, C. M., and Beardall, J. (2017). Addressing calcium carbonate cycling in blue carbon accounting. *Limnology Oceanography Lett.* 2 (6), 195–201. doi: 10.1002/lol2.10052

Maher, D. T., and Eyre, B. D. (2012). Carbon budgets for three autotrophic Australian estuaries: Implications for global estimates of the coastal air-water CO2 flux. *Global Biogeochemical Cycles* 26, GB1032. doi: 10.1029/2011GB004075

McKee, K. L., Cahoon, D. R., and Feller, I. C. (2007). Caribbean Mangroves adjust to rising sea level through biotic controls on change in soil elevation. *Global Ecol. Biogeography* 16 (5), 545–556. doi: 10.1111/j.1466-8238.2007.00317.x

McLeod, E., Chmura, G. L., Bouillon, S., Salm, R., Björk, M., Duarte, C. M., et al. (2011). A blueprint for blue carbon: Toward an improved understanding of the role of vegetated coastal habitats in sequestering CO2. *Front. Ecol. Environ.* 9, 552–560. doi: 10.1890/110004

Menshutkin, V. V., Rukhovets, L. A., and Filatov, N. N. (2014). Ecosystem modeling of freshwater lakes (review): 2. models of freshwater lake's ecosystem. *Water Resour.* 41 (1), 32–45. doi: 10.1134/S0097807814010084

Murdiyarso, D., Purbopuspito, J., Kauffman, J. B., Warren, M. W., Sasmito, S. D., Donato, D. C., et al. (2015). The potential of Indonesian mangrove forests for global climate change mitigation. *Nat. Climate Change* 5 (12), 1089–1092. doi: 10.1038/nclimate2734

Nakayama, K., Komai, K., Tada, K., Lin, H. C., Yajima, H., Yano, S., et al. (2020). Modeling dissolved inorganic carbon considering submerged aquatic vegetation. *Ecol. Model.* 431, 109188. doi: 10.1016/j.ecolmodel.2020.109188

Nellemann, C., Corcoran, E., Duarte, E, , C., Valdes, M., DeYoung, L., Fonseca, C., et al (2009). *Blue carbon*. A rapid response assessment. Birkeland: UNEP, GRID-Arendal, Bikeland Trykkeri A.S. 78 p.

Niu, L., van Gelder, P., Zhang, C., Guan, Y., and Vrijling, J. K. (2016). Physical control of phytoplankton bloom development in the coastal waters of jiangsu (China). *Ecol. Model.* 321, 75–83. doi: 10.1016/j.ecolmodel.2015.10.008

Raven, J. A., and Falkowski, P. G. (1999). Oceanic sinks for atmospheric CO2. *Plant Cell Environ.* 22, 741–755. doi: 10.1046/j.1365-3040.1999.00419.x

Raymond, P. A., Hartmann, J., Lauerwald, R., Sobek, S., McDonald, C., Hoover, M., et al. (2013). Global carbon dioxide emissions from inland waters. *Nature* 503 (7476), 355–359. doi: 10.1038/nature12760

Saderne, V., Fietzek, P., and Herman, P. M. J. (2013). Extreme variations of pCO2 and pH in a macrophyte meadow of the Baltic Sea in summer: Evidence of the effect of photosynthesis and local upwelling. *PLoS One* 8 (4), e62689–e62689. doi: 10.1371/journal.pone.0062689

Shamberger, K. E. F., Feely, R. A., Sabine, C. L., Atkinson, M. J., DeCarlo, E. H., Mackenzie, F. T., et al. (2011). Calcification and organic production on a Hawaiian coral reef. *Mar. Chem.* 127, 64–75. doi: 10.1016/j.marchem.2011.08.003

Shim, J., Kim, D., Kang, Y. C., Lee, J. H., Jang, S.-T., and Kim, C.-H. (2007). Seasonal variations in pCO2 and its controlling factors in surface seawater of the northern East China Sea. *Continental Shelf Res.* 27 (20), 2623–2636. doi: 10.1016/j.csr.2007.07.005

Simpson, J. H., Brown, J., Matthews, J., and Allen, G. (1990). Tidal straining, density currents, and stirring in the control of estuarine stratification. *Estuaries* 13 (2), 125–132. doi: 10.2307/1351581

Sohma, A., Shibuki, H., Nakajima, F., Kubo, A., and Kuwae, T. (2018). Modeling a coastal ecosystem to estimate climate change mitigation and a model demonstration in Tokyo bay. *Ecol. Model.* 384, 261–289. doi: 10.1016/j.ecolmodel.2018.04.019

Sonoda, Y., Takikawa, K., Kawasaki, S., Aoyama, C., and Saito, T. (2013). CHARACTERISTICS OF WATER QUALITY ENVIRONMENT IN THE YATSUSHIRO SEA AREA. *J. Japan Soc. Civil Engineers Ser. B3 (Ocean Engineering)* 69, I_1240–I_1245. doi: 10.2208/jscejoe.69.I_1240

Sylaios, G., Tsihrintzis, V., and Haralambidou, K. (2006). *Modeling stratification – mixing processes at the mouth of a dam – controlled river*. European Water 13(14), 21–28. Available at: https://www.ewra.net/ew/pdf/EW_2006_13-14_03.pdf.

Tadokoro, M., and Yano, S. (2019). EVALUATION OF EFFECTS OF TEMPERATURE AND RIVER DISCHARGE CHANGES DUE TO CLIMATE CHANGE ON HYPOXIA IN THE ARIAKE SEA. *J. Japan Soc. Civil Engineers Ser. B2 (Coastal Engineering)* 75, I_1231–I_1236. doi: 10.2208/kaigan.75.I_1231

Tokoro, T., Hosokawa, S., Miyoshi, E., Tada, K., Watanabe, K., Montani, S., et al. (2014). Net uptake of atmospheric CO2 by coastal submerged aquatic vegetation. *Global Change Biol.* 20 (6), 1873–1884. doi: 10.1111/gcb.12543

Verspagen, J. M. H., Van de Waal, D. B., Finke, J. F., Visser, P. M., Van Donk, E., and Huisman, J. (2014). Rising CO2 levels will intensify phytoplankton blooms in eutrophic and hypertrophic lakes. *PLoS One* 9 (8), e104325–e104325. doi: 10.1371/journal.pone.0104325

Wakeham, S. G., Howes, B. L., Dacey, J. W. H., Schwarzenbach, R. P., and Zeyer, J. (1987). Biogeochemistry of dimethylsulfide in a seasonally stratified coastal salt pond. *Geochimica Cosmochimica Acta* 51 (6), 1675–1684. doi: 10.1016/0016-7037(87)90347-4

Wang, S.-y., and Zhai, W.-d. (2021). Regional differences in seasonal variation of air–sea CO2 exchange in the yellow Sea. *Continental Shelf Res.* 218, 104393. doi: 10.1016/j.csr.2021.104393

Wanninkhof, R. (1992). Relationship between wind speed and gas exchange over the ocean. *J. Geophysical Research: Oceans* 97 (C5), 7373–7382. doi: 10.1029/92JC00188

Weiss, R. F. (1974). Carbon dioxide in water and seawater: the solubility of a non-ideal gas. *Mar. Chem.* 2 (3), 203–215. doi: 10.1016/0304-4203(74)90015-2

Willmott, C. J., Robeson, S. M., and Matsuura, K. (2012). A refined index of model performance. *Int. J. climatology* 32 (13), 2088–2094. doi: 10.1002/joc.2419

Wiseman, W. J., Rabalais, N. N., Turner, R. E., Dinnel, S. P., and MacNaughton, A. (1997). Seasonal and interannual variability within the Louisiana coastal current: stratification and hypoxia. *J. Mar. Syst.* 12 (1), 237–248. doi: 10.1016/S0924-7963(96)00100-5

Yamaguchi, S., and Hayami, Y. (2018). Impact of Isahaya dike construction on DO concentration in the Ariake Sea. *J Oceanogr* 74, 565–586. doi: 10.1007/s10872-017-0454-9

Yano, S., Winterwerp, J. C., Tai, A., and Saita, T. (2010). Numerical experiments on features of nonlinear tide and its influences on sediment transport in the ariake Sea and the yatsushiro Sea. *J. Japan Soc. Civil Engineers Ser. B2 (Coastal Engineering)* 66, 341–345. doi: 10.2208/kaigan.66.341

Zeebe, R. E., and Wolf-Gladrow, D. (2001). *CO2 in seawater: equilibrium, kinetics, isotopes*. Amsterdam: Elsevier Oceanography Book Series. 65, 346 pp.

Zhai, W., and Dai, M. (2009). On the seasonal variation of air – sea CO2 fluxes in the outer changjiang (Yangtze river) estuary, East China Sea. *Mar. Chem.* 117 (1), 2–10. doi: 10.1016/j.marchem.2009.02.008

frontiers | Frontiers in Marine Science

TYPE Opinion
PUBLISHED 14 November 2022
DOI 10.3389/fmars.2022.1044135

OPEN ACCESS

EDITED BY
Jeng-Wei Tsai,
China Medical University, Taiwan

REVIEWED BY
Chen Xu,
Texas A&M University at Galveston, United States
Yanbin Li,
Ocean University of China, China

*CORRESPONDENCE
Khan M. G. Mostofa
mostofa@tju.edu.cn

SPECIALTY SECTION
This article was submitted to Marine Biogeochemistry, a section of the journal Frontiers in Marine Science

RECEIVED 14 September 2022
ACCEPTED 31 October 2022
PUBLISHED 14 November 2022

CITATION
Mostofa KMG, Sakugawa H, Yuan J, Liu C-Q, Senesi N, Mohinuzzaman M, Liu Y, Yang X, Vione D and Li S-L (2022) Continuous production-degradation of dissolved organic matter provides signals of biogeochemical processes from terrestrial to marine end-members. *Front. Mar. Sci.* 9:1044135. doi: 10.3389/fmars.2022.1044135

Continuous production-degradation of dissolved organic matter provides signals of biogeochemical processes from terrestrial to marine end-members

Khan M. G. Mostofa[1,2]*, Hiroshi Sakugawa[3], Jie Yuan[4], Cong-Qiang Liu[1,2], Nicola Senesi[5], Mohammad Mohinuzzaman[1,6], Yijun Liu[1,2], Xuemei Yang[1], Davide Vione[7,8] and Si-Liang Li[1,2]

[1]School of Earth System Science, Tianjin University, Tianjin, China, [2]Tianjin Key Laboratory of Earth Critical Zone Science and Sustainable Development in Bohai Rim, Tianjin University, Tianjin, China, [3]Graduate School of Biosphere Science, Department of Environmental Dynamics and Management, Hiroshima University, Higashi-Hiroshima, Japan, [4]College of Resources and Environment, Xingtai University, Xingtai, Hebei, China, [5]Dip.to di Scienze del Suolo, della Pianta e degli Alimenti, Università degli Studi di Bari "Aldo Moro", Bari, Italy, [6]Department of Environmental Science and Disaster Management, Noakhali Science and Technology University, Noakhali, Bangladesh, [7]Università degli Studi di Torino, Dipartimento di Chimica, Torino, Italy, [8]Centro Interdipartimentale NatRisk, Grugliasco, Italy

KEYWORDS

Natural dissolved organic matter, fluorescent dissolved organic matter, freshwater, Marine water, photodegradation, microbial degradation

Introduction

Photosynthesis powered by sunlight, which involves plants and microorganisms in terrestrial soils and phytoplankton in fresh and marine waters, is one of the most important biogeochemical processes occurring in the environment. It constantly controls the production of most natural organic matter (NOM), which is a fundamental constituent of all ecosystems of our planet. Dissolved organic matter (DOM) is generated from NOM in terrestrial soils depending on three key sets of properties, i.e. physical, including temperature and moisture, chemical, which comprise nutrient availability, amount of available oxygen and redox activity, and microbial, such as microfloral succession patterns and availability of aerobic and anaerobic microorganisms. Terrestrial DOM is then partially transferred to surface waters

through surface runoff and groundwater leaching (Kritzberg et al., 2004; Catalán et al., 2016; Zark and Dittmar, 2018; Mostofa et al., 2019; Mohinuzzaman et al., 2020; Yi et al., 2021). Differently, autochthonous aquatic DOM originates from phytoplankton in surface water (Yamashita and Tanoue, 2004; Zhang et al., 2009; Guidi et al., 2016; Flemming et al., 2016; Shammi et al., 2017a; Igarza et al., 2019; Yang et al., 2021). Thus, a complex mixture of terrestrial and aquatic DOM occurs in surface-water environments (Kritzberg et al., 2004; Zark and Dittmar, 2018; Yi et al., 2021), which can be efficiently characterized on the basis of fluorescence properties (FDOM) and discriminated by excitation-emission matrix (EEM) fluorescence spectroscopy coupled with parallel factor (PARAFAC) modeling (Yamashita and Tanoue, 2004; Zhang et al., 2009; Shammi et al., 2017a; Mohinuzzaman et al., 2020; Yang et al., 2021; Yi et al., 2021). However, a clear, holistic understanding of terrestrial (allochthonous) and autochthonous aquatic DOM components is still lacking, as well as that of their sources and simultaneous production-degradation processes and pathways during transport from soil to sea through freshwater bodies, and their biogeochemical links.

Transformation of DOM from land source to marine environments

Based on the most recent research results, a detailed picture is provided in Figure 1 and summarized below. Soil DOM is universally recognized to be mostly composed of humic substances (HS), including humic acids (HA), fulvic acids (FA) and protein-like substances (PLS) (Figures 1A–C, forest soil), of which the fluorescence peaks are discussed in detail elsewhere (Mohinuzzaman et al., 2020). Terrestrial HS are partially released into ambient freshwaters *via* groundwater leaching and surface runoff (Figures 1D, E, F). In particular, the two terrestrial components FA and PLS are entirely degraded (Mostofa et al., 2019) due to their lability in photochemical and microbial degradation processes (Figure 1), and only the HA fraction persists during transport from soil to streams to coastal seawater (Mostofa et al., 2019), possibly due to its macromolecular structure (Senesi and Loffredo, 1999; Mohinuzzaman et al., 2020).

In a study on the fluorescence behavior of the terrestrial HA fractions of DOM along their flow (soil → stream → river →

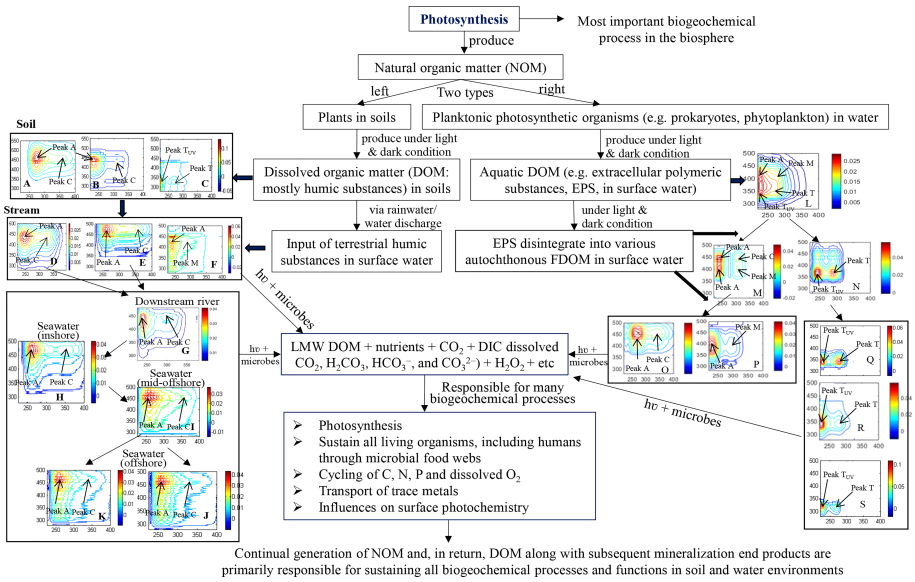

FIGURE 1
Flow diagram of the overall sequential constant photosynthetic production of natural organic matter (NOM) from terrestrial plants, animals and microorganisms in soils, and from planktonic photosynthetic organisms in waters. Figure 1, left: origin of soil humic substances [humic acids-HA **(A)**, fulvic acids-FA **(B)** and protein-like substances-PLS **(C)**] from terrestrial NOM and their subsequent runoff/leaching into surface waters, first into streams [terrestrial HA-like **(D)**, terrestrial FA-like **(E)**, terrestrial PLS-like **(F)**], then into downstream river (only terrestrial HA-like substances, **(G)**, then into inshore seawater (**(H)**, 0-10 m depth) and mid-offshore seawater (**(I)**, 0-10 m depth), and finally into offshore upper (**(J)**, 0-15 m) and deeper **(K)**, 20-300 m) seawaters in Seto Inland Sea. Figure 1, right: origin of extracellular polymeric substances (EPS, **(L)** from phytoplankton and their subsequent degradation, first into a combined form of autochthonous HA-like substances (AHLS) of C- and M-types **(M)** and a newly-released autochthonous protein-like substances (APLS, **(N)**, then into their individual components, i.e. AHLS into C-type **(O)** and M-type **(P)** and APLS into protein-like substances **(Q)**, tryptophan-like substances **(R)**, tyrosine-like substances **(S)**, etc. During all transformation described above for the two DOM systems mineralization end products are constantly produced, with the exception of terrestrial HA-like substances that ultimately did not degrade entirely, whereas autochthonous DOM is entirely degraded over one diurnal 24-h cycle by daytime sunlight-induced and nighttime microbial degradation.

sea), a red-shift from shorter to longer wavelength excitation-emission (Ex/Em) peak maxima has been measured when reaching the sea (peak C: stream 330/455; river 315/402; sea 350/473; peak A: stream 250/455; river 240/402; sea 260/473 nm) (Figure 1) (Mostofa et al., 2019; Mohinuzzaman et al., 2020). This red-shift can be ascribed to salinity effects occurring when terrestrial HAs reach seawater, possibly due to the formation of stable complexes with metal ions (Wu et al., 2004; Plaza et al., 2006; Mostofa et al., 2013; Mostofa et al., 2019). After reaching the sea, the water flows in the offshore direction determine a gradual blue shift of fluorescence peaks (C and A) toward wavelengths (325/461 and 255/461 nm in surface waters and 345/462 and 255/462 nm in deeper waters, respectively) that are shorter than those appearing for inshore to mid-offshore sea waters (345/461 and 260/461 nm, respectively). Apparently, a gradual transformation of terrestrial HA-like substances occurs along their transport in soil, stream, river, and then to coastal, mid-shore and offshore seawaters, where HA reach a relatively chemically recalcitrant nature. This behavior is confirmed by radio-carbon dating, which shows an increase of ^{14}C ages from soil to inland waters and then to marine waters (Catalán et al., 2016). Importantly, photochemical and microbial degradation processes along with hydrological processes, particularly carbonate and silicate weathering, would play important roles in overall transformation processes along with transport of chemical species (Catalán et al., 2016; Igarza et al., 2019; Mostofa et al., 2019; Liu et al., 2020; Zhong et al., 2020; Yi et al., 2021).

Origin of autochthonous DOM from planktonic communities and its transformation

Differently, autochthonous DOM originates from photochemical processes and microbial respiration from planktonic photosynthetic organisms (Yamashita and Tanoue, 2004; Zhang et al., 2009; Flemming et al., 2016; Guidi et al., 2016; Shammi et al., 2017a; Yang et al., 2021; Yi et al., 2021). The latter are thought to be responsible for approximately 50% of oceanic primary production and fuel the global biological carbon pump in marine environments (Guidi et al., 2016). Extracellular polymeric substances (EPS) are primarily originated from the plankton community and are considered the early-stage of newly-formed DOM (Flemming et al., 2016; Shammi et al., 2017a). EPS are not yet converted into individual organic components and are composed mainly of polysaccharides, proteins, nucleic acids, lipids, surfactants and humic-like substances (Flemming et al., 2016). The fluorescence moieties, mostly protein-like and humic-like fractions in EPS are firstly transformed into the following components, which can be monitored/detected by EEM-PARAFAC: (*i*) a combined form of autochthonous humic-like substances (AHLS) of C- and M-types, and (*ii*) newly-released autochthonous protein-like substances (APLS) (Shammi et al., 2017a; Yang et al., 2021). Successively, AHLS evolve into their individual forms, i.e. C- and M-types, whereas APLS are gradually transformed into individual protein-like, tryptophan-like, tyrosine-like and phenylalanine-like substances (Figure 1) (Yang et al., 2021). All these substances are commonly detected in surface waters, particularly in stagnant waterbodies such as ponds and lakes, but also in estuaries and oceans (Yamashita and Tanoue, 2004; Shammi et al., 2017a; Yang et al., 2021; Yi et al., 2021). Finally, all individual components are photochemically and microbially degraded into low molecular weight (LMW) DOM and mineralized end-products, including gaseous CO_2, dissolved inorganic carbon (DIC) and nutrients (e.g., NO_3^- and PO_4^{3-}) (Figure 1) (Igarza et al., 2019; Yang et al., 2021; Yi et al., 2021). Differently, the carbohydrates and lipids moieties in EPS do not show any fluorescence, but undergo hydrolysis along with photochemical and microbial degradation/mineralization in surface waters (Zhang and Bishop, 2003; Adav et al., 2008; Shammi et al., 2017b). Details about the origin of autochthonous DOM and its subsequent daytime photoinduced and nighttime microbial degradation are extensively discussed elsewhere (Yang et al., 2021).

Discussion

On the basis of results described above, the features of the two mentioned DOM systems and their biogeochemical transformation processes can be summarized as follows. Terrestrial FA-like and PLS-like fractions are extensively degraded along their transport, whereas terrestrial HA-like substances are only partially degraded by both photochemical and microbial processes (Amador et al., 1989; Catalán et al., 2016; Mostofa et al., 2019), due to their macromolecular size (Senesi and Loffredo, 1999; Mohinuzzaman et al., 2020). Therefore, the macromolecular size of HA is only one feature that would possibly account for its recalcitrant nature, and so can be used to determine the radio-carbon dating (Catalán et al., 2016; Tadini et al., 2018). Furthermore, various long-chain aliphatic and aromatic organic acids are produced by the photoinduced degradation of humic substances extracted from lakes and prolonged irradiation, which leads to a decrease of their concentrations and concomitant mineralization to end-products (Corin et al., 1996). Similarly, many aliphatic and aromatic byproducts were found to derive from aquatic DOM upon pyrolysis (Leenheer and Croué 2003). Studies also shows that various carboxylic acids (oxalic, malonic, formic, acetic, etc) are often major byproducts of the photoinduced degradation of DOM, which amounts to approximately 25.0–34.4% in surface waters (Bertilsson et al., 1999; Bertilsson and Tranvik 2000; Ma and Green, 2004). Simultaneously, EPS of planktonic origin are rapidly converted into AHLS and APLS, which are further

transformed into individual components that are finally degraded to produce LMW DOM and mineralized end-products (Yang et al., 2021).

The entire degradation of autochthonous aquatic FDOM has been shown to occur within a 24-h cycle under high air/water temperatures during summer, but not during low-temperature months (Yang et al., 2021). Similar results have been obtained for Antarctic glacial environments where exudates from primary production are utilized by heterotrophs within 24 h and support bacterial growth demands (Smith et al., 2017). As well, similar complete photoinduced degradation of humic-like fractions to EPS have been detected experimentally within 58 h,together with a decreasing DOC concentration of approximately 38.4%, from a very high (308.97 ± 1.20 mgL^{-1}) initial DOC concentration (Shammi et al., 2017b).

Thus, the key difference between terrestrial (allochthonous) and aquatic (autochthonous) DOM is that the latter is entirely degraded within a 24-h diurnal period during summer, whereas in the case of terrestrial DOM only the FA-like and PLS-like fractions (but not the HA-like ones) can be completely degraded in waterbodies. The mineralization end-products of both allochthonous and autochthonous DOM are produced continuously under both daytime sunlight-induced degradation and nighttime microbial degradation. In particular, *in-situ* solar irradiation experimental studies showed that the dissolved inorganic carbon (DIC: dissolved CO_2, H_2CO_3, HCO_3^-, and CO_3^{2-}) photoproduction rate is much lower in river waters (0.04–0.22 mg/L) than in lake waters (0.21–0.73 mgC/L), whereas DOC concentrations vary respectively from 33.22-33.22 mg/L and 1.88-2.40 mg/L (Ma and Green, 2004). Similar results for DIC have been obtained for humic lake waters (0.086–0.41 mg C/L day) for *in-situ* photo-irradiation samples (Granéli et al., 1996). Moreover, several experimental studies also showed that autochthonous fluorescent aromatic amino acids (e.g. tryptophan, tyrosine and phenylalanine), PLS and humic-like substances can produce dissolved inorganic nitrogen such as NH_4^+ and NO_x^- in surface waters (Bushaw et al., 1996; Berman and Bronk, 2003; Stedmon et al., 2007; Zhang et al., 2021). As these end-products act as nutrients, they continuously fuel the reproduction of photosynthetic planktonic organisms in surface waters and simultaneously contribute to global carbon cycling as well as to climate change (Mopper et al., 1991; Bushaw et al., 1996; Moran and Zepp, 1997; Berman and Bronk, 2003; Zhong et al., 2020; Mostofa et al., 2013). In conclusion, the continuous production of NOM and its transformation/mineralization represent the primary backbone process in the cycles of carbon, nitrogen, phosphorus, dissolved oxygen and trace metals and in sustaining life of all living organisms, including humans, thus it is of key importance to deepen their understanding, in particular because climate warming determines longer stratification periods to occur in surface waters during summer.

Author contributions

KMGM designed and conceived the project. HS, KMGM, C-QL contributed the key data sources. JY, MM, YL, XY conducted the EEM-PARAFAC analysis. KMGM, NS wrote the manuscript. DV and S-LL reviewed & edited the manuscript. All authors contributed to the article and approved the submitted version.

Funding

This work was financially supported by the National Natural Science Foundation of China (42221001, 41925002) and the Haihe Laboratory of Sustainable Chemical Transformations.

Conflict of interest

The authors declare that the research was conducted in the absence of any commercial or financial relationships that could be construed as a potential conflict of interest.

Publisher's note

References

Adav, S. S., Lee, D.-J., and Tay, J–H. (2008). Extracellular polymeric substances and structural stability of aerobic granule. *Water Res.* 42 (6–7), 1644–1650. doi: 10.1016/j.watres.2007.10.013

Amador, J. A., Alexander, M., and Zika, R. G. (1989). Sequential photochemical and microbial degradation of organic molecules bound to humic acid. *App Environ Microb* 55, 2843–2849.

Berman, T., and Bronk, D. A. (2003). Dissolved organic nitrogen: a dynamic participant in aquatic ecosystems. *Aquat. Microb. Ecol.* 31 (3), 279–305. doi: 10.3354/ame031279

Bertilsson, S., Stepanauskas, R., Cuadros-Hansson, R., Granéli, W., Wikner, J., and Tranvik, L. J. (1999). Photochemically induced changes in bioavailable carbon and nitrogen pools in a boreal watershed. *Aquat Microb Ecol* 19, 47–56.

Bertilsson, S., and Tranvik, L. J. (2000). Photochemical transformation of dissolved organic matter in lakes. *Limnol. Oceanogr.* 45, 753–762.

Bushaw, K. L., Zepp, R. G., Tarr, M. A., Schulz-Jander, D., Bourbonniere, R. A., Hodson, R. E., et al. (1996). Photochemical release of biologically available nitrogen from aquatic dissolved organic matter. *Nature* 381 (6581), 404–407. doi: 10.1038/381404a0

Catalán, N., Marcé, R., Kothawala, D. N., and Tranvik, L. J. (2016). Organic carbon decomposition rates controlled by water retention time across inland waters. *Nat. Geosci.* 9, 501–506. doi: 10.1038/ngeo2720

Corin, N., Backlund, P., and Kulovaara, M. (1996). Degradation products formed during UV-irradiation of humic waters. *Chemosphere* 33, 245–255

Flemming, H. C., Wingender, J., Szewzyk, U., Steinberg, P, Rice, S. A., and Kjelleberg, S. (2016). Biofilms: an emergent form of bacterial life. *Nat. Rev. Microbiol.* 14, 563–575. doi: 10.1038/nrmicro.2016.94

Granéli, W., Lindell, M., and Tranvik, L. (1996). Photo-oxidative production of dissolved inorganic carbon in lakes of different humic content. *Limnol Oceanogr* 41, 698–706.

Guidi, L., Chaffron, S., Bittner, L., Eveillard, D., Larhlimi, A., Roux, S., et al. (2016). Plankton networks driving carbon export in the oligotrophic ocean. *Nature* 532, 465–470. doi: 10.1038/nature16942

Igarza, M., Dittmar, T., Graco, M., and Niggemann, J. (2019). Dissolved organic matter cycling in the coastal upwelling system off central Peru during an "El niño" year. *Front. Mar. Sci.* 6, 198. doi: 10.3389/fmars.2019.00198

Kritzberg, E. S., Cole, J. J., Pace, M. L., Granéli, W., and Bade, D. L. (2004). Autochthonous versus allochthonous carbon sources of bacteria: Results from whole-lake ^{13}C addition experiments. *Limnol. Oceanogr.* 49, 588–596. doi: 10.4319/lo.2004.49.2.0588

Leenheer, J. A., and Croué, J. P. (2003). Characterizing aquatic dissolved organic matter. *Environ Sci Technol* 37, 18–26.

Liu, J., Zhong, J., Ding, H., Yue, F.-J., Li, C., Xu, S., et al (2020). Hydrological regulation of chemical weathering and dissolved inorganic carbon biogeochemical processes in a monsoonal river. *Hydrol. Process.* 34, 2780–2792. doi: 10.1002/hyp.13763

Ma, X., and Green, S. A. (2004). Photochemical transformation of dissolved organic carbon in Lake Superior-an in-situ experiment. *J Great Lakes Res* 30 (suppl 1), 97–112.

Mohinuzzaman, M., Yuan, J., Yang, X., Senesi, N., Mostofa, K. M.G., and Liu, C. Q. (2020). Insights into solubility of soil humic substances and their fluorescence characterisation in three characteristic soils. *Sci. Total Environ.* 720, 137395. doi: 10.1016/j.scitotenv.2020.137395

Mopper, K., Zhou, X., Kieber, R. J., Kieber, D. J., Sikorski, R. J., and Jones, R. D. (1991). Photochemical degradation of dissolved organic carbon and its impact on the oceanic carbon cycle. *Nature* 353, 60–62. doi: 10.1038/353060a0

Moran, M. A., and Zepp, R. G. (1997). Role of photoreactions in the formation of biologically labile compounds from dissolved organic matter. *Limnol Oceanogr* 42, 1307–1316. doi: 10.4319/lo.1997.42.6.1307

Mostofa, K. M. G., Jie, Y., Sakugawa, H., and Liu, C.-Q. (2019). Equal treatment of different EEM data on PARAFAC modeling produces artifact fluorescent components that have misleading biogeochemical consequences. *Environ. Sci. Technol.* 53, 561–563. doi: 10.1021/acs.est.8b06647

Mostofa, K. M. G., Yoshioka, T., Mottaleb, M. A., and Vione, D. (2013). *Photobiogeochemistry of organic matter: Principles and practices in water environments* (Berlin Heidelberg: Springer).

Plaza, C., Brunetti, G., Senesi, N., and Polo, A. (2006). Molecular and quantitative analysis of metal ionbinding to humic acids from sewage sludge and sludge-amended soils by fluorescence spectroscopy. *Environ. Sci. Technol.* 40, 917–923. doi: 10.1021/es051687w

Senesi, N., and Loffredo, E. (1999). "The chemistry of soil organic matter," in *Soil physical chemistry*. Ed. D. L. Sparks (Boca Raton: CRC Press), 239–370.

Shammi, M., Pan, X., Mostofa, K. M. G., Zhang, D., and Liu, C. Q. (2017a). Seasonal variation and characteristic differences in the fluorescent components of extracellular polymeric substances from mixed biofilms in saline lake. *Sci. Bull.* 62, 764–766. doi: 10.1016/j.scib.2017.04.016

Shammi, M., Pan, X. L., Mostofa, K. M. G., Zhang, D., Liu, C. Q., and Song, W. (2017b). Investigating extracellular polymeric substances from microbial mat upon exposure to sunlight. *Polymer Degradation Stabil* 146, 192–200. doi: 10.1016/j.polymdegradstab.2017.10.011

Smith, H., Foster, R. A., McKnight, D. M., Lisle, J. T., Littmann, S., Kuypers, M. M. M., et al. (2017). Microbial formation of labile organic carbon in Antarctic glacial environments. *Nat. Geosci.* 10, 356–360. doi: 10.1038/ngeo2925

Stedmon, C. A., Markager, S., Tranvik, L., Kronberg, L., Slatis, T., and Martinsen, W. (2007). Photochemical production of ammonium and transformation of dissolved organic matter in the Baltic Sea. *Mar. Chem.* 104, 227–240. doi: 10.1016/j.marchem.2006.11.005

Tadini, A. M., Nicolodelli, G., Senesi, G. S., Ishida, D. A., Montes, C. R., Lucas, Y., et al. (2018). Soil organic matter in podzol horizons of the Amazon region: humification, recalcitrance, and dating. *Sci. Total Environ.* 613–614, 160–167. doi: 10.1016/j.scitotenv.2017.09.068

Wu, F. C., Cai, Y. R., Evans, D., and Dillon, P. (2004). Complexation between Hg (II) and dissolved organic matter in stream waters: an application of fluorescence spectroscopy. *Biogeochemistry* 71, 339–351. doi: 10.1007/s10533-004-0058-5

Yamashita, Y., and Tanoue, E. (2004). *In situ* production of chromophoric dissolved organic matter in coastal environments. *Geophys. Res. Lett.* 31, L14302. doi: 10.1029/2004GL019734

Yang, X., Yuan, J., Yue, F.-J., Li, S., Wang, B., Mohinuzzaman, M., et al. (2021). New insights into mechanisms of sunlight- and dark-mediated high-temperature can accelerate diurnal production-degradation transformation of lake fluorescent DOM. *Sci. Total Environ.* 760, 143377. doi: 10.1016/j.scitotenv.2020.143377

Yi, Y., Zhong, J., Bao, H., Mostofa, K. M.G., Xu, S., Xiao, H.-Y., et al. (2021). The impacts of reservoirs on the sources and transport of riverine organic carbon in the karst area: A multi-tracer study. *Water Res.* 194, 116933. doi: 10.1016/j.watres.2021.116933

Zark, M., and Dittmar, T. (2018). Universal molecular structures in natural dissolved organic matter. nat. comm. 9, 3178 zhang x., bishop p., biodegradability of biofilm extracellular polymeric substances. *Chemosphere* 50 (2003), 63–69. doi: 10.1038/s41467-018-05665-9

Zhang, X., and Bishop, P. (2003). Biodegradability of biofilm extracellular polymeric substances. *Chemosphere* 50, 63–69.

Zhang, Y., van Dijk, M. A., Liu, M., Zhu, G., and Qin, B. (2009). The contribution of phytoplankton degradation to chromophoric dissolved organic matter (CDOM) in eutrophic shallow lakes: Field and experimental evidence. *Water Res.* 43, 4685–4697. doi: 10.1016/j.watres.2009.07.024

Zhang, Y., Zhang, R., Li, S. L., Mostofa, K. M. G., Fu, X., Ji, H., et al. (2021). Photo-ammonification of low molecular weight dissolved organic nitrogen by direct and indirect photolysis. *Sci. Total Environ.* 764, 142930. doi: 10.1016/j.scitotenv.2020.142930

Zhong, J., Li, S.-L., Ibarra, D. E., Ding, H., and Liu, C.-Q. (2020). Solute production and transport processes in Chinese monsoonal rivers: Implications for global climate change. glob. *Biogeochem. Cyc.* 34, e2020GB006541. doi: 10.1029/2020GB006541

frontiers | Frontiers in Marine Science

TYPE Original Research
PUBLISHED 23 November 2022
DOI 10.3389/fmars.2022.988340

OPEN ACCESS

EDITED BY
Jeng-Wei Tsai,
China Medical University, Taiwan

REVIEWED BY
Liyang Yang,
Fuzhou University, China
Yantao Liang,
Ocean University of China, China

*CORRESPONDENCE
Jia-Jang Hung
hungjj@mail.nsysu.edu.tw

†These authors have contributed equally to this work

SPECIALTY SECTION
This article was submitted to Marine Biogeochemistry, a section of the journal Frontiers in Marine Science

RECEIVED 07 July 2022
ACCEPTED 27 October 2022
PUBLISHED 23 November 2022

CITATION
Hung J-J, Lu W-T, Yang H-M, Lin Y-H and Guo L (2022) Biophysical controls on spatial and summer/winter distributions of total and chromophoric dissolved organic matter in the Taiwan Strait. *Front. Mar. Sci.* 9:988340. doi: 10.3389/fmars.2022.988340

Biophysical controls on spatial and summer/winter distributions of total and chromophoric dissolved organic matter in the Taiwan Strait

Jia-Jang Hung[1*†], Wan-Tzu Lu[2†], Hsin-Mei Yang[2,3], Yen-Hui Lin[1] and Laodong Guo[4]

[1]Department of Oceanography, National Sun Yat-sen University, Kaohsiung, Taiwan, [2]Institute of Marine Geology and Chemistry, National Sun Yat-sen University, Kaohsiung, Taiwan, [3]National Chunan High School, Hsinchu, Taiwan, [4]School of Freshwater Sciences, University of Wisconsin-Milwaukee, Milwaukee, WI, United States

This study examined the physical and biogeochemical processes that determine the spatial and summer/winter distributions of dissolved organic matter (DOM) and chromophoric dissolved organic matter (CDOM) in the Taiwan Strait (TS). The hydrological conditions in the TS varied between early summer and winter because of differences in terrestrial input as well as input from the poleward South China Sea Water (SCSW) during the warm summer and the strong, nutrient-rich, equatorward China Coastal Water (CCW) in winter. Concentrations of dissolved organic carbon (DOC) ranged from 60 to 100 μM-C in early summer and from 70 to 144 μM-C in winter. The average stoichiometric ratio of DOC : DON:DOP was high (353:49:1) in the land-source impacted zones and low (168:21:1) in the SCSW-laden areas, both of which are higher than the Redfield ratio. The concentrations of DOC and nutrients were higher in the western TS (on the coast of China) than in the eastern TS (on the coast of Taiwan), and the highest concentrations were mostly found in the Minjiang River plume, reflecting the profound effects of freshwater input in early summer and CCW inflow in winter. The absorption and emission characteristics of the CDOM varied to a large extent with locations because of the mixing of the shelf water with different source waters. Although the absorption coefficient ($a_{CDOM}(325)$) and fluorescence intensity of the terrestrial humic-like CDOM (Ft: Ex/Em= 260/400-460) were both strongly inversely correlated with salinity, as an optical tracer, Ft may be more effective than $a_{CDOM}(325)$ in examining the mixing among source waters, given that $a_{CDOM}(325)$ may be subject to various photobleaching effects in the TS. Ft was also significantly correlated with the concentrations of terrestrially derived nitrate and nitrite (N+N) and silicate. The results of factor analysis elucidated the complexity of the hydrological and biological processes that affect the distributions of DOM and CDOM in the TS.

KEYWORDS

DOM, CDOM, nutrients, spatial distribution, optical tracer, factor analysis, Taiwan Strait

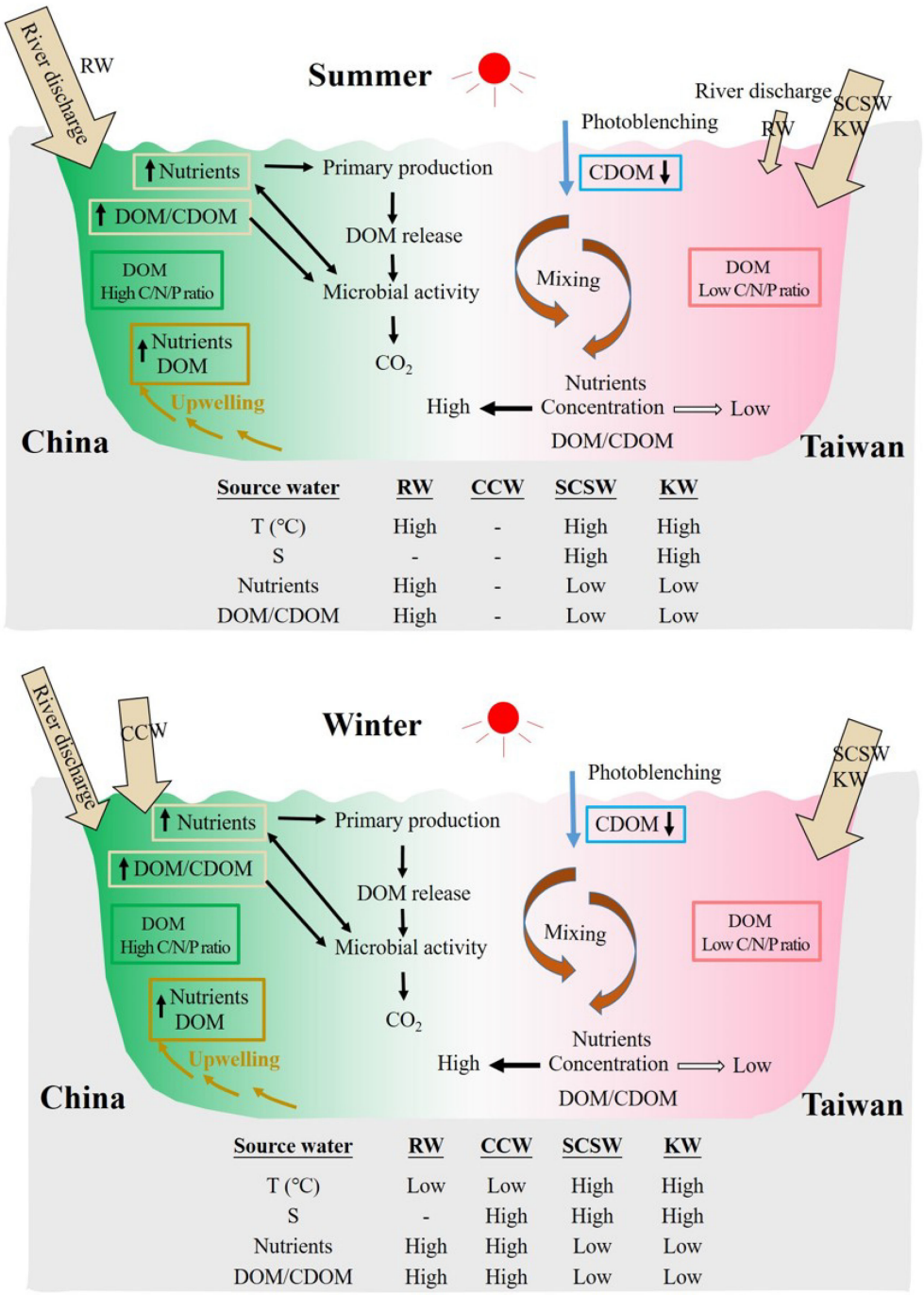

GRAPHICAL ABSTRACT

Introduction

Dissolved organic carbon (DOC; for abbreviations, please refer to Table 1) comprises the largest pool (680–700 Pg C) of reduced carbon in the hydrosphere and is comparable in mass to atmospheric CO2 (Hansell, 2002; Calleja et al., 2019). DOC plays a key role in carbon cycles and is also critical for nutrient transformation and availability in oceans (Abell et al., 2000; Hansell, 2002; Barron and Duarte, 2015; Hansell and Carlson, 2015). A growing body of evidence has revealed that the quality

rather than total concentration of DOC is crucial to microbial metabolism and carbon transfer within oceans and at the boundaries between the atmosphere and oceans (Amon et al., 2001; Benner, 2002; Stepanauskas et al., 2005; Raimbault et al., 2008). Although substantial progress has been made in understanding the reactivity and bioavailability of marine dissolved organic matter (DOM), numerous properties of DOM, especially its chemical composition and optical properties, have not been fully explored in different coastal environments and thus warrant further investigation (Abdulla et al., 2013; Stedmon and Nelson, 2015; Riedel et al., 2016). The chemical composition is also critical for the lability of DOM, and the bioavailability and recycling of DOM are generally dependent on the source, regional and global circulations, and external and oceanic forcing (Hansell, 2002; Benner, 2002; Stepanauskas et al., 2005; Hansell et al., 2012).

The most notable characteristic of DOM in marginal seas, in addition to its derivation from productive regions, may be how it is strongly affected by continental input. The reactivity of terrestrial DOM is generally considered more biologically refractory than that of marine DOM (Guo et al., 1995; Benner, 2002; Abdulla et al., 2013). In addition, the large input of terrestrial DOM may profoundly affect the biogeochemical cycles of carbon-related elements as well as satellite-derived primary productivity in oceans. The sources, sinks, and lability of DOM in marginal seas are complex and poorly understood because they are associated with boundary exchanges, and turbulent mixing and a lack of a clear vertical gradient. Although analyses of the molecule-level composition of DOM are useful for understanding the function and reactivity of DOM, the techniques employed in such analyses are usually not straightforward and require expensive equipment.

TABLE 1 Acronyms used in this study.

Acronyms	Water mass and chemical parameter
CCW	China Coastal Water
KW	Kuroshio Water
SCSW	South China Sea Water
TSW	Taiwan Strait Water
DOC	Dissolved organic carbon
DON	Dissolved organic nitrogen
DOP	Dissolved organic phosphorus
DOM	Dissolved organic matter
CDOM	Chromophoric dissolved organic matter
$A_{CDOM(325)}$	Absorption coefficient of CDOM at 325nm
S_{CDOM}	Spectral slope coefficient of CDOM
Th-like CDOM	Terrestrial human-like CDOM
TDN	Total dissolved nitrogen
TDP	Total dissolved phosphorus
DIN	Dissolved inorganic nitrogen
DIP	Dissolved inorganic phosphorus

As an alternative to these analyses, spectroscopic methods have been widely used to characterize the sources and chemical features of DOM. Chromophoric DOM (CDOM), which can absorb solar radiation in aquatic environments, comprises a large proportion of the bulk DOM pool. The molecular structures of CDOM can be excited using a specific wavelength of radiation and subsequently emit a longer wavelength of radiation as fluorescence, and oceanographers can use such features to identify the sources and evaluate the quality of DOM (Coble, 1996; McKnight et al., 2001; Coble, 2007; Jaffé et al., 2008; Abdulla et al., 2013; Stedmon and Nelson, 2015). The reactivity of CDOM to sunlight may also result in the remineralization of DOM and produce several reactive products and elements that can be used by biota (Miller and Zepp, 1995; Obernosterer and Benner, 2004; Norman et al., 2011). Although the absorption of ultraviolet light can prevent damage to organisms, the absorption of visible light interferes with the estimation of concentrations of satellite-derived chlorophyll in coastal and marginal seas (Blough and Del Vecchio, 2002; Siegel et al., 2002; Romera-Castillo et al., 2011; Dutkiewicz et al., 2019). The fates of DOM and CDOM and their effects on ecosystems in marginal seas are crucial.

The Taiwan Strait (TS) is a shallow marginal sea separating the main island of Taiwan from mainland China and serves as a major connection between the South China Sea (SCS) and the East China Sea (ECS). The seasonal variations in river discharge, seawater circulation, flow patterns, and transport rates in the TS are highly pronounced. Numerous studies and reviews (Jan et al., 2002; Chen, 2003; Wang et al., 2003; Wu and Hsin, 2005; Jan et al., 2006; Chen et al., 2010; Hu et al., 2010; Jan et al., 2010; Hong et al., 2011; Huang et al., 2020) have proposed various seawater transport modes and budgets since Wyrtki (1961) investigated the transport between the SCS and TS in summer (0.5–1.0 Sv northward, 1Sv = 10^6 m^3s^{-1}) and in winter (0.5 Sv southward). The major circulatory features of the TS are a northward current in the eastern TS in summer and a southward current in the western TS in winter. The currents and transport in the TS are generally modulated by monsoon forcing and topographic variations (Jan et al., 2002; Hu et al., 2010). The source waters of the eastern current of the TS in the summer and other seasons are the SCS Water (SCSW) and intruding Kuroshio water (KW), respectively, and that of the western current is the colder and fresher China Coastal Water (CCW) driven southward by the northeast monsoon (Jan et al., 2002). Jan et al. (2006) estimated that the northward transport through the TS ranges from 1.16 to 2.34 Sv between March and August. Findings related to the seasonal variations in seawater volume transport have remained consistent. However, in a summary report, Hu et al. (2010) reported that the volume transport through the TS in summer and winter was approximately 2.3±0.82 Sv and 0.8±0.96 Sv northward, respectively.

In addition to seawater circulation and transport, the TS may also play a key role in the transfer of chemical constituents between the SCS and ECS. (Chen and Sheu, 2006; Chen, 2008) investigated the nutrient contributions of the TS and their benefits for primary

productivity in the ECS in summer. Regarding DOM biogeochemistry in the TS, some studies have reported that the biogeochemical processes and budgets of DOC and CDOM depend not only on physical circulation and boundary transport, but also on local upwelling and continental input in the western TS and its associated estuaries (Du et al., 2010; Guo et al., 2011; Hong et al., 2011). However, few studies have focused on the biogeochemical processes of DOM and CDOM across the entire strait. To address this research gap, this study investigated the physical and biogeochemical processes that affect the distributions and fates of DOM and CDOM for a better understanding of the connection between DOM and CDOM characteristics and the variability of water properties and hydrological conditions in the TS.

Materials and methods

Study area, sampling, and hydrological conditions

The sampling stations in the study area are shown in Figure 1. In early summer (ORII CR1353, 05/20–25/2006), surface seawater samples were collected from the entire TS (Stations 1–33). In winter (ORI CR889, 02/11–13/2009), samples were collected from the stations along the coast of China and from two strait-crossing transects located respectively on the northernmost and southernmost parts of TS. An additional experiment was performed at the Gaoping Estuary in southern Taiwan (Figure 1C) to examine the mixing behavior of terrestrial DOM and CDOM from riverine and oceanic waters.

The seawater samples were collected using cleaned 10-L Niskin bottles mounted on a CTD/Rosette. The CTD and attached probes were used to record the temperature (T), salinity (S), fluorescence, and transmission data. The irradiances of both the surface and subsurface was measured using a PAR sensor (OSP2001, Biospherical Instruments, San Diego, USA). The euphotic depth was defined as the depth at which the light intensity was 1% of the surface irradiation. Dissolved oxygen samples were pickled immediately after the seawater samples were collected, and the concentrations were determined by measuring the absorbance of total iodine in the pickled samples after acidification (Pai et al., 1993). Chlorophyll *a* (Chl-a) was extracted from the filtered particulates with 90% acetone and measured fluorometrically (10AU Fluorometer, Turner Designs) using the non-acidification method (Welschmeyer, 1994).

Measurements of dissolved organic carbon, nitrogen, and phosphorus

DOC and particulate organic carbon (POC) in seawater were separated by the filtration of seawater samples through precombusted GF/F (Whatman) glass-fiber filters immediately after seawater collection, according to the published procedures (Hung et al., 2000; Hung et al., 2003). After filtration, the filters were sealed in cleaned petri-dishes and stored in the frozen condition before being transferred to thelaboratory. The filters were then dried in an oven at 60 °C for POC determination. Aliquot of the filtered seawater was acidified with HCl (0.4%, v/v) and stored in cleaned glass bottles until the measurement of DOC in the laboratory. DOC was measured with the method of high-temperature catalytic oxidation using the Shimadzu TOC-5000A analyzer (Hung et al., 2003; Hung et al., 2007). Consensus reference materials (41-44 µM C) provided by Dr. D. A. Hansell from the University of Miami were regularly checked to ensure data quality. POC was measured with a C/N/S analyzer (Thermo Scientific Flash 2000) following carbonate removal from the filtered particulates (Hung et al., 2007; Hung et al., 2008).

Dissolved organic nitrogen (DON) was determined from the difference between total dissolved nitrogen (TDN) and dissolved inorganic nitrogen (DIN). TDN was measured with the high temperature oxidation and chemiluminescent detection (Antek N/S analyzer) with reproducibility within ±7% for seawater (n = 9) (Hung et al., 2008), while the DIN was determined according to the procedures described in the following section. Dissolved organic phosphorus (DOP) was determined by the difference between dissolved inorganic phosphate (DIP) and total dissolved phosphorus (TDP) that was measured by the UV-persulfate oxidation and colorimetric method (Ridal and Moore, 1990). Reproducibility of TDP measurement in seawater (n = 9) was ±6%.

Measurements of DIN, DIP and silicate

Dissolved inorganic nitrogen (NO_3^-+NO_2^-+NH_4^+, herein DIN) and phosphate (PO_4^{3-}, or DIP) and silicate (H_4SiO_4, or DSi) were determined colorimetrically (Grasshoff et al., 1983) using a UV-Vis spectrophotometer (Hitachi U-2000) equipped with a module of flow injection analysis (Pai and Riley, 1994) with an exception of NH_4^+ determination. The concentration of NH_4^+ was determined with an indophenol blue method using a spectrophotometer (Hitachi U-3030, 5-cm quartz cell) according to Pai et al. (2001).

Measurements of absorption and fluorescence spectra of CDOM

The CDOM absorption spectra were determined using a spectrophotometer (Hitachi U-3310), employing a 10-cm optical quartz cell and Milli-Q water as a blank. The data were corrected for scattering and baseline fluctuation by subtracting each spectrum from the mean value of absorption at 600-700 nm (Bricaud et al., 1981; Green and Blough, 1994). To minimize the

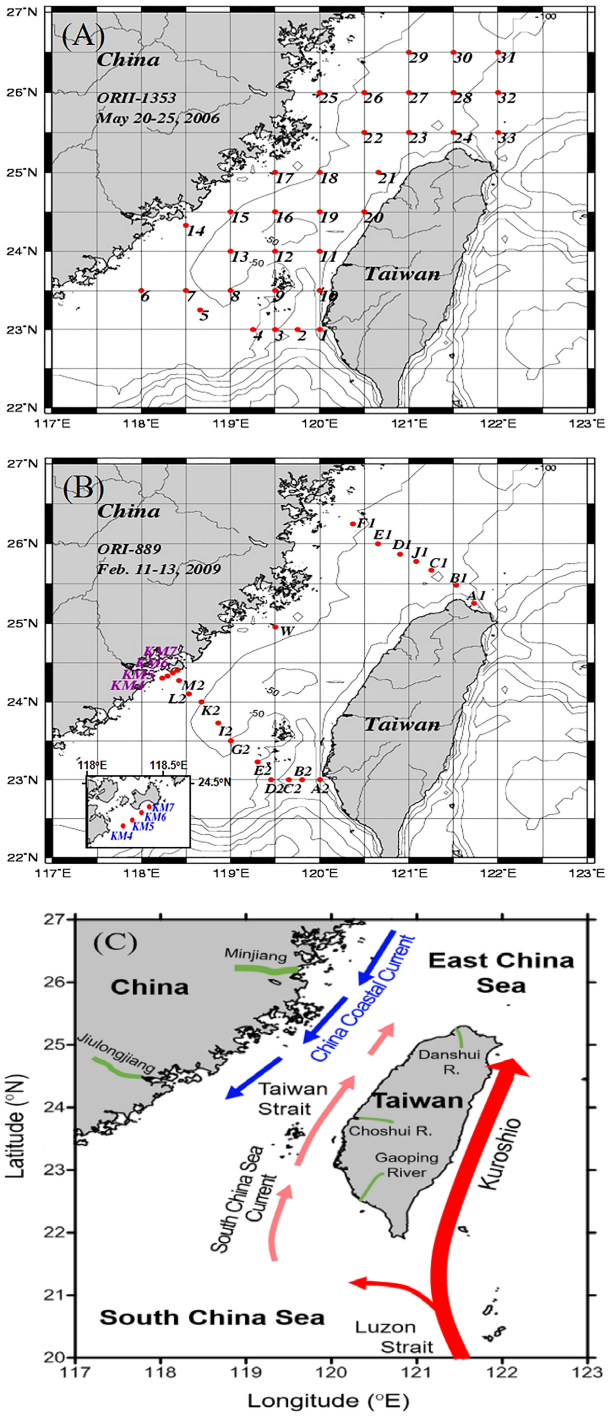

FIGURE 1
Study area and sampling locations in the Taiwan Strait in early summer (**A**, Stations 1–33, ORII CR1353) and winter (**B**, ORI CR889). Arrows represent the regional circulation patterns associated with the Taiwan Strait **(C)**. Different sizes of red and light red arrows represent the difference in warm, saline, and current strength for Kuroshio Current and South China Sea Current, respectively. The blue arrow indicates cold and less saline China Coastal Current during winter. The discharge of river water is shown by the different width of short green line in southeast China and Taiwan. The Kuroshio intrusion into the South China Sea (SCS) tends to be stronger in winter than in summer (Wu et al., 2017), and the China Coastal Current and SCS Current prevail in winter and in summer, respectively (Jan et al., 2002; Hu et al., 2010).

inner filter effect, those samples having an absorbance greater than 0.05 (325 nm) were properly diluted with Mill-Q water before measurements. Absorption coefficients, aCDOM(λ), were calculated using the following equation,

$$aCDOM(\lambda) = 2.303 \times ACDOM(\lambda)/L \quad (1)$$

Where ACDOM(λ) is the absorbance over the pathlength L at the wavelength λ. The absorption of CDOM at 325 nm was used as a proxy for CDOM concentration (Nelson et al., 2007; Swan et al., 2009). The spectra were then fit to an exponential function, using a nonlinear least squares fitting routine (NLF) over the range 280–500 nm,

$$aCDOM(\lambda) = aCDOM(\lambda_0) \quad e^{-S}(\lambda - \lambda_0) \quad (2)$$

Where λ_0 is a reference wavelength and S is the spectral slope.

The measurements of CDOM fluorescence were carried out using a fluorescence spectrometer (Hitachi F-4500), employing a 1-cm optical (quartz) cell and Milli-Q water as a blank. The excitation-emission matrix (EEM) was derived from the emission scans between 200 and 600 nm (λ_{em} = 200–600 nm) at 5 nm intervals and the excitation increased from 200 to 500 nm (λ_{ex} = 200–500 nm) at 5nm intervals (Coble. 1996). A solution of 10 μg/l of quinine sulfate (qs) in 0.5 M H_2SO_4(aq) was employed as a standard with sulfuric acid (0.5M) used as the blank, thus the fluorescence of qs (Fqs) was the mean value recorded from excitation at 355 nm (λ_{ex}) and emission at 430–450 nm (λ_{em}). The sample fluorescence (F_S) recorded through the same excitation-emission (Ex/Em) condition as the standard was normalized to the fluorescence of standard to give a fluorescence unit (FI.U. = 10 × F_S/Fqs). The assignment of peaks at various Ex/Em (nm) was adapted from the previous report (Coble, 1996). The peak A (260/400–460 nm) was the terrestrial humic substances peak, peak C (320–360/420–460 nm) was the terrestrial fulvic substances peak, peak M (290–310/370–410 nm) was the marine fulvic substances peak, and peak T (275/340 nm) was the proteinaceous substances peak. Although the parallel factor analysis (PARAFAC) was widely used for identifying components and gave a EEM interpretation (Stedmon et al., 2003; Murphy et al., 2008; Hong et al., 2012; Stedmon and Nelson, 2015; Carr et al., 2019), we simply pick Coble's assigned peaks particularly peak A as an index of terrestrial humic source. Seawater samples were also measured for the concentration of total suspended matter (TSM) according to methods reported by (Hung et al., 2007; Hung et al., 2008).

Mixing experiments of land-sourced DOC and CDOM in the Gaoping Estuary

Water samples were taken along a salinity gradient in the Gaoping Estuary located in southwestern Taiwan (Figures 1C, 8A) during the dry (winter) season when the estuary was in well-mixed conditions. Salinity was measured using a portable conductivity/salinity meter (WTW, LF-320) with a resolution of 0.01 salinity unit. DOC, aCDOM(325), and terrestrial humic-like (Th-like) CDOM were measured according to methods described in the above sections. DOC and Th-like CDOM were plotted against salinity to elucidate their mixing behavior.

Statistical analysis: Factor analysis

Because of the co-varying nature of the measured variables for a specific season in the TS, a multivariate analysis method, the factor analysis, was performed for the analysis of data collected from the cruise CR 1353 (early summer) or the cruise CR889 (winter) using the statistical software SYSTAT 11. The total variance explained by each factor was employed to elucidate the major associated physical and biogeochemical processes.

Results

Hydrographic conditions in early summer and winter

Figure 2A presents the surface distribution of salinity in the TS in early summer. The salinity generally increased from 26.79 on the coast of mainland China (in the western TS) to 34.2 on the coast of Taiwan (in the eastern TS). The surface temperature distribution (figure not shown) followed the similar pattern, increasing from 20.7°C on the coast of China to 24.7°C on the coast of Taiwan. Accordingly, the temperature–salinity (T–S) diagram reveals that the seawater conditions at the stations in the study area were characterized by low temperature and salinity (Figure 2B), likely resulting from freshwater input mainly from the Minjiang and Jiulongjiang rivers in the early stages of high river discharge (Hong et al., 2012; Zhang et al., 2015), or from the remnants of the southward CCW from the previous winter. The T–S diagram also reveals that seawater conditions at the stations located in the central region of the TS and on the coast of Taiwan had high temperature and salinity and properties between those of the KW and SCSW, which likely resulted from the mixing of the shelf water and the SCSW (Figure 2C). The contribution of the intruding KW would have been limited because of weak Kuroshio intrusion (Wu et al., 2017). The T–S diagram (Figures 3A, B) reveals that, during winter, the SCSW and intruding KW mixed in the southern end of eastern TS, but likely mixing between TS water and coastal water in the northern end of the eastern TS. Chen and Sheu (2006) contended that these saline waters (S >33.00) are present year-round along the eastern TS as the intermittent northward flow of the SCSW and Kuroshio branch current. The waters in

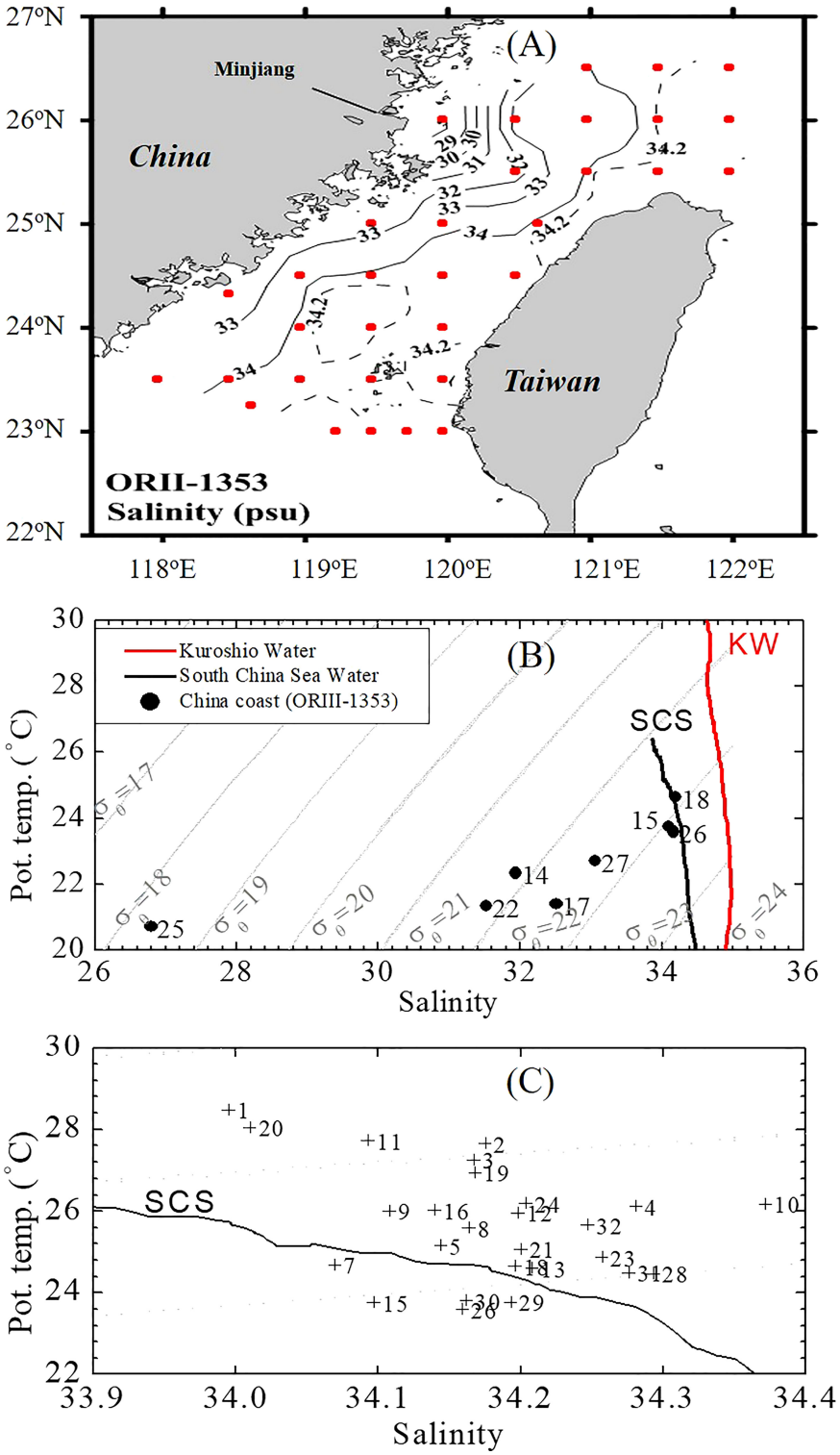

FIGURE 2
Spatial distribution of salinity in surface waters of the TS in early summer (**A**; Cruise CR1353) and plots of the temperature–salinity (T–S) relationship at sampling stations located in the western TS (on the coast of China, **B**) and the central and eastern TS (on the coast of Taiwan, **C**) in early summer (CR1353). The "KW" and "SCS" curves represent the typical T–S features of the Kuroshio Water (KW) and SCS Water (SCSW), respectively. The KW and SCSW represent typical waters collected from the western Philippine Sea and SCS central basin, respectively.

the western TS were dominated by the nutrient-rich CCW, identified on the basis of its low temperature (<15.6°C) and salinity (<32.57), which appears to come from the north. The distributions of various waters in different seasons observed in here are consistent with those observed in previous studies (Jan et al., 2002; Chen, 2003; Chen et al., 2010; Hu et al., 2010; Jan et al., 2006; Hong et al., 2011). Despite the samplings were carried out in two seasons under different years, the different circulation patterns occurring between summer and winter were yearly persistent in the TS (Jan et al., 2002; Chen et al., 2010; Hu et al., 2010; Chen et al., 2021).

Distributions of nutrients

Figure 4A illustrates the surface concentrations of nitrate and nitrite (N+N) in the TS in early summer, which ranged from 0.01 to 1.35 μM and from 0.01 to 5.51 μM in the eastern and western TS, respectively. The surface concentrations of dissolved silicate ranged from 2.0 to 7.2 μM and from 1.8 to 22.4 μM in the eastern and western TS, respectively (Figure 4B). The concentrations of NH_4^+ (not shown) were generally lower than 1.0 μM, except for the station located on the Minjiang River plume (Station 25) where the concentration was as high as 2 μM. The distribution of

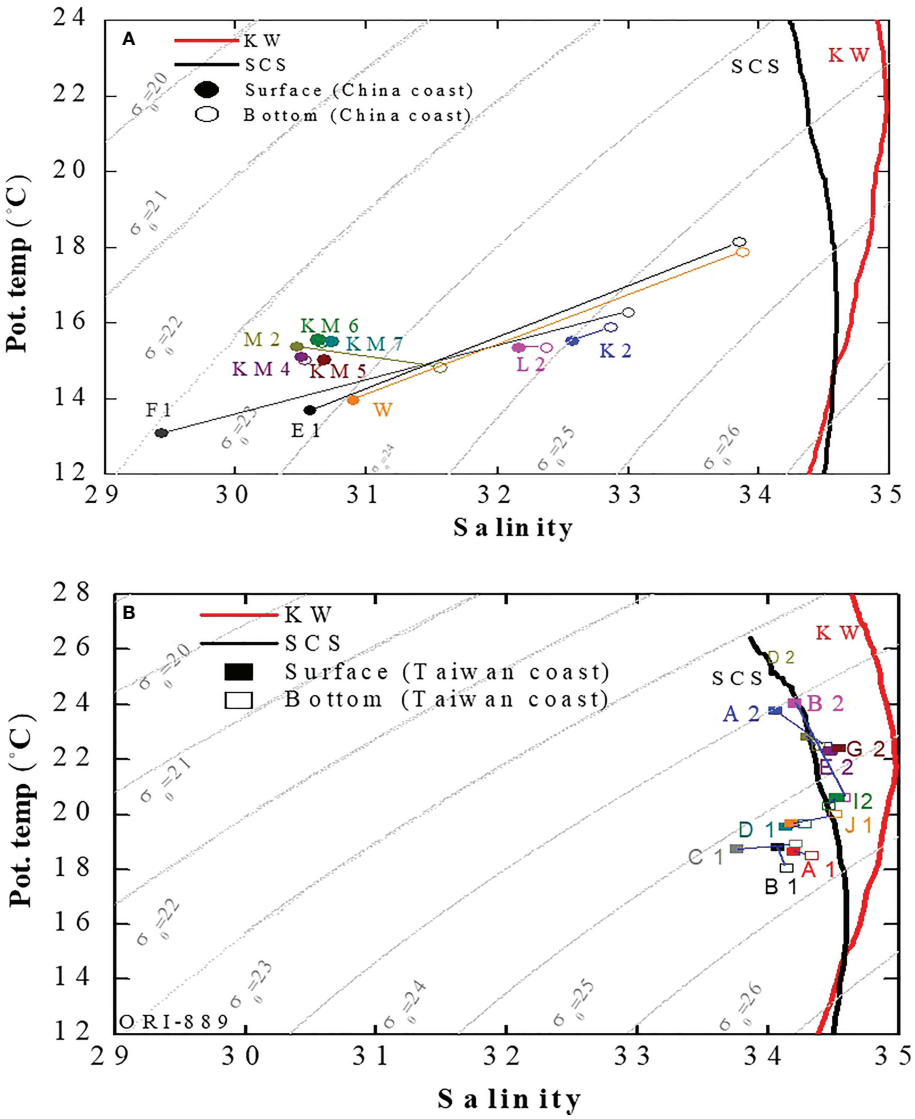

FIGURE 3
Schematic plots of T–S relationships for surface and bottom waters collected from stations located in the western TS (on the coast of China) **(A)** and the central and eastern TS (on the coast of Taiwan, **B**) in winter. The surface and bottom waters at each station are connected by dotted lines. The "KW" and "SCS" curves represent the typical T–S features of the KW and SCSW, respectively. The KW and SCSW represent typical waters collected from the western Philippine Sea and SCS central basin, respectively.

DIP was similar to those of NH_4^+, ranging from 0.05 to 0.42 μM with the highest concentration at Station 25. The concentrations of NH_4^+, N+N, DIP, and silicate were consistently higher in the western TS than in the eastern TS, with the highest concentrations consistently occurring at Station 25.

Despite the lack of available sampling stations in most of the central and eastern TS in winter, the concentrations of N+N increased from 0.24 μM in the eastern TS to 24.5 μM in the western TS, with the highest concentration occurring at Station 25 (Figure 4C). The concentrations of DIP ranged from 0.07 to 0.49 μM and 0.02 to 0.91 μM in the eastern and western TS, respectively (figure omitted). The concentrations of silicate ranged from 1.92 to 11.0 μM and from 5.00 to 29.5 μM in the eastern and western TS, respectively (figure omitted). Similar to the conditions in early summer, the concentrations of N+N, DIP, and silicate were higher in the western TS than in the eastern TS. This difference was particularly notable in winter, when the southward flow of the CCW was most pronounced. The distribution patterns of nutrients result from river input in early summer and the effects of the nutrient-rich CCW on the western TS, which contrast considerably with the effects of the oligotrophic SCSW and intruding KW on the eastern TS in early summer and winter.

Distributions of DOM

The concentrations of DOC, dissolved organic nitrogen (DON), and dissolved organic phosphorus (DOP) in the TS ranged from 60 to 120 μM, 2.92 to 13.8 μM, and 0.07 to 0.38 μM, respectively, in early summer (Figure 5). The concentrations of DOC and DON were slightly higher in the western TS than in the eastern TS; however, the concentrations of DOP were largely confined to the range of 0.2 – 0.3 μM. The highest concentrations of DOC, DON, and DOP were consistently observed in the Minjiang River plume in early summer, reflecting the strong effects of river discharge on DOM distributions. DOP was depleted relative to DOC and DON, with the average DOC:DON:DOP ratio being approximately 330:46:1, which is significantly higher than the Redfield ratio (106:16:1), indicating potential N- and P-limited in the study area. All the DON/DOP ratios fell between the highest (50) and lowest (16) boundaries (Figure 6), which may have corresponded to the largest effects of terrestrial and biological origins, respectively. In addition to DOM, the highest concentrations of nutrients and total suspended matter (TSM) were also observed near the Minjiang River plume, which also had the lowest salinity among the sampling stations. The results suggested that the hydrological conditions and DOM distributions in the TS were considerably affected by terrestrial input, given that the monthly discharge in the Minjiang River peaked in May in 2006 (Zhang et al., 2015). The stations with the impacts of SCSW and KW generally had low concentrations of DOC and DON, except for a few spots near estuaries in the east side of the TS. The surface concentrations of DOP, however, were highest close to the source waters of the SCSW and KW (Hung et al., 2007).

The concentrations of DOC in winter (72–83 μM, data not shown) was much lower than that in early summer in the western TS, where the water was dominated by the southward CCW, a local spot near the Kinmen Islands (144 μM, see Figure 1B for the location) was the exception. The concentrations ranged from 70 to 110 μM in the eastern TS, which are relatively high (90 – 110 μM) near the coast of Taiwan along the northern transect where the water mixed with upwelled water and was characterized by high concentrations of nutrients and Chl-a. The concentrations of DOC were low (70 – 71 μM) in the eastern TS along the southern transect where the water was dominated by the SCSW and KW. The stoichiometric relationship of DOC, DON and DOP in winter could not be derived because DON and DOP data for winter were unavailable.

Distributions of CDOM

The distributions of $a_{CDOM(325)}$ and spectral slope (S) values in the TS are illustrated in Figure 7. In early summer, the $a_{CDOM(325)}$ values were higher in the western TS (0.4 – 0.6 m^{-1}) than in the eastern TS (0.2 – 0.3 m^{-1}; Figure 7A), corresponding to the relatively low S values (0.018 – 0.020 nm^{-1}) in the western TS and relatively high S values (0.019 – 0.021 nm^{-1}) in the eastern TS (Figure 7B). The highest $a_{CDOM(325)}$ value (0.6 m^{-1}) and lowest S value (0.018 nm^{-1}) occurred at the Minjiang River plume (Figures 7A, B). These results strongly suggest that terrestrial input, derived mainly from the Minjiang and Jiulongjiang rivers (China), with higher $a_{CDOM(325)}$ and higher apparent DOM molecular weight (or lower S values), affected the western TS. The CDOM data from the stations near the coast of Taiwan did not reflect a considerable effect of terrestrial input because the river runoff from Taiwanese rivers during the sampling period was relatively small. The high S values at Stations 5 and 6 indicate that a strong photobleaching effect (Figure 7B) occurred in waters shallower than 20 m.

The $a_{CDOM(325)}$ values in the western TS in winter (0.6–1.53 m^{-1}; figure omitted) were higher than those in early summer (0.4 – 0.6 m^{-1}). This may have resulted from the sources of CDOM between early summer and winter. The $a_{CDOM(325)}$ values in the eastern TS in early summer (0.2– 0.3 m^{-1}) did not differ considerably from those in winter (0.2– 0.4 m^{-1}). In general, the S values were slightly higher or lower in DOM molecular weight in winter than in early summer, but the spatial distributions of the S values were similar, with lower values in the western TS and higher values in the eastern TS.

Regarding CDOM fluorescence, concentrations of terrestrial Th-like CDOM were closely examined in this study because Th-like CDOM is generally regarded as an indicator of terrestrial

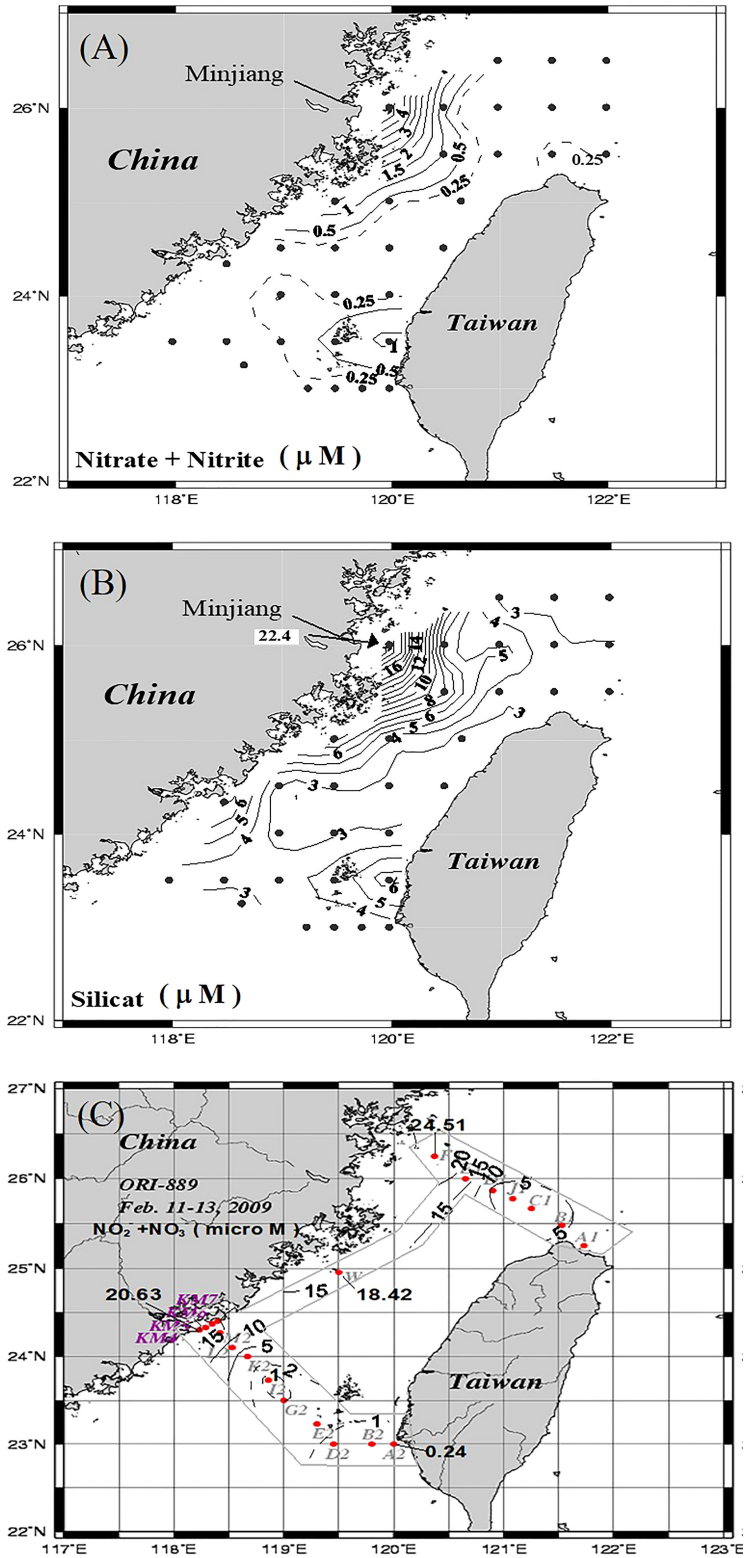

FIGURE 4
Spatial distributions of N+N **(A)** and silicate **(B)** concentrations in surface waters of the TS in early summer (CR1353), and of N+N concentrations in surface waters in winter [(C) CR889]. The concentrations of N+N and sampling stations in winter **(C)** were given with black and gray color, respectively.

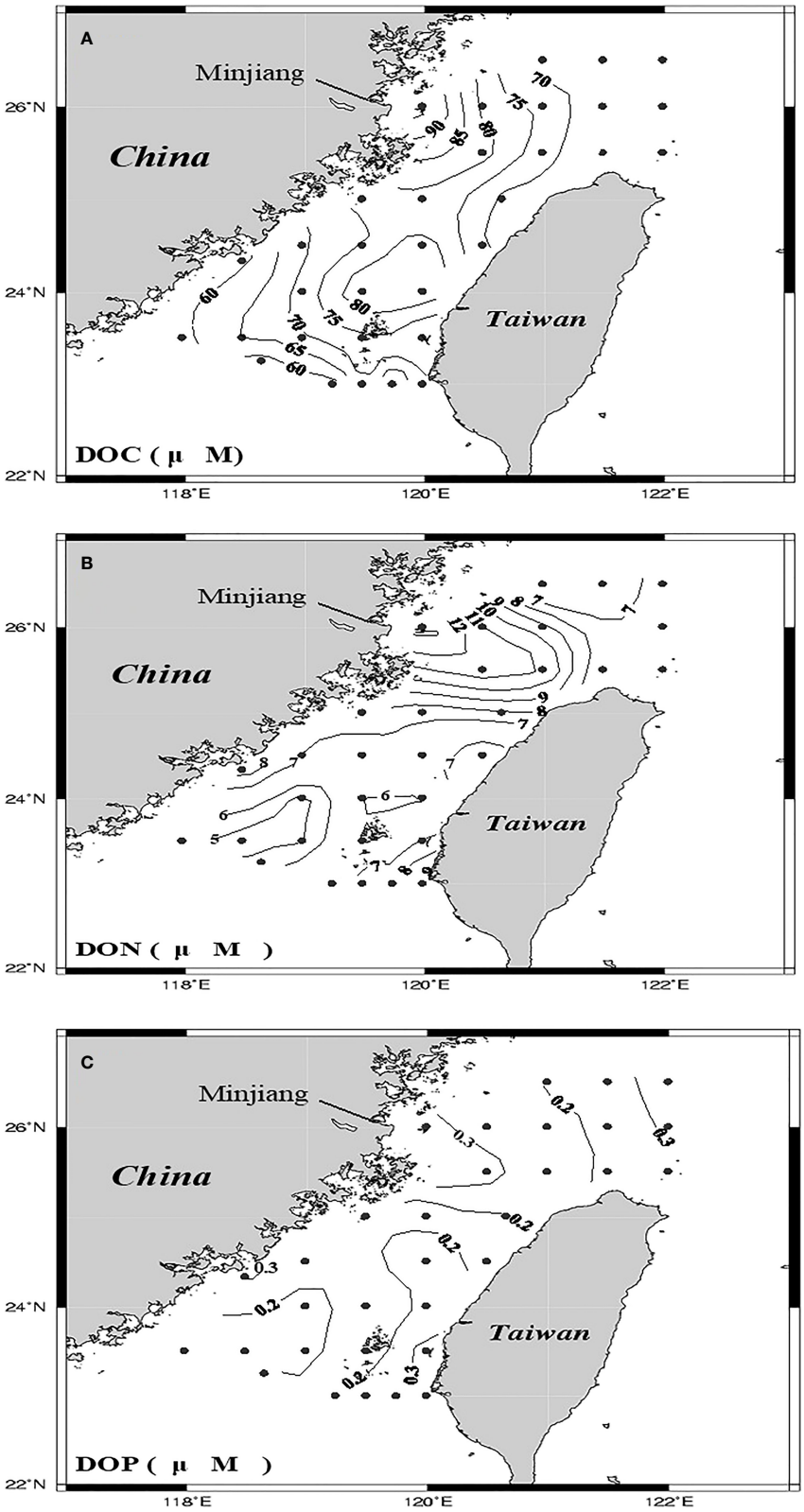

FIGURE 5
Spatial distributions of DOC **(A)**, DON **(B)**, and DOP **(C)** concentrations in surface waters of the TS in early summer (CR1353).

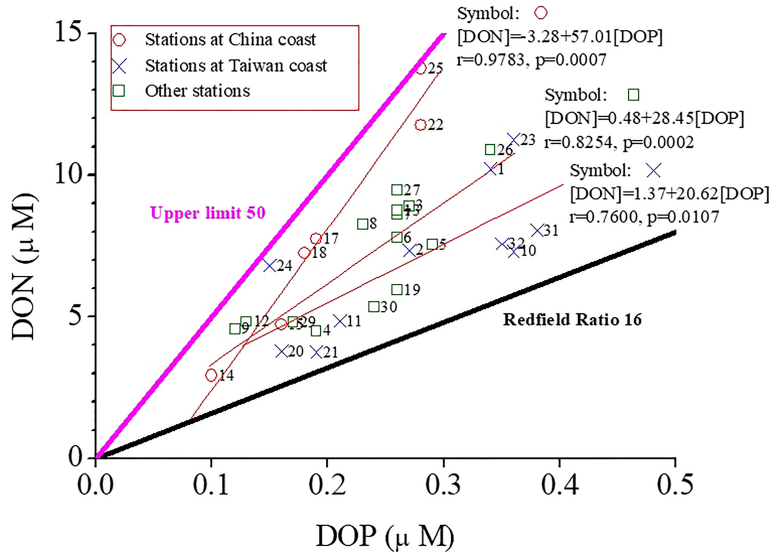

FIGURE 6
Scatter plots of DON and DOP concentrations in TS surface waters in early summer. The DON : DOP ratios ranged from 16 (Redfield ratio) to 50 (upper limit) and were roughly grouped as three ratios (20.62 [×], 28.45 [□], 57.01 [○]), increasing from the coast of Taiwan (20.62) to the coast of China (57.01).

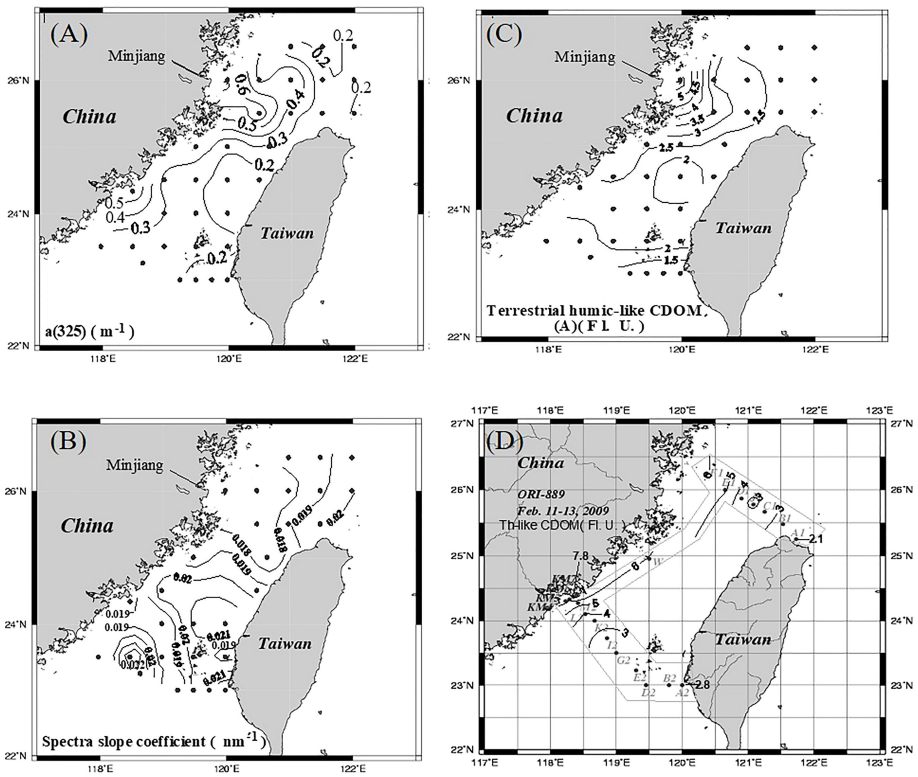

FIGURE 7
Spatial distributions of CDOM absorption coefficient values **(A)**, CDOM spectral slope coefficient values **(B)**, and terrestrial humic-like (Th-like) CDOM concentrations **(C)** in TS surface waters in early summer (CR 1353), and spatial distribution of Th-like CDOM concentrations in TS surface waters **(D)** in winter (CR 889).

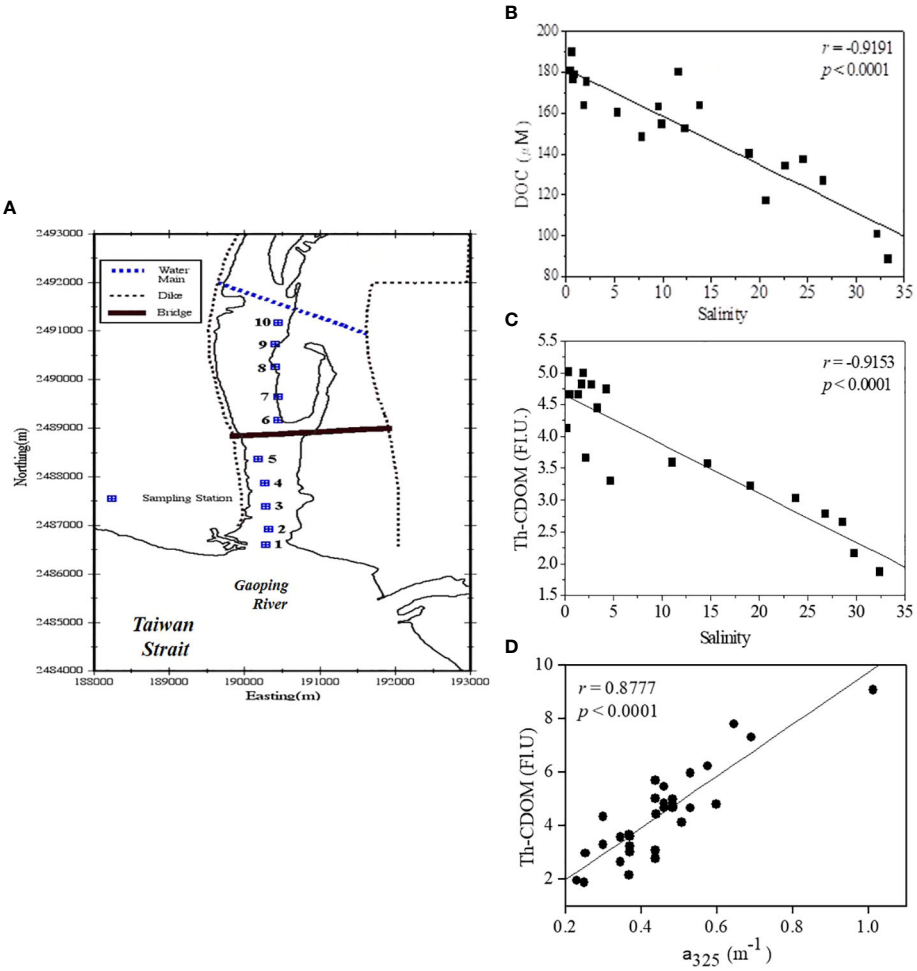

FIGURE 8
Sampling locations **(A)** and conservative mixing evidences of DOC **(B)** and Th-like CDOM [**(C)**, EX/EM: 320–360 nm/420–460 nm] in the Gaoping Estuary (Taiwan). The correlation is highly significant between CDOM absorption coefficient values and CDOM (Th-CDOM) fluorescence intensity **(D)** in the experiment.

input. The distributions of Th-like CDOM are illustrated in Figures 7C, D. The spatial distribution of fluorescence intensity increased significantly from the eastern TS to the western TS both in early summer (Figure 7C) and winter (Figure 7D). The highest value occurred in the Minjiang River plume in early summer and in the Minjiang and Jiulongjiang river plumes in winter, reflecting the contributions of terrestrial sources from the two rivers as well as those of the CDW. Yang et al. (2019) discovered that the Minjiang River exported the largest amount of DOC among the rivers adjacent to the TS, with 72% of annual flux occurring in spring and summer. They also reported the increased river export of terrestrial aromatic and high molecular weight constitutes in summer. The signal intensity of Th-like CDOM was small in the eastern TS in both seasons because the amount of discharge from the rivers on the main island of Taiwan was relatively small.

Conservative mixing behaviors of terrestrial DOC and CDOM

The geochemical and optical properties of DOM and CDOM have been used to trace or understand the mixing behaviors of water masses in estuarine and oceanic waters (Matsuoka et al., 2012; Yang et al., 2013; Yu et al., 2016). To evaluate the mixing behavior of terrestrial DOC (Figure 8B) and Th-CDOM (Figure 8C), the Gaoping River Estuary (Figure 8A) under well-mixed conditions was examplified to trace sources and fates of DOC and Th-CDOM in the TS. In addition to a conservative mixing behavior, the significant correlation between a(325) (an indicator of CDOM concentration) and fluorescence intensity of the Th-CDOM (Figure 8D) indicates that Th-CDOM is the main component of terrestrial CDOM. Yang et al. (2013) also reported a negative linear correlation

between a350 and salinity in most estuaries in western Taiwan. Although limited data have been used to investigate mixing conditions in estuaries in southeast China, Yi et al. (2014) discovered a negative correlation between a350 and salinity in the Jiulong River estuary. Hong et al. (2012) reported that the mixing of land and local pollution sources with seawater determines the distribution of CDOM in the Jiulong River estuary. Therefore, the conservative mixing behavior of terrestrial CDOM may be used to trace the distribution and fate of CDOM in the TS.

Discussion

Hydrological and biological controls on nutrient and DOM distributions

The concentration of N+N varied inversely but not strictly linearly with salinity in early summer and winter (Figure 9), indicating the roles of terrestrial and human sources in determining the elevated surface concentrations of N+N in early summer and of pollution and CCW in determining the N+N concentrations in winter. Zhang et al. (2004, 2015) attributed the recent increase in pollution and hypoxic conditions in the Minjiang Estuary to increased agricultural activity and wastewater input. The surface concentrations of N+N were generally low in early summer except for those at stations close to the Minjiang plume (e.g., Station 25). The inverse relationship of phosphate-salinity was similar to that of (N+N)-salinity, but the relationship of silicate-salinity was stronger than that of (N+N)-salinity because of silicate being derived mainly from terrestrial sources (figures omitted). The high concentration of nutrients at Station 10 (see Figure 1A for location, concentration not shown) relative to those at the neighbouring stations was likely caused by the upwelling of the northward SCSW rather than by river input because of the high salinity (34.37) and relatively low temperature. The response of N+N concentration to changes in salinity in winter was sharper than in early summer, mainly because of the effect of the Changjiang Dilute Water (CDW) being carried southward by the China Coastal Current, particularly on the coast of China. The CDW generally has a salinity of 30–32 and high concentrations of N+N (>18 μM) even in the middle of the coast of China (Chen et al., 2021), causing the TS (especially near the coast of China) to have a higher N+N concentration in winter than in early summer. Figure 10 illustrates the sharp gradients of seawater temperatures, which increased from the coast of China to the coast of Taiwan coast (from 14°C at Station F1 to 19°C at Station A1; Figure 10A) and the concentrations of N+N, which decreased from the coast of China to the coast of Taiwan (from 20 μM at Station F1 to 6 μM at Station A1; Figure 10C) along the northern transect. Similar conditions occurred in the southern section (Figures 10B, D), with temperatures increasing from the coast of China to the coast of Taiwan (from 15°C at Station M2 to 22.6°C at Station D2) and concentrations of N+N decreasing from the coast of China to the coast of Taiwan (from14 μM at Station M2 to 1 μM at Station D2), although temperatures and N+N concentrations were generally higher and lower, respectively, in the southern section than in the northern section. These results indicate the effect of the CDW, with a low temperature and high concentrations of nutrients, on the western TS in winter. The

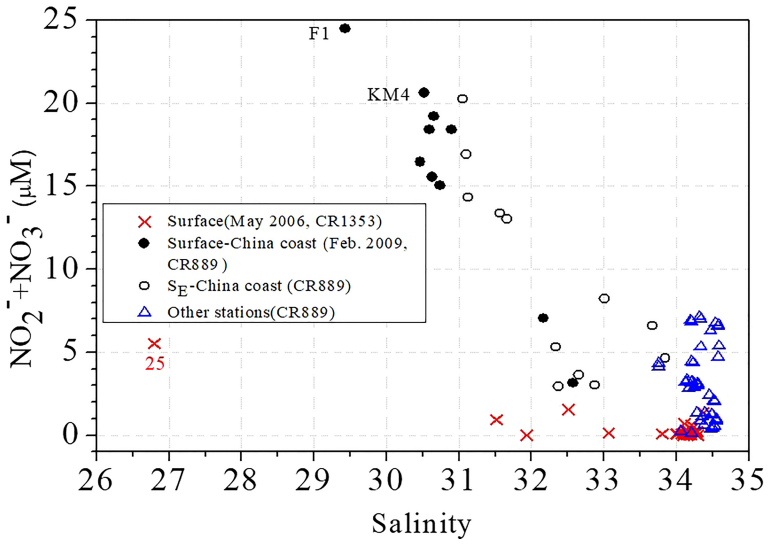

FIGURE 9
Schematic plot of N+N concentrations and salinity in early summer (×, CR1353) and winter (other icons, CR889) in the TS. S_E-China coast is surface-excluded samples in the coast of China. The sampling stations with particularly low salinity and high N+N concentrations (25, F1, KM4) are noted.

distribution patterns of phosphate and silicate (data not shown) were similar to that of N+N in both early summer and winter; however, the variations in silicate concentration between early summer and winter at a given salinity were smaller, likely because the silicate contribution of rivers was higher in early summer than in winter.

The concentration of DOC was inversely correlated with salinity except for at a few stations with particularly high DOC concentrations (Figure 11) but was weakly correlated with Chl-a (data not shown), indicating that the distributions of DOC in early summer and winter were likely determined primarily by terrestrial input and hydrological processes rather than by biological processes. The concentrations of DOC at a given salinity were comparable between early summer and winter, because the contribution of DOC from the CDW was lower in winter. The especially high concentration at KM6 (see location in Figure 1B) and moderately high concentration at A1 in winter were likely caused by pollution in the Jiulongjiang River plume (at KM6) and in water close to the Damshui Estaury in Taiwan (at A1). DON was also inversely correlated with salinity, but DOP concentrations were not strongly correlated with salinity and exhibited little spatial variation in early summer. Unfortunately, DON and DOP data were not collected during winter for further comparisons. The relatively high DOC : DON: DOP ratio (353:49:1) at Station 25 reflects the effect of terrestrial DOM in the Minjiang River plume in early summer. However, the ratios at Station 10 (186:20:1) and Station 31 (168:21:1) were significantly lower and closer to the Redfield ratio, indicating that the DOM at these stations was mainly derived from biological sources. This is because Stations 10 and 31 are located in the upwelling zone and have higher concentrations of nutrients than those at neighboring stations. In general, the DON : DOP ratios were largely confined to the ranges between 16 (lower limit, the Redfield ratio) and 50 (upper limit) in early summer and can be roughly grouped as three zones (with DON/ DOP ratios of 20.6, 28.5, and 57.0) increasing from the coast of

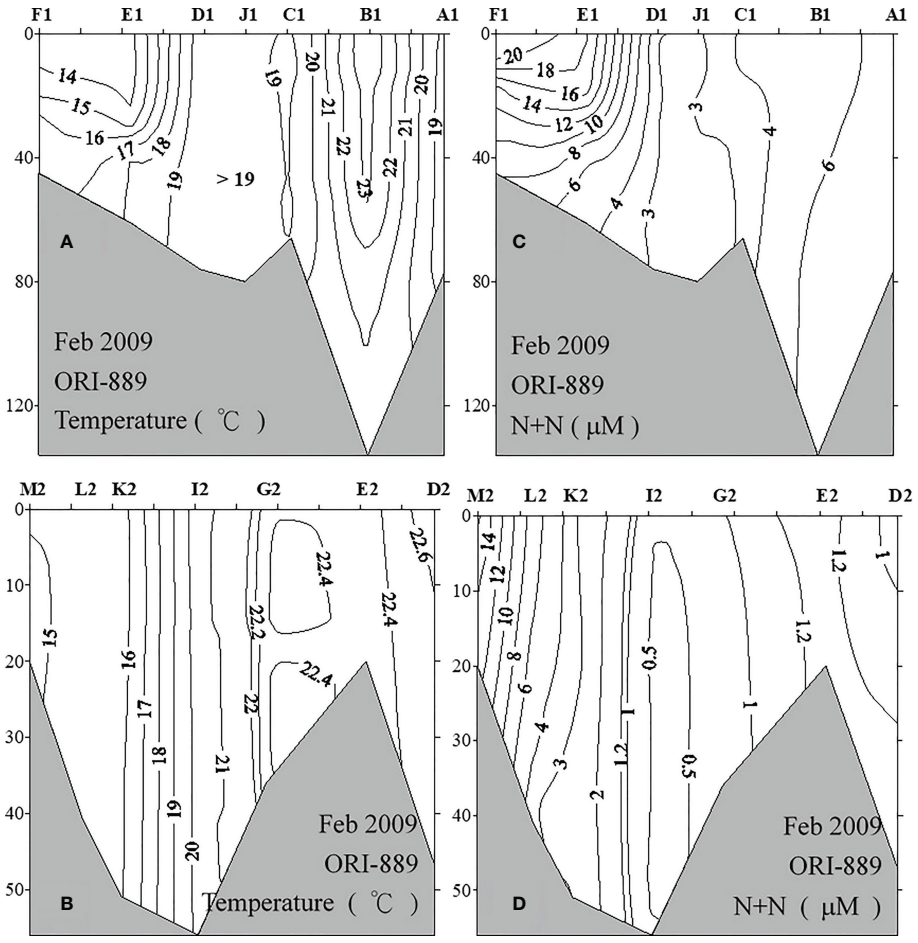

FIGURE 10
Temperature and N+N contours in the profiles of water samples from along the northern (**A**, **C**; upper panel) and southern (**B**, **D**; lower panel) TS-crossing transects in winter (Feb. 2009).

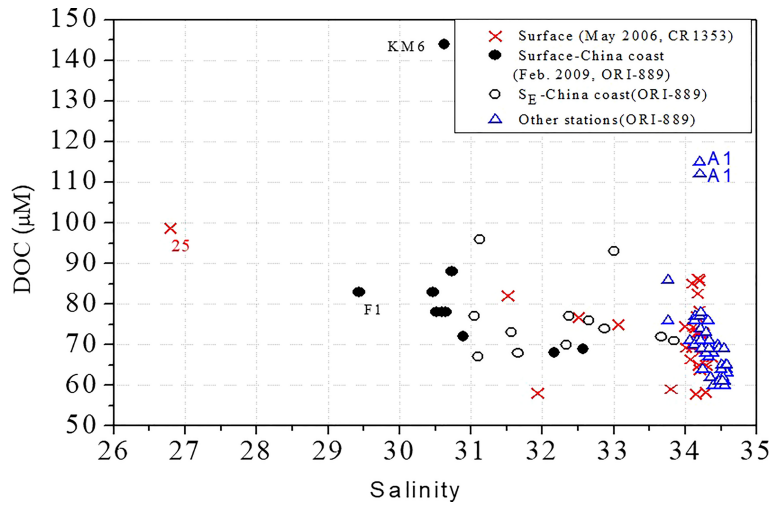

FIGURE 11
Relationship between DOC and salinity in early summer (×, CR1353) and winter (other icons, CR889) in the TS. S_E-China coast is surface-excluded samples in the coast of China. The sampling stations with particularly low salinity and high DOC concentrations (25, F1, KM6, A1) are noted.

Taiwan to the coast of China (Figure 6), following a pattern opposite to that of nutrient distribution.

Characterization and distribution patterns of CDOM

Th-like CDOM was significantly and negatively correlated with salinity (Figure 12) in early summer, suggesting that Th-like CDOM in the TS is mainly derived from terrestrial input. The concentrations of marine-like and Th-like CDOM (data omitted) were also significantly correlated ($r = 0.8445$, $p<0.0001$), indicating that terrestrial nutrient input supports biological productivity and serves as a source of marine-like CDOM. Although aCDOM(325) did not behave conservatively (because it was affected by multiple sources and was subject to a photobleaching effect), the fluorescence intensity of Th-like CDOM was significantly inversely correlated with salinity ($r = -0.8051$, $p<0.0001$) in the TS. This indicates that Th-like CDOM can be effectively used as an optical tracer for predicting the mixing of source waters (the CDW, Minjiang Water, S SCSW, and KW). The validity of Th-like CDOM as an optical tracer is also supported by the significant relationship between salinity and Th-like CDOM concentrations ($r = -0.9153$, $p<0.0001$) in the Gaoping Estuary under well-mixed conditions (Figure 8C). In early summer, the KW and SCSW have the highest salinity and lowest Th-like CDOM concentrations and the CDW and Minjiang Water have the lowest salinity highest Th-like CDOM concentrations. Therefore, salinity and Th-like CDOM concentrations of samples from the TS are scattered linearly between the highest and lowest values.

The distribution profiles of Th-like CDOM along the northern and southern TS-crossing transects (Figures 13A, B) reveal a clear decreasing trend in Th-like CDOM concentration from the western TS to the eastern TS and from the surface to the bottom of the sea. The pattern indicates that the distribution of Th-like CDOM in the TS is determined primarily by mixing between the CDW and the KW in winter. Therefore, Th-like CDOM is inversely correlated with salinity ($r = -0.7896$, $p<0.0001$; Figure 12), and Th-like CDOM can be effectively used as an optical tracer for water mixing in the TS.

Factor analysis of DOM and CDOM distributions

To further elucidate the processes and factors affecting the DOM and CDOM distributions in the TS, factor analysis was used to investigate potential statistical associations among physical and biogeochemical parameters and potential cause-and-effect relationships between such parameters and fates of DOM and CDOM in the TS. The results of the factor analysis (Table 2) indicated that Factor 1 explained 31.6% of the variance in temperature; salinity; and silicate, N+N, terrestrial and marine humic-like CDOM, DOC, and POC concentrations. The concentrations of DOC and CDOM were significantly correlated with those of terrestrial-derived indicators, and the distributions of DOC and CDOM in the TS in early summer are

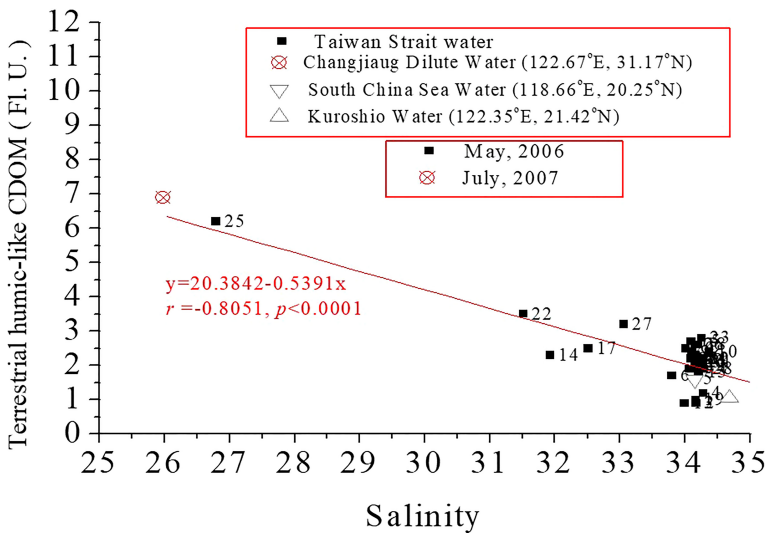

FIGURE 12
Inverse correlation between Th-like CDOM and salinity in TS surface waters in early summer season.

likely controlled primarily by hydrological conditions and physical processes. The Factor 2, which was principally associated with parameters related to biological productivity, could explain 21.7% of the variance in the selected parameters. Chl-a was positively correlated with tryptophan-like CDOM and a(325) but inversely correlated with temperature and salinity. This is likely because the western TS receives fresh water and nutrients that fuel primary productivity and has a lower temperature than does the eastern TS influenced considerably by the SCSW and the warm intruding KW. The variance in DON and DOP concentrations may be associated with biological activity and thus determined by physical and biological processes. Factors 3–5 were less important, explaining only 13.762%, 12.295%, and 8.263% of the variance, respectively. The variance associated with Factors 3–5 was likely associated with the subsurface upwelling around Station 10; biological excretion of DON and DOP; and recycling of DOC, NH_4^+, and tyrosine-like CDOM, respectively (Table 2). Yang et al. (2016) did find a close relationship between apparent oxygen utilization (AOU) and DOM parameters, including DOC and

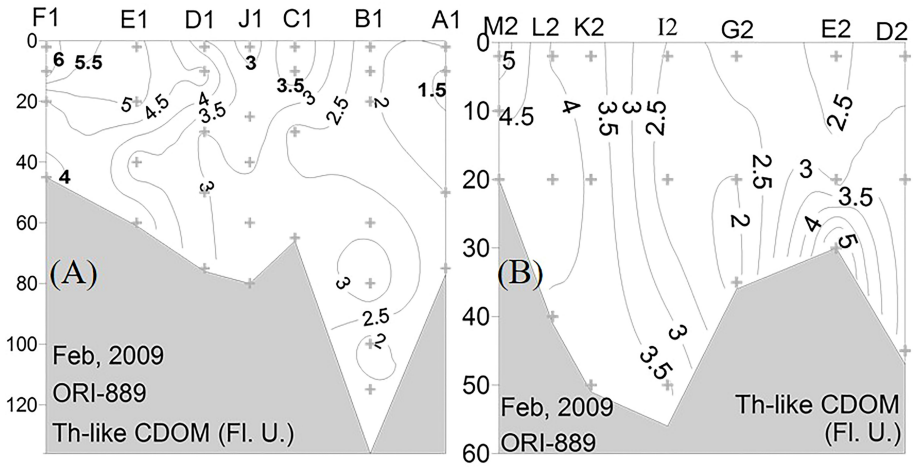

FIGURE 13
Distributions of Th-like CDOM along the northern **(A)** and southern **(B)** TS-crossin transects in winter.

TABLE 2 Factor matrix of hydrological and biogeochemical variables in the TS in early summer (CR1353).

Variables	Factor 1	Factor 2	Factor 3	Factor 4	Factor 5
Salinity	-0.918*	-0.262	-0.043	-0.096	-0.086
Silicate	0.917*	0.184	0.256	0.12	0.034
Nitrate+Ntrite	0.887*	0.042	0.305	0.199	0.129
Terrestrial humic-like CDOM	0.883*	0.396	0.121	0.066	0.099
Marine humic-like CDOM	0.862*	0.315	0.097	0.08	0.141
Tryptophan-like CDOM	0.682*	0.586*	0.158	0.029	-0.224
Temperature	-0.638*	-0.629*	-0.026	0.158	0.032
DOC	0.565*	-0.167	-0.073	0.305	0.591*
POC	0.528*	0.697*	0.378	0.049	-0.163
a(325)	0.022	0.877*	-0.014	-0.122	-0.243
Chlorophyll a	0.286	0.845*	-0.156	0.261	0.074
Spectra slope parameter	-0.226	-0.682*	-0.268	0.234	-0.12
Ammonium	0.127	0.127	0.174	0.093	0.5*
DIP	0.271	0.016	0.929*	0.117	0.124
TSM	0.084	0.085	0.895*	-0.136	-0.24
DOP	-0.059	-0.073	0.271	0.913*	-0.101
DON	0.463	0.091	-0.075	0.828*	-0.015
Tyrosine-like CDOM	-0.084	0.029	0.078	0.166	-0.827*
Percent of total variance explained	31.578	21.712	13.762	12.295	8.263
Probably dominant factor	Terrestrial input	Primary production	Subsurface upwelling	Biological excretion	Recycling

*significance level ($p < 0.05$).

protein-like CDOM in the east TS, suggesting for the influence of microbial activities on the dynamics of DOM. In total, the five factors explained approximately 90% of the variance.

Factor analysis was also performed for the data collected in winter. The results were highly similar to those obtained in the factor analysis of data collected in early summer. Factors 1–5 explained 23.096%, 19.012%, 14.682%, 9.616%, and 10.670% of the variance in the parameters, respectively accounting for approximately 80% of the total variance. Factor 1 explains considerably less variance in the parameters in winter because of the lower amount of terrestrial input.

Conclusion

The distributions of nutrients, DOM, and CDOM in the TS are mainly controlled by local input of polluted river water mixed with the poleward SCSW and Kuroshio branch current (which have low nutrient, DOM, and CDOM concentrations) in early summer and by the CDW (which has high nutrient, DOM, and CDOM concentrations) and the intruding KW in winter. Because of the unique characteristics and conservative behavior of Th-like CDOM in different source waters, Th-like CDOM can be used as an effective optical tracer to examine the mixing of source waters, including the CDW, Minjiang Water, SCSW, and KW, in the TS. The factor analysis performed in the present study revealed the relative importance of hydrological and biogeochemical processes in determining the distributions of nutrients, DOM, and CDOM in the TS in early summer and winter.

Data availability statement

The original contributions presented in the study are included in the article/supplementary material. Further inquiries can be directed to the corresponding author.

Author contributions

J-JH conducted the experiment and data analysis and wrote the manuscript. W-TL conducted sample collection and analysis and data analysis. H-MY performed mixing experiment in the Gaoping Estuary. Y-HL performed data analysis and manuscript preparation. LG performed data discussion and reviewed the draft manuscript. All authors contributed to the article and approved the submitted version.

Funding

This study was supported by the National Science Council and Ministry of Science and Technology, Taiwan, Republic of China (NSC 100-2621-M110-002, MOST 106-2611-M-110-015-, MOST 111-2611-M-110-016) and the "Aim for the Top University Plan" of the National Sun Yat-sen University and Ministry of Education, Taiwan, ROC (06C030203).

Acknowledgments

The authors would like to thank Dr. KT Jiann and Dr. CTA Chen for acting as the chief scientists and helping for sampling in Cruises ORII CR 1393 and ORI CR889, respectively. Thanks are extended to YL Kuo, FH Lee and YC Yeh for their assistance in sampling and the analyses.

Conflict of interest

The authors declare that the research was conducted in the absence of any commercial or financial relationships that could be construed as a potential conflict of interest.

Publisher's note

References

Abdulla, H. A. N., Minor, E. C., Dias, R. F., and Hatcher, P. G. (2013). Transformations of the chemical compositions of high molecular weight DOM along a salinity transect: Using two dimensional correlation spectroscopy and principal component analysis approaches. *Geochim. Cosmochim. Acta* 118, 231246. doi: 10.1016/j.gca.2013.03.036

Abell, J., Emerson, S., and Renaud, P. (2000). Distributions of TOP, TON and TOC in the north pacific subtropical gyre: Implications for nutrient supply in the surface ocean and remineralization in the upper thermocline. *J. Mar. Res.* 58, 203–222. doi: 10.1357/002224000321511142

Amon, R. M. W., Fitznar, H.-P., and Benner, R. (2001). Linkages among the bioreactivity, chemical composition, and diagenetic state of marine dissolved organic matter. *Limnol. Oceanogr.* 46, 287297. doi: 10.4319/lo.2001.46.2.0287

Barron, C., and Duarte, C. M. (2015). Dissolved organic pools and export from the coastal ocean. *Glob. Biogeochem. Cycle* 29 (10), 1725–1738. doi: 10.1002/2014GB005056

Benner, R. (2002). "Chemical composition and reactivity," in *Biogeochemistry of marine dissolved organic matter*. Eds. D. A. Hansell and C. A. Carlson (Amsterdam: Academic Press), 5990.

Blough, N. V., and Del Vecchio, R. (2002). "Chromophoric dissolved organic matter (CDOM) in the coastal environment," in *Biogeochemistry of marine dissolved organic matter*. Eds. D. A. Hansll and C. A. Carlson (San Diego: Academic Press), 509546.

Bricaud, A., Morel, A., and Prieur, L. (1981). Absorption of dissolved organic matter of the sea (yellow substance) in the UV and visible domains. *Limnol. Oceanogr.* 26 (1), 43–53.

Calleja, M. L. I., Al-Otaibi, N., and Morán, X. A. G. (2019). Dissolved organic carbon contribution to oxygen respiration in the central red Sea. *Sci. Rep.* 9, 4690. doi: 10.1038/s41598-019-40753-w

Carr, N., Davis, C. E., Blackbird, S., Danniels, L. R., Preece, C., Woodward, M., et al. (2019) Seasonal and spatial variability in the optical characteristics of DOM in a temperate shelf sea. *Prog. Oceanogr.* 177, 101929. doi: 10.1016/j.pocean.2018.02.025

Chen, C. T. A. (2003). Rare northward flow in the Taiwan strait in winter: A note. *Cont. Shelf. Res.* 23, 387391. doi: 10.1016/S0278-4343(02)00209-1

Chen, C. T. A. (2008). Distributions of nutrients in the East China Sea and the south China Sea connection. *J. Oceanogr.* 66, 737–751. doi: 10.1007/s10872-008-0062-9

Chen, C.-T. A., Bai, Y., Huang, T.-H., He, X., Chen, H.-W., and Yu, S. (2021). Southward spresding of the changjiang diluted water in the la niña spring of 2008. *Sci. Rep.* 11:307. doi: 10.1038/s41598-020-79634-y

Chen, C. T. A., Jan, S., Huang, T.-H., and Tseng, Y.-H. (2010). Spring of no kuroshio intrusion in the southern Taiwan strait. *J. Geophys. Res.* 115, C08011. doi: 10.1029/2009JC005804

Chen, C. T. A., and Sheu, D. D. (2006). Does the Taiwan warm current originate in the Taiwan strait in wintertime? *J. Geophys. Res.* 111, C04005. doi: 10.1029/2005JC003281

Coble, P. G. (1996). Characterization of marine and terrestrial DOM in seawater using excitation-emission matrix spectroscope. *Mar. Chem.* 51, 325346. doi: 10.1016/0304-4203(95)00062-3

Coble, P. G. (2007). Marine optical biogeochemistry: the chemistry of ocean color. *Chem. Rev.* 107, 402418. doi: 10.1021/cr050350+

Du, C., Shang, S., Dong, Q., Hu, C., and Wu, J. (2010). Characteristics of chromophoric dissolved organic matter in the nearshore waters of the western Taiwan strait. *Estu. Coast. Shelf. Sci.* 88, 350356. doi: 10.1016/j.ecss.2010.04.014

Dutkiewicz, S., Hickman, A. E., Jahn, O., Henson, S., Beaulieu, C., and Monier, E. (2019). Ocean colour signature of climate change. *Nat. Commun.* 10, 578. doi: 10.1038/s41467-019-08457-x

Grasshoff, K., Ehrhardt, M., and Kremling, K. (1983). *Methods of seawater analysis* (Weinheim: Verlag Chemie), 419 p.

Green, S. A., and Blough, N. V. (1994). Optical absorption and fluorescence properties of chromophoric dissolved organic matter in natural waters. *Limnol. Oceanogr.* 39, 19031916. doi: 10.4319/lo.1994.39.8.1903

Guo, L., Santschi, P. H., and Warnken, K. W. (1995). Dynamics of dissolved organic carbon (DOC) in oceanic environments. *Limnol. Oceanogr.* 40, 1392–1403. doi: 10.4319/lo.1995.40.8.1392

Guo, W., Yang, L., Hong, H., Stedmon, C. A., Wang, F., Xu, J., et al. (2011). Assessing the dynamics of chromophoric dissolved organic matter in a subtropical estuary using parallel factor analysis. *Mar. Chem.* 124, 125–133. doi: 10.1016/j.marchem.2011.01.003

Hansell, D. A. (2002). "DOC in the global ocean carbon cycle," in *Biogeochemistry of marine dissolved organic matter*. Eds. C. A. Hansell and C. A. Carlson (Amsterdam: Academic Press), 685716.

Hansell, D. A., and Carlson, C. A. (2015). "DOM sources, sinks, reactivity, and budgets," in *Biogeochemistry of marine dissolved organic matter*. Eds. D. A. Hansell and C. A. Carlson (Amsterdam: Academic Press), 65126.

Hansell, D. A., Carlson, C. A., and Schlitzer, R. (2012). Net removal of major marine dissolved organic carbon fractions in the subsurface ocean. *Glob. Biogeochem. Cycle.* 26, GB1016. doi: 10.1029/2011GB004069

Hong, H., Chai, F., Zhang, G., Huang, B., Jiang, Y., and Hu, J. (2011). An overview of physical and biogeochemical processes and ecosystem dynamics in the Taiwan strait. *Cont. Shelf. Res.* 31, S3S12. doi: 10.1016/j.csr.2011.02.002

Hong, H., Yang, L., Guo, W., Wang, F., and Yu, X. (2012). Characterization of dissolved organic matter under contrasting hydrologic regimes in a subtropical watershed using PARAFAC model. *Biogeochem.* 109, 163–174. doi: 10.1007/s10533-011-9617-8

Huang, T.-H., Chen, C.-T. A., Bai, Y., and He, X. (2020). Elevated primary productivity triggered by mixing in the quasi-cul-de-sac Taiwan strait during the NE monsoon. *Sci. Rep*. 10:7846. doi: 10.1038/s41598-020-64580-6

Hu, J. Y., Kawamura, H., Li, C. Y., Hong, H. S., and Jiang, Y. W. (2010). Review on current and seawater volume transport through the Taiwan strait. *J. Oceanogr.* 66, 591610. doi: 10.1007/s10872-010-0049-1

Hung, J.-J., Chen, C.-H., Gong, G.-C., Sheu, D. D., and Shiah, F.-K. (2003). Distributions, stoichiometric patterns and cross-shelf exports of dissolved organic matter in the East China Sea. *Deep-Sea Res. II.* 50, 11271145. doi: 10.1016/S0967-0645(03)00014-6

Hung, J.-J., Hung, C. S., and Su, H.-M. (2008). Biogeochemical responses to the removal of maricultural structures from an eutrophic lagoon (Tapong bay) in Taiwan. *Mar. Environ. Res.* 65, 1–17. doi: 10.1016/j.marenvres.2007.07.003

Hung, J.-J., Lin, P.-L., and Liu, K.-K. (2000). Dissolved and particulate organic carbon in the southern East China Sea. *Cont. Shelf. Res.* 20, 545569. doi: 10.1016/S0278-4343(99)00085-0

Hung, J.-J., Wang, S.-M., and Chen, Y.-L. (2007). Biogeochemical controls on distributions and fluxes of dissolved and particulate organic carbon in the northern south China Sea. *Deep-Sea Res. II.* 54, 1486–1503. doi: 10.1016/j.dsr2.2007.05.006

Jaffè, R. D., McKnight, D., Maie, N., Cory, R., McDowell, W. H., and Campbell, J. L. (2008). Spatial and temporal variations in DOM composition in ecosystems: The importance of long-term monitoring of optical properties. *J. Geophys. Res.* 113, G04032. doi: 10.1029/2008JG000683

Jan, S., Sheu, D. D., and Kuo, H.-M. (2006). Water mass and throughflow variability in the Taiwan strait. *J. Geophys. Res.* 111, C12012. doi: 10.1029/2006JC003656

Jan, S., Tseng, Y.-H., and Dietrich, D. E. (2010). Sources of water in the Taiwan strait. *J. Oceanogr.* 66, 211221. doi: 10.1007/s10872-010-0019-7

Jan, S., Wang, J., Chern, C.-S., and Chao, S.-Y. (2002). Seasonal variations of the circulation in the Taiwan strait. *J. Mar. System.* 35, 249268. doi: 10.1016/S0924-7963(02)00130-6

Matsuoka, A., Bricaud, A., Benner, R., Para, J., Sempéré, R., Prieur, L., et al. (2012). Tracing the transport of colored dissolved organic matter in water masses of the southern Beaufort Sea: relationship with hydrographic characteristics. *Biogeosci* 9, 925940. doi: 10.5194/bg-9-925-2012

McKnight, D. M., Boyer, E. W., Westerhoff, P. K., Doran, P. T., Kulbe, T., and Andersen, D. T. (2001). Spectrofluorometric characterization of dissolved organic matter for indication of precusor organic material and aromaticity. *Limnol. Oceanogr.* 46, 3848. doi: 10.4319/lo.2001.46.1.0038

Miller, W. L., and Zepp, R. G. (1995). Photochemical production of dissolved inorganic carbon from terrestrial organic matter: Significance to the oceanic organic carbon cycle. *Geophys. Res. Lett.* 22, 417420. doi: 10.1029/94GL03344

Murphy, K. R., Stedmon, C. A., Waite, T. D., and Ruiz, G. M. (2008). Distinguishing between terrestrial and autochthonous organic matter sources in marine environments using fluorescence spectroscopy. *Mar. Chem.* 108, 40–58. doi: 10.1016/j.marchem.2007.10.003

Nelson, N. B., Siegel, D. A., Carlson, C. A., Swan, C., Smethie, W. M., and Khatiwala, S. (2007). Hydrography of chromophoric dissolved organic matter in the north Atlantic. *Deep-Sea Res.* 54, 710–731. doi: 10.1016/j.dsr.2007.02.006

Norman, L., Thomas, D. N., Stedmon, C. A., Cranskog, M. A., Papadimitrious, S., Krapp, R. H., et al. (2011). The characteristics of dissolved organic matter (DOM) and chromophoric dissolved organic matter (CDOM) in anarctic sea ice. *Deep-Sea Res. II.* 58, 1075–1091.

Obernosterer, I., and Benner, R. (2004). Composition between biological and photochemical processes in the mineralization of dissolved organic carbon. *Limnol. Oceanogr.* 49 (1), 117–124.

Pai, S.-C., Gong, G.-C., and Liu, K.-K. (1993). Determination of dissolved oxygen in seawater by direct spectrophotometry of total iodine. *Mar. Chem.* 41, 343351. doi: 10.1016/0304-4203(93)90266-Q

Pai, S. C., and Riley, J. P. (1994). Determination of nitrate in presence of nitrite in natural water by flow injection analysis with a non-quantitative on-line cadmium reactor. *Inter. J. Environ. Anal. Chem.* 57, 263277. doi: 10.1080/03067319408027460

Pai, S. C., Tsau, Y. J., and Yang, T. (2001). pH and buffering capacity problems involved in the determination of ammonia in saline water using the indophenol blue spectrophotometric method. *Anal. Chim. Acta* 434, 209216. doi: 10.1016/S0003-2670(01)00851-0

Raimbault, P., Garcia, N., and Cerutti, F. (2008). Distribution of inorganic and organic nutrients in the south pacific ocean - evidence for long-term accumulation of organic matter in nitrogen-depleted waters. *Biogeosci.* 5, 281–298. doi: 10.5194/bg-5-281-2008

Ridal, J. J., and Moore, R. M. (1990). A re-examination of the measurement of dissolved organic phosphorus in seawater. *Mar. Chem.* 29, 1931. doi: 10.1016/0304-4203(90)90003-U

Riedel, T., Zark, M., Vähätalo, A. V., Niggemann, J., Spencer, R. G. M., Hemes, P. J., et al. (2016). Molecular signatures of biogeochemical transformations in dissolved organic matter from ten world rivers. *Front. Earth Sci.* 4. doi: 10.3389/feart.2016.00085

Romera-Castillo, C., Nieto-Cid, M., Castro, C. G., Marrase, C., Largier, J., Barton, E. D., et al. (2011). Fluorecence: Absorption ratio- tracing photochemical and microbial degradation processes affecting colored dissolved organic matter in a coastal system. *Mar. Chem.* 125, 2638. doi: 10.1016/j.marchem.2011.02.001

Siegel, D. A., Maritorena, S., Nelson, N. B., Hansell, D. A., and Lorenzi-Kayser, M. (2002). Global distribution and dynamics of colored dissolved and detrital organic materials. *J. Geophys. Res.* 107(C12), 3228. doi: 10.1029/2001JC000965

Stedmon, C. A., Markager, S., and Bro, R. (2003). Tracing dissolved organic matter in aquatic environments using a new approach to fluorescence spectroscopy. *Mar. Chem.* 82, 239254. doi: 10.1016/S0304-4203(03)00072-0

Stedmon, C. A., and Nelson, N. B. (2015). "The optical properties and signatures of DOM in the ocean," in *Biogeochemistry of marine dissolved organic matter*. Eds. D. A. Hansell and C. A. Carlson (London: Academic Press), 481508.

Stepanauskas, R., Moran, M. A., Bergamasch, B. A., and Hollibaugh, J. T. (2005). Sources, bioavailabitity, and photoreactivity of dissolved organic carbon in the Sacramento-San Joaquin river delta. *Biogeochem.* 74, 131–149. doi: 10.1007/s10533-004-3361-2

Swan, C. M., Siegel, D. A., Nelson, N. B., Carlson, C. A., and Nasir, E. (2009). Biogeochemical and hydrographic controls on chromophoric dissolved organic matter distribution in the pacific ocean. *Deep-Sea Res. I.* 56, 2175–2192. doi: 10.1016/j.dsr.2009.09.002

Wang, Y. H., Jan, S., and Wang, D. P. (2003). Transports and tidal current estimates in the Taiwan strait from shipboard ADCP observation–2001). *Estu. Coast. Shelf. Sci.* 57, 193–199. doi: 10.1016/S0272-7714(02)00344-X

Welschmeyer, N. A. (1994). Fluormetric analysis of chlorophyll a on the presence of chlorophyll b and pheopigments. *Limnol. Oceanogr.* 39, 19851992. doi: 10.4319/lo.1994.39.8.1985

Wu, C. R., and Hsin, Y. C. (2005). Volume transport through the Taiwan strait: A numerical study. *Terrest. Atmos. Ocean. Sci.* 16 (2), 377–391. doi: 10.3319/TAO.2005.16.2.377(Oc)

Wu, C.-R., Wang, Y.-L., Lin, Y.-F., and Chao, S.-Y. (2017). Intrusion of the kuroshio into south and East China seas. *Sci. Rep*. 7:7895. doi: 10.1038/s41598-017-08206-4

Wyrtki, K. (1961). "Physical oceanography of the southeast Asian waters," in *Scientific results of marine investigations of the south China Sea and the gulf of Thailand*, vol. vol 2. (California: Scripps Institution of Oceanography), 195p.

Yang, L., Cheng, Q., Zhuang, W.-E., Wang, H., and Chen, W. (2019). Seasonal changes in the chemical composition and reactivity of dissolved organic matter at the land-ocean interface of a subtropical river. *Environ. Sci. pollut. Res.* 26, 2459524608. doi: 10.1007/s11356-019-05700-2

Yang, L., Chen, C.-T. A., Lui, H.-K., Zhuang, W.-E., and Wang, B.-J. (2016). Effects of microbial transformation on dissolved organic matter in the east Taiwan strait and implications for carbon and nutrient cycling. *Est. Coast. Shelf. Sci.* 180, 5968. doi: 10.1016/j.ecss.2016.06.021

Yang, L., Hong, H., Chen, C.-T. A., Guo, W., and Huang, T.-H. (2013). Chromophoric dissolved organic matter in the estuaries of populated and mountainous Taiwan. *Mar. Chem.* 157, 1223. doi: 10.1016/j.marchem.2013.07.002

Yi, Y., Zheng, A., Guo, W., Yang, L., and Chen, D. (2014). Optical properties of estuarine dissolved organic matter using cross-flow ultrafiltration. *Acta Oceanol. Sin.* 33, 2229. doi: 10.1007/s13131-014-0451-4

Yu, X., Shen, F., and Liu, Y. (2016). Light absorption properties of CDOM in the changjiang (Yangtze) estuarine and coastal waters: An alternative approach for DOC estimation. *Estu. Coast. Shelf. Sci.* 181, 302311. doi: 10.1016/j.ecss.2016.09.004

Zhang, Z. L., Hong, H. S., Zhou, J. L., and Yu, G. (2004). Phase association of polycyclic aromatic hydrocarbons in the minjiang river estuary, China. *Sci. Total. Environ.* 323, 71–86. doi: 10.1016/j.scitotenv.2003.09.026

Zhang, P., Pang, Y., Pan, H., Shi, C., Huang, Y., and Wang, J. (2015). Factors contributing to hypoxia in the minjiang river estuary, southeast China. *Inter. J. Environ. Res. Pub. Health* 12 (8), 9357–9374. doi: 10.3390/ijerph120809357

frontiers | Frontiers in Marine Science

TYPE Original Research
PUBLISHED 08 December 2022
DOI 10.3389/fmars.2022.1049744

OPEN ACCESS

EDITED BY
Jeng-Wei Tsai,
China Medical University (Taiwan), Taiwan

REVIEWED BY
Abhra Chanda,
Jadavpur University, India
Tatsuki Tokoro,
Port and Airport Research Institute (PARI), Japan

*CORRESPONDENCE
Evan Lechner
elechner@hawaii.edu

SPECIALTY SECTION
This article was submitted to Marine Biogeochemistry, a section of the journal Frontiers in Marine Science

RECEIVED 21 September 2022
ACCEPTED 21 November 2022
PUBLISHED 08 December 2022

CITATION
Lechner E, Rii YM, Ruttenberg K, Kotubetey K and Sabine CL (2022) Assessment of CO_2 and O_2 spatial variability in an indigenous aquaculture system for restoration impacts. *Front. Mar. Sci.* 9:1049744. doi: 10.3389/fmars.2022.1049744

Assessment of CO_2 and O_2 spatial variability in an indigenous aquaculture system for restoration impacts

Evan Lechner[1*], Yoshimi M. Rii[1,2,3], Kathleen Ruttenberg[1], Keli'iahonui Kotubetey[4] and Christopher L. Sabine[1]

[1]Department of Oceanography, University of Hawai'i at Mānoa, Honolulu, HI, United States, [2]Hawai'i Institute of Marine Biology, Kāne'ohe, HI, United States, [3]He'eia National Estuarine Research Reserve, Kāne'ohe, HI, United States, [4]Paepae o He'eia, Kāne'ohe, HI, United States

Spatial variability in carbon dioxide (CO_2) and oxygen (O_2) was assessed within an Indigenous Hawaiian fishpond undergoing active ecosystem restoration. The brackish, tidal fishpond is located within Kāne'ohe Bay, Hawai'i. Following a year of monthly discrete sampling, a significant shift in DIC and percent O_2 saturation was observed along the North-South axis within the pond. The south end of the pond was higher in DIC (+35 µmol·kg^{-1}) and lower in percent O_2 saturation (-19%) than the north end, which exhibited values similar to those observed in water entering the fishpond from the bay. Water quality parameters and inequal proximity to water flux sites suggested that a difference in residence time may exist along the north-south axis. In addition, ΔTA/ΔDIC relationships revealed a respiration signal in south end of the pond, which was enhanced at depth. While physical processes strongly affect CO_2 and O_2 across various temporal scales, spatial patterns in biological processes may also affect variability within the fishpond. These findings demonstrate that changes in water chemistry within the fishpond are the result of ecosystem restoration efforts. In turn, future management decisions at the fishpond will play an important role in preserving its viability as a healthy habitat for the intended marine species.

KEYWORDS

total alkalinity, dissolved inorganic carbon, dissolved oxygen, carbon dynamics, ecosystem restoration, blue carbon ecosystem

1 Introduction

A steady increase in atmospheric carbon dioxide (CO_2) and decrease in global dissolved oxygen (DO) in the open ocean have had profound effects on the chemistry of ocean waters (e.g., Bacastow and Keeling, 1973; Riebsell et al., 2000; Brix et al., 2004; Andersson, 2005; Dore et al., 2009; Goodwin & Lauderdale, 2013; Breitburg et al., 2018).

Uptake of elevated atmospheric CO_2 into seawater leads to the formation of carbonic acid in a process known as ocean acidification (e.g., Caldeira & Wickett, 2003; Orr et al., 2005; Cao et al., 2014; Ono et al., 2019), while the decline in DO creates new stressors for ocean life and ecosystems as oxygen becomes less biologically available (e.g., Breitburg et al., 2018). To date, much of the focus on these topics has been oriented towards large-scale patterns and processes in the open ocean. However, the prioritization of sustainable coastal development has created new interest in coastal and estuarine systems. Wetlands and flooded-field ecosystems, often found within estuarine spaces, occupy a critical boundary between land and sea, where the concentration of natural and anthropogenic activity can give rise to spatially confined changes in coastal chemistry that deviate from broader global trends, such as coastal acidification (Rixen et al., 2015; Chan et al., 2017; Hall et al., 2020) coastal deoxygenation (Rixen et al., 2015; Bednaršek et al., 2016; Feely et al., 2017) and eutrophication (Flynn et al., 2015; Laurent et al., 2017). Importantly, this space hosts aquatic life of immense biodiversity and productivity, while also serving as a major focus of human development and activity (Andersson, 2005; Doney et al., 2020; Jokiel et al., 2011).

Serving as an exemplar of sustainable bioengineering in estuarine environments, Native Hawaiians recognized the immense potential for productivity in estuaries and utilized this setting for Indigenous aquaculture systems, or loko iʻa (Kikuchi, 1976; Keala et al., 2007). Loko iʻa are often built-in areas that represent the brackish mixing zone of the ahupuaʻa, a Native Hawaiian social-ecological land and water management system. In this system, stream water collects and transports organic matter and nutrients as it runs through the watershed and through agro-ecological systems, such as loʻi, which are flooded-field wetlands with taro that provide nutritive sustenance as well as habitat for native fauna (Winter et al., 2018). The loʻi system results in increased ecosystem services, whic include habitat for native flora and fauna as well as serving as sediment retention basins (Koshiba et al., 2013; Bremer et al., 2018; Winter et al., 2020a). Likewise, high nutrient streamflow and groundwater discharge is consumed for primary production within the coastal fishpond, which is situated landward of the reef, thereby promoting healthy nearshore reef communities (Winter et al., 2018). The locations of loko iʻa thus represented deep ecological and biogeochemical understanding of the seasonal and spatial patterns of the landscape by Indigenous Hawaiians, such as land-based (Ringuet and Mackenzie, 2007; De Carlo et al., 2007) and groundwater (Kleven et al., 2014; Dulai et al., 2016) input of nutrients into coastal regions, as well as the biological response and subsequent effects on estuarine and marine food webs. In this way, loko iʻa were continuously maintained for hundreds of years and provided a resilient, reliable source of food, such as herbivorous fish and macroalgae for Hawaiian communities (Maly and Maly, 2003; Demopoulos et al. 2007).

The functioning of the ahupuaʻa system of watershed management was upended in the post contact period of Hawaiian history, as plantation-based agriculture supplanted community-based subsistence farming (Camvel, 2020). The current restoration of a loko iʻa presents an opportunity to quantitatively study what Native Hawaiians likely knew empirically about maintaining a biogeochemical balance in the fishponds. Analysis of restoration efforts will both further the understanding of historic fishpond use and provide insight into the future stability of long-term agro-ecological systems.

Prior research at the study site (Drupp et al., 2011; D'Andrea et al., 2015; Drupp et al., 2016; McCoy et al., 2017) has correlated past incidents of hypoxia and fish mortality with physical processes, such as wind strength and thermal stress. Efforts to better manage aquaculture resources and safeguard the health of cultivated species are likely to benefit from this baseline assessment. CO_2 and O_2 respond to a wide range of biogeochemical processes, making them useful indicators for understanding ecosystem change. As such, a baseline dataset of CO_2 and O_2 variability will be a valuable tool to support management of fishpond for both planning further restoration and anticipating ecosystem response to climate change.

The work presented here aims to expand the understanding of Hawaiian loko iʻa by characterizing the concentrations of carbonate parameters and DO, allowing us to assess the balance of production and respiration within Indigenous resource management systems. The initiation of this study follows a large-scale invasive plant species removal effort and will provide insight into the effects of this aspect of restoration and ecosystem management.

2 Study area

Loko Iʻa o Heʻeia is located on the windward side of Oʻahu along the western side of Kāneʻohe Bay. The ambient temperature in Kāneʻohe varies between 28.17-21.78 °C during the year. Likewise, the bay experiences average annual precipitation of 136.65 cm (Western Regional Climate Center, Kāneʻohe Station 838.1, 1905-2016). Kāneʻohe Bay typically experiences mixed semi-diurnal tides with a mean tidal height of 0.36 m (± 0.29 m) (Young, 2011). The fishpond itself is part of the broader Heʻeia ahupuaʻa (Figure 1) that includes the land, streams, and the offshore reef systems. A portion of the Heʻeia ahupuaʻa was designated as the 29th National Estuarine Research Reserve (NERR) in 2017, with restoration of Indigenous resource management systems as one of its main goals (Winter et al., 2020b). One of the main efforts undertaken to restore Indigenous agro-ecological systems such as loʻi and loko iʻa has been the removal of invasive species, including invasive mangroves such as *Rhizophora mangle*, and invasive algae, such as *Gracilaria salicornia* and *Acanthophora spicifera*. In Heʻeia, introduction and proliferation of invasive mangroves

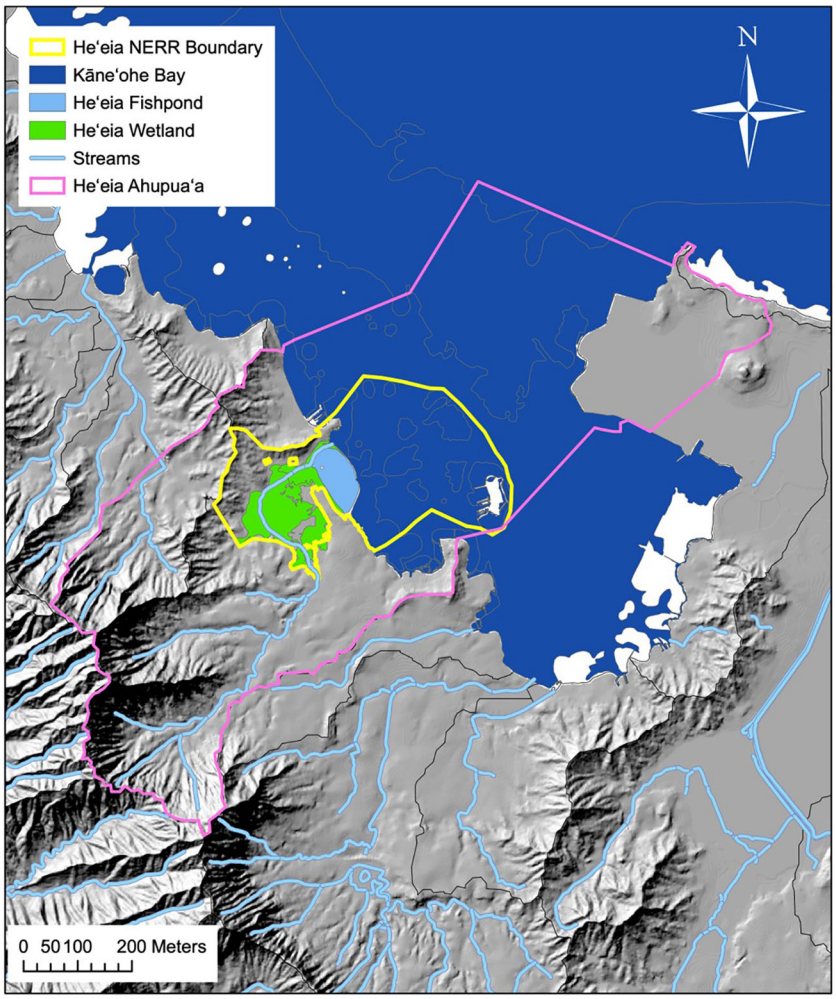

FIGURE 1
He'eia ahupua'a, Ko'olaupoko, O'ahu. Solid orange line represents ahupua'a boundaries in the Hawai'i Statewide GIS Program, with lines extended to include the approximately represented historical He'eia fishery following the ahupua'a of He'eia land commission award (L.C.Aw.10613, Ap.1 to A. Paki. From Public archives of Hawai'i, Letter Folder 244-B, H.A. & R.L. 3/3/47). Map credit: He'eia NERR.

built up a thick bank of organic rich sediment around the landward pond perimeter, restricting stream flow into the fishpond. The subsequent removal of these mangroves has resulted in elevated fresh water supply, decreasing fishpond salinity and temperature, as well as increasing dissolved oxygen over the last decade of restoration work. (Leon Soon, 2017; McCoy et al., 2017; Möhlenkamp et al., 2019; Lopera, 2020).

He'eia Fishpond (Figure 2) is a 0.356 km^2 embayment enclosed by approximately 2.5 km of basalt and coral rubble wall. Along this wall are seven sluice gates, called mākāhā, which allow for tidally influenced flow of water into and out of the fishpond. There are four mākāhā along the seaward wall (Figure 2, 15, 17-19), allowing for water exchange from Kāne'ohe bay, and three mākāhā along He'eia Stream (Figure 2, 12 &13) allowing for fresh/brackish water exchange. Brackish water forms a gradient, running along the landward edge of the pond from the freshwater stream mākāhā in the north, towards the south end of the pond. The fishpond has an average depth of 0.7 m but is not uniform, being generally shallower at the southern end of the fishpond and deeper at the north end and at each of the mākāhā (Yang, 2000; Young, 2011). The remains of a mangrove island removed during a previous phase of restoration (2018-2019) are situated near the stream mākāhā in the north and cause the pond bathymetry to shoal around it. The fishpond interior sits on a fossilized reef previously covered in sand and coral debris. There has been an increase in land derived organic-rich sediments over the last century however, as a result of land use changes upstream. (Costa-Pierce, 1987)

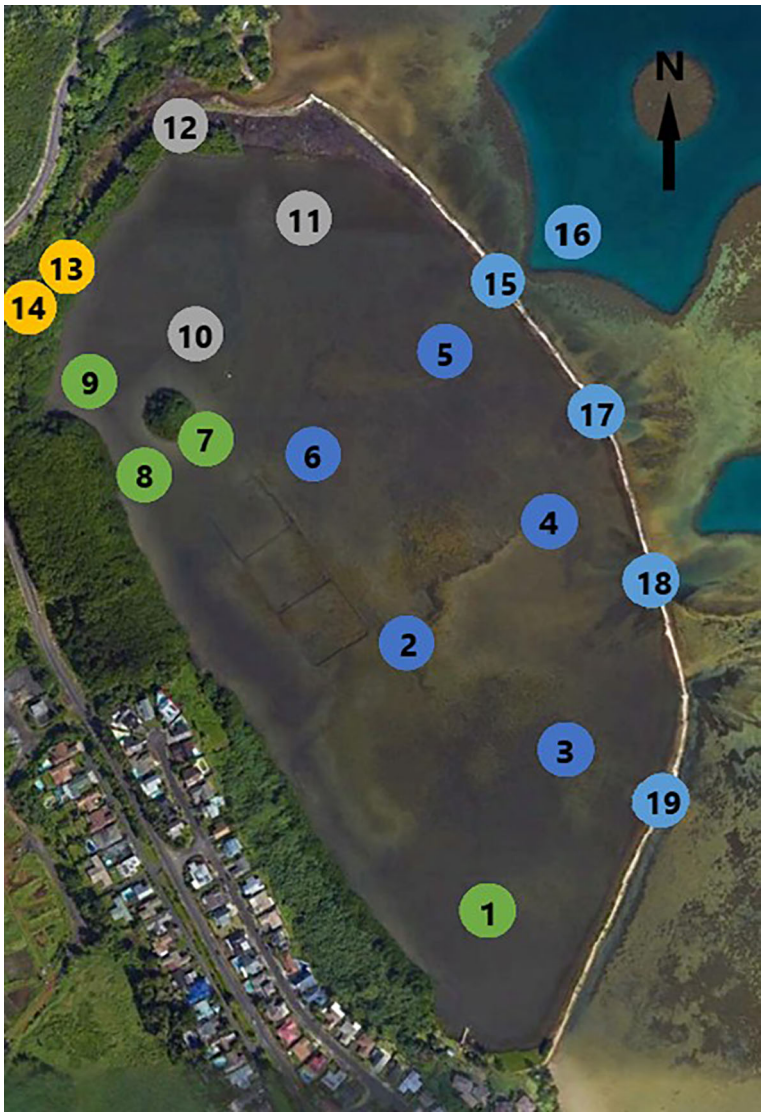

FIGURE 2
He'eia Fishpond, sampling locations numbered: in pond 1-11; Stream facing mākāhā 12 & 13; Ocean facing mākāhā 15, 17, 18, 19; Stream and Ocean endmembers 14 & 16. Station color matches spatial groupings identified in Figure 3. (Image from Google Earth modified by Evan Lechner).

3 Materials/methods

3.1 Sampling frequency and sites

Sampling was conducted (Summarized Table 1) on a monthly basis between August 2019-August 2020. Fieldwork was timed to occur across a neap low tide each month to minimize the potential effect of tidal variability during the course of the sampling day (Young, 2011). Likewise, sampling was conducted over the same early morning period to minimize the effect of diurnal variability.

A sampling grid (Figure 2) was chosen to line up with past field campaigns and build upon an existing library of overlapping measurements (Young, 2011; Dulai et al., 2016; Möhlenkamp et al., 2018; Lopera, 2020). In-pond samples were taken at 11 separate stations, numbered 1-11. Sampling was also conducted at 6 of the 7 mākāhā, including 2 stream-facing mākāhā (12, 14) and 4 bay-facing mākāhā (15, 17, 18, 19). A 7th mākāhā, a stream-facing mākāhā near station 9, was not included in the sampling plan because it was constructed near the end of the project. Lastly, endmember reference samples were collected, with the freshwater endmember (14) collected

from He'eia Stream just stream-ward of 13, and the ocean endmember (16) collected from Kāne'ohe Bay several meters beyond bay-facing mākāhā 15.

At each of the in-pond stations, sampling was conducted at two depths for all sampled parameters. One sample was collected from 5-10 cm below the air-sea interface, and a second was collected from 5-10 cm above the pond bottom. All samples were performed manually, using a 0.5 m length of tubing to prevent excess bubbles from altering the composition of sampled water. For all 6 mākāhā stations and the 2 endmember stations a single sample was collected 5-10 cm below the air-sea interface. The operating assumption was that the mākāhā stations were well mixed due to the vigorous nature of water flowing through the sluice gates.

3.2 Sample collection

Samples for analysis of Totally Alkalinity (TA) and Dissolved Inorganic Carbon (DIC) were collected in 250 mL Biological Oxygen Demand (BOD) bottles, while samples were collected for Dissolved Oxygen (DO) analysis using volumetrically calibrated 60mL BOD bottles. Replicate samples were taken for surface and depth at 1-2 sites per trip on a randomized, rotating basis.

All bottles used for sampling were soap and water washed prior to each field visit. Additionally, bottles for TA/DIC were combusted (550 °C) after washing to incinerate any remaining organic material.

During sample collection, each bottle was rinsed three times with ambient water from the depth being sampled. TA/DIC samples were poisoned with 200 µL of $HgCl_2$ and sealed with Apezion grease to preserve gas composition within the sample and headspace. Likewise, DO samples were subjected to the Winkler method (Codispoti, 2001), in which manganous chloride ($MnCl_2$), sodium hydroxide (NaOH), and sodium iodide (NaI) were added to the sample to precipitate dissolved oxygen in the form of a tetravalent oxide of manganese ($2MnO(OH)_2$). Once treated, samples were stored in a light-proof box until returned to the lab for analysis. All samples were stored in the dark at lab room temperature (~20 °C). DO samples were analyzed within a maximum of 48 hours, while TA/DIC samples were analyzed within a maximum of one month.

Casts were conducted for measurements of conductivity, temperature, and depth using a 10 m range Van Essen CTD Diver (Model# DI281) in tandem with the carbon parameter sample collections at a 10 second measurement frequency for a duration of approximately 120 seconds at the sampled depth. Mean salinity and temperature values were determined from the data set of CTD measurements at each station and at each depth.

Weather data was collected from the HIMB Weather Station at Moku o Lo'e (Rodgers et al., 2005). Mean He'eia streamflow data was approximated using data from the Ha'ikū Stream Gauge (USGS Station #16275000).

3.2.1 Tidal variability measurements

Additional sampling was conducted during the month of July 2020 in order to highlight the relative effect of tidal variability at the study site. Sampling occurred at times targeting both the usual neap tide (7/11/2020), as well as a spring tide (7/04/2020), to examine the range of variability between the two tidal extremes. This timing was particularly advantageous, as the 7/04/2020 spring tide was also the king tide for the year (University of Hawaii Sea Grant, 2018), allowing for examination of the maximum tidal variability at the site. Sampling followed the previously described methodology and samples were collected consistent with the stations and depths sampled throughout the rest of the project. While the results of this tidal sampling campaign are not included here, the sampling plan was a critical step in isolating the various forms of temporal and spatial variability that were expected to influence measurements at He'eia. While tidal variability was found to be significant at He'eia, the results demonstrated the selected neap tide sampling was effective at minimizing the effect of tidal change.

3.2.2 Diurnal variability measurements

Two neap tide sampling dates were selected during August 2020 for a diurnal study. For the first neap tide (8/11/2020), two sampling trips were conducted over a 24-hour period to examine the extent of day/night variability. The sampling times of 2am and 2pm were selected to capture peak respiration and peak photosynthesis recorded in the bay, respectively (Shamberger et al., 2011). The date for this experiment was chosen because the pond experienced a weak diurnal tide, rather than the usual mixed semi-diurnal. Targeting an unusually weak neap tide for this experiment limited the effects of tidal variability during sampling.

For this experiment a narrowed sampling grid was adopted in order to complete the sampling run over a shorter 1–2 hour

TABLE 1 Station groups by geographic location with referenced station IDs, sampled depths, and measured parameters.

Station Group	Station IDs	Sampling Depths	Parameters Sampled
In-pond	1-11	Surface & Depth	TA/DIC, DO, CTD
Stream	12-14	Surface	TA/DIC, DO, CTD
Bay	15-19	Surface	TA/DIC, DO, CTD

window, allowing for a more accurate representation of the timed peaks in photosynthesis and respiration. Eight in-pond sites (1, 2, 3, 4, 5, 6, 8, 11) were selected and sampled at surface and depth. In selecting these sites, special consideration was made to cover a wide spatial range, while still capturing the typical mixing gradients observed during this and previous field campaigns. Just as with the tidal variability results, the results of the diel variability are not included here. The observation of potential diel variability was needed in order to appropriately contextualize any spatial variability within diel cycles in ecosystem production and respiration.

3.3 Water sample analysis

3.3.1 Carbon parameters

All carbon analyses followed the best practices guide (Dickson et al., 2007) and were validated using Certified Materials (Dickson, 2001). TA and DIC analyses were conducted with a standard accuracy of ± 2 µmol·kg^{-1} (Knor et al., 2018).

TA samples were analyzed with an automated open-cell acid-base titration system designed by Dr. Andrew Dickson for high-precision GO-SHIP measurements (personal communication, 2018). Titrations were conducted using an 876 Dosimat Metrohm Plus, an Agilent 34970A Data Acquisition Unit, and a Sierra SmartTrack 50 Mass Flow Controller. Auto-titration was controlled *via* the Alkalinity 2.9j program (Dickson personal communication, 2018).

DIC samples were analyzed on an Apollo DIC Analyzer (Model AS-C3). Sample temperature was taken immediately prior to analysis *via* Fluke 51ii Digital Thermometer.

The results of TA & DIC analyses were entered into the CO2Sys program v2.5 (Pierrot et al., 2006) to determine the other two carbon parameters pCO_2 and pH, allowing the carbon system to be fully described. Due to the large salinity range observed at the study site, the dissociation constants defined by Cai and Wang (1998) were selected, which particularly focused on the salinity ranges typically observed in estuaries. Constraining the carbon system in this way also allowed for the derivation of other parameters, such as the saturation state of aragonite, Ω_{Ar}. In addition to the derivation of these additional parameters, the uncertainty of each parameter was also calculated. pCO_2 was calculated as having an uncertainty of ±9.82 µatm, pH uncertainty was ±0.01, and Ω_{Ar} ± 0.16.

3.3.2 Dissolved oxygen

Analyses of DO samples were conducted *via* Modified Winkler Titration as described by Codispoti (2001). Preserved samples were acidified with sulfuric acid (28% v/v) to convert manganic hydroxide to manganic sulfate and were then titrated with sodium thiosulfate. Standardization of sodium thiosulfate titrant was conducted for each round of sampling using a 0.1 N Potassium Iodate standard as described in Codispoti (2001). Dissolved oxygen data was subsequently combined with collected temperature and salinity data to derive the percent oxygen saturation for the sample (Benson and Krause, 1980; Benson and Krause, 1984; U.S. Geological Survey, 2011). Dissolved oxygen analyses were conducted with a standard accuracy of 0.19%, typical of the normal range 0.1% - 0.3% (Carpenter, 1965; Codispoti, 2001; Wong, 2012).

4 Results

4.1 Spatial survey

Organizing salinity data by stations (Figure 3), the estuary was divided into three identifiable water types. The first was a relatively uniform seawater source (33.73, 2σ=*1.08*) derived from Kāneʻohe Bay. This salinity characterizes the four ocean mākāhā and the ocean endmember, stations 15-19. Similarly, there was a uniform fresh-water source (0.29, 2σ=*0.32*) fed by Heʻeia Stream, represented by the upstream freshwater mākāhā and the stream endmember, stations 13 & 14. Lastly, the pond interior was treated as a non-uniform brackish mixture (29.45, 2σ=1.79) of the two previously described water types. Stations 1-11 covered the pond interior, while 12, despite being a mākāhā, was included in the brackish category as well. Due to its position at the mouth of Heʻeia stream, 12 exhibited salinities that more closely resembled the conditions within the pond, rather than the conditions of either of the source water types.

Baseline temporal variability observed during the field campaign was largely connected to the arrival of the wet season in January and February. Salinity was observed to vary by 8.73 was observed between October (34.36) and January (25.63). TA varied by 173.3 µmol·kg^{-1} over this same period between a high of 2141.2 µmol·kg^{-1} and a low of 1967.9 µmol·kg^{-1}. Temporal variability in DIC was 142.2 µmol·kg^{-1} between the October high (1984.9) and the January low (1842.7). Oxygen variability presented an inversed temporal pattern, varying by 27.02% between an October low (67.19%) and a February high (94.21%). The temporal variability in pH was 0.22, while Ω_{Ar} varied by 0.86.

4.2 Salinity

The collected salinity data (Figure 3A) further revealed three spatial zones within the pond. Stations 2-6, located at the center of the pond, are in the closest proximity to the bay-facing

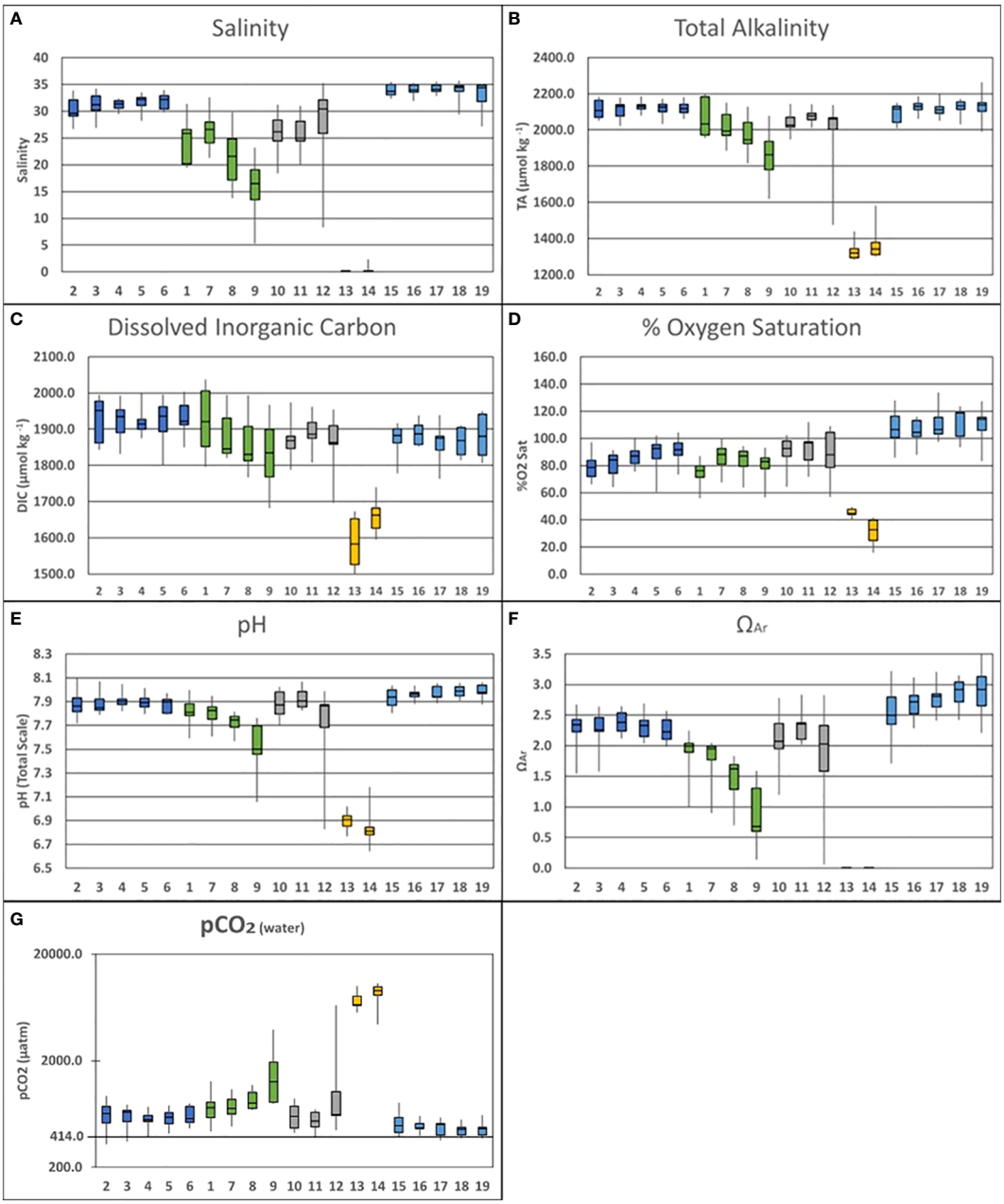

FIGURE 3
Vertically and temporally averaged data [**(A)**Salinity; **(B)**Total Alkalinity; **(C)** Dissolved Organic Carbon; **(D)** % O_2 Saturation; **(E)** pH; **(F)** Ω_{Ar} **(G)** $pCO_{2(water)}$] separated by sampling stations and organized into the designated spatial groups: Pond Center (Dark Blue: Stations 2-6); Fresh Water Lens (Green: Stations 1, 7, 8 & 9); North Pond (Gray: Stations 10, 11 & 12); Stream Water Source (Yellow: Stations 13 & 14); Bay Water Source (Light Blue: Stations 15-19).

mākāhā. Averaged together these stations exhibited a mean salinity of 32.87 *(2σ=0.97)* varying between 32.23 *(2σ=1.53)* at the surface and 33.51 *(2σ=1.12)* at depth. Stations 10 & 11 were positioned furthest to the north in the pond adjacent to both stream and bay-facing mākāhā. These stations were fresher with a mean salinity of 28.58 *(2σ=3.20)* varying between 28.88 *(2σ=2.51)* at the surface and 29.01 (2σ=3.55) at depth. Lastly, stations 1 & 7-9 were closest to land, and displayed a freshwater lens running north to south from station 9 towards station 1. The mean salinity across this gradient was 25.42 *(2σ=2.65)* varying between 23.47 (2σ=3.93) at the surface and 27.58 (2σ=2.65) at depth.

4.3 Total alkalinity

Within the pond, TA (Figure 3B) followed a distribution similar to salinity. Stations 2-6 exhibited a mean alkalinity of 2119.1 µmol·kg^{-1} (*2σ*=20.3) varying between 2115.6 µmol·kg^{-1} (*2σ*=30.8) at the surface and 2122.5 µmol·kg^{-1} (*2σ*= 27.8) at depth. Stations 10 & 11 were characterized by a mean alkalinity of 2037.5 µmol·kg^{-1} (*2σ*=60.5) varying between 2056.4 µmol·kg^{-1} (*2σ*=35.3) at the surface and 2067.5 µmol·kg^{-1} (*2σ*=35.3) at depth. Lastly, the mean alkalinity across the gradient comprised of stations 1 & 7-9 was 1977.5 µmol·kg^{-1} (*2σ*=60.8), varying between 1937.2 µmol·kg^{-1} (*2σ*=67.2) at the surface and 2021.4 µmol·kg^{-1} (*2σ*=67.4) at depth.

4.4 Dissolved inorganic carbon

The distribution of DIC (Figure 3C) differed from the pattern observed in salinity and TA. Stations 2-6 exhibited the highest concentrations with a mean DIC of 1924.0 µmol·kg^{-1} (*2σ*=24.3), varying between 1924.5 µmol·kg^{-1} (*2σ*=35.9) at the surface and 1923.6 µmol·kg^{-1} (*2σ*=34.3) at depth. Stations 10 & 11 had a lower mean DIC at 1876.4 µmol·kg^{-1} (*2σ*=32.8), varying between 1883.5 µmol·kg^{-1} (*2σ*=38.2) at the surface and 1883.8 µmol·kg^{-1} (*2σ*=34.0) at depth. DIC concentration at Stations 1 & 7-9 was similar to that observed at Stations 10 & 11, with the mean value across this gradient of 1878.0 µmol·kg^{-1} (*2σ*=41.4), varying between 1861.0 µmol·kg^{-1} (*2σ*=67.2) at the surface and 1896.7 µmol·kg^{-1} (*2σ*=46.4) at depth.

4.5 %Oxygen saturation

The % oxygen saturation data (Figure 3D) shows an inverse pattern with respect to DIC. The three main macroscale water types (the bay, the stream, and the in-pond) remained distinct. The highest % saturation values were observed in the bay sourced waters, where all sampling sites were supersaturated with respect to oxygen. On the other end, the lowest % saturation values were observed in the stream source waters. Within the pond, $\%O_2$ varied between these two extremes.

Stations 2-6 exhibited a mean $\%O_2$ of 84.91% (*2σ*=5.09) varying between 84.39% (*2σ*=7.36) at the surface and 85.44% (*2σ*=7.35) at depth. Mean $\%O_2$ at Stations 10 & 11 was 90.21% (*2σ*=7.83) varying between 90.64% (*2σ*=8.33) at the surface and 92.34% (*2σ*=8.86) at depth. The North-South gradient across stations 1 & 7-9 displayed a mean $\%O_2$ of 80.86% (*2σ*=5.84) varying between 82.64% (*2σ*=8.38) at the surface and 78.93% (*2σ*=8.28) at depth.

The in-pond percent oxygen saturation data significantly builds upon previously described North-South patterns. In general, landward-seaward position within the fishpond seem to affect the measured oxygen saturation, with lower values observed among the more landward stations (1, 2, 8 & 9; mean O_2 = 78.9% ± 12.1) while higher values were observed among the more seaward stations (4, 5, 6, 7; mean O_2 = 87.9% ± 11.2).

4.6 $pCO2_{(water)}$

pCO_2 data derived from discrete sampling of TA and DIC demonstrated a pattern in spatial variability between station groups that follows the trend in mixing of bay and stream derived waters outlined in the salinity data. The highest pCO_2 (Figure 3G) values were observed in the stream where the mean value between stations 13 & 14 was 7994.1 µatm (*2σ*=1551.9). The lowest values were observed in Kāneʻohe Bay & mākāhā stations (15-19) where the mean value was 477.7 µatm (*2σ*=57.2). Station groups within the pond varied in pCO_2 values but were within the high and low extremes exhibited by the stream and bay water sources. The center of the pond (stations 2-6) exhibited a mean pCO_2 of 605.5 µatm (*2σ*=85.3). The mean pCO_2 in the north of the pond (stations 10 & 11) 845.0 µatm (*2σ*=505.8). Meanwhile, the south of the pond (stations 1 & 7-9) was observed to have a mean pCO_2 of 997.9 µatm (*2σ*=293.0).

4.7 pH

The subdivided spatial regime that has been outlined in the data examined so far also applies to the other measured parameters of the constrained carbon system. Looking to the spatial variability of pH (Figure 3E), ocean source waters maintained a relatively uniform pH of 7.97 (*2σ=0.04*), with a slight trend towards higher pH in stations further south. In the same vein, the stream waters were a distinct and separate source, providing weakly acidified water (pH 6.87; *2σ=0.10*) to the estuary.

Stations 2-6 exhibited a mean pH of 7.89 (*2σ*=0.04) varying between 7.89 (*2σ*=0.06) at the surface and 7.88 (*2σ*=0.05) at depth. Stations 10 & 11 had a mean pH of 7.84 (*2σ*=0.11) varying between 7.89 (*2σ*=0.06) at the surface and 7.91 (*2σ*=0.07) at depth. Lastly, the North-South gradient across stations 1 & 7-9 held a mean pH across this gradient was 7.71 (*2σ*=0.08) varying between 7.67 (*2σ*=0.11) at the surface and 7.76 (*2σ*=0.09) at depth. The in-pond pH data resembles the distribution visible in salinity and TA, in which the largest variability is associated with the North-South freshwater gradient running from station 9 to station 1.

4.8 Ω_{Ar}

Aragonite saturation state was observed highest closest to the bay. Likewise, the stream source waters were extremely undersaturated with respect to aragonite, consistent with the

acidic conditions reported by the pH data. The undersaturation carried over to in-pond conditions as well, with station 9 presenting a slight undersaturation with respect to aragonite as well.

In the Ω_{Ar} data set (Figure 3F) Stations 2-6 exhibited a mean Ω_{Ar} of 2.28 (2σ=0.13) varying between 2.25 (2σ=0.19) at the surface and 2.30 (2σ=0.18) at depth. Mean Ω_{Ar} Stations 10 & 11 was 2.09 (2σ=0.29) varying between 2.14 (2σ=0.24) at the surface and 2.25 (2σ=0.25) at depth. Lastly, the North-South gradient across stations 1 & 7-9 displayed a mean Ω_{Ar} of 1.49 (2σ=0.25), varying between 1.29 (2σ=0.34) at the surface and 1.71 (2σ=0.31) at depth.

5 Discussion

Previous research has determined that approximately 58% of pond volume is exchanged across neap tide conditions, such as those sampled during this project (Möhlenkamp et al., 2018). Likewise, of this 58% volume exchange, 90-95% was found to be exchanged through the bay-facing mākāhā (15, 17, 18, & 19). Since that time, restoration work on the fishpond has largely focused on enhancing streamflow. So, it is reasonable to expect that indicators of water volume exchange may have changed since the last estimates were made by Möhlenkamp et al. (2018).

During this study, it was assumed that any change to neap tide pond volume was negligible and that the only significant perturbations to pond salinity derive from ocean and stream water sources. The mean salinity for the pond interior was 29.57 (2σ=5.66) and a mean salinity of 33.67 (2σ=1.80) was calculated for the ocean endmember. These mean salinities were used to derive a bay-facing volume exchange of 87.6% to the pond interior. The decline in mean salinity represents a small net reduction in the contribution of bay-derived water to the bulk composition of the fishpond. The change in salinity is likely derived from an enhancement of stream flow, a change in the balance of water volume flux, and/or a change in the residence time within the fishpond. While data from the current study does not allow definitive determination of the causal factors at play in setting pond salinity, further experimentation could shed light on drivers of these changes.

5.1 North-south spatial variability

The primary objective of this study was to examine spatial trends within the fishpond and characterize the carbon and oxygen systems. In order to accomplish this, salinity and alkalinity data were used to establish a baseline understanding of how bay-derived water and stream derived water were mixing within the fishpond. The largest feature in the salinity and alkalinity data (Figure 4) was a central zone situated between the remnants of the mangrove island and the bay-facing wall. This zone includes stations 2-6, all of which were observed to have salinity and alkalinity values that were internally consistent throughout the area. Likewise, this zone was heavily influenced by the adjacent ocean endmember, varying from measurements in the bay by less than 1%. On account of this homogeneity, it was evident that stream derived water did not flow directly into the center of the pond.

Separate from the center pond zone were distinct north (stations 10 & 11) and south (stations 1 & 7-9) brackish zones. The brackish gradient observed in the north of the pond ran

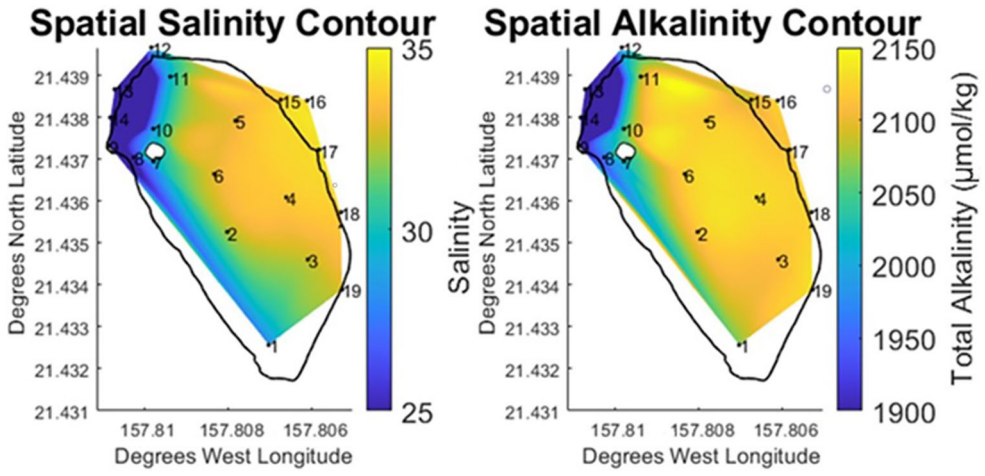

FIGURE 4
Vertically and temporally averaged contours of horizontal variability in Salinity and Total Alkalinity at He'eia Fishpond during the study period. Stations IDs (numbered in black) are plotted on contour to show sampling locations.

from the stream mākāhā at 13 towards the stream mouth mākāhā (12). Across this brackish gradient in the north, salinity decreased by 15% (-5.1) while TA fell by 6% (-81.1 µmol·kg^{-1}). A similar salinity mixing gradient ran south along the landward edge of the pond from the stream mākāhā at 13 towards station 1 at the south end of the pond. This southward oriented gradient exhibited a 24% decline in salinity (-8.1) and 9% in TA (-145.1 µmol·kg^{-1}). For these stations in the north and south brackish zones, the pattern observed in the salinity and alkalinity data (Figure 4) showed stream water entering the pond near station 9. From there the stream water exhibited traditional estuarine mixing, branching to the north and south around the former mangrove island.

Flow direction was not measured directly in this study. However, the two salinity gradients provide an indication of the direction of stream water flow within the pond. Using gradients in salinity as a proxy for water flow direction, provides further detail to distinguish between the brackish zones observed in the north and south of the pond. Due to the close proximity of the north zone to four mākāhā, brackish mixing occurred over a shorter spatial area, relative to the brackish mixing in the southward direction, which was spread out across the length of landward edge of the pond. While alkalinity was observed to be conservative with salinity throughout the pond, the large variability in salinity and TA observed in the south of the pond underscores a relative concentration of stream water in this area, due to its spatial isolation from mākāhā. The north of the pond exhibited the opposite behavior, where a smaller distance to multiple mākāhā was represented by a smaller variability in both salinity and TA. Therefore, proximity to the mākāhā water flux sites played a significant role in determining the magnitude of brackish mixing within the pond and the balance of stream and bay water contributions in the north and south of the pond.

While the north and south zones in the pond were relatively similar with respect to salinity and TA, these areas diverged more noticeably when examined using DIC & % O_2 data. The north end of the pond exhibited DIC concentrations similar to those measured at the ocean endmember (+3 µmol·kg^{-1}), while the % O_2 data were slightly lower (-10% O2 saturation). The south and center of the pond displayed a 4% elevation in DIC (+51 µmol·kg^{-1}) above what was observed at the ocean endmember. Likewise, the south and center of the pond exhibited a 30% drop in O_2 saturation relative to the bay. The spatial contour plots for these parameters (Figure 5) clearly shows a low oxygen, high DIC region starting at the south of the pond and expanding north through the pond center. Given what is known about the generalized path of brackish water circulation within the pond, this data suggests both a DIC source located in the south of the pond as well as a difference in the residence times between the north and south of the pond.

Water entering the pond through the bay-facing mākāhā was super saturated with oxygen due to the vigorous mixing that occurs while passing through the slotted sluices gates. As has been described, bay-water exerts the vast majority of control on pond composition. However, since sampling was conducted across neap ebb tides, it is reasonable to expect that O_2 super-saturated bay water will have minimal effect on measurements conducted within the pond. The data supports this assumption, as the mean %O_2 saturation measured at the mākāhā was 109%, while mean oxygen values in the pond were below 93%. DIC measurements were similarly consistent between the mākāhā (1874.0 µmol·kg^{-1}, 2σ=29.6). Measurements within the pond clearly demonstrated modification of oxygen and DIC

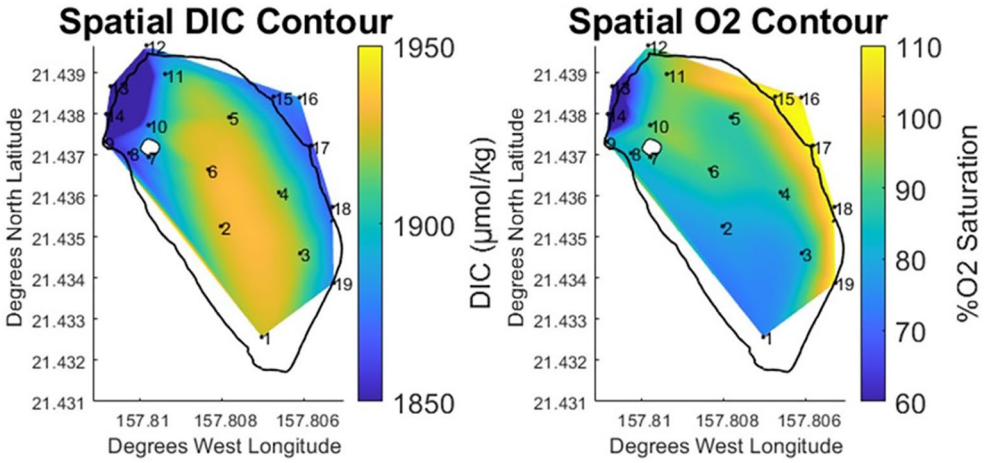

FIGURE 5
Vertically and temporally averaged contours of horizontal variability in % Oxygen Saturation and DIC at He'eia Fishpond during the study period. Stations IDs (numbered in black) are plotted on contour to show sampling locations.

parameters, particularly at the south of the pond. A signal of enhanced respiration was observed at station 1, where oxygen saturation fell to 73.67%, while DIC increased to 1923.8 $\mu mol \cdot kg^{-1}$. This signal extends up through the center of the pond, where all of the stations (2-6) exhibit similarly high DIC, while oxygen slowly increases moving northward. Based on the known path of the brackish gradient running down the landward edge of the fishpond, and the relative abundance of organic matter found in stream water in comparison with bay-derived water, the likely cause of the observed respiration signal is the breakdown of stream-derived organic matter deposited at the south end of the pond (Alongi et al., 2004; Bouillon et al., 2008).

The observed pattern in respiration makes the north south difference more apparent. As stated, brackish waters to the north (stations 10 & 11) have compositions similar to those measured in the south (station 1), so it is likely that stream derived organic matter is present in the north end of the pond. As previously observed, primary difference between the north and south ends of the pond is their position relative to the location of stream and bay-facing mākāhā. The south end of the pond is at the far end of the brackish water gradient, fed by the freshwater stream mākāhā. This position is at the opposite end of the pond from both the bay-facing mākāhā and the stream mākāhā, with the result that water travels southward along the brackish gradient, before recirculating north through center of the pond, towards the bay-facing mākāhā. In comparison, the north end of the pond is located between the freshwater stream mākāhā, the bay-facing mākāhā, as well as the stream mākāhā at the mouth of He'eia stream (12). This likely means that the north end of the pond is flushing more completely and with higher frequency than the south end of the pond. The consequent difference in residence time would support the observed difference in DIC and oxygen measurements between the north and south zones in the pond, as the breakdown of organic matter is likely occurring at both locations, but the shorter residence time at the north end of the pond prevents the respiration signal from manifesting as significantly as it does in the south end of the pond.

Comparing these results with other carbon parameters measured (Figure 3), it does not appear that TA, pH, and Ω_{Ar} exhibit the same north/south pattern observed in the DIC and O_2 saturation data. Whereas the DIC peak and O_2 saturation minima were located around station 1, the lowest measurements for TA, pH and Ω_{Ar} were all collocated at station 9, near the freshwater stream mākāhā. Given this spatial shift and the proximity to the stream, the observed variability in TA, pH, and Ω_{Ar} was more directly controlled by the balance between fresh and bay-water during brackish mixing rather than by *in-situ* biogeochemical processes.

The pCO_2 data (Figure 3G) shows that He'eia was a net source of CO_2 during the study period. The annual mean atmospheric pCO_2 reported by the NOAA Mauna Loa Observatory in 2020 (414 µatm) was visualized alongside the pCO_2 data to better show sink/source behavior. Given that both He'eia Stream and Kāne'ohe Bay were observed to behave as CO_2 sources, it was expected that the stations within the pond would exhibit values between the two water sources for the pond. Furthermore, the station groups followed pattern in pCO_2 that mirrored the variability in salinity. The lower mean pCO_2 observed within the center of the pond (605.5 µatm) further underscores the connection to the mākāhā stations (477.7 µatm). Likewise, pCO_2 was observed to rise in both the north (845.0 µatm) and south (997.9 µatm) of the pond, as these more brackish regions of the pond were more heavily influenced by effect of the high pCO_2 values in He'eia Stream (7994.1 µatm). While the stream values for pCO_2 were exceptionally high, the influence of stream waters on the pond were limited, as evidenced by the increases in pCO_2 observed in brackish regions in both the north and south of the pond. These north and south regions in the pond were still significant CO2 sources. However, the approximately 7000 µatm drop in mean pCO_2 suggests that the pond source behavior is more directly controlled by the sink/source behavior in Kāne'ohe Bay (Fagan and Mackenzie, 2007; Massaro et al., 2012; Drupp et al., 2013). This is likely due to He'eia Stream having a small spatial area and volume, as well as supplying a smaller volume of water to the pond relative what is supplied by Kāne'ohe Bay.

5.2 Benthic respiration

Weak stratification has been observed at the fishpond in previous studies (Möhlenkamp et al., 2018). In order to better understand how any potential stratification would influence the carbon system during this project, samples were taken at surface and at depth at each station within the fishpond throughout the study period. Comparing the vertically averaged data (Figure 5) with the surface/depth data (Figure 6) it is clear that the previously described respiration signal is enhanced at depth. The contour of peak elevated DIC covers a wider spatial area at the south end of the pond. Likewise, the lower range of elevated DIC extends north along the landward edge of the pond towards stations 8 & 9. Previous studies documented benthic diatoms (Vasconcellos, 2007) and invasive benthic algae (Murphy, 2012) in the fishpond. Higher concentrations of chlorophyll-a were observed at stations along the landward edge of the pond and near the freshwater mākāhā.

Temperature and salinity data reveal clear differences in the potential for stratification between north and south regions along the landward edge of the pond. In the same southern space as the expanded peak DIC elevation at depth, the salinity data was observed to be vertically homogenous. Meanwhile, temperature increased by approximately 1 °C at depth. The temperature and salinity data would suggest that the south end of the pond is not significantly stratified. Likewise, assuming that the elevated temperature at depth is associated with biological activity in the sediments, the observed respiration signal is likely

predominately derived from microbial breakdown of organic matter deposited in benthic sediments. This corroborates previous research examining sediment microbial oxygen consumption related to benthic algae (Murphy, 2012) and benthic organic matter remineralization (Briggs, 2011; Briggs et al., 2013a; Briggs et al., 2013b) within the fishpond. Both studies conducted diurnal experiments and documented sediment O_2 drawdown between sundown and sunrise, when respiration dominated over photosynthetic O_2 production, in bottom sediments.

The station 8 & 9 area to the north of the pond displayed a trend in salinity, which decreased significantly at the surface, opposite to that observed in the south. The decrease in salinity is likely due to the close proximity of the freshwater stream mākāhā. Meanwhile, a vertical temperature inversion was visible, similar to that described in the south of the pond. In this case, stratification seems likely as the salinity data shows a concentration of stream water input at the surface. Given this stratification, the temperature inversion in the north is better explained by the relatively cooler stream water remaining vertically confined at the surface.

Since stratification does not appear to be spatially uniform within the pond, it is unclear whether the benthic-derived respiration signal varies spatially within the pond. While neither microbial activity nor pore water chemistry were collected during this study, the ratio of TA and DIC can be used to examine the dominant biological processes interacting with the carbon system (Borges, 2003; Rixen et al., 2012; Sippo et al., 2016). TA and DIC are influenced by a number of biological processes in predictable ways. The dissolution of calcium carbonate produces TA and DIC at a ratio of 2:1. Likewise, aerobic respiration of organic matter reduces TA while increasing DIC at a ratio of 1:10 (Rixen et al., 2012; Sippo et al., 2016).

In order to understand how the balance of TA and DIC was driven at each of the in-pond stations, the TA and DIC

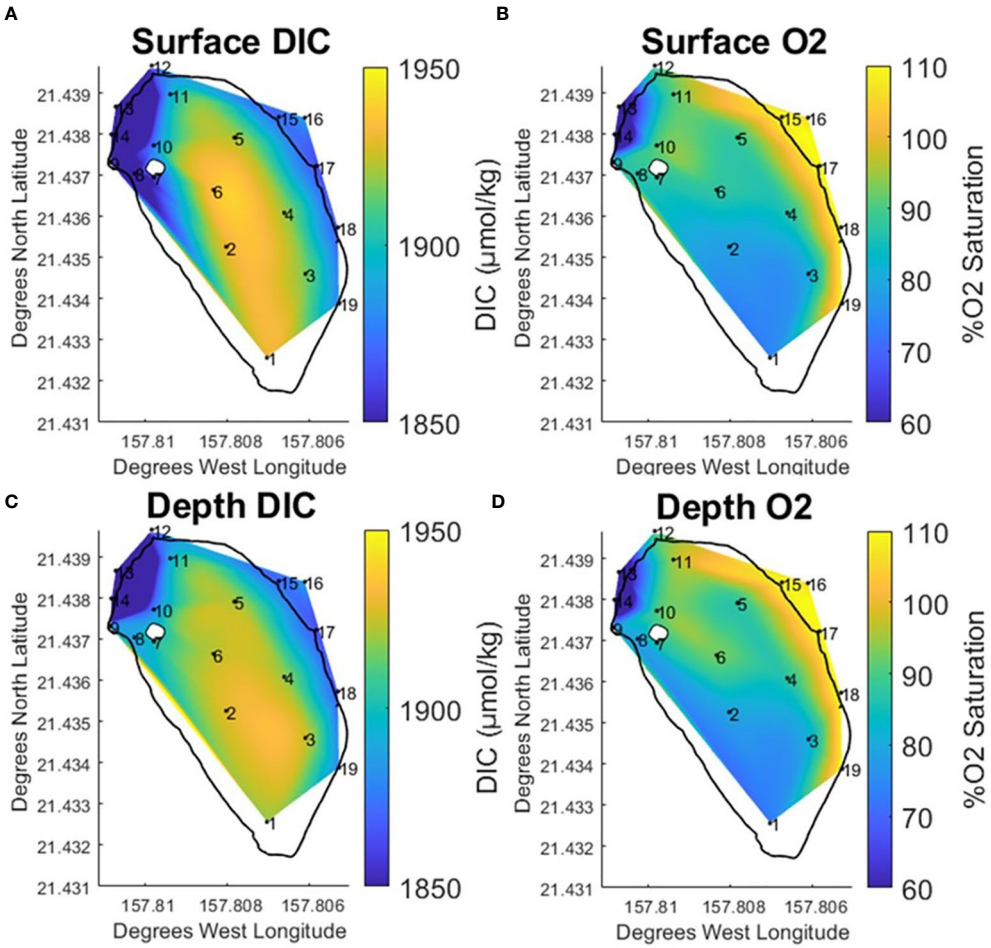

FIGURE 6
Temporally averaged contours for surface DIC **(A)** and % O2 Saturation **(B)** and Depth DIC **(C)** and % O2 Saturation **(D)** at He'eia Fishpond during the study period. Stations IDs (numbered in black) are plotted on contour to show sampling locations.

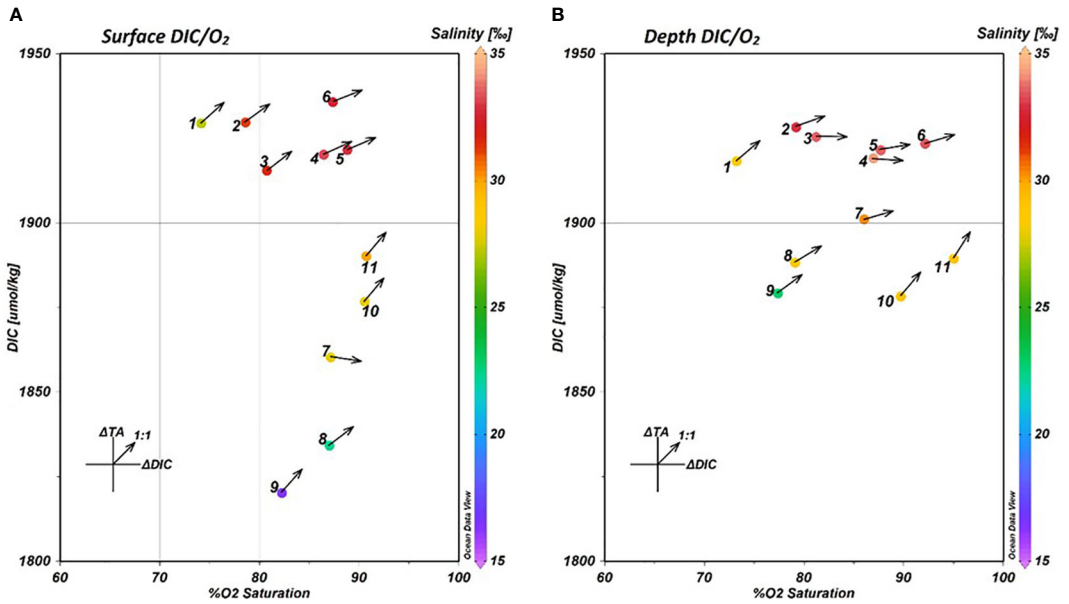

FIGURE 7
DIC-O2 Saturation plots for surface **(A)** and depth **(B)** measurements at the 11 in-pond sampling stations. The color bar indicates the mean salinity observed at each plotted station and depth. The arrows plotted from each point indicate the slope of the fitted curve of the ΔTA/ΔDIC relationship at that station and depth.

measurements were normalized to endmember measurements to account for traditional estuarine mixing. For this experiment, traditional estuarine mixing was defined as the dilution of seawater with freshwater, resulting in a linear mixing gradient in salinity. The normalized values were then subtracted from the measured values to arrive at ΔTA and ΔDIC values capturing only the effects of *in situ* biogeochemical alteration. This data was plotted alongside surface and depth data for DIC and precent O_2 saturation (Figure 7) to examine the net biological activity at each station and depth within the fishpond. The arrows plotted over each point denote the slope of the curve fit to the ΔTA and ΔDIC data at that station and depth, with 1:1 slope line provided as a visual reference for an approximate balance between calcium carbonate dissolution and respiration.

The DIC-O_2 data reveal that while the north and south ends of the pond remain largely unchanged between surface and depth measurements, there is a large shift in the DIC-O_2 relationship observed in the brackish water gradient (stations 7-9). A large increase in DIC was observed at depth at all three of the stations, in addition to a small decrease in O_2 saturation at stations 8 and 9. On account of the large shift in salinity between surface and depth at these stations, and the previously identified stratification, it is likely that this shift in DIC is driven by a difference in the balance of fresh and bay-derived water between surface and depth.

The water measured in He'eia Stream was found to have a significantly lower concentration of DIC (1623.2 μmol·kg^{-1}) than the water from Kāne'ohe Bay (1874.0 μmol·kg^{-1}). Therefore, given that stream water was observed to be concentrated in the stratified surface layer at stations 7-9, the observed variability in DIC at those stations is likely due to the increased proportion of stream-derived water in the surface layer.

The ΔTA/ΔDIC relationships (Arrows, Figures 7A, B) support an increased concentration of stream-derived water as the ΔTA/ΔDIC ratios at stations 8 & 9 do not significantly change between surface and depth. Similarly, the north end of the pond, stations 10 & 11, do not exhibit a change in the ΔTA/ΔDIC ratio between surface and depth, supporting the previous finding that the shorter residence time at the north end of the pond inhibits the biogeochemical alteration observed at stations in the south end of the pond. Likewise, the ΔTA/ΔDIC relationships show up clearly in the south and center pond stations (1-6) associated with the respiration signal. At each of these stations, the ΔTA/ΔDIC ratio decreases significantly with depth, indicating an increased influence of aerobic respiration.

6 Conclusion

Coastal and estuarine ecosystems are complex and highly dynamic. The carbon system has been historically understudied in these environments, and the spatial variability in carbon system parameters is thus poorly understood. The aim of this

study was to constrain spatial variability in a model Hawaiian estuarine ecosystem. DIC and percent oxygen saturation were observed to vary significantly across the fishpond, as the distance from water flux locations and the direction of stream water flow controlled the magnitude of biogeochemical alteration of these parameters within pond. At the south end of the pond an enhanced respiration signal consisting of elevated DIC and undersaturated conditions with respect to oxygen was identified. Analysis of the biogeochemical effect on TA and DIC indicated that the enhanced respiration signal was more prevalent at depth. Prior studies observed higher concentrations of benthic algae in the organic matter rich sediments along the landward edge of the fishpond. The same benthic algae may be responsible for the respiration signal observed here. The comparison of this south pond pattern with other regions of the pond suggests significant differences in the mixing regimes and residence times, which may influence the distribution of nutrients and organic rich sediments that support benthic algae and other organisms. Future studies could build upon the observed patterns in carbon and oxygen by examining composition of benthic microbial communities and the distribution of macronutrients to better describe the drivers of this spatial variability. Likewise, additional carbon and oxygen work in He'eia stream and Kāne'ohe Bay would provide valuable context for how the management of this productive coastal space influences the broader estuarine environment.

Coastal managers working in the He'eia estuarine space have encountered a range of challenges from anoxia and thermal stress events to wet season pulses of agro-ecological run off. Ten years of restoration work separate the benthic respiration signal observed here from previous studies documenting benthic algae and sediment oxygen consumption. While this restoration has improved water quality within the fishpond, it does not seem to have significantly altered benthic biological processes. The results here demonstrate a clear connection between how water sources mix within the fishpond and the spatial variability of carbon and oxygen. This data is a powerful tool for planning future management decisions within the estuary and the fishpond. The continued restoration work along the landward edge of He'eia fishpond, the opening of additional mākāhā, and the enhancement of streamflow into the pond, would all likely reshape apparent residence times within the fishpond as well as the distribution of carbon and oxygen. In this way, understanding the drivers of spatial variability in carbon and oxygen better equips coastal communities to anticipate and respond to ecosystem change.

Data availability statement

The raw data supporting the conclusions of this article will be made available by the authors, without undue reservation.

Author contributions

All authors listed have made a substantial, direct, and intellectual contribution to the work and approved it for publication.

Funding

We acknowledge the financial support of our research provided in part by a grant/cooperative agreement from the National Oceanic and Atmospheric Administration, CMAR award # NA21NMF4320043. The views expressed herein are those of the author(s) and do not necessarily reflect the views of NOAA or any of its subagencies. This is SOEST contribution number 11610.

Acknowledgments

We would like to thank Hi'ilei Kawelo and Kawika Winter who organized connections between researchers and community partners at the outset of this research. We are immensely grateful to groups working at Paepae o He'eia, Kākoʻo ʻŌIwi, and the He'eia National Estuarine Research Reserve whose tireless ecosystem restoration work made this research possible. We would also like to thank Charles "Aka" Beebe and Rosie Alegado for their guidance during field preparation and site selection, as well as Paula Möhlenkamp for her assistance developing code in MATLAB. Likewise, we would like to thank Dan Sadler for his expertise and support while assembling the materials and equipment for conducting Winkler analyses. We are grateful to Kyle Conner, Lucie Knor, and Noah Howins for their technical and field support during this research. This research also benefited from the review and critique of Melissa Melendez and Nick Hawco, which helped improve the quality of this manuscript.

Conflict of interest

The authors declare that the research was conducted in the absence of any commercial or financial relationships that could be construed as a potential conflict of interest.

Publisher's note

References

Alongi, D. M., Sasekumar, A., Chong, V. C., Pfitzner, J., Trott, L. A., Tirendi, F., et al. (2004). Sediment accumulation and organic material flux in a managed mangrove ecosystem: Estimates of land–ocean–atmosphere exchange in peninsular Malaysia. *Mar. Geology* 208, 383–402. doi: 10.1016/j.margeo.2004.04.016

Andersson, A. J. (2005). Coastal ocean and carbonate systems in the high CO2 world of the anthropocene. *Am. J. Sci.* 305, 875–918. doi: 10.2475/ajs.305.9.875

Bacastow, R. D., and Keeling, C. D. (1973). "Atmospheric carbon dioxide and radiocarbon in the natural carbon cycle: II. changes form A.D. 1700 to 2070 as deduced from a geochemical model," in *Carbon in the biosphere*. Eds. G. M. Woodwell and E. V. Pecan (Washington, D.C.:U.S. A.E.C.,), 86–135.

Bednaršek, N., Harvey, C. J., Kaplan, I., and Feely, R. (2016). Pteropods on the edge: Cumulative effects of ocean acidification, warming, and deoxygenation. *Prog. Oceanography* 145 (2):1-24. doi: 10.1016/j.pocean.2016.04.002

Benson, B. B., and Krause, D. J. R. (1980). The concentration and isotopic fractionation of gases dissolved in freshwater in equilibrium with the atmosphere. 1. oxygen. *Limnology Oceanography* 25 (4), 662–671. doi: 10.4319/lo.1980.25.4.0662

Benson, B. B., and Krause, D. J. R. (1984). The concentration and isotopic fractionation of oxygen dissolved in freshwater and seawater in equilibrium with the atmosphere. *Limnology Oceanography* 29 (3), 620–632. doi: 10.4319/lo.1984.29.3.0620

Borges, A. V. (2003). Atmospheric CO $_2$ flux from mangrove surrounding waters. *Geophys. Res. Lett.* 30, 1558. doi: 10.1029/2003GL017143

Bouillon, S., Borges, A. V., Castañeda-Moya, E., Diele, K., Dittmar, T., Duke, N. C., et al. (2008). Mangrove production and carbon sinks: A revision of global budget estimates: Global mangrove carbon budgets. *Global Biogeochem. Cycles* 22, n/a–n/a. doi: 10.1029/2007GB003052

Breitburg, D., Levin, L. A., Oschlies, A., Grégoire, M., Chavez, F. P., Conley, D. J., et al. (2018). Declining oxygen in the global ocean and coastal waters. *Science* 359, eaam7240. doi: 10.1126/science.aam7240

Bremer, L., Falinski, K., Ching, C., Wada, C., Burnett, K., Kukea-Shultz, K., et al. (2018). Biocultural restoration of traditional agriculture: Cultural, environmental, and economic outcomes of lo'i kalo restoration in he'eia, OA'hu. *Sustainability* 10, 4502. doi: 10.3390/su10124502

Briggs, R.A 2011 *Organic Matter Remineralization in Coastal Sediments in and around Kaneohe Bay, Hawaii.* University of Hawaii

Briggs, R. A., Padilla-Gamiño, J. L., Bidigare, R. R., Gates, R. D., and Ruttenberg, K. C. (2013a). Impact of coral spawning on the biogeochemistry of a Hawaiian reef. *Estuarine Coast. Shelf Sci.* 134, 57–68. doi: 10.1016/j.ecss.2013.09.013

Briggs, R. A., Ruttenberg, K. C., Glazer, B. T., and Ricardo, A. E. (2013b). Constraining sources of organic matter to tropical coastal sediments: Consideration of nontraditional end-members. *Aquat Geochem* 19, 543–563. doi: 10.1007/s10498-013-9219-2

Brix, H., Gruber, N., and Keeling, C. D. (2004). Interannual variability of the upper ocean carbon cycle at station ALOHA near Hawaii: Interannual variability at station ALOHA. *Global Biogeochem. Cycles* 18. doi: 10.1029/2004GB002245

Cai, W., and Wang, Y. (1998). The chemistry, fluxes, and sources of carbon dioxide in the estuarine waters of the satilla and altamaha rivers, Georgia. *Limnology Oceanography* 4, 657-668. doi: 10.4319/lo.1998.43.4.0657

Caldeira, K., and Wickett, M. E. (2003). Anthropogenic carbon and ocean pH. *Nature* 425, 365–365. doi: 10.1038/425365a

Camvel, D. (2020). *Ho'oulu 'Āina: Restoration in the he'eia ahupua'a* (Honolulu, HI:University of Hawaii).

Cao, L., Zhang, H., Zhang, M., and Wang, S. (2014). Response of ocean acidification to a gradual increase and decrease of atmospheric CO2. *Environ. Res. Lett.* 9 (2). doi: 10.1088/1748-9326/9/2/024012

Carpenter, H. J. (1965). The Accuracy of the Winkler Method for Dissolved Oxygen Analysis. *Limnology and Oceanography*. 10, 1. doi: 10.4319/LO.1965.10.1.0135

Chan, F., Barth, J. A., Blanchette, C. A., and Byrne, R. H. (2017). Persistent spatial structuring of coastal ocean acidification in the California current system. *Sci. Rep.* 7, (1). doi: 10.1038/s41598-017-02777-y

Codispoti, L. (2001). One man's advice on the determination of dissolved oxygen in seawater 23.

Costa-Pierce, B. A. (1987). Aquaculture in ancient Hawaii. *BioScience* 37, 320–331. doi: 10.2307/1310688

D'Andrea, B. (2015). *Water exchange and circulation in he'eia fishpond: Building blocks for establishing a water budget* (Honolulu, HI:University of Hawaii).

De Carlo, E., Hoover, D., Young, C., Hoover, R., and Mackenzie, F. (2007). Impact of storm runoff from tropical watersheds on coastal water quality and productivity. *Appl. Geochemistry* 22, 1777–1797. doi: 10.1016/j.apgeochem.2007.03.034

Demopoulos, A. W. J., Fry, B., and Smith, C. R. (2007). Food web structure in exotic and native mangroves: a Hawaii–Puerto Rico comparison. *Oecologia* 153, 675–686. doi: 10.1007/s00442-007-0751-x

Dickson, A. (2001). Reference materials for oceanic CO_2 measurements. *Oceanography (Washington D.C.)* 14, 21–22.

Dickson, A. G., Sabine, C. L., and Christian, J. R. (Eds) (2007). Guide to best practices for ocean CO2 measurements. *PICES Special Publicationn* 3, 191 pp.

Doney, S. C., Busch, D. S., Cooley, S. R., and Kroeker, K. J. (2020). The impacts of ocean acidification on marine ecosystems and reliant human communities. *Annu. Rev. Environ. Resour.* 45, 11.1–11.30. doi: 10.1146/annurev-environ-012320-083019

Dore, J. E., Lukas, R., Sadler, D. W., Church, M. J., and Karl, D. M. (2009). Physical and biogeochemical modulation of ocean acidification in the central north pacific. *Proc. Natl. Acad. Sci.* 106, 12235–12240. doi: 10.1073/pnas.0906044106

Drupp, P., De Carlo, E. H., and Mackenzie, F. T. (2016). Porewater CO2-carbonic acid geochemistry in sandy sediments. *Mar. Chem.* 185, 48–64. doi: 10.1016/j.marchem.2016.04.004

Drupp, P., De Carlo, E. H., Mackenzie, F. T., Bienfang, P., and Sabine, C. L. (2011). Nutrient inputs, phytoplankton response, and CO2 variations in a semi-enclosed subtropical embayment, kaneohe bay, Hawaii. *Aquat Geochem* 17, 473–498. doi: 10.1007/s10498-010-9115-y

Drupp, P., De Carlo, E. H., Mackenzie, F. T., and Sabine, C. L. (2013). A comparison of CO2 dynamics and air-Sea exchange in differing tropical reef environments. *Aquat. Geochemistry* 19, 371–397. doi: 10.1007/s10498-013-9214-7

Dulai, H., Kleven, A., Ruttenberg, K., Briggs, R., and Thomas, F. (2016). "Evaluation of submarine groundwater discharge as a coastal nutrient source and its role in coastal groundwater quality and quantity," in *Emerging issues in groundwater resources*. Ed. A. Fares (Cham: Springer International Publishing), 187–221. doi: 10.1007/978-3-319-32008-3_8

Fagan, K. E., and Mackenzie, F. T. (2007). Air–sea CO2 exchange in a subtropical estuarine-coral reef system, kaneohe bay, Oahu, Hawaii. *Mar. Chem.* 106, 174–191. doi: 10.1016/j.marchem.2007.01.016

Feely, R., Okazaki, R. R., Cai, W., and Bednaršek, N. (2017). The combined effects of acidification and hypoxia on pH and aragonite saturation in the coastal waters of the California current ecosystem and the northern gulf of Mexico. *Continental Shelf Res.* 152, (2). doi: 10.1016/j.csr.2017.11.002

Flynn, K. J., Clark, D. R., Mitra, A., and Fabian, H. (2015). Ocean acidification with (de)eutrophication will alter future phytoplankton growth and succession. *Proc. R. Soc. B: Biol. Sci.* 282 (1804). doi: 10.1098/rspb.2014.2604

Goodwin, P., and Lauderdale, J. M. (2013). Carbonate ion concentrations, ocean carbon storage, and atmospheric CO2. *Global Biogeochemical Cycles* 27 (3), 882–893. doi: 10.1002/gbc.20078

Hall, E. R., Wickes, L. N., Burnett, L. E., and Scott, G. I. (2020). Acidification in the U.S. southeast: Causes, potential consequences and the role of the southeast ocean and coastal acidification network. *Front. Mar. Sci.* 7. doi: 10.3389/fmars.2020.00548

Jokiel, P. L., Rodgers, K. S., Walsh, W. J., Polhemus, D. A., and Wilhelm, T. A. (2011). Marine resource management in the Hawaiian archipelago: The traditional Hawaiian system in relation to the Western approach. *J. Mar. Biol.* 2011, 1–16. doi: 10.1155/2011/151682

Keala, G., Hollyer, J. R., and Castro, L. (2007). *Loko i'a: a manual on Hawaiian fishpond restoration and management* (Honolulu: College of Tropical Agriculture and Human Resources, University of Hawai'i at Mānoa).

Kikuchi, W. K. (1976). Prehistoric Hawaiian fishponds. *Science* 193 (4250), 295–299. doi: 10.1126/science.193.4250.295

Kleven, A. (2014). *Coastal groundwater discharge as a source of nutrients to heeia fishpond, Oahu, HI* (Honolulu, HI:University of Hawaii).

Knor, L., Meléndez, M., Howins., N., Boeman, D., Lechner, E., De Carlo, E., et al. (2018). Dissolved inorganic carbon, total alkalinity, water temperature and salinity collected from surface discrete observations using coulometer, alkalinity titrator and other instruments from the coral reef MPCO2 buoys at ala wai, CRIMP-2, kaneohe, and kilo nalu from 2016-01-08 to 2020-12-20 (NCEI accession 0176671). *NOAA Natl. Centers Environ. Information* doi: 10.25921/pe6v-qg74

Koshiba, S., Besebes, M., Soaladaob, K., Isechal, A. L., Victor, S., and Golbuu, Y. (2013). Palau's taro fields and mangroves protect the coral reefs by trapping eroded

fine sediment. *Wetlands Ecol. Manage* 21, 157–164. doi: 10.1007/s11273-013-9288-4

Laurent, A., Fennel, K., Cai, W., Huang, W., Barbero, L., and Wanninkhof, R. (2017). Eutrophication-induced acidification of coastal waters in the northern gulf of Mexico: Insights into origin and processes from a coupled physical-biogeochemical model: Acidification in NGOM eutrophic waters. *Geophysical Res. Lett.* 44 (2), 946-956. doi: 10.1002/2016GL071881

Leon Soon, S. (2017). *Biophysical interactions: Influence of water flow on nutrient distribution and nitrate uptake by marine algae*. [Dissertation/PhD Thesis]. (Honolulu, HI:University of Hawaii)

Lopera, D. (2020). *Understanding change: Examining the effect of ahupua'a restoration efforts on water circulation in loko i'a o he'eia, a native Hawaiian fishpond* (Honolulu, HI:University of Hawaii).

Maly, K., and Maly, O. (2003). *Ka hana lawai'a a me nā ko'a o na kai 'ewalu : a history of fishing practices and marine fisheries of the Hawaiian islands* (Keeau, HI: Kumu Pono Associates).

Massaro, R. F. S., De Carlo, E. H., Drupp, P. S., Mackenzie, F. T., Jones, S. M., Shamberger, K. E., et al. (2012). Multiple factors driving variability of CO2 exchange between the ocean and atmosphere in a tropical coral reef environment. *Aquat Geochem* 18, 357–386. doi: 10.1007/s10498-012-9170-7

McCoy, D., McManus, M. A., Kotubetey, K., Kawelo, A. H., Young, C., D'Andrea, B., et al. (2017). Large-Scale climatic effects on traditional Hawaiian fishpond aquaculture. *PloS One* 12, e0187951. doi: 10.1371/journal.pone.0187951

Möhlenkamp, P., Beebe, C., McManus, M., Kawelo, A., Kotubetey, K., Lopez Guzman, M., et al. (2019). Kū hou kuapā: Cultural restoration improves water budget and water quality dynamics in he'eia fishpond. *Sustainability* 11, 161. doi: 10.3390/su11010161

Murphy, J. L. (2012). *Linking Benthic Algae to Sediment Oxidation-Reduction Dynamics: Implications for Sediment-Water Interface Nutrient Cycling*. [Dissertation/PhD Thesis]. [Honolulu (HI)]: University of Hawaii

Ono, H., Kosugi, N., Toyama, K., and Tsujino, H. (2019). Acceleration of ocean acidification in the Western north pacific. *Geophysical Res. Lett.* 46 (22), 13161-13169. doi: 10.1029/2019GL085121

Orr, J. C., Fabry, V. J., Aumont, O., Bopp, L., Doney, S. C., Feely, R. A., et al. (2005). Anthropogenic ocean acidification over the twenty-first century and its impact on calcifying organisms. *Nature* 437, 681–686. doi: 10.1038/nature04095

Pierrot, D. E., Lewis, E., and Wallace, D. W. R. (2006). *MS excel program developed for CO2 system calculations* (Oak Ridge, Tennessee: Carbon Dioxide Information Analysis Center, Oak Ridge National Laboratory, U.S. Department of Energy). doi: 10.3334/CDIAC/otg.CO2SYS_XLS_CDIAC105a

Riebesell, U., Zondervan, I., Rost, B., et al. (2000). Reduced calcification of marine plankton in response to increased atmospheric CO2. *Nature* 407, 364–367. doi: 10.1038/35030078

Ringuet, S., and Mackenzie, F. (2005). Controls on nutrient and phytoplankton dynamics during normal flow and storm runoff conditions, southern kaneohe bay, Hawaii. *Estuaries* 28, 327–337. doi: 10.1007/BF02693916

Rixen, T., Jiménez, C., and Cortés, J. (2012). Impact of upwelling events on the sea water carbonate chemistry and dissolved oxygen concentration in the Gulf of Papagayo (Culebra Bay), Costa Rica: Implications for coral reef. *Revista de Biologia Tropical* 60, 6 187. doi: 10.15517/rbt.v60i2.20004

Rixen, T., Jiménez, C., and Cortés, J. (2015). Impact of upwelling events on the sea water carbonate chemistry and dissolved oxygen concentration in the gulf of papagayo (Culebra bay), Costa Rica: Implications for coral reefs. *Revista de Biologia Tropical* 60, 187. doi: 10.15517/rbt.v60i2.20004

Rodgers, K. S., Jokiel, P. L.Western Weather Group, Inc (2005). *HIMB weather station: Moku o loe (Coconut island), Oahu, Hawaii* (Honolulu, HI:Pacific Islands Ocean Observing System). Available at: http://pacioos.org/metadata/AWS-HIMB.html.

Shamberger, K. E. F., Feely, R. A., Sabine, C. L., Atkinson, M. J., DeCarlo, E. H., Mackenzie, F. T., et al. (2011). Calcification and organic production on a Hawaiian coral reef. *Mar. Chem.* 127, 64–75. doi: 10.1016/j.marchem.2011.08.003

Sippo, J. Z., Maher, D. T., Tait, D. R., Holloway, C., and Santos, I. R. (2016). Are mangroves drivers or buffers of coastal acidification? insights from alkalinity and dissolved inorganic carbon export estimates across a latitudinal transect. *Global Biogeochem. Cycles* 30, 753–766. doi: 10.1002/2015GB005324

University of Hawaii Sea Grant (2018) *Kingtide*. Available at: https://seagrant.soest.hawaii.edu/coastal-and-climate-science-and-resilience/ccs-projects/what-is-a-king-tide (Accessed August 25, 2022).

U.S. Geological Survey (2011) *Change to solubility equations for oxygen in water: Office of water quality technical memorandum* (Accessed July 15, 2011).

U.S. Geological Survey (2016) *National water information system data available on the world wide web (USGS water data for the nation)*. Available at: https://waterdata.usgs.gov/usa/nwis/uv?16275000 (Accessed August 25, 2022).

Vasconcellos, S. (2007). Distribution and characteristics of a photosynthetic benthic microbial community in a marine coastal pond, Vol. 25. Pacific Internship Programs for Exploring Sciences (PIPES) Final Report (Hilo, Hawaii:University of Hawaii).

Winter, K., Beamer, K., Vaughan, M., Friedlander, A., Kido, M., Whitehead, A., et al. (2018). The moku system: Managing biocultural resources for abundance within social-ecological regions in hawai'i. *Sustainability* 10, 3554. doi: 10.3390/su10103554

Winter, K. B., Lincoln, N. K., Berkes, F., Alegado, R. A., Kurashima, N., Frank, K. L., et al. (2020a). Ecomimicry in indigenous resource management: optimizing ecosystem services to achieve resource abundance, with examples from hawai'i. *E&S* 25, art26. doi: 10.5751/ES-11539-250226

Winter, K. B., Rii, Y. M., Reppun, F. A. W. L., Hintzen, K. D., Alegado, R. A., Bowen, B. W., et al. (2020b). Collaborative research to inform adaptive comanagement: a framework for the he'eia national estuarine research reserve. *E&S* 25, art15. doi: 10.5751/ES-11895-250415

Wong, G. T. F. (2012). Removal of nitrite interference in the winkler determination of dissolved oxygen in seawater. *Mar. Chem.* 130, 28–32. doi: 10.1016/j.marchem.2011.11.003

Yang, L. (2000). *A circulation study of Hawaiian fishponds; university of Hawaii* (Department of Ocean and Resources Engineering: Honolulu, HI).

Young, C. W. (2011). *Perturbation of nutrient level inventories and phytoplankton community composition during storm events in a tropical coastal system: Heeia fishpond* (Honolulu HI: University of Hawaii).

frontiers | Frontiers in Marine Science

TYPE Original Research
PUBLISHED 14 December 2022
DOI 10.3389/fmars.2022.1001295

OPEN ACCESS

EDITED BY
Nicholas David Ward,
Pacific Northwest National Laboratory (DOE), United States

REVIEWED BY
Jeremy Testa,
University of Maryland, United States
Charles William Martin,
University of Florida, United States

*CORRESPONDENCE
K. Nakayama
nakayama@phoenix.kobe-u.ac.jp

SPECIALTY SECTION
This article was submitted to Marine Biogeochemistry, a section of the journal Frontiers in Marine Science

RECEIVED 23 July 2022
ACCEPTED 23 November 2022
PUBLISHED 14 December 2022

CITATION
Matsumura K, Nakayama K and Matsumoto H (2022) Influence of patch size on hydrodynamic flow in submerged aquatic vegetation. *Front. Mar. Sci.* 9:1001295. doi: 10.3389/fmars.2022.1001295

Influence of patch size on hydrodynamic flow in submerged aquatic vegetation

K. Matsumura[1], K. Nakayama[1]* and H. Matsumoto[2]

[1]Graduate School of Engineering, Kobe University, Kobe, Japan, [2]Marine Environment Control System Department, Port and Airport Research Institute, Yokosuka, Kanagawa, Japan

Blue carbon, or carbon dioxide captured and stored by submerged aquatic vegetation (SAV) in ecosystems, has been attracting attention as a measure to mitigate climate change. Since the scale of SAV meadows is smaller than that of topography length scale, with the former often occurring in patches, the flexibilities of SAV motion induce complicated interactions with water flows and make it difficult to estimate carbon sequestration rates. Therefore, this study aims to clarify the influences of SAV patches on water flows and mass transport using laboratory experiments and numerical simulations. An SAV model was successfully applied to analyze the results of laboratory experiments, revealing good agreement and showing that the size of an SAV patch significantly affects the water flows. The extent to which the patch occupies the channel width was revealed to be the most substantial factor in controlling carbon absorption by SAV, and deflection was found to be another significant factor. Implementing global warming countermeasures is a critical goal of climate change mitigation, so our study outcome is expected to be helpful for improving and promoting blue carbon as a negative emission strategy.

KEYWORDS

deflected vegetation height, SAV, laboratory experiment, pCO_2, mass transport, blue carbon

Introduction

Natural disasters such as extreme heavy rains, droughts, and large typhoons have intensified worldwide due to climate change (IPCC, 2018; IPCC, 2021). As a climate change mitigator, the expansion of blue carbon—i.e., atmospheric carbon dioxide that is captured and stored in coastal ocean waters through the photosynthetic activity of

ecosystems—has been promoted (Nellemann et al., 2009). Nellemann et al. (2009) demonstrated that blue carbon from only two of the various forms of submerged aquatic vegetation (SAV)—namely, seagrass meadows and kelp systems—accounts for 55% of the earth's total carbon in storage due to photosynthesis. Coastal regions have high biodiversity due to the mixing of fresh and sea waters in habitats such as estuaries and lagoons. The other significant factor is the long residence time of carbon in those areas due to the highly enclosed nature of such habitats (Cotovicz et al., 2015; Nakayama et al., 2020a and Nakayama et al., 2022). Seagrass meadows exist entirely in shallow water areas and grow in patches, meaning that their interactions with coastal flows may induce complex rates of carbon transport (Adhitya et al., 2014; Adams et al., 2016).

Complex mass transport influences the carbon capture rate, making estimation difficult (Nakayama et al., 2020a). For instance, Vilas et al. (2017) revealed from field observations that SAV at high density in a freshwater lake inhibits water exchange between inside and outside of an SAV meadow, reducing dissolved oxygen (DO) in the meadow's center, and ultimately leading to a ring-shaped meadow due to anoxia at the center of the field. Those authors revealed the occurrence of anoxia using a three-dimensional numerical model, and they expected the partial pressure of carbon dioxide (pCO2) to be very high at the center because of the strong relationship between DO and pCO2. Therefore, it is necessary to understand (1) how an SAV patch interacts with flows and (2) how flows influence the transport rate of materials around an SAV meadow.

Previous studies have investigated the interactions between flows and SAV using laboratory experiments. Luhar and Nepf (2011) successfully applied the Cauchy number (Ca) and the buoyancy parameter (B) to reconfigure the leaf blade model (Nepf, 2012; Luhar and Nepf, 2013 and Luhar and Nepf, 2016). In addition, in the case of seagrass meadows, the exchange zone extends as it goes downstream, leading to more significant mass transport in the canopy (Murphy et al., 2007; Ghisalberti and Nepf, 2009). Moreover, Infantes et al. (2012) estimated equivalent bottom roughness due to SAV and the friction coefficient by measuring actual velocities using bottom-mounted acoustic doppler velocimeters in field observations. Regarding the effect of waves on seagrass meadows, Luhar et al. (2013) successfully measured the mass drift around an SAV meadow driven by waves in a coastal ocean environment; their results suggested that pCO2 has a spatial distribution influenced by SAVs, and the carbon dioxide flux between the atmosphere and water surface is associated with waves and currents interacting with SAV meadow.

In addition to laboratory experiments and field observations, numerical simulations are also helpful for analyzing the interactions between flows and SAV (Infantes et al., 2012; Boothroyd et al., 2016). Suzuki et al. (2011) proposed an energy attenuation model that analyzes the effect of SAV on shallow water waves in bulk. They named the model the Simulating WAves Nearshore model (SWAN), and it showed high applicability to a wide variety of shallow wave habitats. However, they ignored the bend in leaf blades, which would influence the carbon capture rate. In order to overcome this limitation of the SWAN model, other authors have considered the flexible motion of SAV by modeling each shoot or leaf blade precisely instead of using the bulk method used in previous studies (Stoesser et al., 2003; Anderson et al., 2006; Noarayanan et al., 2012; Li et al., 2014; Busari and Li, 2015). For example, Abdelrhman (2007) divided a blade into several sections in order to consider the drag, lift, friction, and buoyancy forces, and provided evidence of the shelter effect shown by Seginer et al. (1976). Still, Abdelrhman (2007) ignored elastic force, which was a significant factor in the flexible motion of SAV (Nepf, 2012). Also, the interaction between SAV and flows was neglected in the Abdelrhman's model.

As examples modeling each shoot and leading leaf blade precisely, Dijkstra and Uittenbogaard (2010) proposed a method similar to that of Abdelrhman (2007) by including the modulus of elasticity; that method well predicted the results of their laboratory experiments because all necessary forces were included in the model. Marjoribanks et al. (2014) applied Large Eddy Simulation to develop an accurate high-resolution hydrodynamic model that included interactions between flow and river vegetation by accounting for plant rigidity. However, their models require a high-capacity computer, and cannot be applied using an ordinary PC. Nakayama et al. (2020b) proposed an SAV model that can be used on an ordinary PC. Their SAV model considers drag, lift, friction, buoyancy, and elastic forces, as well as the interaction between flows and SAV, by dividing each blade into segments, resulting in good agreement with the results of laboratory experiments. Since the SAV model is based on object-oriented programming, it is easy to analyze many different lengths and characteristic of SAV.

Since SAV bends by the force of currents or waves, an SAV patch induces complex flows around an SAV meadow, resulting in a change in the carbon sequestration rate. Mass transport characteristics around an SAV patch have not been solved fully in previous studies, indicating the difficulty of estimating carbon capture precisely in an SAV patch. Therefore, this study aims to clarify the interactions between flows and SAV patches using laboratory experiments and numerical simulations. Based on the results, we also sought to elucidate the effect of an SAV patch on carbon sequestration. We conducted laboratory experiments to understand how an SAV patch influences flows. Additionally, we applied an SAV model to reproduce the experimental results, after which we investigated the currents modified by the SAV patch. We also investigated how carbon capture around a patch is affected by the extent to which the patch occupies the channel width (occupancy: the ratio of patch width to channel width) and by the elasticity of the leaf blade.

Materials and methods

Laboratory experiments

To investigate the fidelity of an SAV model to the flows around an SAV patch under a uniform flow, we conducted laboratory experiments using an SAV replica in an open channel, whose channel length and width were 25 m and 0.9 m (Figure 1). We used low-foam polyethylene, which is easy to cut and shape, to make SAV replicas with an elasticity of 0.2 GPa and a density of 600 kg m^{-3}. Because of the pump capacity limitation, the experimental width was narrowed to 0.6 m with a length of 11.4 m to give a water depth of 0.3 m. The flow discharge was given as 0.022 m^3 s^{-1}. The leaf of the SAV replica was 0.3 m long, 0.0024 m wide, and 0.001 m thick. The SAV patch was set at 0.2 m wide and 2.0 m long in an open channel (Figure 1). We prepared two spatial intervals of SAV: case E1 with an interval of 0.1 m and case E2 with an interval of 0.05 m (Table 1). Particle image velocity (PIV) was used to measure velocities inside the SAV meadow in the laboratory. The velocity vectors were visualized by sliding a laser sheet (Japan Laser DPGL-2w) using crushed nylon particles with a representative scale of 80 μm. The velocities were measured around only the front of the SAV meadow

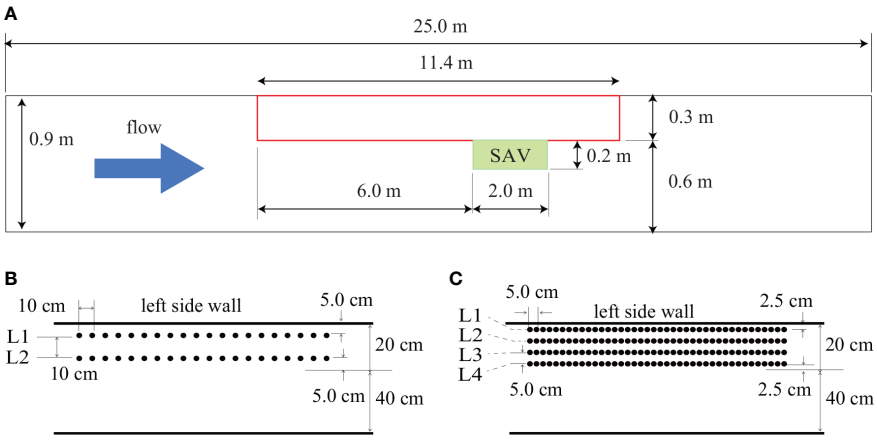

FIGURE 1
Open channel tank in the laboratory experiment. **(A)** The SAV replica was installed in the green-highlighted area. The SAV intervals were **(B)** 0.10 m and **(C)** 0.05 m.

TABLE 1 Conditions for laboratory experiments and numerical simulations.

	E(GPa)	SAV interval (m)	Width of SAV patch (m)	Occupancy (P_C)
case E1	0.2	0.10	0.2	1/3
case E2	0.2	0.05	0.2	1/3
case E2s	0.1		0.2	1/3
case A1-1	∞	0.05	0.15	0.25
case A1-2			0.30	0.5
case A1-3			0.45	0.75
case A1-4			0.60	1.0
caseA2-1	0.2	0.05	0.15	0.25
case A2-2			0.30	0.5
case A2-3			0.45	0.75
case A2-4			0.60	1.0
caseA3-1	0.1	0.05	0.15	0.25
case A3-2			0.30	0.5
case A3-3			0.45	0.75
case A3-4			0.60	1.0

In all cases, the channel is 0.6 m wide. The discharge is 0.022 m^3 s^{-1}, and density is 600 kg m^{-3}.
"E" and "A" correspond to laboratory experiments and numerical simulations, respectively.

because the SAV interacted with a laser sheet inside the meadow. The mean velocity was about 0.12 m s^{-1}, and video images were taken at 100 fps using a Katokoken K-4YH high-speed camera with a resolution of 3840x2160.

To mimic SAV patches, Luhar and Nepf (2011) attempted to use several kinds of materials in their laboratory experiments, such as high-density polyethylene and silicone foam, with densities of about 950 kg m^{-3} and 600 kg m^{-3}, respectively. The elastic modulus of high-density polyethylene is about 1.0 GPa, and silicone foam has an elastic modulus of about 0.5 GPa. Nakayama et al. (2020b) demonstrated that the density and the elastic modulus of *Zostera marina* were 970 kg m^{-3} to 995 kg m^{-3} and about 1.0 GPa. Thus, superficial comparisons suggest that high-density polyethylene is similar to *Zostera marina*. However, we have a scale problem because eelgrass leaves grow to more than 1.0 m in length, 0.01 m in width, and 0.001 m thickness; it is not easy to conduct laboratory experiments using a tank with a water depth of more than 1.0 m. We attempted to use the ratio of the deflected vegetation height (DVH) to the leaf length as one of the similarity rules in order to decide on a material to replicate SAV. DVH is the height of a deflected SAV interacting with currents. In previous studies, interactions between SAV and flow have been evaluated based on the extent of the flow-induced reconfiguration of aquatic vegetation using the Cauchy number, *Ca*, and buoyancy parameter, *B*. *Ca* indicates the relative magnitude of the drag force and elasticity, and *B* indicates the relative magnitude of the buoyancy and elasticity. DVH is a function of the Cauchy number, *Ca*, and the buoyancy parameter, *B* (Luhar and Nepf, 2011).

$$Ca = \frac{1}{2}\frac{\rho C_D b U_w^2 l^3}{EI} \tag{1}$$

$$B = \frac{(\rho - \rho_v) g b d l^3}{EI} \tag{2}$$

$$\frac{\mathrm{DVH}}{l} = 1 - \frac{1 - 0.9Ca^{-1/3}}{1 + Ca^{-3/2}\left(8 + B^{3/2}\right)} \tag{3}$$

Here, ρ is the water density (kg m^{-3}), ρ_v is the vegetation density (kg m^{-3}), b is the vegetation width (m), d is the vegetation thickness (m), l is the vegetation height without current (m), U_w is the horizontal velocity (m s^{-1}), g is the gravitational acceleration (m s^{-2}), C_D is the drag coefficient of SAV, and EI is the flexural rigidity (N m^2).

Therefore, we may suggest modeling *Ca* and *B* in laboratory experiments similar to those in the field. It is possible to use a similar velocity in the laboratory experiment, but, as mentioned above, the leaf length and width of the leaf length and width of the replica leaf are less than those of an actual SAV leaf in nature. Thus, a less-elastic modulus and a denser replica are needed to give similar *Ca* and *B*. Thus silicone foam, rather than high-density polyethylene, is recommended in a tank with a water depth of 0.3 m. Note that the characteristics of the low-foam polyethylene used in this study are similar to those of silicone foam.

SAV model interaction with hydrodynamics

We used the SAV model developed by Nakayama et al. (2020b) to investigate the interactions between the flows and the flexible motion of SAV (Figure 2). Dividing each leaf into segments and nodes enables us to properly include the drag, friction, buoyancy, lift, and elastic forces. Also, the feedback forces from SAV to the flows are included, further contributing to the high fidelity of this realistic model. The computational domain was set at 250 m to remove the reflection effect of waves from the downstream end to the SAV meadow. This meadow was placed 30 m further from the upstream end to provide a steady uniform current to the SAV patch. The open channel width was 0.6 m. The finest grid size, 0.05 m, was used around the SAV meadow, and the grid size changed from 0.05 m to 0.1 m, 0.2 m, 0.25 m, 0.5 m, and 1 m as the distance from the SAV meadow increased. The vertical grid size was 2.5 cm, and the uniform inflow discharge was given at the upstream end, 0.022 m^3 s^{-1}.

$$\rho_a V_s \frac{\partial u_a}{\partial t} = \rho_w \frac{|\mathbf{u} - \mathbf{u_a}|(u - u_a)}{2}\left(C_D A_x + f_c A_z\right) - (EI)_s L_s \frac{\partial^4 \xi_x}{\partial z^4} \tag{4}$$

$$\rho_a V_s \frac{\partial v_a}{\partial t} = \rho_w \frac{|\mathbf{u} - \mathbf{u_a}|(v - v_a)}{2}\left(C_D A_y + f_c A_z\right) - (EI)_s L_s \frac{\partial^4 \xi_y}{\partial z^4} \tag{5}$$

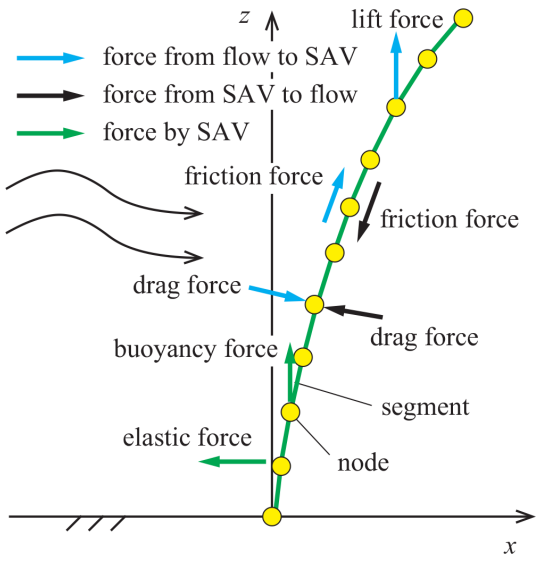

FIGURE 2
SAV model using segments and nodes. Blue arrows indicate the forces from the flow to the SAV. Black arrows indicate the reaction forces from the SAV to the flow. Green arrows indicate the forces due to buoyancy and elasticity.

$$\rho_a V_s \frac{\partial w_a}{\partial t} = \rho_w \frac{|\mathbf{u}-\mathbf{u_a}|(w-w_a)}{2}\left(C_D A_z + f_c\sqrt{A_x^2+A_y^2}\right) + \rho_w \frac{C_L}{2}|\mathbf{u}-\mathbf{u_a}|^2 A_x + (\rho_w-\rho_a)gV_s \quad (6)$$

In the equations above, ρ_a is the density of SAV (kg m^{-3}), V_s is the volume of a segment (m^{-3}), $\boldsymbol{u}$ is the vector of current velocity (m s^{-1}), $\boldsymbol{u_a}$ is the vector of SAV nodes (m s^{-1}), u is the horizontal current velocity (m s^{-1}), u_a is the horizontal velocity of SAV nodes (m s^{-1}), A_x is the vertical projected area in the x direction (m^2), A_y is the vertical projected area in the y direction (m^2), A_z is the horizontal projected area (m^2), ξ_x is the displacement of nodes in the x direction (m), ξ_y is the displacement of nodes in the y direction (m), ρ_w is the water density (kg m^{-3}), C_D(= 1.3) is the drag coefficient of SAV, f_c(= 0.3) is the friction coefficient of SAV, C_L(=0.1) is the lift force coefficient of SAV, E is the elastic modulus (N m^{-2}), I is the second moment of inertia (m^4), L_s is the length of a segment, v is the current velocity in the y direction (m s^{-1}), v_a is the velocity of SAV nodes in the y direction, w is the vertical current velocity (m s^{-1}), and w_a is the vertical velocity of SAV nodes (m s^{-1}).

Results

Velocities and deflected vegetation height

We found that DVH on L1 and DVH on L2 were not significantly different in case E1, where the SAV interval was 0.1 m in the laboratory experiments (Figure 3). In contrast, the deflection was significantly greater on L4 than on L1 in case E2, with an SAV interval of 0.05 m. Since SAV aggregated more in case E2 than in case E1, and the bulk drag force was larger in case E2, we conclude that the flow went around the front of the SAV patch in case E2 more than in case E1, resulting in a more significant deflection on L4 than on L1. PIV provided satisfactory horizontal velocities in case E1 (Figure 4). However, there were substantial fluctuations in case E2 because it was difficult to remove the silhouette of the SAV patches due to the high density of SAV, which also made it impossible to make the velocity measurements from 0.06 m to 0.10 m in the vertical axis.

Influence of SAV on flows in the laboratory experiments

The SAV model agreed well with the laboratory experiments in regard to the root mean squared percentage error (RMSPE) for the DVH (Table 2), which was calculated as

$$\mathrm{RMSPE} = \sqrt{\frac{1}{N}\sum_{i=1}^{N}\left(\frac{y_{n,i}-y_{e,i}}{y_{e,i}}\right)^2} \quad (7)$$

where N is the number of samples, $y_{n,i}$ is the computed DVH, and $y_{e,i}$ is the measured DVH.

A numerical simulation showed the same tendency, i.e., the DVH on L1 in case E1 was almost the same as that on L2 (Figures 3A, B). In contrast to case E1, in case E2 the DVH on L4 was slightly smaller than that on L1, though the DVH difference from the laboratory experiments was more significant than that in the SAV model (Figures 3C, D). The velocities obtained by the PIV agreed very well with the numerical simulation in case E1 (Figure 4A). Although there were large fluctuations in the PIV in

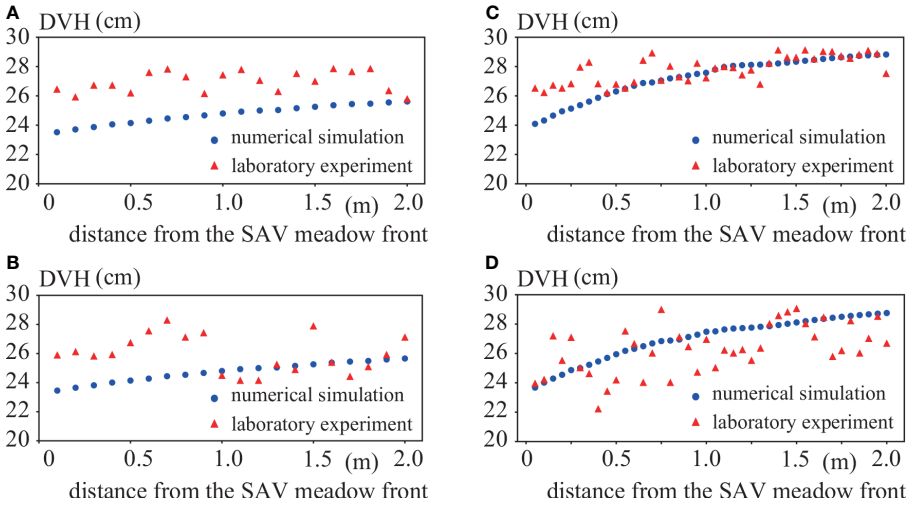

FIGURE 3
Comparisons of DVH between laboratory experiments and numerical simulations. Blue circles and red triangles indicate the laboratory experiment and the numerical simulation, respectively. **(A)** L1 in case E1, **(B)** L2 in case E1, **(C)** L1 in case E2, **(D)** L4 in case E2.

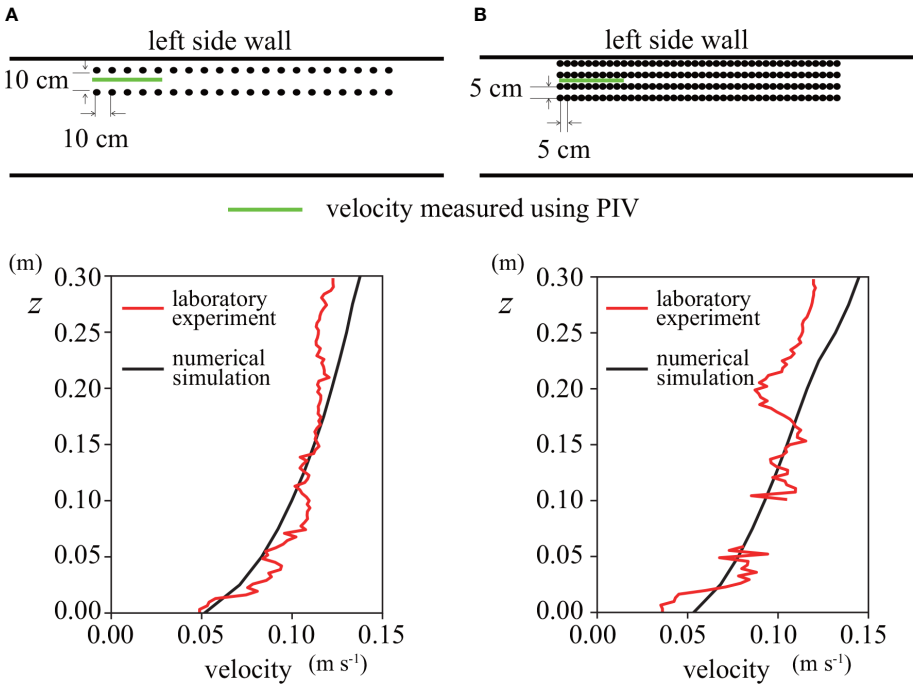

FIGURE 4
Comparison of the vertical profiles of horizontal velocities between laboratory experiments and numerical simulations. Red and black lines indicate the laboratory experiment and the numerical simulation, respectively. **(A)** Case E1, **(B)** Case E2.

TABLE 2 Root mean squared percentage error (RMSPE) on DVH between laboratory experiments and numerical simulations.

	L1	L2	L3	L4
case E1	8.66	7.28	–	–
case E2	3.97	4.31	4.88	6.65

Unit: %.

case E2, the velocities mostly agreed between the laboratory experiment and the numerical simulations (Figure 4B).

To understand the effect of elasticity on the flows around an SAV patch, we conducted a numerical simulation in which the elastic modulus was half that in case E2; this new case is called case E2s (Table 1). The maximum velocity occurred at the front above the SAV meadow on L4 in case E2, which caused a more significant deflection on L4 than on L1 (Figure 5B). However, the maximum velocity occurred at the end above the SAV on L4 in case E2s (Figure 5D). In addition, the velocity reduction inside the SAV meadow was more remarkable in case E2s than in case E2.

Influence of elasticity and the patch occupancy on flows

To investigate the effect of patch occupancy on water flows, we compared the horizontal velocity between occupancies of 25% and 100% for cases A1 to A3 (Figure 6). The horizontal velocity at the SAV patch center is smaller in the case with an occupancy of 25% than in the case with an occupancy of 100% because the currents go around the SAV patch. Moreover, the horizontal velocity inside an SAV patch is significantly lower at 25% compared to 100% occupancy. Additionally, it is apparent that the lower the elasticity, the greater the horizontal velocity above the SAV meadow. Since more water goes around the SAV patch at an occupancy of 25% than at an occupancy of 100%, the SAV bends more in the latter case.

Since the results shown in Figure 6 indicated the significance of the water flows around an SAV patch, we next investigated the elasticity effect on the dominant currents at an occupancy of 50% (Figure 7). When there is no elasticity, the horizontal velocity is the largest at L5 of case A1-2, and the water flows most significantly around the SAV patch (Figures 7A, B). In case A3-2, the water flows above the SAV patch, resulting in the smallest horizontal velocity at L5 among cases with an occupancy of 50%.

Discussion

Luhar and Nepf (2011) successfully proposed an equation to predict the DVH. However, they found that their equation overestimated the drag force when Ca >> 1.0. In this study,

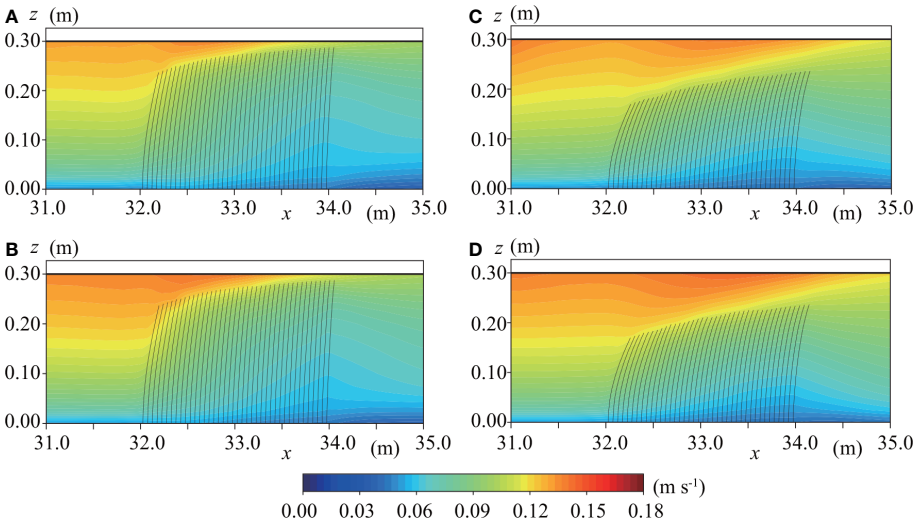

FIGURE 5
Horizontal velocity distributions at **(A)** L1 in case E2, **(B)** L4 in case E2, **(C)** L1 in case E2s, and **(D)** L4 in case E2s.

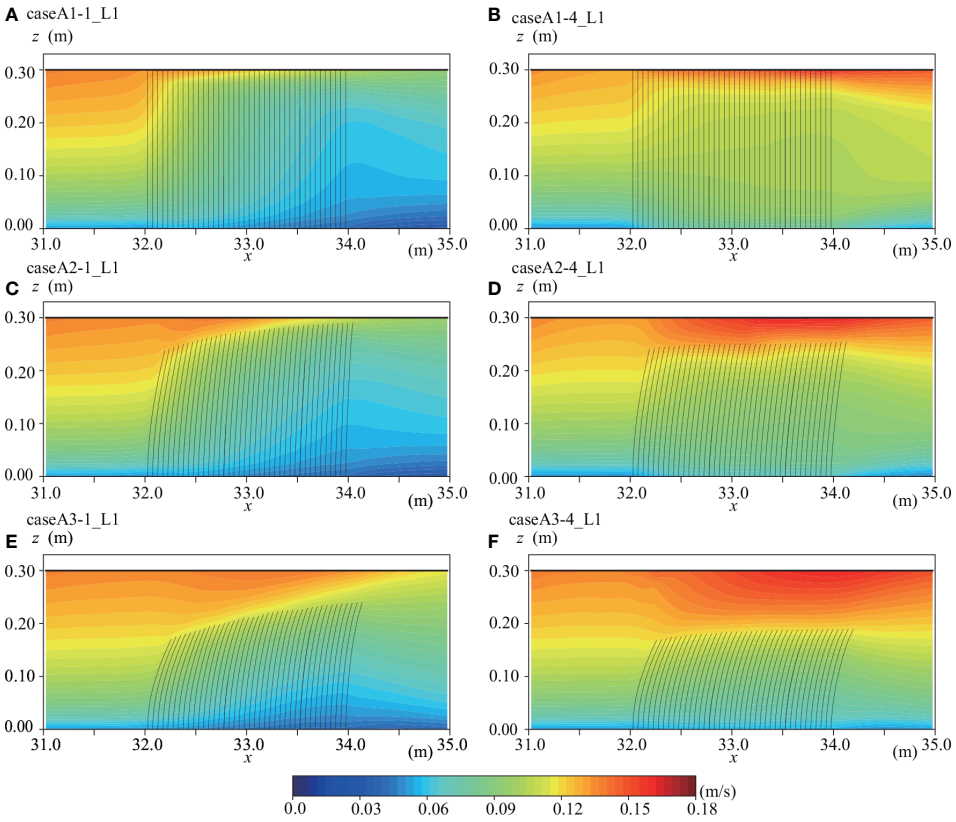

FIGURE 6
Horizontal velocity distributions at L1 in **(A)** case A1-1, **(B)** case A1-4, **(C)** case A2-1, **(D)** case A2-4, **(E)** case A3-1, and **(F)** case A3-4.

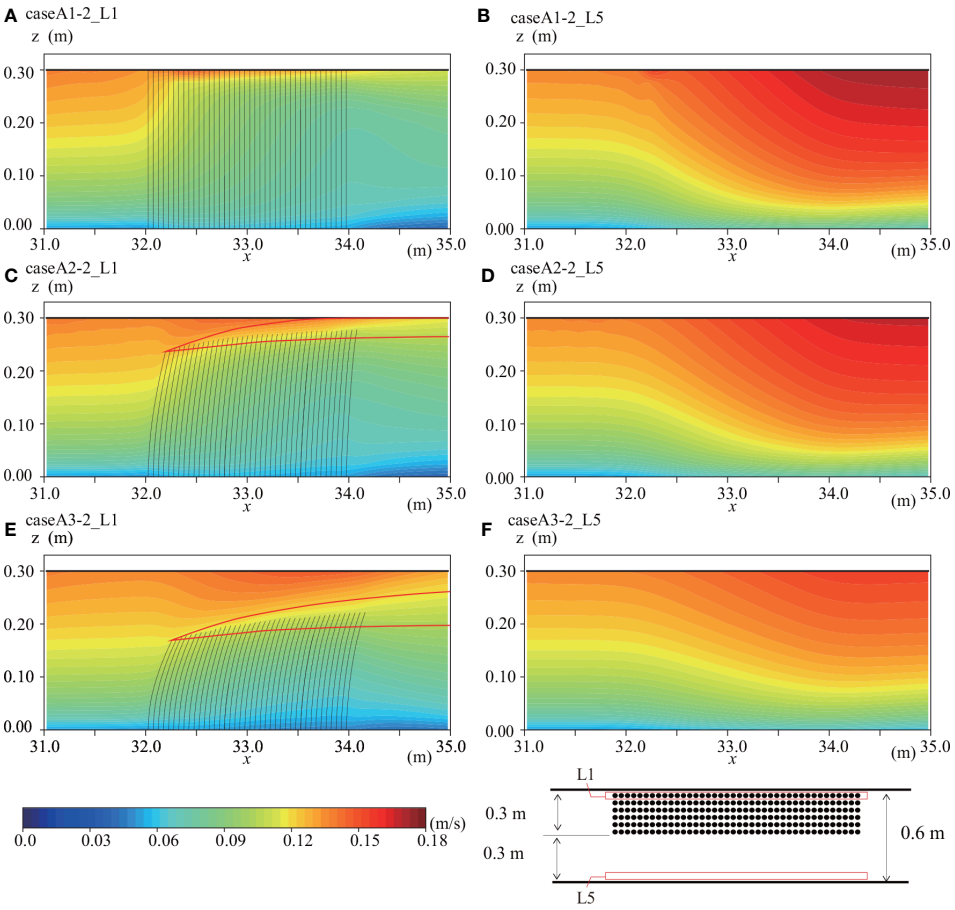

FIGURE 7
Horizontal velocity distributions at **(A)** L1 in case A1-2, **(B)** L5 in case A1-2, **(C)** L1 in case A2-2, **(D)** L5 in case A2-2, **(E)** L1 in case A3-2, and **(F)** L5 in case A3-2.

TABLE 3 Comparisons of DVH for one blade.

	DVH (cm)	DVH/*l*
Laboratory experiment	22.52	0.75
SAV model	22.71	0.76
Luhar and Nepf (2011)	16.51	0.55

therefore, to investigate the validity and robustness in the SAV model reconfigured using the equation of Luhar and Nepf, we compared the DVH for a single leaf blade (Table 3). In our study, Ca was 15.01 and B was 6.35 for one blade with a length of 0.3 m. Therefore, the drag force was overestimated in the theoretical solution, as we expected. Still, the SAV model predicted the DVH almost perfectly, suggesting the effectiveness of this model for analyzing various types of submerged aquatic vegetation (Figure 8).

Duarte et al. (2013) demonstrated that the velocity inside the SAV meadow decreased due to the deflection enhancing the current above the meadow, resulting in the accumulation of particulate organic carbon and nutrients. The SAV model also showed a similar reduction of currents inside the meadow with a high-speed current above it (Figure 5). This may suggest that the current tends to go around an SAV patch when the level of SAV bending is low, but over the patch when the level of SAV bending is high (Figures 7, 9).

Adams et al. (2016) demonstrated the importance of the blade bending angle on water movement and turbidity inside a seagrass meadow. The more the blade bends, the more significantly the sediment is accumulated. It is apparent that the smaller elasticity, the lower the DVH when occupancy is 100% (Pc = 1.0 in Figure 10). Intriguingly, the DVH increases linearly with the decrease in occupancy (Pc). Furthermore, the reduction rate of DVH by Pc is almost the same between cases A2 and A3. Therefore, the DVH was likely predicted by Pc in our experiments using DVH with an occupancy of 100%, even though we did not conduct numerical simulations with other occupancy ratios.

To investigate the decrease in velocity inside the SAV meadow due to the blade bending (Duarte et al., 2013) from the perspective of flux, we computed the normalized discharge inside an SAV patch. The normalization was done using the discharge with an occupancy of 100% and no elasticity blade (Figure 11). Similar to the results for DVH, we found that the

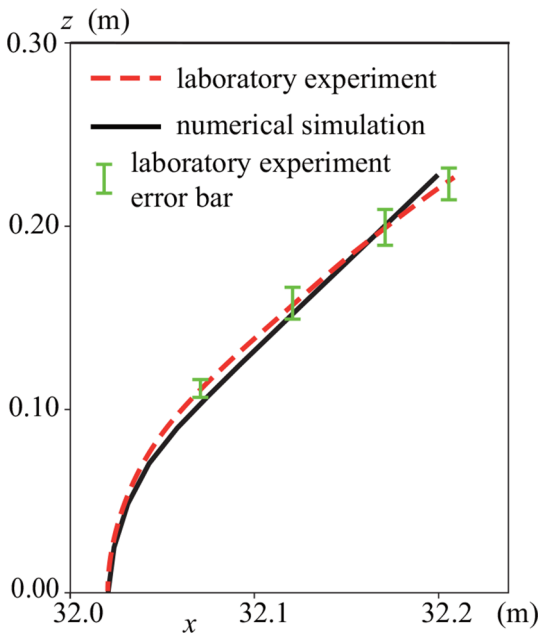

FIGURE 8
Blade shapes of laboratory experiments and numerical simulations. Black solid and red broken lines are the model predictions and measured postures. Vertical green bars indicate the error bar, which was calculated by averaging the results of the three experiments.

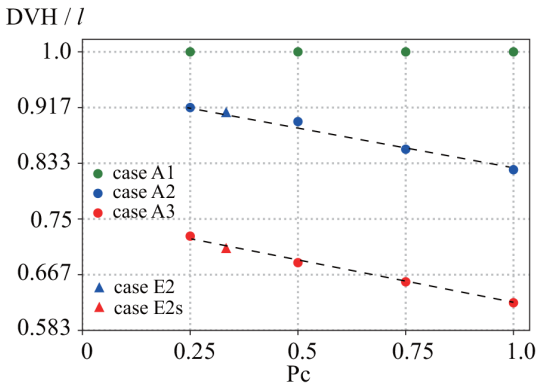

FIGURE 10
DVH obtained from numerical simulations for cases E2 and E2s, and cases A1 to A3. Broken lines indicate the approximate straight lines obtained using the least-squares method.

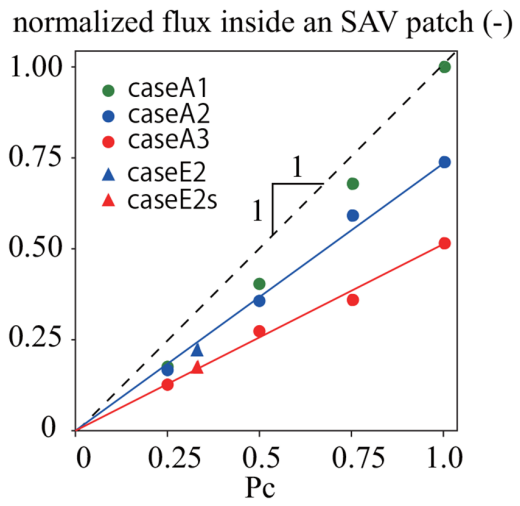

FIGURE 11
Normalized flux inside an SAV patch from numerical simulations for cases E2 and E2s, and cases A1 to A3. Blue and red solid lines indicate the approximate straight lines obtained using the least-squares method.

smaller the elasticity, the less the normalized flux inside an SAV patch when the occupancy was 100% (Pc = 1.0 in Figure 11). Importantly, the normalized flux inside an SAV patch for each elasticity was revealed to be a linear function of Pc (blue and red solid lines in Figure 11). Therefore, the normalized flux inside an SAV patch can be predicted by Pc using the normalized flux with an occupancy of 100% for each elasticity. Note that the normalized flux inside an SAV patch cannot be modelled using a linear function when there is no blade bending. Conditions that do not include blade bending may have different characteristics compared to those which incorporate blade bending, suggesting the necessity of a model that includes

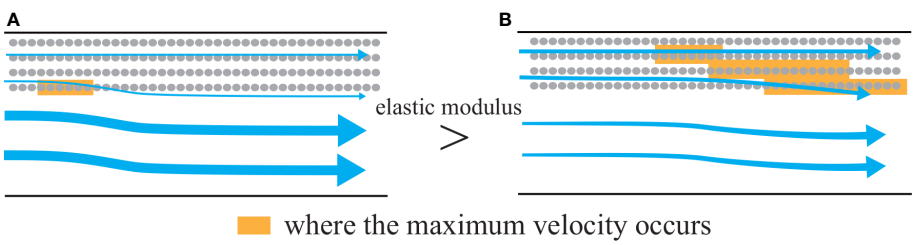

FIGURE 9
Flow modification due to an SAV patch. Arrows indicate the mean fluxes on a horizontal plane. The elasticity is larger in case E2 than in case E2s, resulting in the larger DVH in case E2 than in case E2s. **(A)** Case E2, **(B)** case E2s.

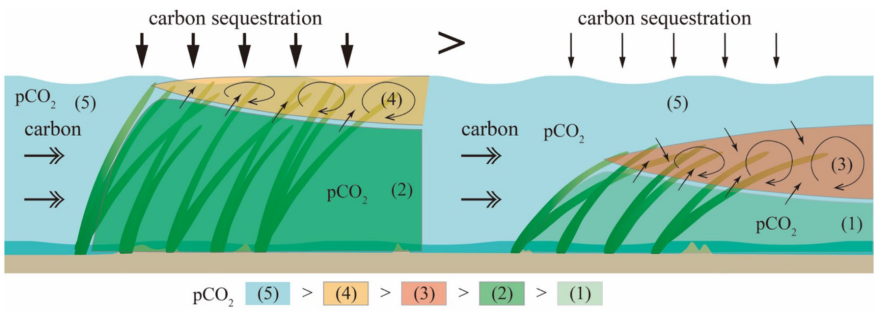

FIGURE 12
Carbon dioxide flux difference due to the formation of a mixing boundary layer at the top of the SAV meadow and DVH.

blade bending in order to analyze the water flows and mass transport around the SAV meadow.

Ghisalberti and Nepf (2006) demonstrated that a typical boundary layer is present along the top of the seagrass meadow. In our numerical simulations, we also confirmed the occurrence of a mixing boundary layer along the top of SAVs (the regions enclosed by red lines in Figures 7C, E). Here, the important point is that the boundary layer cannot reach the water surface when a blade bending angle is large (Figure 7E). Therefore, we hypothesize that the carbon flux between the atmosphere and the water surface proceeds as shown in Figure 12. The pCO2 inside an SAV patch is lower than that in the atmosphere due to the photosynthesis activity during the daytime (Figure 12). However, the blade bending angle is too large to enable the boundary layer to reach the water surface, suggesting that the absorption of pCO2 from the atmosphere would be lower (Figure 12). Therefore, it is necessary to investigate the SAV motion under the currents and waves to clarify the pCO2 flux between the atmosphere and the water surface.

Conclusion

The SAV numerical model was successfully applied to analyze flows around a patch-like SAV meadow, and the results were in good agreement with those of the laboratory experiments. Numerical simulations revealed that, when the SAV bended considerably, larger velocities occurred above the SAV meadow, with the lowest velocity being adjacent to the SAV bottom. When the SAV did not bend significantly, the velocities went around the SAV meadow more substantially than they did in the low-elastic modulus case. The extent to which the patch occupies the channel width was revealed to be the most substantial factor in controlling hydrological conditions and mass transport due to SAV, and deflection was found to be another important factor. Planning and implementing global warming countermeasures are acute goals for climate change mitigation, and efficient planting and management of SAV are urgently needed. Therefore, our study outcome is expected to make an important contribution to the improvement of SAV models that can eventually be applied to quantify the enhancement of blue carbon as a negative emission strategy.

Data availability statement

The raw data supporting the conclusions of this article will be made available by the authors, without undue reservation.

Author contributions

KM: Formal analysis, Investigation, Writing – Original Draft. KN: Funding acquisition, Conceptualization, Methodology, Investigation, Formal analysis, Investigation, Writing – Original Draft. HM: Methodology, Investigation, Formal analysis, Writing – Review & Editing. All authors contributed to the article and approved the submitted version.

Funding

This work was supported by the Japan Society for the Promotion of Science under grant nos. 22H01601, 22H05726, and 18KK0119. The authors declare that they have no conflicts of interest.

Conflict of interest

The authors declare that the research was conducted in the absence of any commercial or financial relationships that could be construed as a potential conflict of interest.

Publisher's note

References

Abdelrhman, M. A. (2007). Modeling coupling between eelgrass zostera marina and water flow. *Mar. Ecol. Prog. Ser.* 338, 81–96. doi: 10.3354/meps338081

Adams, P. A., Hovey, R. K., Hipsey, M. R., Bruce, L. C., Ghisalberti, M., Lowe, R. J., et al. (2016). Feedback between sediment and light for seagrass: Where is it important? *Limnol. Oceanogr.* 61, 1937–1955. doi: 10.1002/lno.10319

Adhitya, A., Bouma, T. J., Folkard, A. M., van Katwijk, M. M., Callaghan, D., de Iongh, H. H., et al. (2014). Comparison of the influence of patch-scale and meadow-scale characteristics on flow within seagrass meadows: a flume study. *Mar. Ecol. Prog. Ser.* 516, 49–59. doi: 10.3354/meps10873

Anderson, B. G., Rutherfurd, I. D., and Western, A. W. (2006). An analysis of the influence of riparian vegetation on the propagation of flood waves. *Environ. Model. Softw.* 21, 1290–1296. doi: 10.1016/j.envsoft.2005.04.027

Boothroyd, R. J., Hardy, R. J., Warburton, J., and Marjoribanks, T. I. (2016). The importance of accurately representing submerged vegetation morphology in the numerical prediction of complex river flow. *Earth Surf. Process. Landf.* 41 (4), 567–576. doi: 10.1002/esp.3871

Busari, A. O., and Li, C. W. (2015). A hydraulic roughness model for submerged flexible vegetation with uncertainty estimation. *J. Hydro-Environ. Res.* 9, 268–280. doi: 10.1016/J.JHER.2014.06.005

Cotovicz, L. C.Jr., Knoppers, B. A., Brandini, N., Costa Santos, S. J., and Abril, G. (2015). A strong CO2 sink enhanced by eutrophication in a tropical coastal embayment (Guanabara bay, Rio de Janeiro, Brazil). *Biogeosciences* 12, 6125–6146. doi: 10.5194/bg-12-6125-2015

Dijkstra, J. T., and Uittenbogaard, R. E. (2010). Modeling the interaction between flow and highly flexible aquatic vegetation. *Water Resour. Res.* 46, W12547. doi: 10.1029/2010WR009246

Duarte, C. M., Losada, I. J., Hendriks, I. E., Mazarrasa, I., and Marbà, N. (2013). The role of coastal plant communities for climate change mitigation and adaptation. *Nat. Clim. Change* 3 (11), 961–968. doi: 10.1038/nclimate1970

Ghisalberti, M., and Nepf, H. (2006). The structure of the shear layer in flows over rigid and flexible canopies. *Environ. Fluid. Mech.* 6, 277–301. doi: 10.1007/s10652-006-0002-4

Ghisalberti, M., and Nepf, H. (2009). Shallow flows over a permeable medium: The hydrodynamics of submerged aquatic canopies. *Transp. Porous. Media.* 78, 309–326. doi: 10.1007/s11242-008-9305-x

Infantes, E., Orfila, A., Simarro, G., Terrados, J., Luhar, M., and Nepf, H. (2012). Effect of a seagrass (Posidonia oceanica) meadow on wave propagation. *Mar. Ecol. Prog. Ser.* 456, 63–72. doi: 10.3354/meps09754

IPCC (2018). *Global warming of 1.5°C. an IPCC special report on the impacts of global warming of 1.5°C above pre-industrial levels and related global greenhouse gas emission pathways, in the context of strengthening the global response to the threat of climate change, sustainable development, and efforts to eradicate poverty*. Eds. V. Masson-Delmotte, P. Zhai, H.-O. Pörtner, D. Roberts, J. Skea, P. R. Shukla, A. Pirani, W. Moufouma-Okia, C. Péan, R. Pidcock, S. Connors, J. B. R. Matthews, Y. Chen, X. Zhou, M. I. Gomis, E. Lonnoy, T. Maycock, M. Tignor and T. Waterfield Geneva, Switzerland, 616.

IPCC (2021). *Summary for policymakers. in: Climate change 2021: The physical science basis. contribution of working group I to the sixth assessment report of the intergovernmental panel on climate change*. Eds. V. Masson-Delmotte, P. Zhai, A. S. Pirani, L. Connors, C. Péan, S. Berger, N. Caud, Y. Chen, L. Goldfarb, M. I. Gomis, M. Huang, K. Leitzell, E. Lonnoy, J. B. R. T. Matthews, K. Maycock, T. Waterfield, O. Yelekçi, R. Yu and B. Zhou Geneva, Switzerland, 41.

Li, Y., Wang, Y., Anim, D. O., Tang, C., Du, W., Ni, L., et al. (2014). Flow characteristics in different densities of submerged flexible vegetation from an open-channel flume study of artificial plants. *Geomorphology* 204, 314–324. doi: 10.1016/j.geomorph.2013.08.015

Luhar, M., Infantes, E., Orfila, A., Terrados, J., and Nepf, H. (2013). Field observations of wave-induced streaming through a submerged seagrass (Posidonia oceanica) meadow. *J. Geophys. Res.* 118, 1955–1968. doi: 10.1002/jgrc.20162

Luhar, M., and Nepf, H. (2011). Flow-induced reconfiguration of buoyant and flexible aquatic vegetation. *Limnol. Oceanogr.-Meth.* 56 (6), 2003–2017. doi: 10.4319/lo.2011.56.6.2003

Luhar, M., and Nepf, H. (2013). From the blade scale to the reach scale: A characterization of aquatic vegetative drag. *Adv. Water Resour. Res.* 51, 305–316. doi: 10.1016/j.advwatres.2012.02.002

Luhar, M., and Nepf, H. (2016). Wave-induced dynamics of flexible blades. *J. Fluid. Struct.* 61, 20–41. doi: 10.1016/j.jfluidstructs.2015.11.007

Marjoribanks, T. I., Hardy, R. J., Lane, S. N., and Parsons, D. R. (2014). High-resolution numerical modelling of flow-vegetation interactions. *J. Hydraul. Res.* 52 (6), 775–793. doi: 10.1080/00221686.2014.948502

Murphy, E., Ghisalberti, M., and Nepf, H. (2007). Model and laboratory study of dispersion in flows with submerged vegetation. *Wat. Resour. Res.* 43, W05438. doi: 10.1029/2006WR005229

Nakayama, K., Kawahara, Y., Kurimoto, Y., Tada, K., Lin, H. C., Hung, M. C., et al. (2022). Effects of oyster aquaculture on carbon capture and removal in a tropical mangrove lagoon in southwestern Taiwan. *Sci. Total. Environ.* 838, 156460. doi: 10.1016/j.scitotenv.2022.156460

Nakayama, K., Komai, K., Tada, K., Lin, H. C., Yajima, K., Yano, S., et al. (2020a). Modelling dissolved inorganic carbon considering submerged aquatic vegetation. *Ecol. Modell.* 431, 109188. doi: 10.1016/j.ecolmodel.2020.109188

Nakayama, K., Shintani, T., Komai, K., Nakagawa, Y., Tsai, J. W., Sasaki, D., et al. (2020b). Integration of submerged aquatic vegetation motion within hydrodynamic models. *Water Resour. Res.* 56, e2020WR027369. doi: 10.1029/2020WR027369

Nellemann, C., Corcoran, E., Duarte, C. M., Valdes, L., DeYoung, C., Fonseca, L., et al. (2009). Blue carbon. a rapid response assessment. united nations environmental programme. *GRID-Arendal. Birkeland* 78.

Nepf, H. M. (2012). Flow and transport in regions with aquatic vegetation. *Annu. Rev. Fluid. Mech.* 44, 123–142. doi: 10.1146/annurev-fluid-120710-101048

Noarayanan, L., Murali, K., and Sundar, V. (2012). Manning's 'n' co-efficient for flexible emergent vegetation in tandem configuration. *J. HYDRO-ENVIRON. Res.* 6, 51–62. doi: 10.1016/j.jher.2011.05.002

Seginer, I., Mulhearn, P. J., Bradley, E. F., and Finnigan, J. J. (1976). Turbulent flow in a model plant canopy. *Boundary. Layer. Meteorol.* 10, 423–453. doi: 10.1007/BF00225863

Stoesser, T., Wilson, C. A. M. E., Bates, P. D., and Dittrich, A. (2003). Application of a 3D numerical model to a river with vegetated floodplains. *J. Hydroinform.* 5 (2), 99–112. doi: 10.2166/hydro.2003.0008

Suzuki, T., Zijlema, M., Burger, B., Meijer, M. C., and Narayan, S. (2011). Wave dissipation by vegetation with layer schematization in SWAN. *Coas. Eng.* 59, 64–71. doi: 10.1016/j.coastaleng.2011.07.006

Vilas, M. P., Marti, C. L., Adams, M. P., Oldham, C. E., and Hipsey, M. R. (2017). Invasive macrophytes control the spatial and temporal patterns of temperature and dissolved oxygen in a shallow lake: A proposed feedback mechanism of macrophyte loss. *Front. Plant Sci.* 8. doi: 10.3389/fpls.2017.02097

frontiers | Frontiers in Marine Science

TYPE Original Research
PUBLISHED 09 January 2023
DOI 10.3389/fmars.2022.1036248

OPEN ACCESS

EDITED BY
Khan M. G. Mostofa,
Tianjin University, China

REVIEWED BY
Anirban Akhand,
Hong Kong University of Science and Technology, Hong Kong SAR, China
Jay Mar D. Quevedo,
The University of Tokyo, Japan

*CORRESPONDENCE
Satoshi Watanabe
watanabe.satoshi.6t@kyoto-u.ac.jp

SPECIALTY SECTION
This article was submitted to Marine Biogeochemistry, a section of the journal Frontiers in Marine Science

RECEIVED 04 September 2022
ACCEPTED 16 December 2022
PUBLISHED 09 January 2023

CITATION
Watanabe S, Maruya Y, Yano S and Nakayama K (2023) Perceptions of practitioners on the importance and achievement of research and social implementation activities on marine and freshwater carbon.
Front. Mar. Sci. 9:1036248.
doi: 10.3389/fmars.2022.1036248

Perceptions of practitioners on the importance and achievement of research and social implementation activities on marine and freshwater carbon

Satoshi Watanabe[1]*, Yasuyuki Maruya[2], Shinichiro Yano[2] and Keisuke Nakayama[3]

[1]Disaster Prevention Research Institute, Kyoto University, Uji, Japan, [2]Department of Urban and Environmental Engineering, Kyushu University, Fukuoka, Japan, [3]Department of Civil Engineering, Kobe University, Kobe, Japan

Research and social implementation related to carbon in marine and freshwater ecosystems are increasingly gaining emphasis in the global quest to achieve carbon neutrality. It is important not only to advance academic research, but also to solve practical problems for improved understanding, maintenance, and dissemination of information on carbon in marine or freshwater areas. In this study, we conducted a questionnaire survey of participants in activities related to carbon in marine or freshwater areas in Japan to clarify which issues were considered important and their understanding of the degree to which activities related to carbon in marine or freshwater areas had been achieved. Based on the responses to all questions, 77.9% of respondents, on average, among the practitioners in marine areas recognized the importance of the program strongly, while 46.5% recognized that the degree of achievement was insufficient. This tendency was more pronounced for carbon in freshwater than in marine areas(72.2% and 48.6%, respectively). The results, grouped by respondent attributes, revealed that the perception of importance and level of achievement varied depending on the organization of the activity, age, and years of knowledge of carbon in marine and/or freshwater areas. Practitioners with greater experience and those working on specific implementations perceived implementation-related aspects as more important and less accomplished than academic ones. This study provides valuable insights into the research aspects of carbon in marine and/or freshwater areas to achieve carbon neutrality.

KEYWORDS

blue carbon, climate change mitigation, carbon neutrality, social implementation of research results, attitude survey

1 Introduction

The achievement of carbon neutrality, which is the balance between carbon emissions and carbon absorption from the atmosphere, is a global issue. The carbon neutrality goal and the path to carbon neutrality have been analyzed by previous research in various fields (Wu et al., 2022). Technologies reducing emissions and promoting capture from the atmosphere are important to this goal (Wang et al., 2021). The potential for various ecosystems to absorb and store atmospheric carbon dioxide has also been calculated. For instance, approximately 55% of the carbon on Earth is absorbed by marine organisms, which is currently referred to as the blue carbon (BC) concept (Nellemann et al., 2009). Specifically, shallow coastal sea areas with vegetation, such as seagrass meadows, have a high affinity for storing carbon in sediment, and therefore play an important role in reducing atmospheric CO_2, a greenhouse gas (Watanabe and Kuwae, 2015).

The ecosystem conditions that can enhance or disrupt carbon capture and storage remain of topical interest for BC (Lavery et al., 2013). Seagrass meadow and kelp are considered dominant carbon dioxide sinks for BC. Empirical evidence proved that sequestration rates were highly variable for BC capture in seagrass systems (Lavery et al., 2013; Nakayama et al., 2020). The target areas of BC research have mainly focused on marine and coastal ecosystems, with less attention paid to inland waters where dense submerged aquatic vegetation exists. However, Lin et al. (2022) revealed that ecosystems, such as phytoplankton in a subtropical mountainous shallow lake, capture and accumulate carbon through photosynthesis even though terrestrial carbon is supplemented through inflows and autochthonous carbon is produced (Lin et al., 2021). Freshwater areas (5.0 million km^2) are larger than coastal areas (1.8 million km^2) and are expected to have greater potential for carbon sequestration (Downing et al., 2006; Verpoorter et al., 2014).

Studies of BC have included enhanced clarification of ocean currents, nutrient dynamics in the ocean, carbon dynamics in relation to carbon fluxes between the atmosphere and seawater, ocean water temperature changes, climate change projections, freshwater inflow from rivers, and ocean acidification. These are factors that can positi or negatively influence BC and were analyzed considering land use in coastal areas, for example, oyster cultivation (Nakayama et al., 2022). Undoubtedly, one of the most significant factors was the high biodiversity in coastal regions owing to the mixing of fresh and oceanic waters. Another factor was that hydraulic retention (residence time) was longer in coastal regions than in other areas because of the closed nature of these regions (Cotovicz et al., 2015; Kubo et al., 2017; Nakayama et al., 2020; Nakayama et al., 2022). Freshwater is also more enclosed than estuaries and lagoons. Similar to BC, in inland waters, submerged aquatic vegetation may significantly reduce carbon dioxide across the entire lake. However, few ongoing studies have investigated carbon dioxide sequestration in freshwater areas in terms of freshwater carbon.

Color-based descriptions are used to describe the nature and distribution of carbon (Zinke, 2020). The term BC was defined by Nellemann et al. (2009). Although the term freshwater BC was used in Lovelock and Duarte (2019), the definition differs from the term used in this study because it was related to the marine tidal system. Nahlik and Fennessy (2016) used the term teal carbon to describe carbon stored in inland freshwater wetlands. The concept of carbon in freshwater areas has not been clearly defined in existing studies. In Japan, the term BC is currently used by the government and private sector implementations to refer to freshwater carbon, which is not strictly identical to the original definition of BC, and there is no academic evidence to support this. Thus, considering the aim of this study, for clarification, the terms marine carbon and freshwater carbon are used hereafter.

Marine carbon has also been investigated from an economic perspective (Bertram et al., 2021). Offset credits, which are well established in forests and agroecosystems as an incentive for climate change mitigation, are also recognized for marine carbon (Kelleway et al., 2017; Sapkota and White, 2020). In some countries, marine carbon is included as a numerical target for greenhouse gas emission reduction (Crooks et al., 2018; Kelleway et al., 2017). In addition, marine carbon ecosystems are increasingly being restored and protected because of their potential to mitigate climate change and other benefits, such as coastal protection and fishery enhancement (Mcleod et al., 2011; Macreadie et al., 2019). However, although freshwater carbon may have significant potential for carbon dioxide sequestration, offset credit has yet to be established for it.

In conjunction with international efforts, the importance of marine and freshwater carbon has been recognized in Japan, and efforts are being made toward its social implementation, such as carbon credit (Kuwae et al., 2022a). The government is working on the dissemination of information and the promotion of policies in marine and freshwater carbon, and many institutions are working on environmental education in the region. For example, the Japan Blue Economy Association was established in 2020 for various organizations and practitioners related to marine and freshwater carbon to collaborate, conduct research, and develop practical methods to conserve and restore coastal areas (https://www.blueeconomy.jp/en/). Therefore, substantial research has been conducted, and the implementation of research findings has progressed.

To promote the understanding, maintenance, and dissemination of information on marine and freshwater carbon, it is important not only to advance academic research, but also to solve practical problems. For example, the restoration of marine carbon ecosystems is a major concern (Wiley et al., 2016). Additionally, it is necessary to solve the problem of waste in water bodies, which is a barrier to restoration and protection. The amount of discarded waste

and its flow from rivers to the sea and other freshwater areas requires investigation, as removal of such waste is critical. Furthermore, in freshwater areas, the issue of alien species should be addressed for proper restoration and protection. In addition, public education is essential to promote the understanding, maintenance, and promotion (Barracosa et al., 2019).

All research is crucial for improving basic knowledge of marine and/or freshwater carbon; however, responding to society's expectations to promote marine and/or freshwater carbon expansion as an urgent issue is also important. Therefore, it is necessary to determine the issues that are considered important by those involved in practical work and the promotion of marine and/or freshwater carbon. Moreover, it is necessary to determine the research topics that should be studied by examining whether the research addresses concerns that are considered important in practice and promotion. In this regard, studies have been conducted to investigate people's perceptions to determine the importance of various implementation and research issues. Dutta et al. (2011) used a questionnaire to understand stakeholders' views on the likely impacts of various levels of coastal inundation on crucial issues. Marine ecosystem services, including marine carbon, have also been investigated in a variety of target sites (Quevedo et al., 2021a; Quevedo et al., 2021b; Afonso et al., 2022).

This study aims to clarify which issues are considered important by those who participate in activities related to carbon in marine or freshwater areas in Japan, whether on the job or not, and how they understand the degree to which they these goals have been achieved based on a questionnaire survey. Consequently, the issues that are important in promoting marine and/or freshwater carbon awareness, but are currently not sufficiently addressed, are clarified. This also clarifies the shortcomings of current academic research. In addition, this study aimed to understand the differences between freshwater and marine carbon. Since freshwater carbon is relatively unexplored in comparison to marine carbon, it is important to identify the measures necessary for its promotion. This study addresses the achievement of carbon neutrality from the perspective of marine and freshwater carbon.

2 Project approach and methods

In July 2022, an anonymous survey was conducted. The questionnaire was distributed *via* e-mail to an unspecified number of practitioners and citizens involved in activities related to marine and/or freshwater carbon in Japan. Responses were accepted on a website created by a web form service or in hard copy (see Supplementary materials for details). The questions were divided into three main categories: questions about the respondents' socio-demographic attributes, respondents' perceived level of progress on marine- and/or freshwater-carbon-related initiatives, and respondents' perceived level of importance and achievement of marine- and/or freshwater-carbon-related topics.

First, respondents were asked questions related to themselves, which included the attributes of their organization, their age, and the number of years they had known about marine and/or freshwater carbon (Table 1). The organizations were classified as universities and research institutes, ministries and government organizations, prefectural and other local government offices, commercial enterprises, NPO/NGO/student/citizen groups, etc., and others. Age was classified as 25 years or younger, 25 to 75 years in 10-year increments, and 75 years or older. Participants classified their years of marine and/or freshwater carbon knowledge as: unknown, less than one year, one to three years, or more than three years.

Next, questions on perceptions on the progress of efforts related to marine and/or freshwater carbon and the importance and achievement of the elements were asked for marine and freshwater areas, respectively. Marine- and freshwater-carbon-related questions were asked only if the participants had prior awareness of either, respectively. Regarding perceptions of the progress of efforts related to marine and/or freshwater carbon, respondents were asked whether they felt that efforts in "understanding the roles and effects of marine and/or freshwater carbon ", "maintenance of the marine and/or freshwater carbon ecosystem", and "dissemination and promotion of marine and/or freshwater carbon ", were progressing, on a five-point scale where 1 is "not progressing

TABLE 1 Classification of respondent attributes in the questionnaire.

Individual/Organizational Attributes	Age	Number of years of marine and/or freshwater carbon awareness
➢ Universities and research institutes	➢ < 25	➢ unknown
➢ Ministries and government organizations	➢ 25 to 34	➢ < 1
➢ Prefectural offices	➢ 35 to 44	➢ 1 to 3
➢ Local government offices	➢ 45 to 54	➢ > 3
➢ Commercial enterprises	➢ 55 to 64	
➢ NPO/NGO/student/citizen groups, etc.	➢ 65 to 74	
➢ Others	➢ > 75	

at all" and 5 is "progressing well". The statistical significance of the differences in means between respondent attributes for these questions was confirmed with a two-sample t-test.

Regarding the perceptions of the importance and achievement of elements, several elements related to the understanding, maintenance, dissemination of information, and promotion of marine and/or freshwater carbon were listed, from both research and implementation perspectives. These questions were also asked on a 5-point scale, excluding those who answered "I don't know". Specific ocean-related elements included the following (Table 2): clarification of ocean/freshwater currents, clarification of nutrient dynamics, clarification of carbon dynamics in relation to carbon fluxes between the atmosphere and sea surface, clarification of water temperature changes in the ocean, climate change projection, clarification and prediction of freshwater inflow from rivers, clarification and prediction of ocean acidification, regeneration of marine and/or freshwater carbon ecosystem, clarification of the amount of garbage dumped and the inflow of garbage from rivers, garbage removal, and education on marine and/or freshwater carbon. Regarding freshwater areas, the question of "extermination of alien species" was added, and "clarification and prediction of ocean acidification" was excluded (Table 3). This was based on the issue of alien species feeding on algae and aquatic organisms, which are the main elements of freshwater carbon ecosystems.

Based on the answers obtained, each element was classified as follows (pertaining to the degree of importance and degree of achievement): high importance and high degree of achievement, important but not achieved, and low importance. Furthermore, by using each group categorized by participant attributes, and responses to their recognition of the progress of marine and/or freshwater carbon efforts, relative comparisons of their responses could be made, according to the characteristics of participants. Through these analyses, the differences in recognition by respondent groups were clarified, as well as the requisite efforts related to research on marine and/or freshwater carbon and implementation of the research results.

3 Results

3.1 Survey implementation

Ninety-four (92 online and 2 hardcopy) valid responses to the questionnaire were received, excluding the five participants who either answered that they were not aware of both marine and freshwater carbon or did not agree to the use of their answers for this study. Figure 1 shows respondents' attributes, age, and years of involvement. Owing to the small number of respondents for some attributes, multiple sections were combined to facilitate statistical analysis. Specifically, the organization classifications became broader and were redivided into five groups: universities and research institutes, ministries and government organizations, prefectural offices, local government offices, and others. Regarding age, one group was defined as those aged 55 and over.

3.2 Marine carbon

Using a 5-point rating scale, the results for the progress of initiatives related to understanding the roles and effects of marine carbon, maintaining ecosystems, and dissemination

TABLE 2 The average and variance of the answers to the eleven questions regarding marine carbon.

		Degree of importance		Degree of achievement	
		mean	variance	mean	variance
A	Clarification of ocean currents	4.11	0.81	2.73	0.84
B	Clarification of nutrient dynamics	4.16	0.81	2.73	0.89
C	Clarification of carbon dynamics in relation to carbon fluxes between the atmosphere and sea water	4.30	0.82	2.70	0.90
D	Clarification and prediction of water temperature changes in the ocean	4.31	0.74	2.78	0.98
E	Climate change projection	4.43	0.78	2.86	0.98
F	Clarification and prediction of freshwater inflow from rivers	3.86	0.93	2.92	1.02
G	Clarification and prediction of ocean acidification	4.01	0.88	2.55	0.93
H	Regeneration of marine carbon ecosystem	4.54	0.72	2.25	0.93
I	Clarification of the amount of marine debris dumped and the inflow of garbage from rivers	3.85	1.04	2.52	1.09
J	Marine debris removal	4.14	1.02	2.32	0.96
K	Education on marine carbon	4.22	0.88	1.95	1.03

TABLE 3 The average value and variance of the answers to the ten questions regarding freshwater carbon.

		Degree of importance		Degree of achievement	
		mean	variance	mean	variance
A	Clarification of freshwater currents	4.11	0.81	2.80	1.00
B	Clarification of nutrient dynamics	4.05	0.86	2.88	0.97
C	Clarification of carbon dynamics in relation to carbon fluxes between the atmosphere and water surface	4.10	0.85	2.67	0.96
D	Clarification and prediction of water temperature changes in freshwater area	3.95	0.88	2.89	0.93
E	Climate change projection	4.17	0.88	2.57	1.03
F	Eradication of alien species	4.21	0.80	2.34	0.83
G	Regeneration of freshwater carbon ecosystem	4.14	0.83	2.19	0.88
H	Clarification of the amount of garbage dumped and the inflow of garbage from rivers	3.72	1.07	2.44	0.97
I	Garbage removal	4.05	1.00	2.32	0.94
J	Education on freshwater carbon	4.10	0.88	1.91	1.10

and promotion were averaged at 2.50, 2.51, and 2.36, respectively. Many answered that efforts had not progressed to all of the questions.

Subsequently, the answers were grouped by organization, age, and number of years they had known about marine carbon (Figure 2). The group that was aware of marine carbon for longer gave higher ratings (2.81) than others for questions regarding the roles and effects of marine carbon, indicating that they consider efforts to be progressing. Regarding the question about the maintenance of the marine carbon ecosystem, the answers from the group that was 25 years old or younger (3.06) or whose organization was a university (2.83) were more positive than those from others. Responses to the dissemination and promotion questions were lower, regardless of age or organization. However, these differences were not statistically significant, as the overall trend was the same, even when the respondent groups were divided.

Subsequently, the average value and variance of the answers to the 11 questions regarding the degree of importance and achievement were calculated for all respondents (excluding those

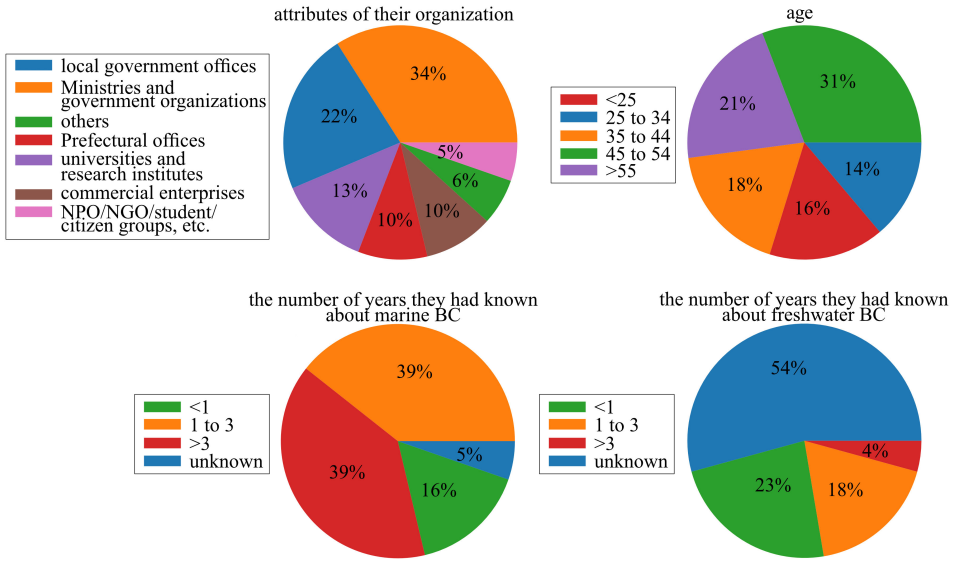

FIGURE 1
Respondent attributes in the results.

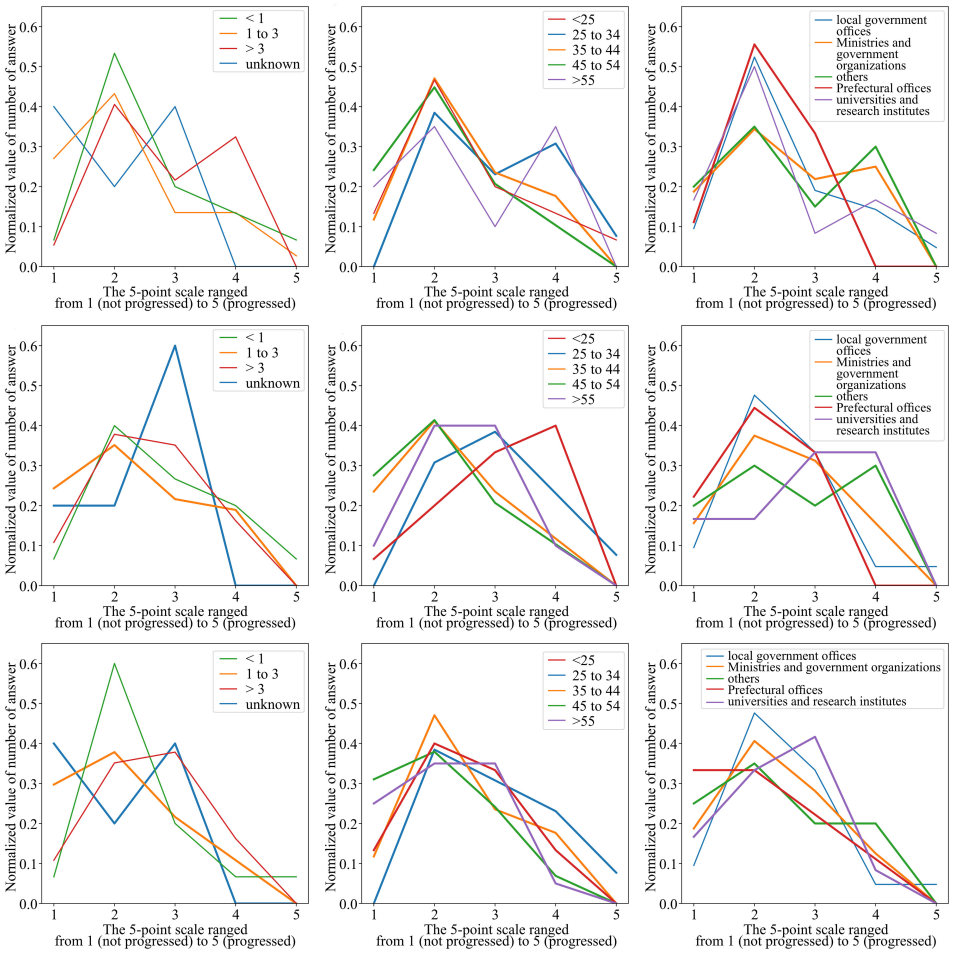

FIGURE 2
Results on the progress of marine carbon-related efforts grouped by attributes. For each of the three questions (each row), the results are shown for each of the three respondent attributes (each column). The questions are "understanding the roles and effects of marine carbon" (left column), "maintenance of the marine carbon ecosystem"(center column), and "dissemination and promotion of marine carbon"(right column). The respondent attributes are "the number of they had known about marine carbon" (top row), "age" (center row), and "organization" (bottom row).

who answered that they did not know) (Table 2). The percentage of respondents who rated the importance as 4 or 5 was 77.9% on average for all questions, while the percentage of respondents who rated achievement as 1 or 2 was 46.5%.

Furthermore, the distributions of the combinations of degrees of importance and achievement for each question were calculated (Figure 3). While the average score for the degree of importance exceeded 3 for all questions, that for the degree of achievement was below 3. These results indicated that the question on restoring the marine carbon ecosystem had the highest average degree of importance (4.54), the second lowest degree of achievement (2.25), and strong recognition that the degree of achievement had not progressed despite its importance. The results showed that the degree of achievement of aspects directly related to activities, such as marine debris removal (2.32) and marine carbon ecosystem restoration (2.25), was low compared to academic content, such as nutrient dynamics (2.73) and carbon dynamics (2.70). The analysis results of the combination of the degrees of importance and achievement showed that the recognition of the degree of importance of the carbon flux (between the atmosphere and sea surface) was divided between 3 and 5. However, the other answers had a unimodal distribution centered on the mode; therefore, the tendency of the answer results to be divided into two groups could not be confirmed.

The answers regarding education displayed the lowest degree of achievement (1.95). The answers indicated that the respondents who thought education was important also thought that the degree of achievement was low. Conversely, the results

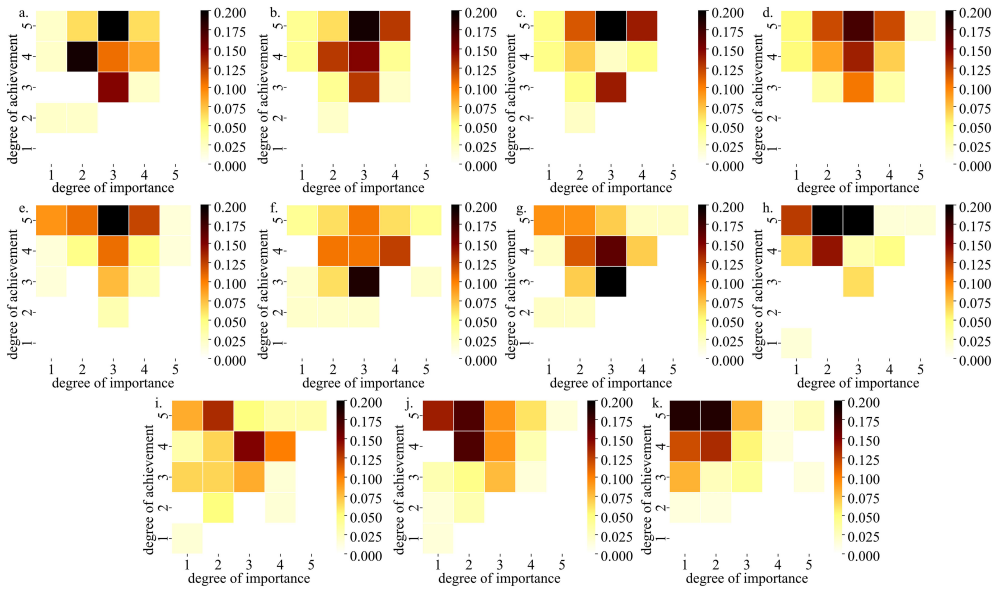

FIGURE 3
Distributions of the combinations of degrees of importance and achievement for each question (**A**–**K**, corresponding to Table 2) regarding marine carbon.

showed that the second least degree of importance was for freshwater inflow from rivers (3.86), and the degree of achievement was the highest (2.92), but still less than 3.

In terms of academic issues, trends differed between wide-area phenomena (climate change and water temperature) and local phenomena (flow, nutrient dynamics, and carbon dynamics). Freshwater inflow and ocean acidification had a lower percentage of low responses than the others, with 3 being the most frequent response (18.7% and 20.9%, respectively). However, the results for water temperature change and climate change showed a combination of high importance and medium degree of achievement. The most frequent values for the degree of importance and achievement were 3 and 5 (27.7% and 17.2%, respectively).

3.3 Freshwater carbon

Figure 4 shows the attributes of the participants who answered that they knew about freshwater carbon. Compared to marine carbon, many local government officials and others (in terms of organizations) responded; however, the percentage of ministry and government officials with the largest number of answers decreased considerably. No significant changes were observed in any age group. Regarding the number of years of knowledge of freshwater carbon, many answers were “less than one year.” This was vastly different from marine carbon, where 78% of the respondents had known about it for more than one year.

The responses on the progress of initiatives related to understanding the roles and effects of freshwater carbon, maintaining freshwater carbon ecosystems, and dissemination and promotion averaged 2.11, 2.18, and 2.09, respectively. Additionally, the answer to many questions was that efforts had not progressed beyond marine carbon. The response results were then checked by organization, generation, and number of years they had known about freshwater carbon (Figure 5). The results showed that the understanding of roles and effects was high among universities and research institutes (2.87). Additionally, regarding administration, there were higher responses among ministries and government officials (2.60) compared to local governments (1.84) and prefectures (1.67). Similarly, many young respondents answered that efforts were progressing (3.00). Conversely, the age groups of 35-45 and 45-55, which are considered to be central groups for rating efforts, gave low ratings (1.86 and 1.68, respectively). Regarding the maintenance of freshwater carbon ecosystems, the same tendency had been observed in efforts to understand their roles and effects. As for dissemination and promotion, similar to the responses regarding administration, those from local governments and prefectures were particularly low (average 1.85 and 1.90, respectively), while ministry and government responses were slightly higher (average 2.40). Regarding dissemination and promotion, the number of answers with

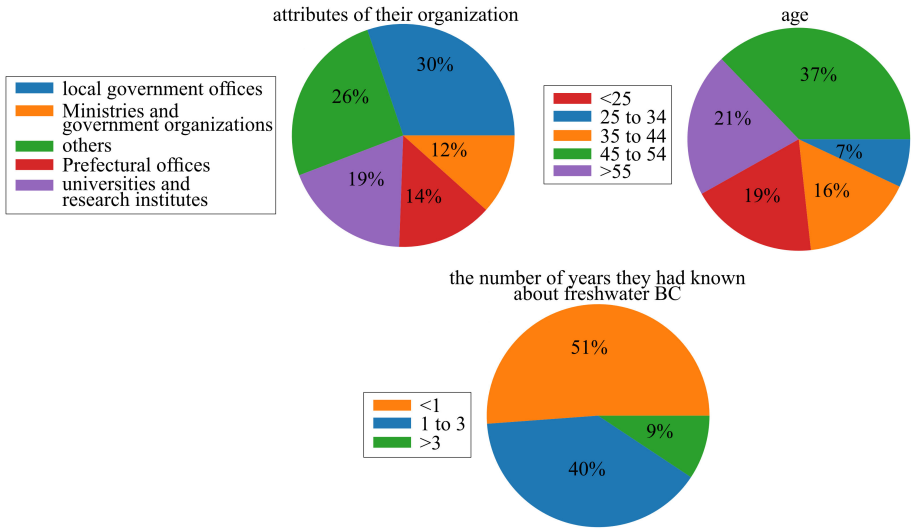

FIGURE 4
Respondent attributes in the results regarding freshwater carbon.

low values tended to decrease as the years of freshwater carbon awareness increased.

Next, responses to the 10 questions about the degree of importance and achievement were examined in the same way as for marine carbon (Table 3; Figure 6). Resembling the marine carbon results, the average degree of importance responses exceeded 3 for all questions, while the average degree of achievement was less than 3. The percentage of respondents who rated the importance as 4 or 5 was 72.2% on average for all questions, while the percentage of respondents who rated achievement as 1 or 2 was 48.6%.

The highest average degree of importance was for invasive alien species control (4.21) (which was asked only for freshwater bodies). Their degree of achievement was the fourth lowest (2.34). Clarification of water temperature change had the highest average degree of achievement (2.89), and its importance was second lowest (3.95). Results with a large variance in degree of importance were related to garbage waste (1.07 and 1.00), which differed by region. Eradication of alien species and restoration of the freshwater carbon ecosystem had the smallest variance in terms of degree of achievement (0.83 and 0.88, respectively), and these average values were also low, which indicated that although the respondents commonly recognized this as an issue, it had not been achieved.

From the distribution of the responses, the degree of importance of nutrient dynamics, carbon flux, and garbage removal were medium (3) or high (5). There were no clear layers of distinction in terms of degree of achievement. Additionally, there were only a few responses with greater values for the degree of achievement than for the degree of importance. Regarding the combination of answers for the degrees of importance and achievement, there were three general responses. The four elements of freshwater currents, nutrient dynamics, carbon flux, and climate change showed a high degree of importance (4.11, 4.05, 4.10 and 4.17, respectively) and a medium degree of achievement (2.80, 2.88, 2.67 and 2.57, respectively). For the elements of eradication of alien species, regeneration of freshwater carbon ecosystem, garbage removal, and education: a high degree of importance (4.21, 4.14, 4.05 and 4.10, respectively) but a low degree of achievement (2.34, 2.19, 2.32 and 1.91, respectively). Lastly, the two elements of water temperature changes, and the amount of garbage dumped and inflow of garbage from rivers, showed a comparatively low degree of importance (3.95 and 3.72, respectively). The tendency shown in the results for marine carbon, in which academic elements were accomplished to a greater extent and practical items to a lesser extent, was more clearly demonstrated in the results for freshwater carbon.

3.4 Relative analysis of perceived importance and achievement by respondent attributes

Finally, a relative comparison was made of the responses of each respondent group according to their attributes (Figures 1, 4) regarding the degree of importance and achievement (Figure 7). From the analysis results differences in what was considered important and how much was perceived to be achieved clearly depended on the attributes of the respondents.

Regarding the difference in recognition by affiliation, respondents belonging to the local government tended to

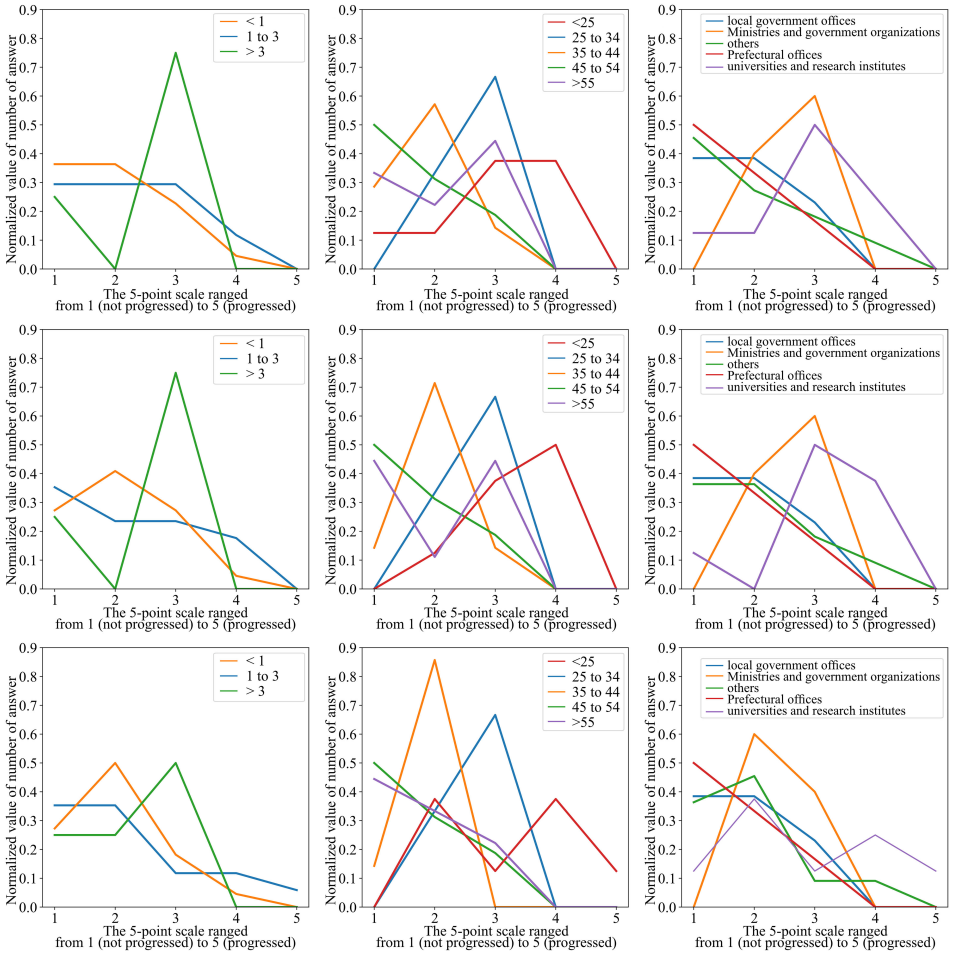

FIGURE 5
Results on the progress of freshwater carbon-related efforts grouped by attributes. As in Figure 2, the results of the three questions are summarized for each of the three attributes. The questions are "understanding the roles and effects of freshwater carbon" (left column), "maintenance of the freshwater carbon ecosystem"(center column), and "dissemination and promotion of freshwater carbon"(right column). The respondent attributes are "the number of they had known about freshwater carbon" (top row), "age" (center row), and "organization" (bottom row).

perceive the degree of importance as low across all questions, whereas those belonging to the ministry and government tended to recognize it as high. Respondents belonging to prefectures tended to recognize the degree of importance of marine carbon as high, whereas they recognized the degree of achievement related to fields such as education and waste removal as lower than others. Additionally, universities and research institutes recognized the degree of achievement of academic content, such as the clarification of nutrient dynamics. The importance of freshwater carbon has also been recognized by this group as high.

As for the difference in recognition by age, younger people rated the degree of achievement higher than average, whereas those between 45 and 55 years had the highest recognition of the degree of importance and the lowest evaluation of the degree of achievement. However, recognition of the degree of importance was low among those aged between 25 and 35 years, as well as among those aged over 55 years. Additionally, the recognition of the degree of importance related to freshwater carbon was higher than average for participants between 35 and 45, except for the amount of waste dumped and the clarification/prediction of the actual state of waste inflow from rivers.

Regarding the difference in recognition by the number of years of marine and/or freshwater carbon knowledge, where the number of years was long (>3), implementation-related issues (e.g., regeneration of marine and/or freshwater carbon ecosystem, amount of garbage dumped and the inflow of garbage from rivers, and garbage removal) had a low degree of

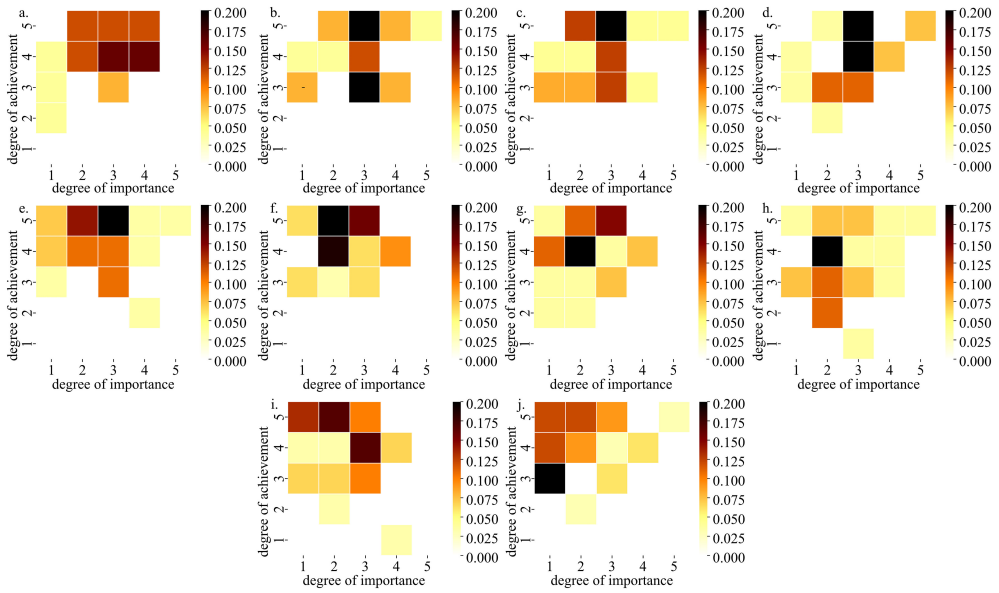

FIGURE 6
Distributions of the combinations of degrees of importance and achievement for each question (**A**–**J**, corresponding to Table 3) regarding freshwater carbon.

achievement, whereas academic issues (such as ocean or freshwater currents, nutrient dynamics, carbon dynamics, and water temperature changes) had a high degree of achievement. However, the degree of importance was generally slightly lower when the number of years of marine and/or freshwater carbon awareness was high.

4 Discussion and conclusion

In this study, to clarify the research and practical issues that need to be addressed for the information distribution and promotion of marine and/or freshwater carbon, a survey was conducted to clarify what practitioners and citizens that participate in activities related to marine and/or freshwater carbon recognize as challenges and to what extent they have been achieved.

The results indicated that the importance of marine and freshwater carbon is highly recognized, although the achievement of marine and freshwater carbon is inadequate. For marine carbon, Nellemann et al. (2009) and many other studies have revealed its importance. While studies on freshwater carbon are still limited, results indicating its potential have been revealed in recent years. For example, Lin et al. (2021); Lin et al. (2022) showed that pCO_2 partial pressure can be lower than that of the atmosphere throughout the year in freshwater lakes above mesotrophic levels, indicating the feasibility of freshwater carbon through the planting of water plants. Additionally, Gu et al. (2020) revealed the high possibility of carbon capture and storage by Phragmites australis (common reed) in a St. Lawrence Estuary Marsh. Since Phragmites australis is a cosmopolitan species growing in inland waters, there could be a high potential to enhance freshwater carbon sequestration. The accumulation of these studies has contributed to enhance awareness of the importance of this issue.

The pattern of responses to questions regarding the importance and achievement of elements considered relevant to the understanding, maintenance, and dissemination of information and promotion of marine and freshwater carbon showed a trend toward higher achievement related to understanding marine and freshwater carbon ecosystems and the surrounding environment, and lower achievement in other elements. This was especially true in freshwater areas. This suggests that research issues related to implementation have not been adequately addressed compared to physics- and chemistry-related research issues. Specifically, there is a need to accumulate research results to promote its implementation in freshwater areas. Implementation contributes to achieving carbon neutrality because it is essential to increase carbon credit certifications. Regeneration of marine and freshwater carbon ecosystems is a direct effort to increase carbon credit certification. Education is also important for gaining public

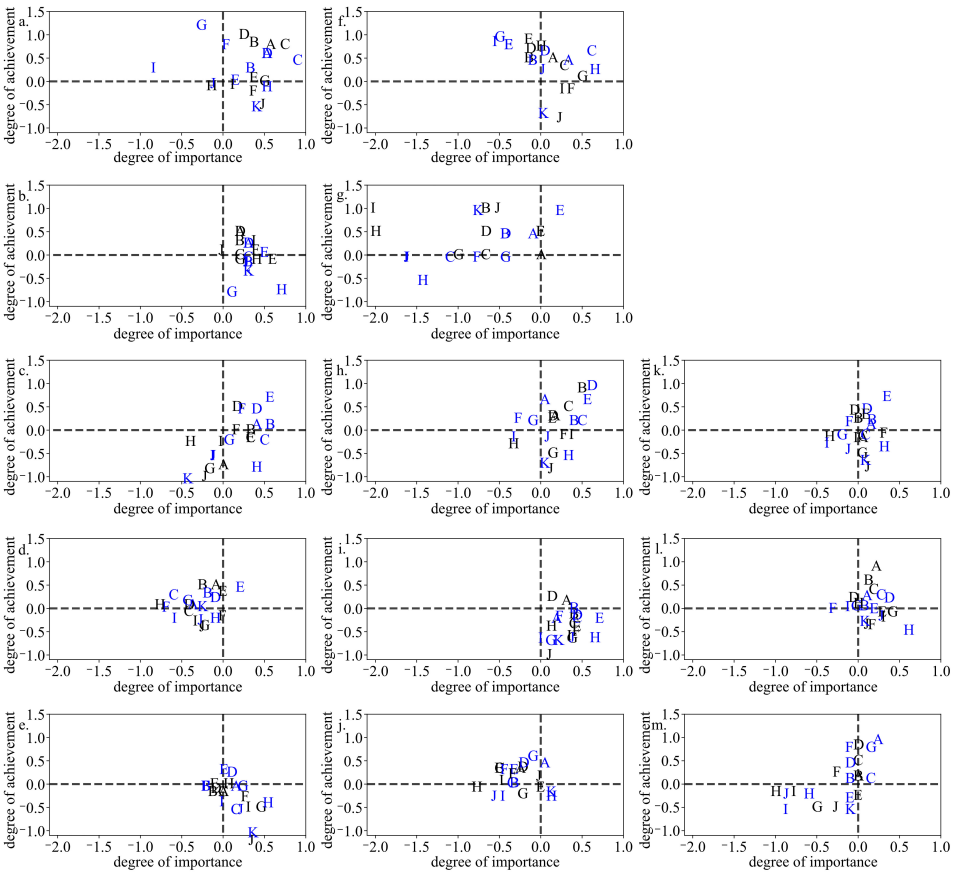

FIGURE 7
Relative comparisons of importance and achievement perceived by the respondent. The alphabets plotted in each figure are the relative importance and achievement, which is the difference of mean between each attribute and all, for the 10 questions (**A** through **I**, questions common to Tables 2, 3). Comparisons performed for each of the organizations (left column), ages (center column), and the number of years are presented (light column). Organizations are university and research institutes **(A)**, ministries and government offices **(B)**, prefectures **(C)**, local governments **(D)**, others **(E)**. Ages are less than 25 **(F)**, 25 to 34 **(G)**, 35 to 44 **(H)**, 45 to 54 **(I)**, and more than 55(j). The number of years are less than 1 **(K)**, 1 to 3 **(L)**, and more than 3(m).

support for marine and freshwater carbon implementation. Issues related to implementation vary widely among regions, and this can be a hindrance to increasing achievement. Kuwae et al. 2022b reviewed three marine carbon implementation projects in Japan. The accumulation and sharing of case studies are important to resolve this issue.

The results of the classification of respondents by attributes showed that the organization in which the activity was conducted, the respondent's age, and the number of years of knowledge of marine and/or freshwater carbon tended to make a difference in the perception of importance and achievement. This result is consistent with the analysis in Dutta et al. (2013). The organizations that carried out activities related to marine and/or freshwater carbon had many responses pertaining to actual sites. Respondents from these organizations recognized less progress in terms of dissemination and promotion of information than those in ministries and governments. Additionally, the low degree of importance of academic consideration in the results signifies that practitioners may not sufficiently recognize their importance. It is essential to understand the perceptions of each respondent group to resolve this difference. Progress in mutual understanding can lead to the identification of new research topics and the implementation of measures by the ministry and government, which in turn is expected to further promote mutual understanding, thereby generating positive feedback.

Kim et al. (2022) evaluated the economic value of marine carbon determined by the general public and showed that marine carbon restoration is socially profitable. Previous studies have conducted economic analyses of carbon in forested and marine areas. Commercially viable and scientifically robust analyses of marine carbon initiatives have also been conducted (Vanderklift et al., 2019). The difference between the two may be that these economic values have not yet

been evaluated for freshwater areas. Economic analysis needs to be conducted in the same manner as in the ocean. The difference between freshwater and marine areas can be attributed to the difference in progress regarding the evaluation of economic value. The same economic analysis needs to be conducted in freshwater areas as in marine areas.

When considering this survey, it must be noted that those who responded to the survey were more concerned about marine and/or freshwater carbon than the general public. Based on the results of the grouped respondents, there is a possibility that the general public, who were not the target of the questionnaire, had low awareness of the importance of marine and/or freshwater carbon. The key to the promotion of marine and/or freshwater carbon is to get these groups to recognize its importance. Most of the general public and government agencies know about biodiversity and waste issues, even if they do not know about marine and/or freshwater carbon. It is expected that association with familiar issues can increase awareness of them. In addition, the linkage with the perspective of disaster prevention, which is a globally important issue in climate adaptation, is also important. Ecosystem protection also contributes to reducing disaster risks.

The survey results revealed the perceived importance and achievement of the issues by practitioners and citizens participating in activities related to marine and freshwater carbon. The perceptions varied depending on the attributes of the respondents. Further analysis of these differences in perceptions could provide valuable insights into research and implementation efforts to achieve marine and freshwater carbon implementation. Advancing mutual understanding between researchers and practitioners through analysis as in this study is necessary for ensuring marine and freshwater carbon implementation.

Data availability statement

The original contributions presented in the study are included in the article/Supplementary Material. Further inquiries can be directed to the corresponding author.

Ethics statement

The studies involving human participants were reviewed and approved by Kobe university. The patients/participants provided their written informed consent to participate in this study.

Author contributions

SW, SY and KN contributed to the conceptualization and design of the basic framework of the survey. SW and YM contributed to the data analysis and visualization of survey results. All authors contributed to the writing of the manuscript and approved the submitted version.

Funding

This work was supported by JSPS KAKENHI Grant Number JP21H05178 JP22H05726, JP22H01601, JP18KK0119 and JP22K18832, and Ministry of Education, Culture, Sports, Science and Technology (MEXT), Japan, Grant Number JPMXD0722678534.

Acknowledgments

The authors would like to thank the respondents of the survey.

Conflict of interest

The authors declare that the research was conducted in the absence of any commercial or financial relationships that could be construed as a potential conflict of interest.

Publisher's note

Supplementary material

The Supplementary Material for this article can be found online at: https://www.frontiersin.org/articles/10.3389/fmars.2022.1036248/full#supplementary-material

References

Afonso, F., Félix, P. M., Chainho, P., Heumüller, J. A., de Lima, R. F., Ribeiro, F., et al. (2022). Community perceptions about mangrove ecosystem services and threats. *Reg. Stud. Mar. Sci.* 49, 102114. doi: 10.1016/j.rsma.2021.102114

Barracosa, H., de los Santos, C. B., Martins, M., Freitas, C., and Santos, R. (2019). Ocean literacy to mainstream ecosystem services concept in formal and informal education: The example of coastal ecosystems of southern Portugal. *Front. Mar. Sci.* 6. doi: 10.3389/fmars.2019.00626

Bertram, C., Quaas, M., Reusch, T. B. H., Vafeidis, A. T., Wolff, C., and Rickels, C.. (2021). The blue carbon wealth of nations. *Nat. Clim. Change* 11, 704–709. doi: 10.1038/s41558-021-01089-4

Cotovicz, L. C.Jr., Knoppers, B. A., Brandini, N., Costa Santos, S. J., and Abril., G. (2015). A strong CO2 sink enhanced by eutrophication in a tropical coastal embayment (Guanabara bay, Rio de Janeiro, Brazil). *Biogeosciences* 12, 6125–6146. doi: 10.5194/bg-12-6125-2015

Crooks, S., Sutton-Grier, A. E., Troxler, T. G., Herold, N., Bernal, B., Schile-Beers, L., et al. (2018). Coastal wetland management as a contribution to the US national greenhouse gas inventory. *Nat. Clim. Chang.* 8, 1109–1112. doi: 10.1038/s41558-018-0345-0

Downing, J. A., Prairie, Y. T., Cole, J. J., Duarte, C. M., Tranvik, L. J., Striegl, R. G., et al. (2006). The global abundance and size distribution of lakes, ponds, and impoundments. *Limnol. Oceanogr.* 51 (5), 2388–2397. doi: 10.4319/lo.2006.51.5.2388

Dutta, D., Wright, W., Nakayama, K., and Sugawara, Y. (2013). Design of synthetic impact response functions for flood vulnerability assessment under climate change conditions: Case studies in two selected coastal zones in Australia and Japan. *Nat. Hazard. Rev.* 14, 52–65. doi: 10.1061/(ASCE)NH.1527-6996.0000085

Dutta, D., Wright, W., and Rayment, P. (2011). Synthetic impact response functions for flood vulnerability analysis and adaptation measures in coastal zones under changing climatic conditions: a case study in gippsland coastal region, Australia. *Nat. Hazard.* 59 (2), 967–986. doi: 10.1007/s11069-011-9812-x

Gu, J., van Ardenne, L. B., and Chmura, G. L. (2020). Invasive phragmites increases blue carbon stock and soil volume in a st. Lawrence estuary marsh. *J. Geophys. Res.: Biogeosci.* 125, e2019JG005473. doi: 10.1029/2019JG005473

Kelleway, J., Serrano, O., Baldock, J., Cannard, T., Lavery, P., Lovelock, C. E., et al. (2017). *Technical review of opportunities for including blue carbon in the Australian government's emissions reduction fund* (Canberra, ACT, Australia: CSIRO).

Kim, J. H., Nam, J., and Yoo., S. H. (2022). Public perceptions of blue carbon in south Korea: Findings from a choice experiment. *Mar. Policy* 144, 105236. doi: 10.1016/j.marpol.2022.105236

Kubo, A., Maeda, Y., and Kanda, J. (2017). A significant net sink for CO2 in Tokyo bay. *Sci. Rep* 44355. doi: 10.1038/srep44355

Kuwae, T., Watanabe, A., Yoshihara, S., Suehiro, F., and Sugimura, Y. (2022a). Implementation of blue carbon offset crediting for seagrass meadows, macroalgal beds, and macroalgae farming in Japan. *Mar. Policy* 138, 104996. doi: 10.1016/j.marpol.2022.104996

Kuwae, T., Yoshihara, S., Suehiro, F., and Sugimura, Y. (2022b). "Implementation of Japanese blue carbon offset crediting projects," in *Green infrastructure and climate change adaptation. ecological research monographs*. Ed. F. Nakamura (Singapore: Springer). doi: 10.1007/978-981-16-6791-6_22

Lavery, P. S., Mateo, M., Serrano, O., and Rozaimi, M. (2013). Variability in the carbon storage of seagrass habitats and its implications for global estimates of blue carbon ecosystem service. *PloS One* 8 (9), e73748. doi: 10.1371/journal.pone.0073748

Lin, H. C., Chiu, C. Y., Tsai, J. W., Liu, W. C., Tada, K., and Nakayama, K. (2021). Influence of thermal stratification on seasonal net ecosystem production and dissolved inorganic carbon in a shallow subtropical lake. *J. Geophys. Res. Biogeosci.* 126, e2020JG005907. doi: 10.1029/2020JG005907

Lin, H. C., Tsai, J. W., Tada, K., Matsumoto, H., Chiu, C. Y., and Nakayama, K. (2022). The impacts of the hydraulic retention effect and typhoon disturbance on the carbon flux in shallow subtropical mountain lakes. *Sci. Total Environ.* 803, 150044. doi: 10.1016/j.scitotenv.2021.150044

Lovelock, C. E., and Duarte, C. M. (2019). Dimensions of blue carbon and emerging perspectives. *Biol. Lett.* 15, 20180781. doi: 10.1098/rsbl.2018.0781

Macreadie, P. I., Anton, A., Raven, J. A., Beaumont, N., Connolly, R. M., Friess, D. A., et al. (2019). The future of blue carbon science. *Nat. Commun.* 10, 3998. doi: 10.1038/s41467-019-11693-w

Mcleod, E., Chmura, G. L., Bouillon, S., Salm, R., Björk, M., Duarte, C. M., et al. (2011). A blueprint for blue carbon: toward an improved understanding of the role of vegetated coastal habitats in sequestering CO2. *Front. Ecol. Environ.* 9, 552–560. doi: 10.1890/110004

Nahlik, A., and Fennessy, M. (2016). Carbon storage in US wetlands. *Nat. Commun.* 7, 13835. doi: 10.1038/ncomms13835

Nakayama, K., Kawahara, Y., Kurimoto, Y., Tada, K., Lin, H. C., Hung, M. C., et al. (2022). Effects of oyster aquaculture on carbon capture and removal in a tropical mangrove lagoon in southwestern Taiwan. *Sci. Total Environ.* 838, 156460. doi: 10.1016/j.scitotenv.2022.156460

Nakayama, K., Komai, K., Tada, K., Lin, H. C., Yajima, K., Yano, S., et al. (2020). Modelling dissolved inorganic carbon considering submerged aquatic vegetation. *Ecol. Modell.* 431, 109188. doi: 10.1016/j.ecolmodel.2020.109188

Nellemann, C., Corcoran, E., Duarte, C. M., Valdes, L., De Young, C., Fonseca, L., et al. (2009). *Blue carbon. a rapid response assessment. united nations environmental programme* (Birkeland Trykkeri AS, Birkeland: GRID-Arendal).

Quevedo, J. M. D., Uchiyama, Y., and Kohsaka, R. (2021b). Local perceptions of blue carbon ecosystem infrastructures in panay island, Philippines. *Coast. Eng. J.* 63, 227–247. doi: 10.1080/21664250.2021.1888558

Quevedo, J. M. D., Uchiyama, Y., Muhamad Lukman, K., and Kohsaka, R. (2021a). How blue carbon ecosystems are perceived by local communities in the coral triangle: Comparative and empirical examinations in the Philippines and Indonesia. *Sustainability* 13, 127. doi: 10.3390/su13010127

Sapkota, Y., and White, J. R. (2020). Carbon offset market methodologies applicable for coastal wetland restoration and conservation in the united states: a review. *Sci. Total Environ.* 701, 134497. doi: 10.1016/j.scitotenv.2019.134497

Vanderklift, M. A., Marcos-Martinez, R., Butler, J. R. A., Coleman, M., Lawrence, A., Prislan, H., et al. (2019). Constraints and opportunities for market-based finance for the restoration and protection of blue carbon ecosystems. *Mar. Policy* 107, 103429. doi: 10.1016/j.marpol.2019.02.001

Verpoorter, C., Kutser, T., Seekell, D. A., and Tranvik., L. J. (2014). A global inventory of lakes based on high-resolution satellite imagery. *Geophys. Res. Lett.* 41 (18), 6396–6402. doi: 10.1002/2014GL060641

Wang, F., Harindintwali, J. D., Yuan, Z. Z., Wang, M., Wang, F., Li, S., et al. (2021). Technologies and perspectives for achieving carbon neutrality. *Innovation* 2, 100180. doi: 10.1016/j.xinn.2021.100180

Watanabe, K., and Kuwae, T. (2015). How organic carbon derived from multiple sources contributes to carbon sequestration processes in a shallow coastal system? *Global Change Biol.* 21, 2612–2623. doi: 10.1111/gcb.12924

Wiley, L., Sutton-Grier, A. E., and Moore, A. (2016). Keys to successful blue carbon projects: lessons learned from global case studies. *Mar. Pol.* 65, 76–84. doi: 10.1016/j.marpol.2015.12.020

Wu, X., Tian, Z., and Guo, J. (2022). A review of the theoretical research and practical progress of carbon neutrality. *Sustain. Oper. Comput.* 3, 54–66. doi: 10.1016/j.susoc.2021.10.001

Zinke, L. (2020). The colours of carbon. *Nat. Rev. Earth Environ.* 1, 141. doi: 10.1038/s43017-020-0037-y

frontiers | Frontiers in Marine Science

TYPE Original Research
PUBLISHED 11 January 2023
DOI 10.3389/fmars.2022.1016199

OPEN ACCESS

EDITED BY
Keisuke Nakayama,
Kobe University, Japan

REVIEWED BY
Chung-Chi Chen,
National Taiwan Normal University, Taiwan
Anirban Akhand,
Hong Kong University of Science and Technology, Hong Kong SAR, China
Xiaogang Chen,
Westlake University, China

*CORRESPONDENCE
Jun Sasaki
jsasaki@k.u-tokyo.ac.jp

SPECIALTY SECTION
This article was submitted to Marine Biogeochemistry, a section of the journal Frontiers in Marine Science

RECEIVED 10 August 2022
ACCEPTED 21 November 2022
PUBLISHED 11 January 2023

CITATION
Endo M, Zhao Y, Nakamura W and Sasaki J (2023) A practical pCO_2 estimation and carbonate dynamics at an event of hypoxic water upwelling in Tokyo Bay.
Front. Mar. Sci. 9:1016199.
doi: 10.3389/fmars.2022.1016199

A practical pCO_2 estimation and carbonate dynamics at an event of hypoxic water upwelling in Tokyo Bay

Masanori Endo, Yue Zhao, Wataru Nakamura and Jun Sasaki*

Department of Socio-Cultural Environmental Studies, Graduate School of Frontier Sciences, The University of Tokyo, Kashiwa, Japan

Urban bays have been considered to have a high CO_2 absorption function due to the high nutrient load and resultant primary production. It is expected to enhance the function by promoting a blue carbon policy co-beneficial with strengthening ecosystem services such as fisheries. Estimates of CO_2 absorption in urban bays have been based mostly on fragmentary information from shipboard observations, and an evaluation based on continuous observation of water quality is necessary considering the large spatiotemporal variability of such bay environment. In particular, Tokyo Bay has a specific feature of water pollution problem of hypoxia and anoxia leading to emitting high CO_2. Bottom hypoxic and anoxic waters develop from early summer to autumn in the central part of the bay and enclosed areas such as navigation channels and borrow pits. It is known that pCO_2 becomes very high in these waters, and their upwelling (called blue tide in the bay from the discoloration of the sea surface) is thought to cause high CO_2 emissions; however, the actual situation is unknown. We developed a practical method for continuous estimation of pCO_2 by appropriately combining continuous observation of water quality using sensors and measurements of carbonate parameters by water sampling. The results show that a highly reproducible and practical method for continuous estimation of pCO_2 was possible by combining *in situ* salinity and pH meters and the total alkalinity and calc. pH measured by a total alkalinity titrator for water samples. This method was then applied to the duration of blue tide that occurred in the head of the bay in the summer and autumn of 2021. The pCO_2 in the surface water was found to increase significantly and exceed 2000 µatm due to the upwelling of anoxic bottom water containing high pCO_2. Mean CO_2 emissions of approximately +2150 and +1540 µmol m^{-2} h^{-1} were observed at two stations during the upwelling period. The mean values rose to +2390 and +2190 µmol $m^{-2}h^{-1}$ with the blue tide and lowered to +810 and +1120 µmol m^{-2} h^{-1} without it, suggesting that high CO_2 emissions may occur due to upwelling, especially with blue tides.

KEYWORDS

blue carbon, urban bay, hypoxia and anoxia, hydrogen sulfide, continuous field observation, CO_2, total alkalinity, dissolved inorganic carbon

1 Introduction

The enhancement of carbon removal was mentioned as a mitigation measure for climate change in the Paris Agreement in 2015. Blue carbon, defined as carbon sequestered and stored by marine ecosystems (Nellemann et al., 2009; Kuwae and Hori, 2019), has been attracting attention in this context. In coastal marine ecosystems, mangrove forests, salt marshes, seagrass meadows, and seaweed beds are considered significant carbon sinks (Breithaupt et al., 2012; Krause-Jensen and Duarte, 2016; Duarte and Krause-Jensen, 2017). Eutrophic urban bays have also been reported to contribute to a net carbon sink (Kuwae et al., 2016; Tokoro et al., 2021). Tokyo Bay, Japan, is a typical eutrophic urban bay with the Tokyo metropolitan area as its watershed. During the period of rapid economic growth from the 1960s, water pollution due to eutrophication became more serious, resulting in sediment organic pollution; the formation of bottom hypoxic and anoxic waters in summer and coastal upwelling of these waters lead to the mortality of benthic animals (Kodama and Horiguchi, 2011; Furukawa, 2015; Amunugama and Sasaki, 2018). To alleviate the problem, the Environment Agency (now the Ministry of the Environment) introduced a Total Pollutant Load Control System policy (TPLCS) in 1979, with COD as the target water quality item. Since 2001, total nitrogen and total phosphorus have been added as target items, achieving a significant decrease in pollutant loads (Tomita et al., 2016). By contrast, cultural oligotrophication caused by the TPLCS has been pointed out in recent years; it could be one of the causes of the significant decrease in fishery resources, including the impact on seaweed culture with the discoloration of edible larver (Yamamoto, 2003; Aoki et al., 2022). In addition, protecting coastal areas is becoming increasingly important to mitigate the growing severity of storm surge disasters associated with intensified typhoons due to climate change and tsunami disasters, raising expectations for green infrastructure (Sasaki et al., 2012; Liu et al., 2022). Environmental management of the bay must be thus reconsidered to realize a safe, beautiful, and abundant estuary, and there are growing expectations for blue carbon to contribute to enhancing these ecosystem services in a win–win relationship.

In Tokyo Bay, stratification appears from May to September due to increasing river runoffs and water temperatures. Extensive primary production lowers pCO_2 and contributes to the absorption of atmospheric CO_2 in the upper layer. The decomposition of organic matter increases dissolved inorganic carbon (DIC) and decreases pH, resulting in increasing pCO_2 in the lower layer. In addition, waters in navigation channels and borrow pits (mining sediments for the foreshore reclamation) in the inner part of the bay are extensively stagnant, causing the appearance of anoxic waters with high concentrations of sulfides (Sasaki et al., 2009a; Sasaki et al., 2009b). Although CO_2 is thought to be emitted to the atmosphere during coastal upwelling (Feely et al., 2008; Norman et al., 2013; Tokoro et al., 2021), the actual status of CO_2 emissions and DIC dynamics are not fully understood because coastal upwelling, as well as anoxia and hypoxia, is an episodic event in the bay (Sasaki et al., 2009b). Sulfate reduction becomes the main pathway for organic matter decomposition under anoxic conditions, resulting in sulfide accumulation in bottom waters. The sunlight scattering of particulate sulfur generated by sulfide oxidation during the upwelling is known as blue tides, in which the surface seawater turns milky blue (Otsubo et al., 1991; Higa et al., 2020). The DIC dynamics, including pCO_2 during blue tides, have not been well investigated. Although the upwelling of anoxic waters has been observed in other urban bays in Japan, such as Osaka Bay and Mikawa Bay, there have not been many reported cases worldwide (Gallardo and Espinoza, 2008; Minghelli-Roman et al., 2011; Schunck et al., 2013; Ma et al., 2021). However, the global trend of expansion of hypoxic waters due to climate change and the effects of upwelling of such waters are considered problematic; knowledge on CO_2 emissions associated with the upwelling of hypoxic and anoxic waters is considered essential (Diaz and Rosenberg, 2008; Vaquer-Sunyer and Duarte, 2008; Gilbert et al., 2010; Testa et al., 2017; Breitburg et al., 2018; Lee et al., 2018; Hong et al., 2022; Pearson et al., 2022). Direct and continuous measurements of air–seawater CO_2 fluxes have been made using eddy covariance (Zemmelink et al., 2009; Tokoro et al., 2014) and floating chamber methods (Tokoro et al., 2007; Tokoro et al., 2014); these are, however, generally costly and present many challenges for practical deployment. Therefore, the bulk method is widely employed to estimate the CO_2 fluxes. When applying the bulk method, it is necessary to estimate the pCO_2 in seawater. The method of analyzing water samples using a total alkalinity titrator is versatile, reliable, and widely used (Dickson et al., 2007; Tokoro et al., 2014). There are also estimation methods that combine salinity and pH from shipboard or mooring observations (Johnson et al., 2016; Williams et al., 2016; Williams et al., 2017). However, there is no universal formula, and developing an appropriate estimation method for each environment is essential. Other methods for estimating surface seawater pCO_2 include using satellite imagery (Stephens et al., 1995; Sarma et al., 2006; Lohrenz et al., 2019; Mohanty et al., 2022) and a combination of satellite imagery with field observations using statistical methods based on multivariate analysis and machine learning (Lefévre et al., 2005; Friedrich and Oschlies, 2009; Signorini et al., 2013; Majkut et al., 2014; Moussa et al., 2016; Benallal et al., 2017). Although these are considered adequate for evaluation in a wide area, applying them to episodic coastal upwelling events with a narrow band of affected areas along the coastline is challenging.

Several continuous monitoring stations for water quality are currently operated in Tokyo Bay by the Ministry of Land, Infrastructure, Transport and Tourism (MLIT); some of the

water quality parameters necessary for estimating pCO_2 have been continuously observed. Estimating continuous pCO_2 based on such monitoring will enable continuous monitoring of carbon absorption and emission, including during episodic events, which is expected to arouse public interest in environmental management and policy implementation for strengthening blue carbon with the co-benefits of enhanced ecosystem services in urban bays. We hypothesize that continuous measurement using water quality sensors in combination with periodic calibration by water sampling will enable continuous observation of pCO_2 with reasonable accuracy for each specific estuarine and coastal water. This study aims to develop a practical method for continuously estimating pCO_2 from measured water quality parameters using moored sensors combined with water sampling analysis using a total alkalinity titrator and clarify DIC dynamics, including pCO_2, during the upwelling of anoxic waters in Tokyo Bay.

2 Materials and methods

2.1 Study area

Tokyo Bay is a eutrophic semi-enclosed estuarine embayment surrounded by the Tokyo metropolitan area, with major and minor lengths of approximately 60 and 20 km and a mean depth of 17 m (see Figure 1). Major rivers flow into the bay from the western coast, and stratification develops from spring to autumn. Appearance of hypoxia and anoxia in the bottom waters between spring and autumn has been a serious water quality problem causing mortality of fishes and benthic animals in tidal flats and shallow water areas. The bottom anoxic waters often contain hydrogen sulfide generated by sulfate reduction (Kodama and Horiguchi, 2011; Furukawa, 2015; Amunugama and Sasaki, 2018). In addition, navigation channels and borrow pits (dredged for the foreshore reclamation) exist at the bay head, in which anoxic waters with a high concentration of hydrogen sulfide often appear (Sasaki et al., 2009a; Sasaki et al., 2009b). The upwelling of such anoxic waters causes discoloration of surface water due to the oxidation of hydrogen sulfide generating particulate sulfur, which scatters the sunshine and the surface watercolor turned to milky blue called blue tide in Tokyo Bay (Otsubo et al., 1991; Sasaki et al., 2009b; Higa et al., 2020; Wang et al., 2022).

2.2 Field observation

We conducted an observation of water quality to identify carbonate processes at an event of blue tide at the bay head. Observation stations were deployed as shown in Figure 1C. Stns. S_F, S_K, and S_C are buoy stations for continuous water quality monitoring adjoining to the seawall in Funabashi, Kemigawa, and Chiba, respectively. Stns. with initials of F, N, and P are observation stations using a boat at the flat bottom, the Funabashi and Chiba navigation channels, and the off-Makuhari borrow pit. Stns. with initials C are the fixed camera monitoring stations to observe the occurrence of blue tides. Stn. M is a water quality monitoring station managed by MLIT.

2.2.1 Observation at buoy monitoring stations

We conducted continuous measurements of water quality at 10-min intervals using self-recording sensors attached to buoys at Stns. S_F (August 27–September 17), S_K (August 31–September 10), and S_C (August 27–September 10) adjoining to the seawalls at Funabashi, Kemigawa, and Chiba to observe the upwelling processes of hypoxic and anoxic waters (see Figure 1C). The sensors were deployed at the surface and bottom at Stns. S_F and S_C, and at the surface, middle, and bottom at Stn. S_K. The water depth is about 4–5.5 m at Stn. S_F, about 7–9m at Stn. S_K, and about 4–6m at Stn. S_C. The measured items at each depth and station were the water pressure (CO-U20L-04/02, HOBO), temperature and salinity (ACTW-CMP, JFE Advantech), turbidity (ACTW-CMP, JFE Advantech), and dissolved oxygen (DO) (CO-U26-001, HOBO, or ADOW-CMP, JFE Advantech). A pH sensor (CO-MX2501, HOBO) was installed only at the surface at each station.

We visited the continuous monitoring stations and measured the vertical profiles of multiparameter water quality of temperature, salinity, turbidity, DO, and pH using a throw-in water quality meter (AAQ-RINKO 177, JFE Advantech) on September 1, 2, 3, and 10 at the three stations. In addition, we conducted the measurements on August 27 and September 17 at Stn. S_F, on August 31 at Stn. S_K, and on August 27 at Stn. S_C. We also took water samples at each depth at the three stations using a 1300 mL RIGO-B water sampler (5023-A, Rigo-sha) on the same days. Furthermore, only surface water samples were collected using a bucket at the three stations on September 8. A 50% saturated solution of mercury (II) chloride was added to the water samples in Duran bottles at twice the standard dosage range for saturated solutions (0.02–0.05%) for measuring pH, TA, and DIC following Dickson (2007). Water samples to be analyzed for sulfide concentrations were poured into 100 mL brown bottles, immediately fixed by adding three granular sodium hydroxides to make them alkaline with a pH of about 12. These samples were immediately taken back to the laboratory and stored in the dark at room temperature.

2.2.2 Observation using a boat

Water quality observation using a boat was carried out at stations with initials F, N, and P in Figure 1C in the inner part of the bay for collecting offshore data on July 16, August 20, September 16, October 12, and October 19. Measurements of

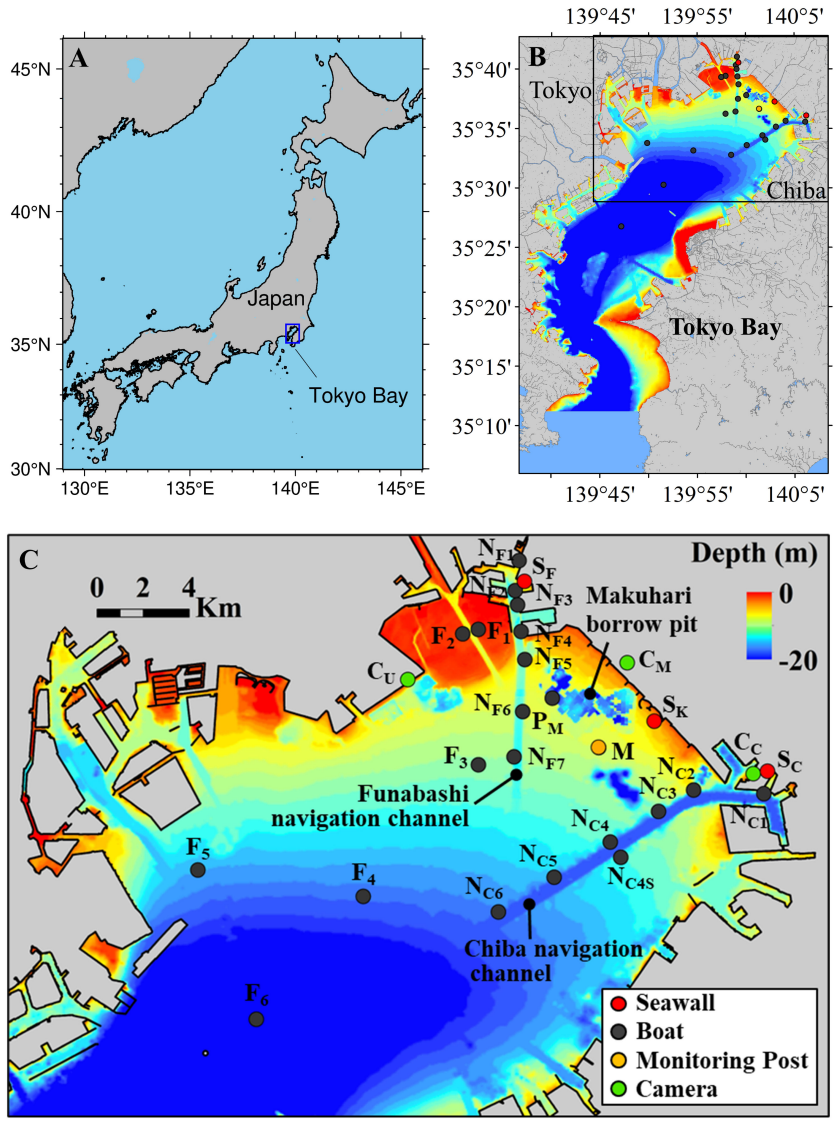

FIGURE 1
Map of Tokyo Bay with observation stations. **(A)** Location of Tokyo Bay in Japan. **(B)** The whole of Tokyo Bay. **(C)** Northern part of Tokyo Bay corresponding to the box in **(B)** with observation stations. The red filled circles of Stns. S_F, S_K, and S_C are buoy stations for continuous water quality monitoring adjoining to the seawall in Funabashi, Kemigawa, and Chiba, respectively. The gray filled circles are boat cruising stations: Stns. F_1 to F_6 are in flat bottoms; Stns. N_{F1} to N_{F7} are in the Funabashi navigation channel; N_{C1} to N_{C6} are in the Chiba navigation channel; Stn. P_M is in the off-Makuhari borrow pit. The green filled circles of Stns. C_U, C_M, and C_C are the fixed camera monitoring stations for observing seawater color at Urayasu, Makuhari, and Chiba, respectively. The yellow filled circule of Stn. M is a water quality monitoring station managed by MLIT.

the vertical profile of the same multiparameter water quality were conducted using a throw-in water quality meter (AAQ-RINKO 177, JFE Advantech) with an interval of 0.1 m. Water samples were collected using a 6000 mL of Van Dorn water sampler (5026-C, Rigo-sha) at the surface, middle, and bottom. The water samples were pre-processed following the same method described in the previous subsection.

2.2.3 Fixed camera monitoring

In order to capture the occurrence of blue tides at the bay head, we used high-rise towers of C_U (Tokyo Bay Tokyu Hotel, 60 m height, 35;38;18N 139;55;54E), C_M (APA Hotel & Resort Tokyo Bay Makuhari, 183.1 m height, 35;38;36N 140;2;12E), C_C (Chiba Port Tower, 125.2 m height, 35;36;0N 140;5;54E) and a fixed-point camera (SP108-J, HykeCam or KG770, Keep Guard)

were installed on the roof of each of the three towers and at the mooring observation points. Interval photography of the sea surface was conducted at 5-min intervals between sunrise and sunset.

2.2.4 Collecting archived data of MLIT

We collected a dataset of vertical profiles of hourly water quality at Stn. M (35;36;39N 140;1;24E) acquired by the website of MLIT. The items of temperature, salinity, turbidity, chlorophyll *a*, and DO were available at 1 m intervals, whereas pH was available only at the surface, middle, and bottom.

2.3 Analysis of carbonate parameters

For the analysis of TA and DIC of the water samples, hydrochloric acid titration was performed using a total alkalinity analyzer (ATT-05, Kimoto Electric Co., Ltd.). A closed-cell method, in which acid titration is performed in the presence of carbonate in seawater, was selected as the measurement method. This method focused on the relationship between the changes in DIC and TA due to hydrochloric acid titration. DIC and TA are determined based on the standard potential E0, which maximizes the coefficient of determination of the single regression equation in this relationship, and K1Factor, which is related to the acid dissociation constant. The DIC and TA are determined based on the standard potential E0 and the K1Factor related to the acid dissociation constant that maximize the coefficient of determination of the single regression equation in this relationship. By giving this optimum E0 to Nernst's equation, the pH before hydrochloric acid titration (calc. pH) is obtained. This calc. pH was used when calculating pCO_2, which is described later. During the analysis, the temperature in the laboratory was adjusted to approximately 20°C by air conditioning.

2.4 Estimation of TA using salinity

Since there is a strong correlation between TA and salinity, we considered a method to estimate TA from salinity. To obtain a continuous estimate of TA from salinity measured in our field observation and collected by MLIT, we examined the correlation between the salinity and TA of the water samples. Figure 2 shows the relationships between TA and salinity measurements for (A)

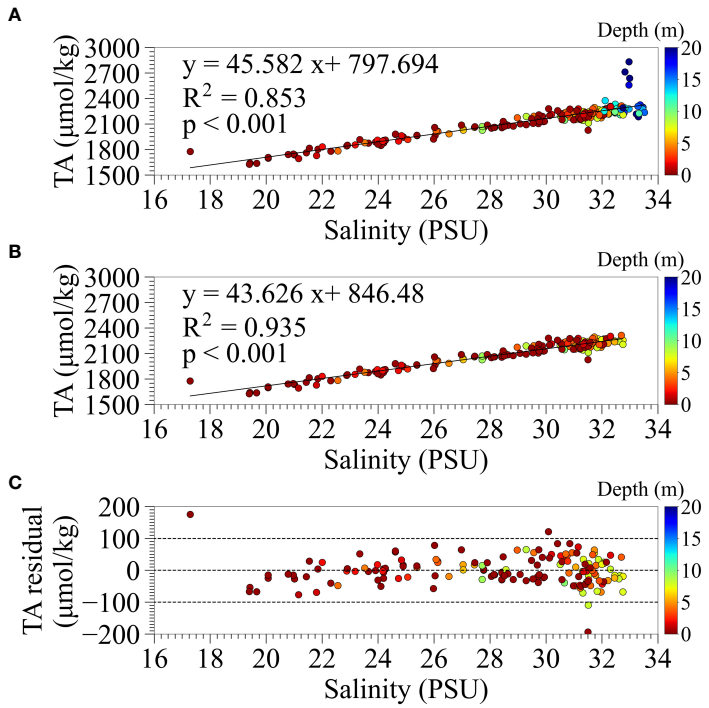

FIGURE 2
The relationship between TA and salinity measurements for **(A)** all water samples and **(B)** for samples shallower than 10 m in depth. **(C)** The residual from the measured TA and the estimated TA by the regression equation for samples shallower than 10 m in depth.

all water samples and (B) for the samples shallower than 10 m, and (C) the residual from the measured TA and the estimated TA by the regression for samples shallower than 10 m. There was a positive highlinear correlation between TA and salinity of all water samples except in the high-salinity range where TA values deviated significantly, taking higher than 2500 μmol/kg, and low-salinity range. The outliers in the high-salinity range were sampled deeper than 18 m in the borrow pit (Stn. P_M) under anoxic conditions. As shown in the middle panel of Figure 2B, the relationship between TA and salinity at depths shallower than 10 m was better fitted, which was used further in the present study. There was, however, one outliner in the lowest salinity of around 17 PSU. This sample was taken from the surface water at the far end of the Funabashi navigation channel (Stn. N_{F3}) on August 24 under normal conditions without upwelling, where the influence of river discharge was significant. There may be a limitation in estimating TA from salinity under low-salinity conditions directly influenced by river discharges.

2.5 Estimation of pCO_2

pCO_2 for each water sample was calculated using PyCO2SYS (Humphreys et al., 2022) from TA analysis values and calc. pH by ATT-05. We activated the option of the influence of sulfide as some samples contained sulfide generated under the anoxic condition. The required water temperature and salinity as input parameters were given as observed values at the time that the samples were taken. Among several choices for the values of parameters such as equilibrium constants, we selected the total scale for pH scale, Mojica Prieto and Millero (2002) for K_1 and K_2, Dickson (1990) for KHSO4, Lee et al. (2010) for B_T, and Dickson and Riley (1979) for KHF were selected. For samples in which sulfide ions were detected, pCO_2 was calculated taking sulfide concentrations into account.

Continuous pCO_2 was calculated using PyCO2SYS from continuously estimated TA using measured salinity explained in subsection 2.4 and measured pH. The adopted parameters and their values for PyCO2SYS were the same as those for water samples. The estimated pCO_2 were, however, found to be inconsistent with those of the corresponding water samples. As the major cause of the inconsistency was considered due to a bias of the continuously measured pH values, we developed a correlation equation between calc. pH obtained by ATT-05 under stable environmental conditions and the measured pH.

2.6 Estimation of CO_2 flux between the atmosphere and seawater

The commonly adopted bulk equation (1) was used to calculate the continuous CO_2 flux (F_{CO_2}) between the atmosphere and seawater at Stns. S_F, S_K, S_C, and Stn. M, where continuous water quality measurements were conducted.

$$F_{CO2} = kK_0(pCO_{2sw} - pCO_{2air}) \quad (1)$$

where K_0 is the solubility equilibrium constant for CO_2 (mol atm^{-1} kg^{-1}) using the formula (Weiss, 1974); pCO_{2sw} and pCO_{2air} are pCO_2 (μatm) in the surface water and atmosphere, respectively, and k is the piston velocity (cm/h) estimated by the following formula proposed by Wanninkhof (2014) updating that by Wanninkhof (1992);

$$k = 0.251 \times U_{10}^2 \left(\frac{S_c}{660}\right)^{-0.5} \quad (2)$$

where U_{10} is the wind speed at 10 m above the sea surface at Stn. M, and S_C is the Schmidt number for CO_2 (Jähne et al., 1974). Although the piston velocity may also be influenced by the current velocity and depth (Call et al., 2015), we did not consider them as the current velocity was not measured. The adopted formula may be acceptable supposing that the wind speed may influence more significantly than the current velocity as the observation was conducted at the bay head, where the current velocity is relatively weak. The pCO_{2air} was given as a constant (470 ppm) averaged over the shipboard observations on September 16, 2021, which was converted to pCO_{2air} by subtracting the vapor pressure at the Chiba Meteorological Observation Station, Japan Meteorological Agency. Following Orr et al. (2018) and using PyCO2SYS, we estimated propagated uncertainties for the CO_2 flux supposing the standard uncertainties for TA and pH of ATT-05 to be 2 μmol/kg and 0.01, respectively.

3 Results

3.1 Observed water quality at Stn. M by MLIT and occurrences of blue tide

Figure 3 shows the time series of observed wind vectors with the durations of blue tide occurrences, tidal heights, and water quality parameters at Stn. M from June to October 2021. The durations of blue tide occurrences were identified by visual and camera monitoring of sea color changes during field observations and as reported by Chiba Prefecture. The occurrences of blue tides in the inner part of Tokyo Bay were identified six times from mid-June to late October in 2021. Blue tides occur due to the upwelling of anoxic water containing hydrogen sulfide caused by the offshore-ward wind-driven current caused by the north-eastward wind. The scale and duration of the blue tides are related to the magnitude of the anoxic water mass prior to the onset and the wind direction and speed during the blue tide. The blue tides in early summer (June 17) and mid-autumn (October 14) before and after the strong

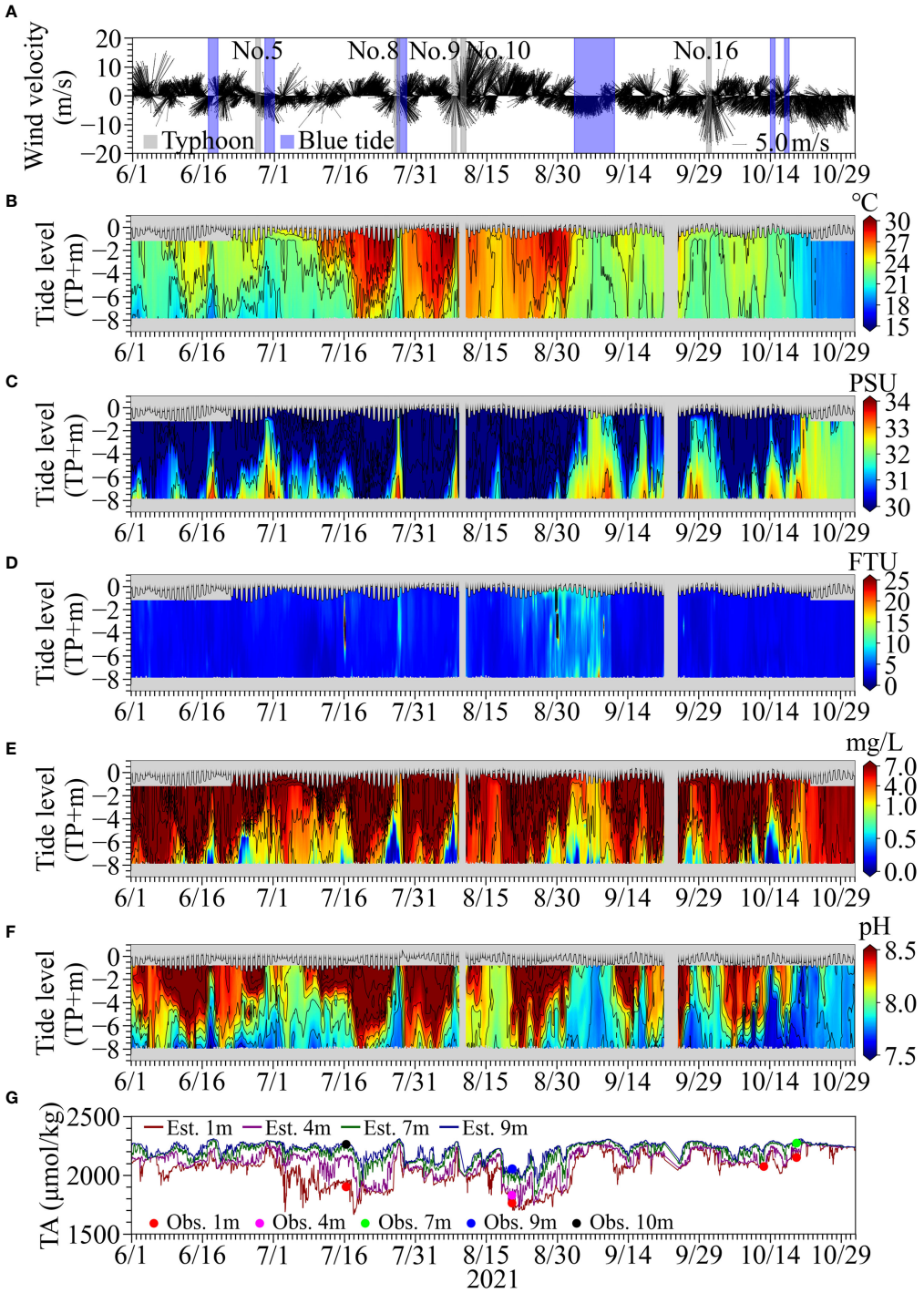

FIGURE 3
(A) Time series of observed wind vectors with the durations of the occurrences of blue tide (hatched in blue) and the events of typhoon approaching (hatched in gray). The time series of vertical profiles of **(B)** temperature, **(C)** salinity, **(D)** turbidity, **(E)** DO, and **(F)** pH, with tide level. **(G)** The time series of estimated TA using continuously observed salinity and measured TA using ATT-05 for water samples.

stratification and those (June 29 and July 27) during typhoon approaching were small and ceased within a couple of days due to the extensive water mixing. On the other hand, the blue tide from September 2 to 9 was the largest in 2021 caused by northerly weak continuous winds lasted for more than 1 week.

Sudden decrease in temperature and increase in salinity were observed when this largest blue tide occurred, which reflects the upwelling of the offshore dense bottom water. The turbidity became high, indicating the generation of particulate sulfur due to the oxidation of sulfide. DO and pH became lower as hypoxic and anoxic waters approached Stn. M.

The variation in TA was similar to that in salinity; higher TA was observed in deeper water. TA tended to become high and uniform in the vertical when the upwelling events occurred. The difference between the TA measured using ATT-05 minus the TA estimated from continuously observed salinity at nearby depths ranged from −27.2 μmol/kg to 4.4 μmol/kg (N = 6) at the surface, −48.0 μmol/kg (N = 1) at a depth of 4m, −68.0 μmol/kg (N = 1), −28.8 μmol/kg to 14.7 μmol/kg (N = 2) at 9-m depth, and −0.6 μmol/kg (N = 1) at 10-m depth. Although the estimated TA tended to be slightly higher than the observed values, the estimated TA values were generally consistent with the measured TA using ATT-05 for the corresponding water samples, suggesting the validity of the TA estimation method.

The blue tide occurred in early September was observed at our observation stations in the bay head. Figure 4 shows fixed camera photos at (A) Chiba Port (C_C), (B) Makuhari (C_M), and (C) Urayasu (C_U). Generally, blue tides in the bay are initiated by the upwelling of anoxic waters in the Funabashi and Chiba navigation channels due to the continuous blowing of northeasterly winds. The upwelling of the offshore bottom waters expands the blue tide area along the coast of the bay head. The intrusion of the offshore bottom waters with high density also causes pushing out the anoxic waters in borrow pits, thus enhancing the blue tide. Blue tides are often terminated by strong winds or a change in the wind direction, promoting mixing and dispersion of the blue tide waters. Our observed blue tide followed a similar pattern but lasted longer than usual due to persistent light northeasterly winds.

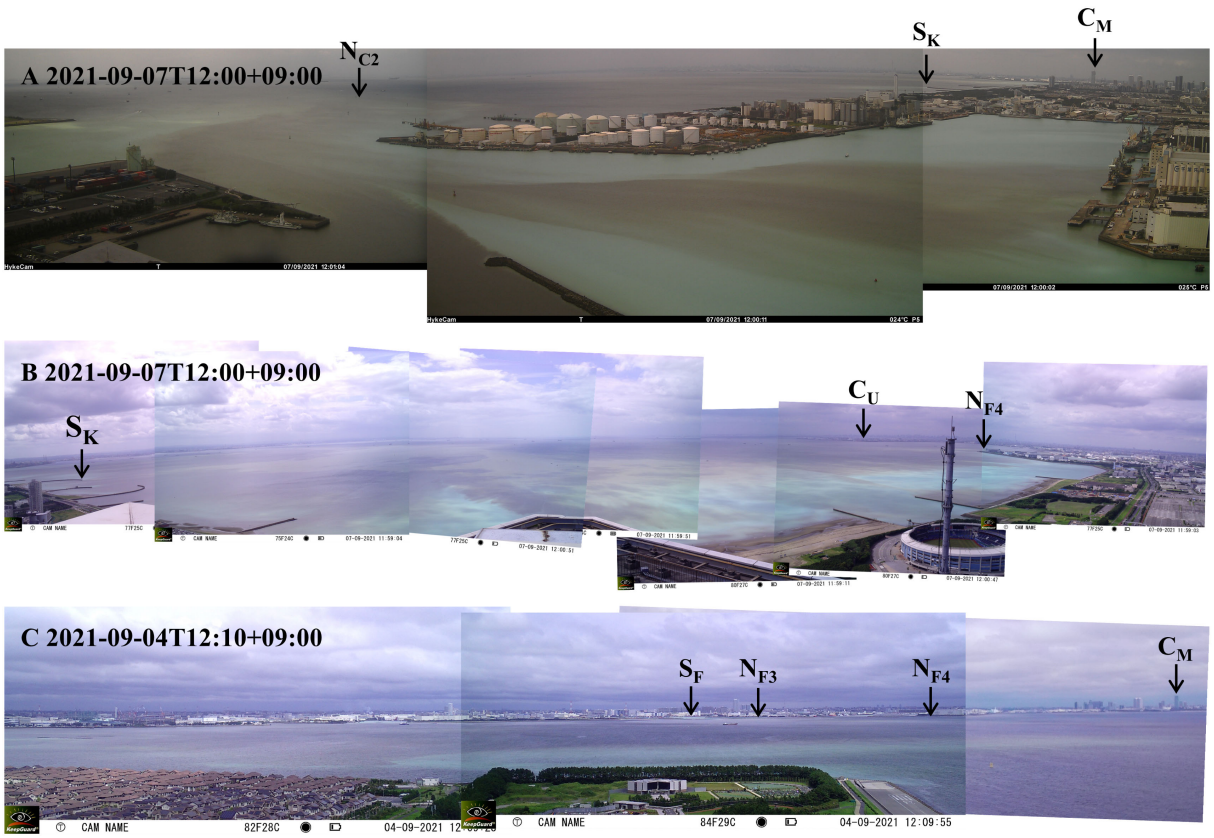

FIGURE 4
Fixed camera photos of the occurrence of blue tide in early September at **(A)** Stn. C_C, **(B)** Stn. C_M, and **(C)** Stn. C_U. The locations of some stations are specified in the photos.

3.2 Vertical profiles of water quality in navigation channel and borrow pit

Figures 5, 6 show that under normal conditions in August before the outbreak of blue tide, pCO_2 in the surface water was significantly less than 400 µatm, much lower than pCO_2 in the atmosphere, indicating the bay at the stations being the absorber of CO_2 under the stratified condition (Figures 5A, B, 6A–D). The TA values in the surface layer at this time were larger than those of the DIC, ranging approximately from 200 µmol/kg to 500 µmol/kg.

At the borrow pit (Stn. P_M), pCO_2 increased with increasing depth approximately from 1000 µatm at a depth of 10 m to greater than 4000 µatm at the bottom, where the waters were rather stagnant (Figures 5A, B). These pCO_2 were much higher than those in the atmosphere, suggesting potential high CO_2 emission to the atmosphere when these waters upwell. The difference between TA and DIC showed a decreasing trend, and DIC was higher than TA in the bottom layer, with a difference of more than 130 µ mol/kg. Although a similar trend was observed at the Funabashi navigation channel (Stn. N_{F3}), the pCO_2 in the bottom water varied significantly from approximately 3000 µ atm on July 16 to less than 1300 µatm on August 24 (Figures 6A–D). The waters in the navigation channel is considered more easily mobile than those in the borrow pit, resulting in a large variation in pCO_2. In contrast, the bottom layer pCO_2 at the flat bottom (Stn. M) with 10 m deep was around 1000 µatm, lower than the bottom waters at Stns. P_M and N_{F3} under normal conditions. However, pCO_2 in the bottom waters at the flat bottom was still much higher than that in the atmosphere, which is also considered causing potential large CO_2 emission.

The density stratification disappeared due to the occurrence of upwelling, and the upper layer became hypoxic in September 2 (Figures 6E–H). In the surface layer, turbidity increased with the onset of blue tide, and pCO_2 in the surface layer increased to approximately 1200 µatm at Stn. N_{F3} on September 3. The pCO_2 on September 2 was the maximum value of just under 3000 µatm observed in the middle layer.

3.3 Observed continuous water quality during blue tide

At Stn. S_F, the surface layer became anoxic on September 2 and continued until September 11 (Figure 7A). The slight

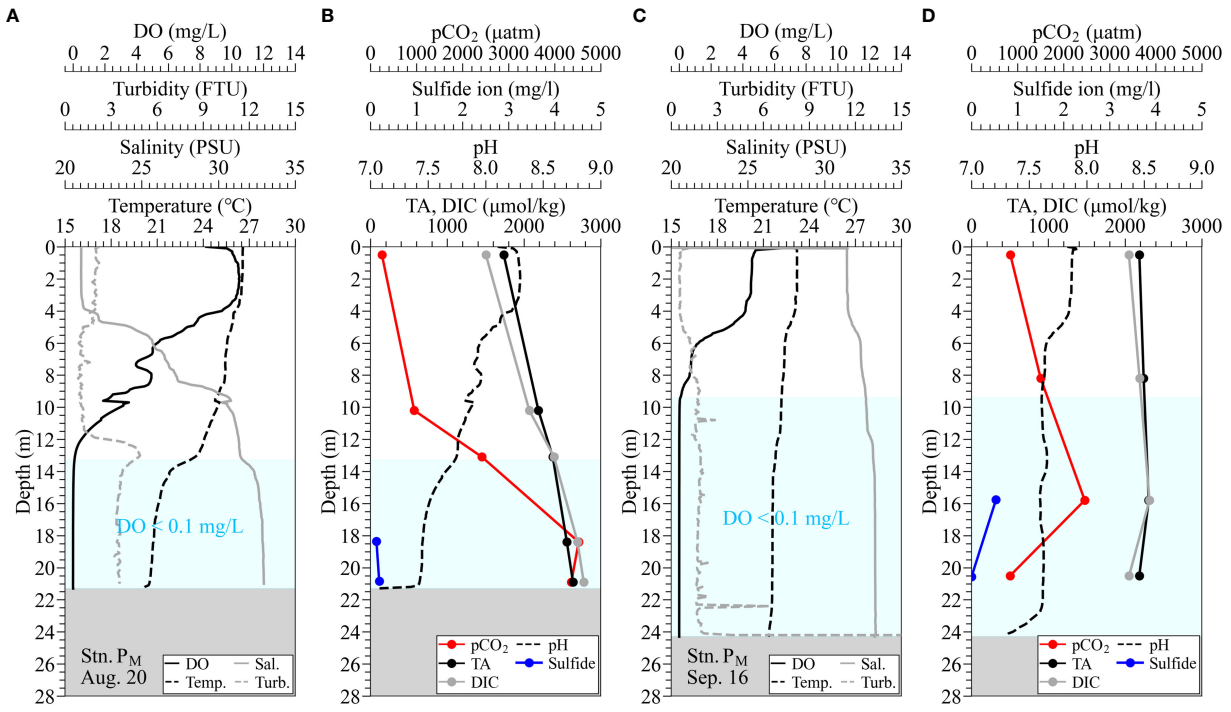

FIGURE 5
Observed vertical profiles of water quality of temperature, salinity, turbidity, DO, and pH using AAQ-RINKO, measured TA, DIC, total sulfide for water samples, and estimated pCO_2 at the borrow pit (Stn. P_M). Panels **(A, B)** are under normal conditions on August 20; panels **(C, D)** are during the upwelling on September 16. Hatched boxes in light blue denote hypoxic water with DO of below 0.1 mg/L.

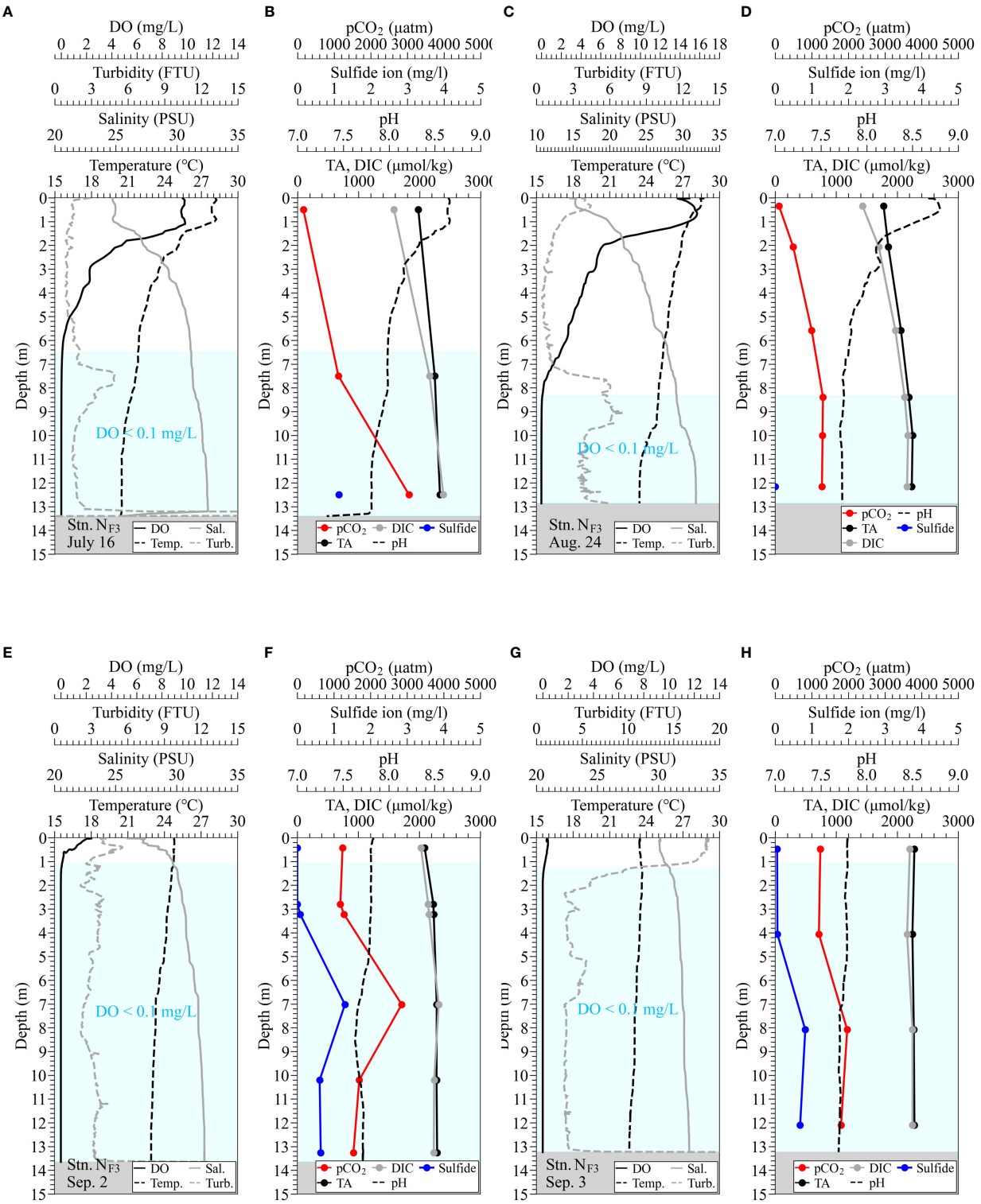

FIGURE 6
Observed vertical profiles of water quality of temperature, salinity, turbidity, DO, and pH using AAQ-RINKO, measured TA, DIC, and total sulfide for water samples, and estimated pCO_2 at the Funabashi navigation channel (Stn. N_{F3}). Panels **(A, B)** are under normal conditions on July 16; panels **(C, D)** are under normal conditions on August 24. Panels **(E, F)** are during the upwelling on September 2; panels **(G, H)** are during the blue tide on September 3. Hatched boxes in light blue denote hypoxic water with DO below 0.1 mg/L.

increase in DO observed on September 5 was found to correspond to the weakening of the discoloration of the surface water caused by the blue tide according to the fixed camera photos. A decrease in DO was also observed after September 15, which was considered a reoccurrence of upwelling associated with the northerly wind, but did not lead to a significant blue tide (Figure 7A).

At Stn. S_C, anoxia of the surface water was observed from around September 3, delayed by the Stn. S_F, and a temporary increase in DO was observed on September 4, which continued until the afternoon on September 8 (Figure 7C). At Stn. S_K, hypoxia in the surface water was observed from the afternoon on September 5, which did not lead to anoxia. The pH in the surface water during the onset of the blue tide decreased from 8.0 to 7.8 at Stn. S_F while remained at about 8.0 at Stn. S_C (Figure 7D). At Stn. S_K, although the recording was stopped midway due to a malfunction of the pH meter, the pH was found to drop below 7.9. The respective differences in TA measured using the ATT-05 in the surface and bottom layers minus TA estimated from continuously observed salinity ranged from −193.9 µmol/kg to 83.7 µmol/kg (N = 8) and from −0.65 µmol/kg to 63.5 µmol/kg (N = 6) at Stn. S_F, from −48.8 µmol/kg to 30.9 µmol/kg (N = 6) and from −19.0 µmol/kg to 20.9 µmol/kg (N = 5) at Stn. S_K; from −50.4 µmol/kg to 54.1 µmol/kg (N = 7) and from −9.5 µmol/kg to 63.7 µmol/kg (N = 6) atStn. S_C (Figures 7E–G). The TA values at Stn. S_F in the surface and bottom waters were approximately 1700 and 2000 µmol/kg before the occurrence of blue tide, showing a difference between the surface and bottom. During the onset of the blue tide, TA in both the surface and bottom waters increased; the difference between them became smaller, ranging from 2200 to 2300 µmol/kg. After September 10, TA showed a gradual decreasing trend and decreased faster in the surface water than in the bottom water. TA, however, did not immediately recover to the level before the blue tide and remained at 2000 µmol/kg a couple of days later. At Stn. S_K, the TA values ranged from 1800 µmol/kg to 1900 µmol/kg in the surface water and more than 2100 µmol/kg in the bottom water before the blue tide. On September 6, the peak of the blue tide at Stn. S_K, both the surface and bottom waters had TA values of more than 2250 µmol/kg. At Stn. S_C, the TA values were around 1900 µmol/kg in the surface water and 2000 to 2200 µmol/kg in the bottom water before the onset of the blue tide, showing a slightly higher tendency than at the other stations. During the onset of the blue tide, the values in both the surface and bottom waters ranged from 2200 to 2300 µmol/kg, similar to those at the other stations.

3.4 Estimation of pCO_2 and CO_2 flux using continuous pH measurements

The estimated continuous pCO_2 values were found to be consistent with the calculated values based on the water sampling analysis using ATT-05 (see Figures 8, 9), suggesting that our continuous pCO_2 estimation method is practical and feasible by correcting the continuously observed pH values appropriately. The pCO_2 in the surface water increased during the upwelling of anoxic water at all stations, with maximum values ranging from 1200 to 1400 µatm at Stns. S_K and S_C, and more than 2000 µatm at Stn. S_F. The pCO_2 in the surface water at Stn. M by MLIT also tended to increase during the same period but at lower values of around 600 µatm than at our three stations. This is considered that the upwelled water released pCO_2 into the atmosphere as it spread offshore, and also was mixed with originally existed surface water with lower pCO_2.

Continuous estimates of CO_2 fluxes at Stns. S_F and S_C showed absorption and emission trends before and after noon on September 1, respectively, due to the upwelling and subsequent blue tide (see Figures 8D, E). The mean CO_2 fluxes during the absorption (normal) period were estimated to be −413 µmol m^{-2} h^{-1} and −491 µmol m^{-2} h^{-1} at Stns. S_F and S_C, respectively. The mean CO_2 fluxes during the emission (upwelling) period were estimated to be 2153 µmol m^{-2} h^{-1} and 1540 µmol m^{-2} h^{-1} at Stns. S_F and S_C, respectively. The absorption trend at Stn. M was similar to those at Stns. S_F and S_C before the onset of the blue tide (see Figure 9B). A slight emission trend was observed during the blue tide, but the degree of emission was estimated to be minor compared to those at Stns. S_F and S_C.

Estimated propagated uncertainties for CO_2 flux were between 1.1 and 17.5 µmol m^{-2} h^{-1} at Stn. S_F and between 1.1 and 18.2 at Stn. S_C during the absorption period, whereas they were between 11.4 and 60.2 at Stn. S_F and between 12.1 and 34.2 at Stn. S_C during the emission period. These uncertainties were around three percent or less of the typical magnitude of CO_2 flux.

4 Discussion

4.1 Practical TA and pCO_2 estimation for blue tides

We investigated a practical method for continuous estimation of pCO_2 using TA and pH especially targeting surface waters during upwelling of hypoxic and anoxic waters, including blue tides. It is thus important to evaluate the accuracy of estimated TA from salinity and measured pH and their respective contributions to the estimation of pCO_2 in such specific environments.

The measured TA is thought to include the influences of the conservative mixing of freshwater and open ocean water and biogeochemical processes such as photosynthesis, organic matter degradation, and calcification (Jiang et al., 2014). Surface waters in the open ocean and inner bays generally have a high linear correlation between TA and salinity (Lee

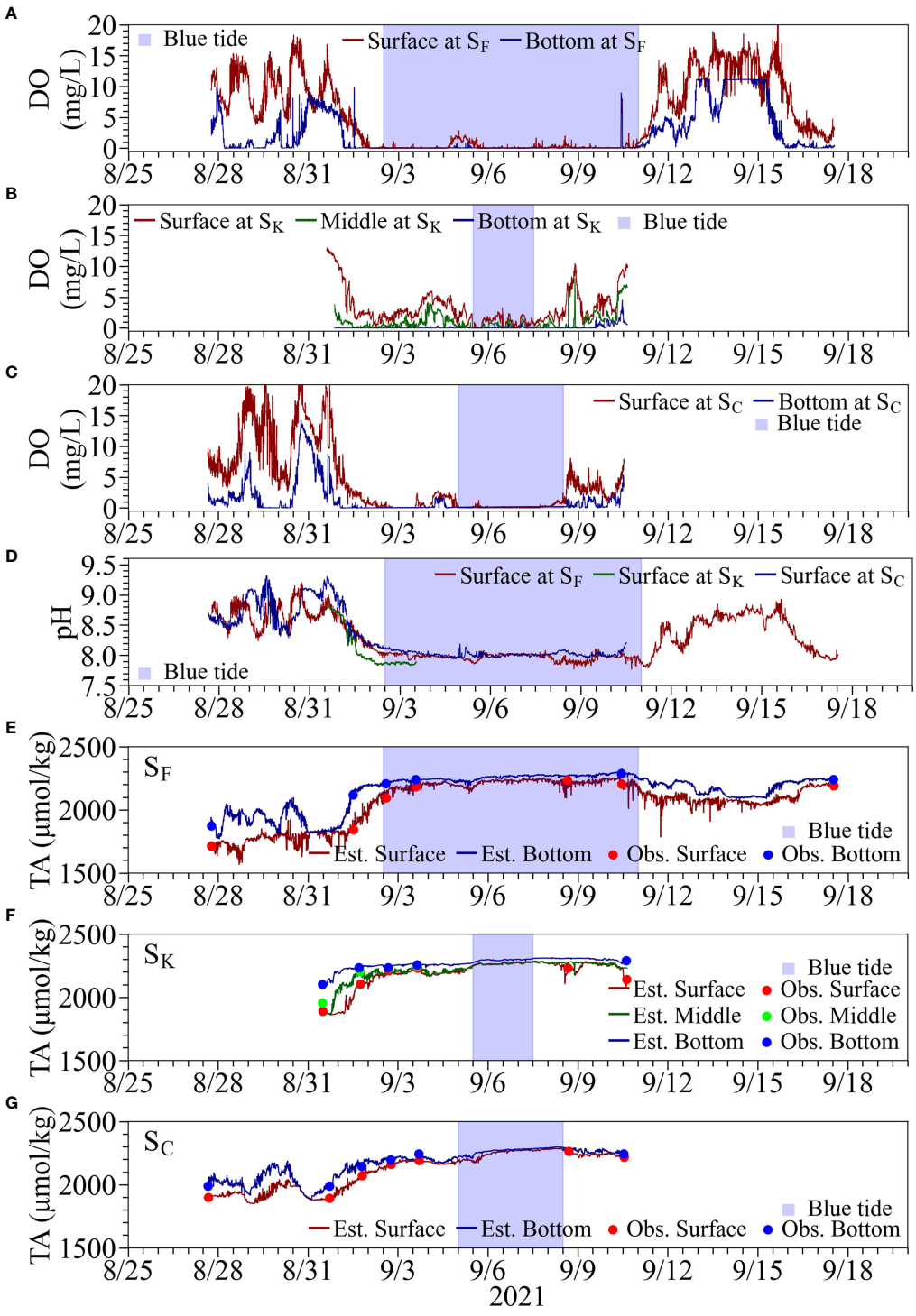

FIGURE 7
Time series of water quality at Stns. S_F, S_K, and S_C. Top three panels are observed DO at the surface and bottom, at **(A)** Stn. S_F, **(B)** Stn. S_K, and **(C)** Stn. S_C. Panel **(D)** shows observed surface pH. The bottom three panels are observed (solid lines) and estimated (filled circles) TA at the surface and bottom at **(E)** Stn. S_F, **(F)** Stn. S_K, and **(G)** Stn. S_C.

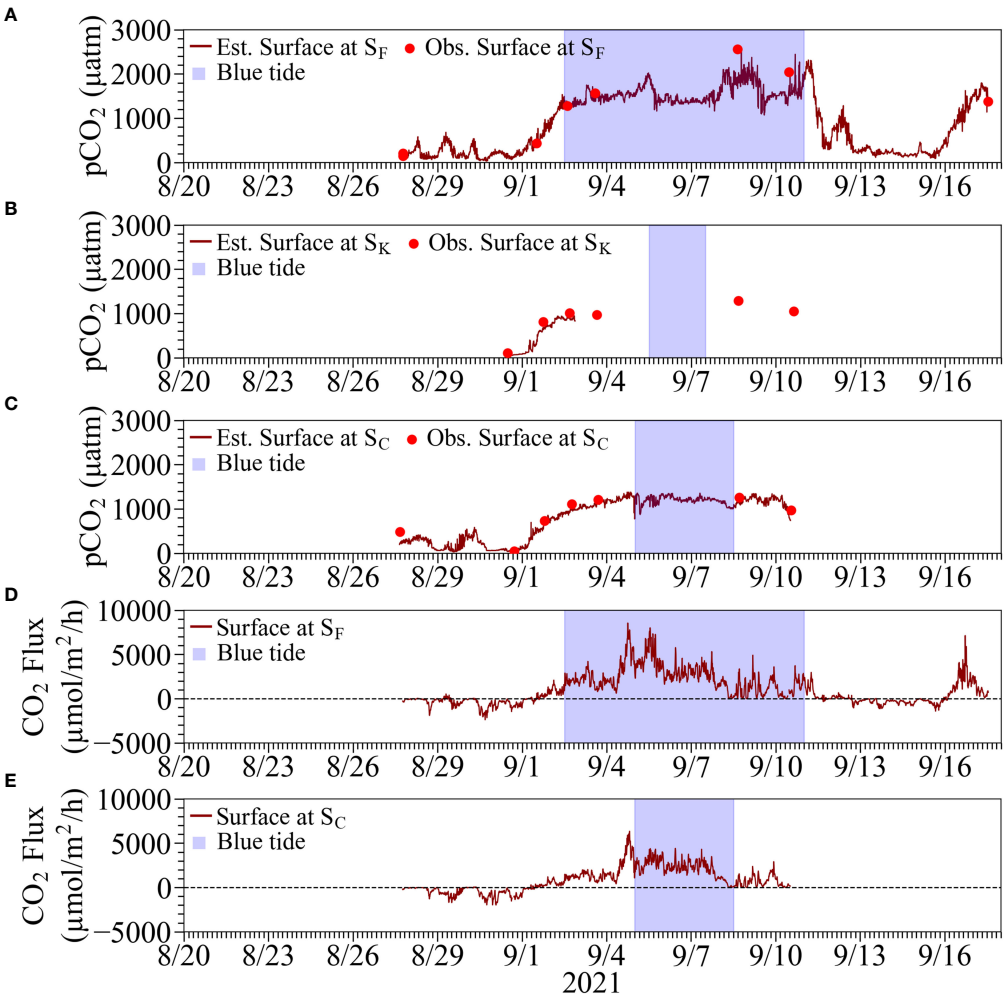

FIGURE 8
Top three panels are comparisons of estimated continuous pCO_2 from the corrected continuous pH and calculated pCO_2 from the measurements of the corresponding water samples using ATT-05 at **(A)** Stn. S_F, **(B)** Stn. S_K, and **(C)** S_C. Bottom two panels are estimated CO_2 flux at the sea surface (positive value denotes emission) at **(D)** Stn. S_F and **(E)** S_C. Results at Stn. S_K were omitted because of the considerable suspension of measurements. The blue tide durations are denoted by hatched boxes in blue.

et al., 2006; Najjar et al., 2020). A high correlation between TA and salinity has also been reported in Tokyo Bay under normal conditions without blue tides (Taguchi et al., 2009). This means that the biogeochemical effect on measured TA is small and almost entirely determined by non-biochemical effects. In this study, a high correlation was observed in surface water, even during the blue tide, strongly influenced by organic matter decomposition (Figure 2). There are, however, some limitations in the estimation of TA, including the slight overestimation and some outliers in the anoxic bottom waters and surface waters with low salinity, as mentioned in subsection 2.4, which should be considered in future research.

The high correlation between TA and salinity, even during the blue tide, is considered the dilution effect of the surface water. Blue tides are caused by the reaction of hydrogen sulfide with oxygen in the surface water to form particulate sulfur during the upwelling of anoxic waters. Therefore, when the water reached the surface, it may have mixed with the original surface water. Figure 6 shows that TA increased rapidly in the anoxic waters at Stn. P_M, the borrow pit, and Figure 2 also shows that TA deviates from the regression line in the bottom layer. This means that biogeochemical effects cannot be neglected in the stagnant anoxic water. However, Figure 7 shows that the measured and estimated TAs of the surface layer were generally consistent even during the blue tide. These results suggest that the biogeochemical effects were minor when the anoxic water reached the surface, due to dilution by the abundant seawater.

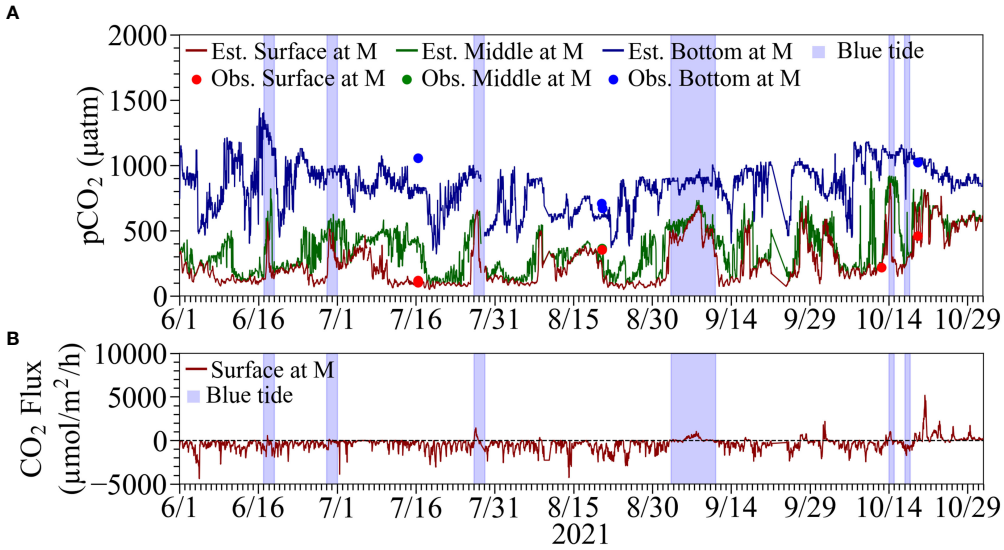

FIGURE 9
(A) Comparisons of estimated continuous pCO_2 from the corrected continuous pH and calculated pCO_2 from the measurements of the corresponding water samples using ATT-05 at Stn. M. **(B)** Estimated CO_2 flux at the sea surface (positive values denote emission) at Stn. M. The blue tide durations are denoted by hatched boxes in blue.

The estimated pCO_2 was found to more sensitive to a change in pH than that in TA especially during upwelling events due to the appearance of a significant decrease in pH. The accuracy of observed *in situ* pH thus plays a key role in obtaining reasonable pCO_2 estimation results. However, the accuracy of self-recording pH sensors for continuous monitoring is considered a challenge. In fact, continuous observations of pH were not suitable for direct use in estimating pCO_2. This is because pH meters moored in the field generally do not meet the accuracy requirements for pCO_2 estimation. It is necessary to correct this by using a higher-accuracy pH meter. We showed that a practical continuous estimation of pCO_2 was possible by calibrating *in situ* pH meter values using the high-precision pH meter of ATT-05 on water samples. The pCO_2 of the water samples can be estimated by inputting two of the three parameters of pH, TA, and DIC measured by ATT-05 into PyCO2SYS; we confirmed that the calculated pCO_2 values from any two of the three parameters were consistent with each other.

Figure 10 shows the difference in calculated pCO_2 using measured pH and TA for the water samples containing sulfide with and without the consideration of its influence in PyCO2SYS; the pCO_2 is considered overestimated without considering the effect of sulfide (Xu et al., 2017). The difference in pCO_2 was less than 1 µatm at sulfide detection limit of 0.05 mg/L, whereas it was less than 20 µatm at sulfide concentrations of less than 1 mg/L, which were typical in our observation. The time series of pCO_2 calculated by estimated TA and pH did not include the effect of sulfide in the surface layer (Figure 8). However, the concentration of sulfide in the surface layer during the onset of the blue tide was almost zero (Figure 6), suggesting that the error in pCO_2 with and without the consideration of sulfide is small.

Although the estimated results in Figure 8 generally reproduces the variation in pCO_2, a relatively large discrepancy was observed in the surface water at Stn. S_F on September 8 during the blue tide (see Figure 8). This discrepancy was attributed to the significant difference between the pH of the water sample (7.309) and the corrected observed pH (7.487), which may have been caused by the freshwater effect specifically observed in the thin surface layer. Another reason for the underestimation of pCO_2 was that the blue tide in Funabashi

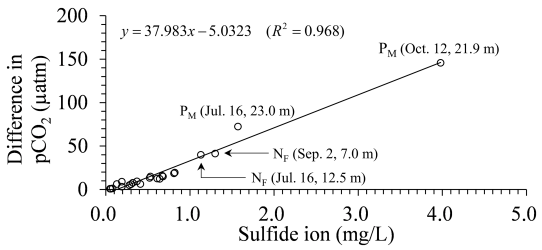

FIGURE 10
Difference in calculated pCO_2 using measured pH and TA for water samples containing sulfide with and without the consideration of its influence.

was the largest in scale, and the TA estimated from salinity was affected by internal production. However, the increasing pCO_2 process before and during the blue tide and the decreasing process after the end of the blue tide were well reproduced. Therefore, the pCO_2 estimation method developed in this study is considered practical.

However, for the bottom layer at Stn. M on July 16, the number of samples used for the correction was limited, and the pH sensor calibration interval was long, ranging from 2 weeks to 1 month, suggesting that a single regression equation may not have been sufficient. Further study is needed to establish a continuous estimation method of pCO_2 over a long period from seasonal to annual variations, considering the balance between accuracy and cost.

4.2 Relationship between DIC, TA, and estimated pCO_2 for water samples

In the estimation of pCO_2, very high values were found in the bottom layer of the borrow pit (e.g., see Figure 5). Using the dataset of TA, DIC, and pH measured by ATT-05 for water samples, we considered coarbonate dynamics, including pCO_2.

The vertical distribution of pCO_2 at Stn. P_M showed values exceeding 1000 µatm at a depth of 10 m and values exceeding 4000 µatm in the bottom layer (Figure 5). Also, at Stn. N_{F3}, pCO_2 in the anoxic water always exceeded 1000 atm (Figure 6). It is known that a high TA/DIC ratio results in a low CO_2/DIC ratio tending to a sink for atmospheric CO_2, whereas a low TA/DIC results in a high CO_2 emission tendency. The carbonate buffering capacity is intensified under a larger TA, leading to a smaller decrease in pH with CO_2 dissolution and more capacity for storing pCO_2 (Egleston et al., 2010). The TA/DIC ratios at the surface layers of Stn. P_M and Stn. N_{F3} under normal conditions were 1.155 and 1.252, and the corresponding pCO_2 were 242 and 160 µatm, respectively (Figures 5B, 6A–D). This means that the carbonate buffering capacity was strong, and the water was a sink of the atmospheric pCO_2. On the other hand, the TA/DIC ratios of the bottom layers at Stn. P_M and Stn. N_{F3} under normal conditions were 0.950 and 0.977, respectively, and pCO_2 exceeded 3000 µatm (Figures 5A, 6A–D). Under normal conditions, the TA/DIC ratio decreased with approaching the bottom, indicating that the area adjacent to the bottom sediment contained high pCO_2 due to the decomposition of organic matter under the stagnant condition.

Figure 11 shows the relationship between DIC and TA for all water samples and calculated pCO_2 using PyCO2SYS considering the influence of sulfide. TA values were higher than DIC for most of the samples. DIC values were higher than TA at the bottom of the navigation channel and borrow pit where sulfides were detected during normal times without blue tide, and at the middle to lower waters where sulfides were detected during the blue tide; pCO_2 values in these waters were higher than 2000 µatm. During the blue tide outbreak, the TA/DIC ratios in the surface layer were 1.029 and 1.034, which were much lower than the values of 1.252 and 1.240 under the normal condition, indicating that the carbonate buffering capacity was weaker (Figures 5D, 6E–H) and thus increasing pCO_2. This is due to the upwelling of anoxic waters affected by organic matter decomposition during the onset of the blue tide. Therefore, during blue tide outbreaks, there was a tendency of high CO_2 emissions.

Next, we discuss the uniformity of carbonate-chemistry parameters in hypoxic and anoxic waters. First, Figures 5, 6 show that the pH at Stn. P_M was lower than 7.7 in anoxic water, whereas the pH at Stn. N_{F3} was higher than that at Stn. P_M, ranging from 7.7 to 8.0. The bottom layer at Stn. P_M on August 20 recorded extremely high pCO_2 with a DIC of 2778 µmol/kg and a TA of 2638 µmol/kg (Figure 5A). On the other hand, on September 16, after the end of the blue tide, pCO_2 rapidly decreased at a depth of 20.54 m (Figure 5D) with a DIC of 2053 µmol/kg and a TA of 2186 µmol/kg in the bottom layer. Even at Stn. N_{F3}, the pCO_2 under normal conditions on July 16 and August 24 was different. This suggests that carbonate-chemistry parameters in the anoxic waters were not uniform and that the bottom waters in the pit and navigation channel were moved during upwelling.

From Figure 5A, the highest pCO_2 was recorded at a depth of 18.35 m, which contained almost no sulfide. By contrast, changes in sulfide corresponded well with those in pCO_2 during the onset of the blue tide (Figures 6E–H). This suggests that DIC and TA fluctuated in the bottom layer under the influence of organic matter decomposition, but the decomposition pathways contributing to the fluctuations were

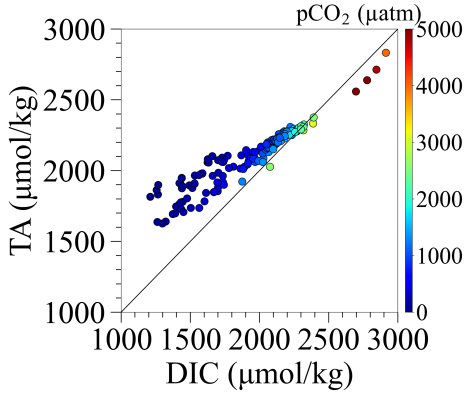

FIGURE 11
The relationship between measured DIC and TA for water samples and calculated pCO_2 from calc. pH and TA.

spatiotemporally different. As a result, carbonate-chemistry parameters in the anoxic water varied widely. Figure 8 also shows that pCO_2 in the surface layer at Stns. S_K and S_C increased even before the onset of the blue tide, indicating that the high pCO_2 values were influenced by organic matter decomposition other than sulfate reduction.

4.3 Impact of blue tide on CO_2 emission

Although surface pCO_2 at the time of upwelling tended to increase at all stations in the bay head, the CO_2 flux suggested that the tendency to release CO_2 to the atmosphere was particularly significant in the period when the blue tide occurred (Figures 8D, E, 9B). These are confirmed by comparing the mean values of CO_2 flux at Stns. S_F and S_C during the emission periods with and without the blue tide as shown in Table 1. The table also shows results using other literature formulas for the piston velocity (Ho et al., 2006; Jiang et al., 2008) not including current speed, which is currently not available. Their results varied, but the absorption and emission trends were consistent among the formulas. Using the formula from Wanninkhof (2014), the CO_2 emissions with blue tide were +2391 μmol m^{-2} h^{-1} between noon on September 2 and 0:00 a.m. on September 11 at Stn. S_F and +2193 μmol m^{-2} h^{-1} between 0:00 a.m. on September 5 and noon on September 8 at Stn. S_C, whereas those without blue tide were +809 and +1124 μmol m^{-2} h^{-1} at Stns. S_F and S_C, respectively. These results suggest that the CO_2 emission was significantly greater with the occurrence of blue tides than without it during the emission period.

At Stn. S_F, where higher pCO_2 was observed, turbidity, which is highly correlated with sulfur concentration causing blue tide discoloration, remained higher than at Stn. S_C throughout the observation period (Figure 8). The surface water at Stn. S_F has considered affected by the upwelled waters from the Funabashi navigation channel and off-Makuhari borrow pit. In these waters, the stratification had been intensified during summer with little oxygen supply, whereas the DIC generated by organic matter decomposition accumulated below the pycnocline, which could be a cause of the appearance of extremely high DIC. In addition, the appearance of hydrogen sulfide decreased pH and increased the portion of pCO_2. This suggests that blue tides with higher sulfur concentrations have higher pCO_2 and a stronger tendency to emit to the atmosphere.

Figure 12 shows the time series of pH, TA, and DIC, and calculated pCO_2 using PyCO2SYS at the surface, middle (6–8 m deep), and bottom at Stn. N_{F3}. The values of these parameters in the surface layer at the time of the blue tide on September 3 were similar to those in the bottom layer on August 24, just before the onset of the blue tide. Therefore, it is considered that the water masses in the bottom layer upwelled while preserving these water quality parameter values. At Stn. N_{F6}, outside the harbor area and located offshore of Stn. N_{F3}, the conservative trend was not clearly seen, suggesting that the dilution effect was dominant. In the innermost part of the harbor, the upwelling of bottom anoxic water to the surface with relatively weak dilution is suggested to contribute significantly to the release of CO_2 to the atmosphere.

Urban bays are expected to be atmospheric CO_2 sinks due to abundant nutrient inputs leading to high primary production and advanced sewage treatment (Kuwae et al., 2016). In particular, Tokyo Bay has been reported to be a year-round atmospheric CO_2 sink because sewage treatment removes labile organic matter more efficiently than nutrient species (Kubo et al., 2017; Tokoro et al., 2021). However, these studies did not adequately account for the effect of the upwelling of anoxic

TABLE 1 Estimated CO_2 fluxes (μmol m^{-2} h^{-1} at Stns. S_F and S_C during the absorption and emission periods using piston velocities from severalliterature sources.

	Absorption		Emission		With blue tide		Without blue tide	
Periods	**-2021-9-1 12:00:00**		**2021-9-1 12:00:00-2021-9-11 12:00:00**		**2021-9-2 12:00:00-2021-9-11 00:00:00**		**2021-9-1 12:00:00-2021-9-2 12:00:00, 2021-9-11 00:00:00-2021-9-11 12:00:00**	
Stations	**Stn. S_F**	**Stn. S_C**	**Stn. S_F**	**Stn. S_C**	**Stn. S_F**	**Stn. S_C**	**Stn. S_F**	**Stn. S_C**
Wanninkhof (2014)	-413	-491	2153	1540	2391	2193	809	1124
Ho et al. (2006)	-437	-520	2282	1632	2534	2324	858	1191
Jiang et al. (2008)	-555	-649	3136	2163	3431	2917	1474	1683
Average of References	-468	-553	2524	1778	2785	2478	1047	1333

The emission period is divided into two periods with and without the occurrence of the blue tide.

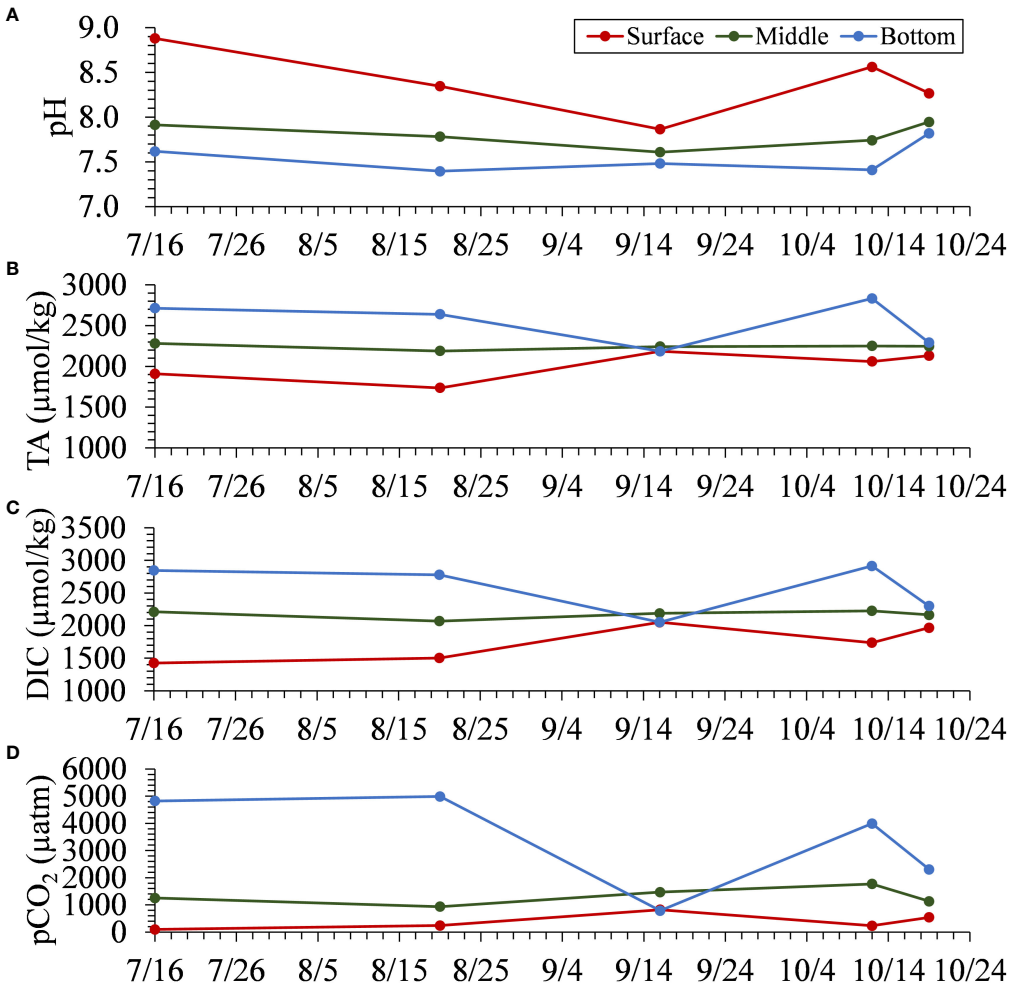

FIGURE 12
The time series of observed **(A)** pH, **(B)** TA, and **(C)** DIC at the surface, middle, and bottom. **(D)** The time series of calculated pCO_2 for water samples collected at the surface, middle, and bottom at Stn. N_{F3}.

water masses. In this study, we show that pCO_2 was highly elevated in the surface layer during the onset of blue tides and that CO_2 tended to be highly emitted during this period. Because blue tides are localized events that occur at the head of the bay during the summer and autumn, their annual impact on the entire bay may be small. However, it is known that anoxic waters develop in the bay from spring to autumn (Ando et al., 2021), and CO_2 in the hypoxic and anoxic waters may be rapidly released into the atmosphere in autumn when the stratification is destroyed. In the future, it is necessary to accumulate high-resolution spatiotemporal data to clarify the exact annual carbon budget in the bay.

Data availability statement

The raw data supporting the conclusions of this article will be made available by the authors, without undue reservation.

Author contributions

JS (PI) and ME conceived the ideas. ME and YZ collected and analyzed data. ME and JS wrote the manuscript. WN contributed to the discussion. All authors contributed to the article and approved the submitted version.

Funding

This study was funded by Yokohama Port and Airport Technical Research Office, Kanto Regional Development Bureau, Ministry of Land, Infrastructure, Transport and Tourism and JSPS KAKENHI Grant Number JP20H02250.

Acknowledgments

We are grateful to Dr. Toru Endo at Osaka Metropolitan University and Dr. Sosuke Otani at Osaka Metropolitan University College of Technology for their valuable comments in JSPS KAKENHI project on urban blue carbon. Supplementary Material templates can be found in the Frontiers LaTeX folder.

Conflict of interest

The authors declare that the research was conducted in the absence of any commercial or financial relationships that could be construed as a potential conflict of interest.

Publisher's note

References

Amunugama, M., and Sasaki, J. (2018). Numerical modeling of long-term biogeochemical processes and its application to sedimentary bed formation in Tokyo Bay. *Water* 10 (5), 572. doi: 10.3390/w10050572

Ando, H., Maki, H., Kashiwagi, N., and Ishii, Y. (2021). Long-term change in the status of water pollution in Tokyo Bay: Recent trend of increasing bottom-water dissolved oxygen concentrations. *J. Oceanogr* 77, 843–858. doi: 10.1007/s10872-021-00612-7

Aoki, K., Shimizu, Y., Yamamoto, T., Yokouchi, K., Kishi, K., Akada, H., et al. (2022). Estimation of inward nutrient flux from offshore into semi-enclosed sea (Tokyo Bay, Japan) based on *in-situ* data. *Estuarine Coast. Shelf Sci.* 274, 107930. doi: 10.1016/j.ecss.2022.107930

Benallal, M., Moussa, H., Lencina-Avila, J., Touratier, F., Goyet, C., Jai, M. E., et al. (2017). Satellite-derived CO_2 flux in the surface seawater of the austral ocean south of australia. *Int. J. Remote Sens.* 38 (6), 1600–1625. doi: 10.1080/01431161.2017.1286054

Breitburg, D., Levin, L. A., Oschlies, A., Grégoire, M., Chavez, F. P., Conley, D. J., et al. (2018). Declining oxygen in the global ocean and coastal waters. *Science* 359 (6371), eaam7240. doi: 10.1126/science.aam7240

Breithaupt, J. L., Smoak, J. M., Smith, T. J.III, Sanders, C. J., and Hoare, A. (2012). Organic carbon burial rates inmangrove sediments: Strengthening the global budget. *Global Biogeochem Cycles* 26, GB3011. doi: 10.1029/2012GB004375

Call, M., Maher, D., Santos, I., Ruiz-Halpern, S., Mangion, P., Sanders, C., et al. (2015). Spatial and temporal variability of carbon dioxide and methane fluxes over semi-diurnal and spring–neap–spring timescales in a mangrove creek. *Geochimica Cosmochim Acta* 150, 211–225. doi: 10.1016/j.gca.2014.11.023

Diaz, R. J., and Rosenberg, R. (2008). Spreading dead zones and consequences for marine ecosystems. *Science* 321 (5891), 926–929. doi: 10.1126/science.1156401

Dickson, A. G. (1990). Standard potential of the reaction: AgCl(s) + 12H2(g) = Ag(s) + HCl(aq), and and the standard acidity constant of the ion HSO4− in synthetic sea water from 273.15 to 318.15 K. *The Journal of Chemical Thermodynamics*, 22(2), 113–127. doi: 10.1016/0021-9614(90)90074-Z

Dickson, A. G., and Riley, J. P. (1979). The estimation of acid dissociation constants in sea-water media from potentiometric titrations with strong base. II. The dissociation of phosphoric acid. *Marine Chemistry* 7, 101–109. doi: 10.1016/0304-4203(79)90002-1

Dickson, A. G., Sabine, C. L., and Christian, J. R. (2007). Guide to best practices for ocean CO_2 measurements. PICES special publication 3. IOCCP report 8 , 191pp. DICKSON2007.

Duarte, C. M., and Krause-Jensen, D. (2017). Export from seagrass meadows contributes to marine carbon sequestration. *Front. Mar. Sci.* 4. doi: 10.3389/fmars.2017.00013

Egleston, E. S., Sabine, C. L., and Morel, F. M. M. (2010). Revelle revisited: Buffer factors that quantify the response of ocean chemistry to changes in dic and alkalinity. *Global Biogeochem cycles* 24, GB1002. doi: 10.1029/2008GB003407

Feely, R. A., Sabine, C. L., Hernandez-Ayon, J. M., Ianson, D., and Hales, B. (2008). Evidence for upwelling of corrosive "acidified" water onto the continental shelf. *Science* 320, 1490–1492. doi: 10.1126/science.1155676

Friedrich, T., and Oschlies, A. (2009). Neural network-based estimates of north atlantic surface pCO_2 from satellite data: A methodological study. *J. Geophysical Research: Oceans* 114 (C3), 12. doi: 10.1029/2007JC004646

Furukawa, K. (2015). "Eutrophication in Tokyo Bay," in *Eutrophication and oligotrophication in Japanese estuaries: The present status and future tasks*. Ed. T. Yanagi (Dordrecht: Springer Netherlands), 5–37. doi: 10.1007/978-94-017-9915-7

Gallardo, V., and Espinoza, C. (2008). The evolution of ocean color. *Proc. SPIE - Int. Soc. Optical Eng.*, 7097. doi: 10.1117/12.794742

Gilbert, D., Rabalais, N., Diaz, R., and Zhang, J. (2010). Evidence for greater oxygen decline rates in the coastal ocean than in the open ocean. *Biogeosciences* 7, 2283–2296. doi: 10.5194/bg-7-2283-2010

Higa, H., Sugahara, S., Salem, S. I., Nakamura, Y., and Suzuki, T. (2020). An estimation method for blue tide distribution in Tokyo Bay based on sulfur concentrations using geostationary ocean color imager (GOCI). *Estuarine Coast. Shelf Sci.* 235, 106615. doi: 10.1016/j.ecss.2020.106615

Ho, D. T., Law, C. S., Smith, M. J., Schlosser, P., Harvey, M., and Hill, P. (2006). Measurements of air-sea gas exchange at high wind speeds in the southern ocean: Implications for global parameterizations. *Geophysical Res. Lett.* 33 (16), 16. doi: 10.1029/2006GL026817

Hong, B., Xue, H., Zhu, L., and Xu, H. (2022). Climatic change of summer wind direction and its impact on hydrodynamic circulation in the pearl river estuary. *J. Mar. Sci. Eng.* 10 (7). doi: 10.3390/jmse10070842

Humphreys, M. P., Lewis, E. R., Sharp, J. D., and Pierrot, D. (2022). PyCO2SYS v1.8: marine carbonate system calculations in Python. *Geoscientific Model. Dev.* 15 (1), 15–43. doi: 10.5194/gmd-15-15-2022

Jähne, B., Heinz, G., and Dietrich, W. (1974). Measurement of the diffusion coefficients of sparingly soluble gases in water. *J. Geophysical Research: Oceans* 92 (C10), 10767–10776. doi: 10.1029/JC092iC10p10767

Jiang, L.-Q., Cai, W.-J., and Wang, Y. (2008). A comparative study of carbon dioxide degassing in river- and marine-dominated estuaries. *Limnol Oceanogr* 53 (6), 2603–2615. doi: 10.4319/lo.2008.53.6.2603

Jiang, Z.-P., Tyrrell, T., Hydes, D. J., Dai, M., and Hartman, S. E. (2014). Variability of alkalinity and the alkalinity-salinity relationship in the tropical and subtropical surface ocean. *Global Biogeochem Cycles* 28 (7), 729–742. doi: 10.1002/2013GB004678

Johnson, K. S., Jannasch, H. W., Coletti, L. J., Elrod, V. A., Martz, T. R., Takeshita, Y., et al. (2016). Deep-sea durafet: A pressure tolerant ph sensor designed for global sensor networks. *Analytical Chem.* 88 (6), 3249–3256. doi: 10.1021/acs.analchem.5b04653

Kodama, K., and Horiguchi, T. (2011). Effects of hypoxia on benthic organisms in Tokyo Bay, Japan: A review. *Mar. Pollut. Bull.* 63, 215–220. doi: 10.1016/j.marpolbul.2011.04.022

Krause-Jensen, D., and Duarte, C. M. (2016). Substantial role of macroalgae in marine carbon sequestration. *Nat. Geosci* 9, 737–742. doi: 10.1038/ngeo2790

Kubo, A., Maeda, Y., and Kanda, J. (2017). A significant net sink for CO_2 in Tokyo Bay. *Sci. Rep.* 7, 44355. doi: 10.1038/srep44355

Kuwae, T., and Hori, M. (2019). *Blue carbon in shallow coastal ecosystems* (Singapore: Springer Singapore). doi: 10.1007/978-981-13-1295-3

Kuwae, T., Kanda, J., Kubo, A., Nakajima, F., Ogawa, H., Sohma, A., et al. (2016). Blue carbon in human-dominated estuarine and shallow coastal systems. *J. Ambio* 45, 290–301. doi: 10.1007/s13280-015-0725-x

Lee, J., Park, K.-T., Lim, J.-H., Yoon, J.-E., and Kim, I.-N. (2018). Hypoxia in korean coastal waters: A case study of the natural Jinhae Bay and artificial Shihwa Bay. *Front. Mar. Sci.* 5, 5. doi: 10.3389/fmars.2018.00070

Lee, K., Kim, T.-W., Byrne, R. H., Millero, F. J., Feely, R. A., and Liu, Y.-M. (2010). The universal ratio of boron to chlorinity for the North Pacific and North Atlantic oceans. *Geochimica et Cosmochimica Acta* 74, 1801–1811. doi: 10.1016/j.gca.2009.12.027

Lee, K., Tong, L. T., Millero, F. J., Sabine, C. L., Dickson, A. G., Goyet, C., et al. (2006). Global relationships of total alkalinity with salinity and temperature in surface waters of the world's oceans. *Geophysical Res. Lett.* 33. doi: 10.1029/2006GL027207

Lefèvre, N., Watson, A. J., and Watson, A. R. (2005). A comparison of multiple regression and neural network techniques for mapping *in situ* pCO_2 data. *Tellus B: Chem. Phys. Meteorol* 57 (5), 375–384. doi: 10.3402/tellusb.v57i5.16565

Liu, F., Sasaki, J., Chen, J., and Wang, Y. (2022). Numerical assessment of coastal multihazard vulnerability in Tokyo Bay. *Natural Hazards* 114, 3597–3625. doi: 10.1007/s11069-022-05533-2

Lohrenz, S. E., Cai, W.-J., Chakraborty, S., He, R., and Tian, H. (2018). Satellite estimation of coastal pCO_2 and air-sea flux of carbon dioxide in the northern Gulf of Mexico. *Remote Sens. Environ.* 207, 71–83. doi: 10.1016/j.rse.2017.12.039

Ma, J., French, K. L., Cui, X., Bryant, D. A., and Summons, R. E. (2021). Carotenoid biomarkers in namibian shelf sediments: Anoxygenic photosynthesis during sulfide eruptions in the benguela upwelling system. *Proc. Natl. Acad. Sci.* 118 (29), e2106040118. doi: 10.1073/pnas.2106040118

Majkut, J. D., Sarmiento, J. L., and Rodgers, K. B. (2014). A growing oceanic carbon uptake: Results from an inversion study of surface pCO_2 data. *Global Biogeochem Cycles* 28 (4), 335–351. doi: 10.1002/2013GB004585

Minghelli-Roman, A., Laugier, T., Polidori, L., Mathieu, S., Loubersac, L., and Gouton, P. (2011). Satellite survey of seasonal trophic status and occasional anoxic malaïgue'crises in the Thau lagoon using MERIS images. *Int. J. Remote Sens.* 32 (4), 909–923. doi: 10.1080/01431160903485794

Mohanty, S., Raman, M., Mitra, D., and Chauhan, P. (2022). Surface pCO_2 variability in two contrasting basins of north indian ocean using satellite data. *Deep Sea Res. Part I: Oceanographic Res. Papers* 179, 103665. doi: 10.1016/j.dsr.2021.103665

Mojica Prieto, F. J., and Millero, F. J. (2002). The values of pK1 + pK2 for the dissociation of carbonic acid in seawater. *Geochimica et Cosmochimica Acta* 66, 2529–2540. doi: 10.1016/S0016-7037(02)00855-4

Moussa, H., Benallal, M., Goyet, C., and Lefèvre, N. (2016). Satellite-derived CO_2 fugacity in surface seawater of the tropical atlantic ocean using a feedforward neural network. *Int. J. Remote Sens.* 37 (3), 580–598. doi: 10.1080/01431161.2015.1131872

Najjar, R. G., Herrmann, M., Valle, S. M. C. D., Friedman, J. R., Friedrichs, M. A., Harris, L. A., et al. (2020). Alkalinity in tidal tributaries of the Chesapeake Bay. *J. Geophysical Research: Oceans* 125, e2019JC015597. doi: 10.1029/2019JC015597

Nellemann, C., Corcoran, E., Duarte, C. M., Valedes, L., De Young, C., Fonseca, L., et al. (2009). *Blue carbon : the role of healthy oceans in binding carbon : a rapid response assessment*, UNEP(02)/B659. (Norway: GRID-Arendal).

Norman, M., Parampil, S. R., Rutgersson, A., and Sahlée, E. (2013). Influence of coastal upwelling on the air–sea gas exchange of CO_2 in a Baltic Sea basin. *Tellus B: Chem. Phys. Meteorol* 65, 21831. doi: 10.3402/tellusb.v65i0.21831

Orr, J. C., Epitalon, J.-M., Dickson, A. G., and Gattuso, J.-P. (2018). Routine uncertainty propagation for the marine carbon dioxide system. *Mar. Chem.* 207, 84–107. doi: 10.1016/j.marchem.2018.10.006

Otsubo, K., Harashima, A., Miyazaki, T., Yasuoka, Y., and Muraoka, K. (1991). Field survey and hydraulic study of "aoshio" in Tokyo Bay. *Mar. Pollut. Bull.* 23, 51–55. doi: 10.1016/0025-326X(91)90649-D

Pearson, J., Resplandy, L., and Poupon, M. (2022). Coastlines at risk of hypoxia from natural variability in the northern indian ocean. *Global Biogeochem Cycles* 36 (6), e2021GB007192. doi: 10.1029/2021GB007192

Sarma, V. V. S. S., Saino, T., Sasaoka, K., Nojiri, Y., Ono, T., Ishii, M., et al. (2006). Basin-scale pCO_2 distribution using satellite sea surface temperature, Chl *a*, and climatological salinity in the North Pacific in spring and summer. *Global Biogeochem Cycles* 20 (3), 13. doi: 10.1029/2005GB002594

Sasaki, J., Ito, K., Suzuki, T., Wiyono, R. U. A., Oda, Y., Takayama, Y., et al. (2012). Behavior of the 2011 tohoku earthquake tsunami and resultant damage in Tokyo Bay. *Coast. Eng. J.* 54, 1250012. doi: 10.1142/S057856341250012X

Sasaki, J., Kanayama, S., Nakase, K., and Kino, S. (2009a). Effective application of a mechanical circulator for reducing hypoxia in an estuarine trench. *Coast. Eng. J.* 51, 309–339. doi: 10.1142/S0578563409002053

Sasaki, J., Kawamoto, S., Yoshimoto, Y., Ishii, M., and Kakino, J. (2009b). Evaluation of the amount of hydrogen sulfide in a dredged trench of Tokyo Bay. *J. Coast. Res.* SI56, 890–894.

Schunck, H., Lavik, G., Desai, D. K., Großkopf, T., Kalvelage, T., Löscher, C. R., et al. (2013). Giant hydrogen sulfide plume in the oxygen minimum zone off Peru supports chemolithoautotrophy. *PloS One* 8 (8), 1–18. doi: 10.1371/journal.pone.0068661

Signorini, S. R., Mannino, A., Najjar, R. G.Jr., Friedrichs, M. A. M., Cai, W.-J., Salisbury, J., et al. (2013). Surface ocean pCO_2 seasonality and sea-air CO_2 flux estimates for the North American east coast. *J. Geophysical Research: Oceans* 118 (10), 5439–5460. doi: 10.1002/jgrc.20369

Stephens, M. P., Samuels, G., Olson, D. B., Fine, R. A., and Takahashi, T. (1995). Sea-Air flux of CO_2 in the North Pacific using shipboard and satellite data. *J. Geophysical Research: Oceans* 100 (C7), 13571–13583. doi: 10.1029/95JC00901

Taguchi, F., Fujiwara, T., Yamada, Y., Fujita, K., and Sugiyama, M. (2009). Alkalinity in coastal seas around Japan. *Bull. Coast. Oceanogr* 47 (1), 71–75. doi: 10.32142/engankaiyo.47.1_71

Testa, J. M., Clark, J. B., Dennison, W. C., Donovan, E. C., Fisher, A. W., Ni, W., et al. (2017). Ecological forecasting and the science of hypoxia in Chesapeake Bay. *BioScience* 67 (7), 614–626. doi: 10.1093/biosci/bix048

Tokoro, T., Hosokawa, S., Miyoshi, E., Tada, K., Watanabe, K., Montani, S., et al. (2014). Net uptake of atmospheric CO_2 by coastal submerged aquatic vegetation. *Global Change Biol.* 20 (6), 1873–1884. doi: 10.1111/gcb.12543

Tokoro, T., Nakaoka, S., Takao, S., Kuwae, T., Kubo, A., Endo, T., et al. (2021). Contribution of biological effects to carbonate-system variations and the air–water CO_2 flux in urbanized bays in japan. *J. Geophysical Research: Oceans* 126 (6), e2020JC016974. doi: 10.1029/2020JC016974

Tokoro, T., Watanabe, A., Kayanne, H., Nadaoka, K., Tamura, H., Nozaki, K., et al. (2007). Measurement of air–water CO_2 transfer at four coastal sites using a chamber method. *J. Mar. Syst.* 66 (1), 140–149. doi: 10.1016/j.jmarsys.2006.04.010

Tomita, A., Nakura, Y., and Ishikawa, T. (2016). New direction for environmental water management. *Mar. Pollut. Bull.* 102, 323–328. doi: 10.1016/j.marpolbul.2015.07.068

Vaquer-Sunyer, R., and Duarte, C. M. (2008). Thresholds of hypoxia for marine biodiversity. *Proc. Natl. Acad. Sci.* 105 (40), 15452–15457. doi: 10.1073/pnas.0803833105

Wang, K., Nakamura, Y., Sasaki, J., Inoue, T., Higa, H., Suzuki, T., et al. (2022). An effective process-based modeling approach for predicting hypoxia and blue tide in Tokyo Bay. *Coast. Eng. J.* 64 (3), 458–476. doi: 10.1080/21664250.2022.2119011

Wanninkhof, R. (1992). Relationship between wind speed and gas exchange over the ocean. *J. Geophysical Research: Oceans* 97, 7373–7382. doi: 10.1029/92JC00188

Wanninkhof, R. (2014). Relationship between wind speed and gas exchange over the ocean revisited. *Limnol Oceanogr: Methods* 12 (6), 351–362. doi: 10.4319/lom.2014.12.351

Weiss, R. (1974). Carbon dioxide in water and seawater: the solubility of a non-ideal gas. *Mar. Chem.* 2 (3), 203–215. doi: 10.1016/0304-4203(74)90015-2

Williams, N. L., Juranek, L. W., Feely, R. A., Johnson, K. S., Sarmiento, J. L., Talley, L. D., et al. (2017). Calculating surface ocean pCO_2 from biogeochemical argo floats equipped with pH: An uncertainty analysis. *Global Biogeochem Cycles* 31 (3), 591–604. doi: 10.1002/2016GB005541

Williams, N. L., Juranek, L. W., Johnson, K. S., Feely, R. A., Riser, S. C., Talley, L. D., et al. (2016). Empirical algorithms to estimate water column pH in the southern ocean. *Geophysical Res. Lett.* 43 (7), 3415–3422. doi: 10.1002/2016GL068539

Xu, Y.-Y., Pierrot, D., and Cai, W.-J. (2017). Ocean carbonate system computation for anoxic waters using an updated CO2SYS program. *Mar. Chem.* 195, 90–93. doi: 10.1016/j.marchem.2017.07.002

Yamamoto, T. (2003). The seto inland Sea —- eutrophic or oligotrophic? *Mar. Pollut. Bull.* 47, 37–42. doi: 10.1016/S0025-326X(02)00416-2

Zemmelink, H. J., Slagter, H. A., van Slooten, C., Snoek, J., Heusinkveld, B., Elbers, J., et al. (2009). Primary production and eddy correlation measurements of CO_2 exchange over an intertidal estuary. *Geophysical Res. Lett.* 36 (19), 5. doi: 10.1029/2009GL039285

Frontiers in Marine Science

Explores ocean-based solutions for emerging global challenges

The third most-cited marine and freshwater biology journal, advancing our understanding of marine systems and addressing global challenges including overfishing, pollution, and climate change.

Discover the latest Research Topics

See more →

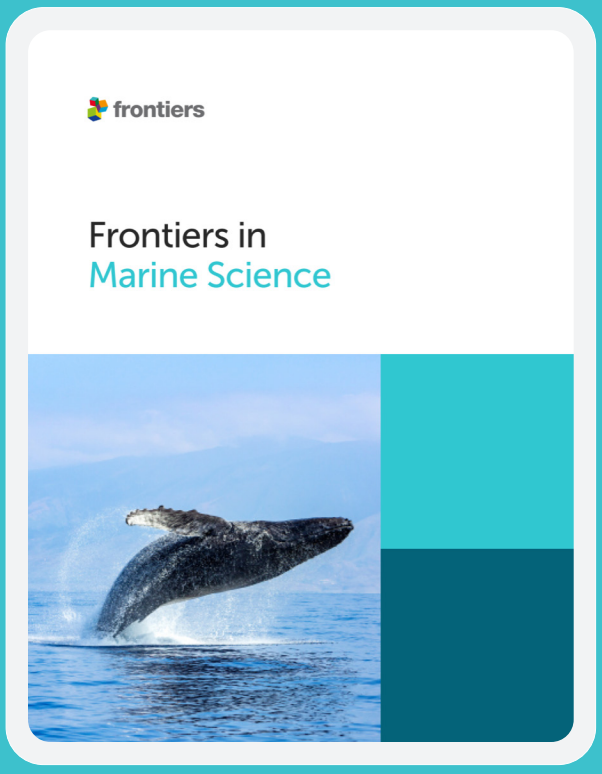

Frontiers

Avenue du Tribunal-Fédéral 34
1005 Lausanne, Switzerland
frontiersin.org

Contact us

+41 (0)21 510 17 00
frontiersin.org/about/contact